An experimental study of localized compaction in high porosity rocks : the example of Tuffeau de Maastricht

Athanasios Papazoglou

Communauté UNIVERSITÉ Grenoble Alpes

THÈSE

Pour obtenir le grade de

DOCTEUR DE LA COMMUNAUTE UNIVERSITE GRENOBLE ALPES

Spécialité : 2MGE : Matériaux, Mécanique, Génie civil, Electrochimie

Arrêté ministériel : 25 mai 2016

Présentée par

ATHANASIOS PAPAZOGLOU

Thèse dirigée par **Gioacchino Viggiani** et codirigée par **Christophe Dano** et **Giuseppe Buscarnera**

préparée au sein du **Laboratoire Sols, Solides, Structures et Risques**
dans **l'École Doctorale I-MEP2 - Ingénierie - Matériaux, Mécanique, Environnement, Energétique, Procédés, Production**

An experimental study of localized compaction in high porosity rocks: the example of Tuffeau de Maastricht

Une étude expérimentale des bandes de compaction dans les roches très poreuses: l'exemple du Tuffeau de Maastricht

Thèse soutenue publiquement le **13 décembre 2018**,
devant le jury composé de :

Monsieur Gioacchino VIGGIANI
Professeur, Université Grenoble Alpes, Directeur de thèse
Monsieur Patrick BAUD
Professeur, EOST, Université de Strasbourg, Rapporteur
Monsieur Manolis VEVEAKIS
Assistant Professor, Duke University, USA, Rapporteur
Monsieur Frederic Victor DONZE
Professeur, Université Grenoble Alpes, Président
Monsieur Pierre BESUELLE
Chargé de recherche, CNRS, Examinateur
Madame Eleni GEROLYMATOU
Associate Professor, Chalmers University of Technology, Sweden, Examinatrice
Monsieur Giuseppe BUSCARNERA
Associate Professor, Northwestern University, USA, Invité
Monsieur Christophe DANO
Maître de Conférences, Université Grenoble Alpes, Invité
Madame Helen LEWIS
Associate Professor, Heriot-Watt University, UK, Invitée

To my wife, Galateia Terti

Acknowledgments

First and foremost, I would like to offer a sincere Thank you to my advisors Cino Viggiani, Christophe Dano, and Giuseppe Buscarnera for being next to me to this challenging and exciting journey. This Ph.D. thesis gives me the title of Doctor that will be attached to my name, but it wouldn't be possible without them. I want to express my sincere gratitude for believing in me and for giving me the opportunity to discover a new world.

Their different personality, background and experience compose one of the most complete, competitive and dynamic groups I have ever met. Among other attributes, Cino's leading profile, Christophe's meekness, plus Giuseppe's passion constitute an excellent supervising scheme. Cino, you believed in me before me, and I will never forget it. You were there at any time of the day with priceless advice on any topic. Your boundless enthusiasm for research was an extra motivation for me. Christophe, your loyalty on your targets and your delicate approach in any problem, makes your colleagues' life must easier. Giuseppe, your desire for knowledge and competitiveness has been a great inspiration for me. Many thanks for hosting me at Northwestern University (U.S.A.).

I would like to express my appreciation to my committee (Dr. P. Baud, Dr. M. Veveakis, Dr. F. Donze, Dr. P. Bésuelle, Dr. E. Gerolymatou, and Dr. H. Lewis) for the insightful comments and the valuable discussion during my thesis defense. It was a great pleasure to exchange opinions and experiences with such high-quality scientists. I hope that we will meet scientifically again in the future.

I would like to acknowledge also the following people who provided expertise and information that were crucial for the completion of this dissertation: Jacques Desrues who was very open to discuss my topic and share his knowledge on strain localization; Pierre Bésuelle for his valuable advice and comments on the experiments; Edward Andò and Nicolas Lenoir who were always willing to help me with x-ray tomography; Steven Hall for hosting me at Lund University; Ferdinando Marinelli who replied to my modeling concerns and struggles in a direct and effective way; Ghassan Shahin who was very open to share his experience in modeling and welcoming me at Northwestern University. Erminio Salvatore, Zeynep Karatza, Max Wiebicke, and Cyrille Couture who were always willing to share with me their experimental expertise.

I would like to extend my gratitude to Prof. Manolis Veveakis as well as to Prof. Jidong Zhao for their interest in my project and their priceless advices during our fruitful discussions. The experience of working with them and their scientific groups (Sotiris Alevizos, Mustafa Sari, and Huaran Wu) broadened my scientific horizons. I am thrilled that these collaborations are sealed with two scientific articles.

I am especially grateful to Pascal Charrier who has helped considerably to the technical side of this work. His unmatched patience with the non-french speakers, the willingness to help at any time of the day and always with a smile gives him the title of the best technician I have ever worked with.

My biggest Thank you goes to my families, prior and new back in Greece. Many thanks to my parents and sisters for being next to me and supporting my choices; and especially to my mother in law who was next to me during this exciting but also challenging journey. She was courageous enough to stay awake all the sleepless nights while I was writing this thesis to support me. I am really grateful for your support.

Special thanks to my lovely wife for being always next to me as an angel on my shoulders guiding my life. Her desire for new things, the courage to face the unknown and her perfectionism on everything she is involved will never stop to surprise me. I am writing these lines now because of her. She knew that I was able to do this step already some years before I did. My dear, I am truly thankful that you are always by my side and thinking for me before me.

I would like to extend gratitude to my real friends back in Greece, Andreas, and Argiro for their friendship that is beyond distance. Of course, I could not forget my new real friends, Spyros and Mathias. They taught me that real friends don't look age or nationality. To continue, I would like to say a big Thank you to the people who came to my life during the last four years and will be forever in my heart. These include people from the Ladoratoire 3SR, Northwestern University and the Greek community in Grenoble. Last but not least I am thankful for the best group of which I have ever been member in my life until now, *The Ph.D. Seeds*.

Abstract

Given their high porosity, carbonates form important water and hydrocarbons reservoirs, and they are also suitable for other applications such as CO_2 storage and nuclear waste disposal. However, localized compaction in carbonates affects the stress field and the hydromechanical properties of these rocks leading to inelastic deformation and failure with potential economic, environmental and social impacts. Previous field and experimental studies have shown that in porous carbonates, unlike sandstones, a variety of micromechanisms such as pore collapse, grain crushing, debonding, crystal plasticity and pressure solution can lead to inelastic compaction. Due to the coexistence of such multiple inelastic processes and the interplay among them, the dominant micromechanism responsible for failure remains poorly understood.

This doctoral thesis presents an experimental investigation into the deformation mechanisms governing the mechanical behavior and failure mode of high porosity carbonate rocks. To this end, Tuffeau de Maastricht, a bioclastic sedimentary limestone exhibiting up to 52% porosity, has been tested under dry conditions. This study focuses on how stress path, confining pressure and bedding orientation affect the onset and propagation of localized compaction. Three main experimental campaigns are conducted on cylindrical specimens of 11.5 mm diameter and 22 mm height to study the brittle-ductile transition: (i) isotropic compression, (ii) uniaxial compression, and (iii) triaxial compression tests at confining pressures ranging from 1 to 5 MPa. A systematic analysis of the anisotropic behavior of Tuffeau de Maastricht is conducted on samples cored perpendicular, oblique (45°) and parallel to the bedding plane. High resolution x-ray computed tomography (CT) is used to obtain 3D images of the entire specimen under loading. The acquired images are processed and full-field measurements have been used to elucidate the mechanics of initiation and propagation of localized compaction. Porosity variations during loading are measured macroscopically as well as locally. The porosity measurements are performed over a REV, which is defined with the use of statistical tools. The systematic use of x-ray micro tomography combined with the use of advanced image analysis and Digital Image Correlation (DIC) provides a quantitative 3D information the strain field inside a sample and its evolution during a test.

Two failure modes are identified, based on porosity measurements and DIC: compactive shear bands at low confining pressure, and compaction bands (perpendicular to the maximum compressive stress) at higher confinement. These bands develop at essentially constant deviator stress and propagate through the whole sample punctuated by episodic stress drops. Triaxial compression tests at much higher axial strain present three distinct phases: (1) an initial quasi-linear increase of deviator stress, followed by (2) a plateau and (3) a post-plateau hardening. The essential observation from these experiments if the occurrence of a debonding phase which converts the specimen from rock-like to sand-like. A second localization, typical of dense sand,

eventually occurs for very high axial strain. Additional experiments that are performed on artificially debonded specimens emphasize this destructuration phase during the plateau of deviator stress. The experimental results also highlight the strong anisotropy of the mechanical behavior of the studied material.

Résumé

En raison de leur porosité élevée, les roches carbonatées forment d'importants réservoirs d'eau et d'hydrocarbures, et conviennent également à d'autres applications telles que le stockage de CO_2 ou des déchets nucléaires. Cependant, le compactage localisé dans les roches carbonatées affecte le champ des contraintes et les propriétés hydromécaniques de ces roches, entraînant des déformations inélastiques et des dommages avec des impacts économiques, environnementaux et sociaux potentiels. Des études antérieures sur le terrain et des études expérimentales en laboratoire que dans les roches carbonatées poreuses, contrairement aux grès, une variété de micromécanismes tels que l'effondrement des pores, le broyage des grains, la petre de cimentation, la plasticité des cristaux et la dissolution sous contrainte peuvent entraîner une densification inélastique. En raison de la coexistence de ces multiples processus inélastiques et de leur interactions, le micromécanisme prédominant à l'origine du processus de localisation et de rupture reste mal compris.

Cette thèse de doctorat présente une étude expérimentale sur les mécanismes de déformation régissant le comportement mécanique et le mode de rupture des roches carbonatées à haute porosité. A cet effet, le Tuffeau de Maastricht, un calcaire sédimentaire bioclastique présentant jusqu'à 52 % de porosité, a été testé à l'état sec. Cette étude s'est concentrée sur la façon dont le chemin des contraintes, la pression de confinement et l'orientation de la stratification influent sur l'apparition et la propagation des bandes de compaction. Trois campagnes expérimentales principales sont menées sur des éprouvettes cylindriques de 11,5 mm de diamètre et de 22 mm de hauteur pour étudier la transition fragile-ductile : (i) compression isotrope, (ii) compression uniaxiale et (iii) compression triaxiale à des pressions de confinement allant de 1 à 5 MPa. Une analyse systématique du comportement anisotrope du Tuffeau de Maastricht est effectuée sur des échantillons qui ont été forés perpendiculairement, obliquement (45°) et parallèlement au plan de la stratification. La micro-tomographie à rayons X à haute résolution est utilisée pour obtenir des images 3D de l'ensemble de l'échantillon en cours de chargement. Les images acquises sont traitées et des mesures de plein champ ont été utilisées pour élucider les mécanismes d'initiation et de propagation des zones de compactage localisées. Les variations de porosité pendant le chargement sont mesurées macroscopiquement et localement. Les mesures de porosité sont effectuées sur un REV, qui est défini à l'aide d'outils statistiques. L'utilisation systématique des rayons X (CT) combinée à l'utilisation de l'analyse d'image avancée et de la corrélation d'images numérique (CIVD) fournit une information 3D quantitative du champ de déformation et de son évolution pendant un test.

Deux modes de rupture sont identifiés, selon les mesures de porosité et la CIVD : les bandes de cisaillement contractantes développées à basse pression de confinement et les bandes de

compaction formées perpendiculairement à la contrainte principale majeure de compression à un confinement plus élevé. Ces bandes se développent à contrante déviatoire presque constante et se propagent dans tout l'échantillon, phase marquée par des chutes épisodiques de la contrainte deviatoire. Les essais de compression triaxiale conduit à des niveux de déformation axiale plus élevée présentent trois phases distinctes : une phase initiale quasi-linéaire, suivie par un plateau de contrainte déviatoire, enfin un durcissement post-plateau. L'observation essentielle de ces expériences est l'existence d'un mécanisme de dégradation del la cimentation entre grains qui transforme l'échantilon cohésif et frottant en un miliu granulaire purement frottant. Une deuxième localisation typique des sables denses se développe dans la phase post-plateau pour de grandes déformation axiales. D'autres expériences réalisées sur du sable obtenu par dégradation artificielle de la roche originelle mettent l'accent sur cette phase de déstructuration qui se produit lors du plateau de la contrainte déviatoire. Les résultats expérimentaux mettent également en évidence la forte influence due à l'anisotropie sur le comportement mécanique du matériau étudié alors que le modèle de localisation n'est pas affecté.

Contents

List of Figures

List of Tables

Chapter 1

Introduction

1.1 Motivation and objectives of the thesis

Highly porous carbonate rocks are of importance in many geotechnical applications. The mechanics of these materials is controlled by interactions among micro-structural units and involves processes such as debonding, crack propagation, grain breakage, and pore collapse. These small-scale processes are responsible for inelastic deformation of carbonate rocks. In general, rocks can undergo volume changes at all stages even during the process of their formation and subsequently when they are loaded. In response to the applied load (mechanical, thermal, hydraulic,...) the pore space of a porous rock may either dilate or compact.

Volumetric deformation in carbonate rocks is a crucial issue in reservoir and geotechnical engineering – especially considered that more than 60% of the world's oil and 40% of the world's gas reserves are held in carbonates (Schlumberger Market Analysis 2007). As production reduces reservoir pressure, effective stress acting on the solid rock matrix is increasing due to the weight of the overlaying formations (Mowar *et al.*, 1996). This phenomenon can impact the stress field and the hydromechanical properties of the carbonates, leading to inelastic deformation and failure manifested by phenomena such as surface subsidence, well failure and induced seismicity (Geertsma *et al.*, 1973, Johnson *et al.*, 1988, Fredrick *et al.*, 1998, Wong *et al.*, 2004). Given their high porosity, carbonates are suitable for other applications such as geological storage of CO_2 (carbon dioxide) and nuclear waste disposal, in which the carbonate rock acts as either a reservoir or a cap rock. In all these cases, it is of paramount importance to deeply understand the mechanical behavior of high porosity carbonate rocks, and in particular their volumetric behavior when approaching failure.

The mechanisms by which high porous rocks such as sandstones and limestones respond to deformation differ fundamentally from those observed in low porosity and non-porous rocks (Fossen *et al.*, 2017). Previous studies have shown that the failure mechanisms in porous rocks are highly dependent on the mean stress level (*e.g.*, Wong *et al.*, 1997, Bésuelle *et al.*, 2000, Sulem and Ouffroukh, 2006, Charalampidou *et al.*, 2011). In geomaterials, failure typically appears in thin or extended strain localization structures, where most of the deformation is concentrated. In porous rocks, three modes of strain localization associated with inelastic compaction are observed in the laboratory: compactive shear bands (*e.g.*, Bésuelle, 2001b, Bésuelle *et al.*, 2003, Charalampidou *et al.*, 2014, Ji *et al.*, 2014), compaction bands (*e.g.*, Baud *et al.*, 2004, Baxevanis *et al.*, 2006), and

homogeneous cataclastic flow (*e.g.*, Menéndez *et al.*, 1996, Wu *et al.*, 2000). Among these strain localization structures, compaction bands in particular have received increasing attention in the recent years. As a kinematic end-member of strain localization, compaction bands are planar zones in which shear is less or comparable to compaction (Hill, 1993, Mollema and Antonellini, 1996). These well-defined compactive zones form at relatively high angles, if not subperpendicular to the major compressive stress. Although these bands are roughly planar, they occur in a variety of configurations with varying thicknesses, spacing, waviness, and orientations. Due to their reduced porosity, compaction bands constitute barriers to fluid flow, affecting the injection and extraction of fluids for storage or energy production.

Inelastic deformation and strain localization in sandstone have been extensively studied over the last two decades (*e.g.*, Aydin *et al.*, 2006, Wong and Baud, 2012). In porous sandstones, a transition of the failure mode from brittle faulting to cataclastic flow occurs as effective pressure increases. Laboratory studies have demonstrated that localized compaction is an important failure mode in porous sandstones particularly at stress states associated with the brittle-ductile transition (*e.g.*, Wong *et al.*, 2001). In particular, localized compaction is most likely to occur when porosity is higher than 16% (Holcomb *et al.*, 2007). Hence, the mechanical behavior and failure mode of a porous sandstone are influenced among other parameters by the porosity (and its changes in response to the applied stress) and the grain size distribution (Zhang *et al.*, 1990a, Wong *et al.*, 1997, Cheung *et al.*, 2012). Microstructural observations on naturally and experimentally deformed samples have highlighted the links between the deformation mechanisms at the grain scale and the failure mode observed at the macroscale. Inelastic compaction in sandstone samples, derives primarily from grain crushing initiated by stress concentrations at grain contacts and by pore collapse (Menéndez *et al.*, 1996, Wu *et al.*, 2000, Charalampidou, 2011). Due to the decrease of porosity, significant permeability reduction is associated with this compaction (Zhu and Wong, 1997, Vajdova *et al.*, 2004b, Baud *et al.*, 2012).

Experimental studies have shown that the compactive behavior of porous carbonates is similar to the less porous limestones as well as to many porous sandstones (Vajdova *et al.*, 2004a, Baud *et al.*, 2009). However, the experimental investigation of strain localization in carbonate rocks has proven more challenging than in sandstones. In carbonates, unlike for sandstone, because of crystal plasticity, microcracking is not always the dominant micromechanism of deformation. A great variety of mechanisms such as pore collapse (Zhu *et al.*, 2010, Vajdova *et al.*, 2012) and grain crushing (Baud *et al.*, 2009, Cilona *et al.*, 2012), but also crystal plasticity and pressure solution (Croize *et al.*, 2013) can potentially play an important role even at room temperature. Additional studies on carbonate rocks have shown that grain rotations (Tondi *et al.*, 2006), pores and grains orientation, as well as the degree of cementation (Baud *et al.*, 2017a) and bedding heterogeneities may lead to inelastic compaction (localized or not). Possibly because of such a complex picture, there is a paucity of mechanical and microstructural laboratory data on the brittle-ductile transition in high porosity carbonates. To the best of our knowledge, the existing experimental data on localized compaction in high-porosity carbonate rock are limited in number and generally restricted to relatively low axial strains.

The purpose of this study is to experimentally investigate the mechanical behavior and failure mode of a high porosity carbonate rock. To this end, Tuffeau de Maastricht, a highly porous limestone with 50% porosity, has been tested under dry conditions, focusing on how stress path, confining pressure and bedding orientation affect the onset of localized compaction. A series of

triaxial compression tests are performed at confining pressures ranging from 0 to 5 MPa on samples cored perpendicular, oblique (45°), and parallel to the bedding plane. This study presents a large set of mechanical data for isotropic and axisymmetric loadings. Localized compaction is studied from a multiscale perspective, focusing on microstructural mechanisms that control the macroscopic behavior. Triaxial compression tests are conducted up to very high axial strain ($\epsilon_a \approx 50\%$) well beyond the end of the relative plateau of deviator stress. It is shown that a second localization typical of dense sand is developed at high axial strain. In order to investigate the strength anisotropy of the material, an extensive experimental campaign is performed on samples cored at 3 different orientations. A few additional experiments are performed on artificially debonded specimens of Tuffeau de Maastricht. These experiments are used as a reference for better understanding the response of the natural material. Last and most important, the majority of these experiments are performed *in-situ* in an x-ray tomograph. The systematic use of x-ray Computed Tomography (CT) combined with the use of advanced image analysis provides a quantitative 3D information of the strain field and its evolution during a test. These full-field measurements add a unique insight into the mechanics of initiation and propagation of localized compaction zones in carbonate rocks. The ultimate objective of this study is to use the data from the full-field experiments to calibrate and validate mechanical models that can capture inelastic compaction in porous rocks.

1.2 Structure of the thesis

The thesis is organized in seven chapters as follows:

- Chapter 1: provides the introduction and motivation of this study.
- Chapter 2: presents findings from a literature review on localized deformation in porous rocks with particular focus on compaction bands. This review covers field and laboratory studies on microstructural mechanisms focusing on pore collapse. Finally, this chapter highlights the use of full-field measurements that provide quantitative data on strain localization.
- Chapter 3: describes all the details about the material tested, the tests performed (procedure and specimen preparation), as well as the devices used during the different experimental campaigns.
- Chapter 4: introduces the methodology and the image analysis tools used for this study. X-ray Computed Tomography and x-ray scanner of Laboratoire 3SR are briefly presented. Details are provided for the method employed to reconstruct 3D images, as well as for the selection of optimum parameters allowing the better visualization of the microstructure of the material. This chapter focuses on the way in which the 3D images are manipulated to extract quantitative information at the grain scale. A detailed analysis to define the Representative Elementary Volume (REV) in order to perform local porosity measurements is presented. Finally, herein is also described the "continuum" local kinematic measurements that can be made between 3D images, using Digital Image Correlation (DIC).
- Chapter 5: presents the results obtained from the experimental campaigns described in chapter 3. The macroscopic mechanical behavior of Tuffeau de Maastricht under isotropic

and triaxial compression is presented. In addition, this chapter describes evolution of porosity and strain fields obtained by the quantitative analysis of the x-ray tomographic images acquired during the tests.

- Chapter 6: presents the calibration of a constitutive model (Buscarnera and Laverack, 2014) based on the experimental data shown in chapter 5. This part of the doctoral work was performed during a six-month stay at Northwestern University, Chicago, IL, (USA). It should be noted that this chapter is prepared as a journal article (submitted).
- Chapter 7: summarizes the major findings of this study, and discusses possible perspectives for future work.

Chapter 2

State of the art

2.1 Experimental studies of localized deformation in porous rocks

Localization structure is the concentration of the intensity of a quantity within one or several zones that are defined geometrically (Grédiac and Hild, 2012). *Strain localization*, the localization of kinematic quantities, is a deformation and failure phenomenon that is pervasive in the Earth's crust. This is due to a mechanical instability referred as bifurcation phenomenon, which is the transition from a homogeneous deformation process to an inhomogeneous one (Rudnicki and Rice, 1975).

Localization can take many, and sometimes complex, configurations. In particular, failure of granular rocks under natural and laboratory loading conditions can be distinguished based on kinematics, geometry, and texture due to a variety of micromechanical processes (Aydin *et al.*, 2006, Fossen *et al.*, 2007). Aydin *et al.* (2006) presented a broad kinematics-based classification of failure modes in granular rocks. A first examination distinguishes between cracks and deformation bands. The first case corresponds to the loss of continuity by the solid itself, leading to what is called as a *sharp discontinuity* of the displacement field. This category includes fractures with predominately shearing surfaces and discontinuities with predominately volumetric deformation (*e.g.*, fractures, pressure solution surfaces). This category of failure mode is not within the scope of the present study. Conversely, the second case is that of a *weak discontinuity* in which the displacement field remains continuous, but one or several of its derivatives are discontinuous (Desrues and Réthoré, 2013). This category encompasses structures that form by strain localization into narrow tabular bands, the so called *deformation bands*. Kinematic classification of deformation bands includes shear, dilation, and compaction bands or a combination of these modes (Figure 2.1). Bands whose primary attribute is shearing, are referred as *shear bands*. These shear bands are further separated into i) *compactive shear bands*, and ii) *dilation shear bands*, depending on additional volume change (compaction or dilation, respectively)(Figure 2.2). In case that volumetric deformation is predominant, the bands are called *volumetric deformation bands*. The latter group can be subdivided into *compaction bands* (volume reduction) or *dilation bands* (volume enlargement) depending on the sign of the volume change.

The mechanisms by which high porous rocks such as sandstones and limestones respond to deformation differ fundamentally from that of low porosity and non-porous rocks (Fossen *et al.*, 2017). Deformation mechanisms depend on internal and external conditions such as mineralogy,

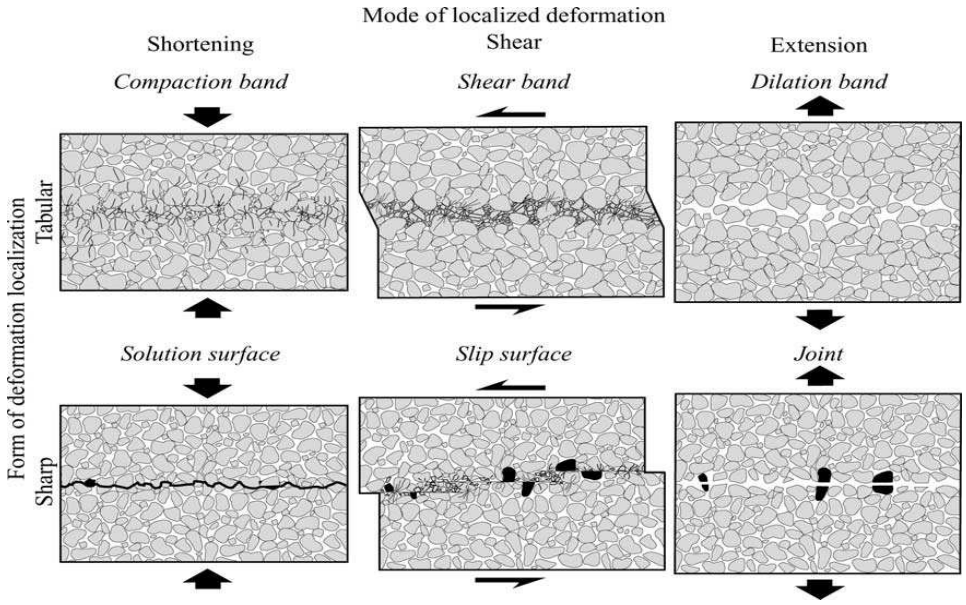

Figure 2.1: Schematic illustration of structures from various failure modes in granular rock. On the top deformation bands appears in narrow tabular zones, such as compaction, shear, and dilation bands. On the bottom row, sharp discontinuities are depicted. After Aydin *et al.* (2006).

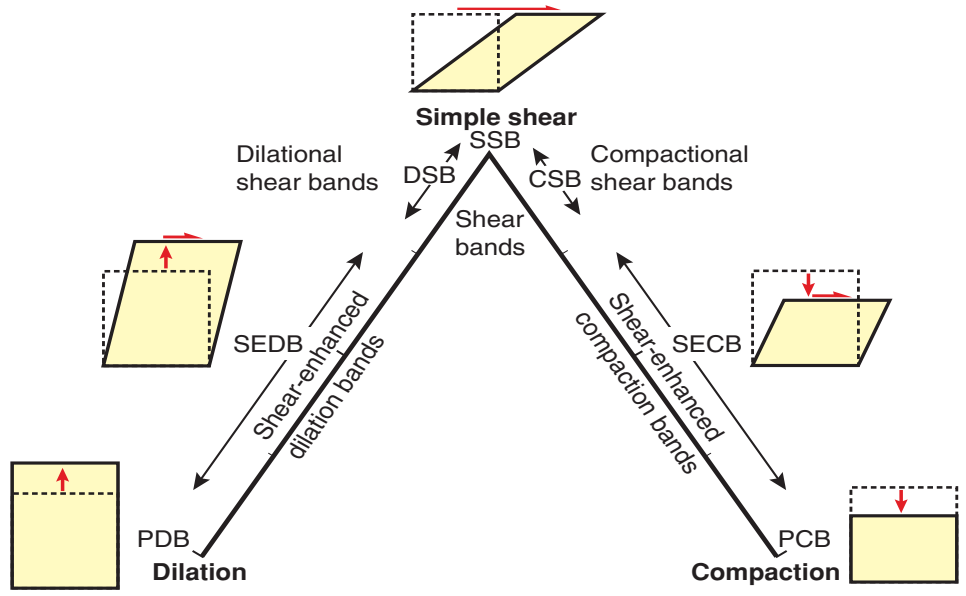

Figure 2.2: Schematic diagram of kinematics-based classification of deformation bands. PDB: pure dilation band, SEDB: Shear-enhanced dilation band, DSB: dilation shear band, SSB: simple shear band, CSB: compaction shear band, SECB: shear-enhanced compaction band, PCB: pure compaction band. After Fossen *et al.* (2017).

grain size, shape, sorting, cementation, porosity, stress state and stress path. In porous rocks, four failure modes associated with localized deformation are observed in the laboratory. At low confining pressures the mechanical response and failure mode of porous sandstone, are typical of brittle faulting regime. The deviatoric stress ($\sigma_1 - \sigma_3$) attains a peak, beyond which strain softening is observed, accompanied by a rapid stress drop. Because of the frictional component of the behavior, the peak stress shows a positive correlation with the confining pressure and mean stress. The volume initially decreases probably due to crack closure and elastic grain contact deformation, but near the peak stress it reverses to an increase indicating the inception of dilatancy. Visual inspection of the failed samples reveal the development of localized failure with a range of inclinations (from 0 to 30°) with respect to the σ_1 direction (*e.g.*, Bésuelle *et al.*, 2003, Klein *et al.*, 2001, Menéndez *et al.*, 1996, Bésuelle *et al.*, 2000, Wu *et al.*, 2000,Klein *et al.*, 2001, Bésuelle *et al.*, 2003). Similar behavior, at low confining pressure is observed also in porous carbonates (Vajdova *et al.*, 2004a). However, for a number of high-porosity limestones, instead of dilatancy, shear-enhanced compaction is observed even at low confining pressures (Baud *et al.*, 2009, 2017a).

Brace (1978) proposed that the comparison of the isotropic and deviatoric data, can provide critical information on the onset and development of inelastic compaction. Any deviation from the isotropic compression curve would imply that the porosity change is induced by the deviator stress in the axisymmetric conditions (Figure 2.3). At stress levels beyond the inflection point, the deviator stress provides significant contribution to the compactive strain, and this phenomenon is referred as *shear-enhanced compaction* (Wong *et al.*, 1997). Klein *et al.* (2001) notice that for a relative broad range of confining pressures, the mechanical behavior and failure mode of Bentheim sandstone samples cannot be identified as in the brittle or ductile regime. A small amount of strain softening follows the peak-stress, dilatancy is negligible and the failure mode is described by several conjugate shear bands. In the transitional regime, also referred as semi-brittle regime (Bésuelle *et al.*, 2000, 2001a), at "medium" pressures, shear bands develop at an angle (relative to the maximum compression direction) significantly larger than that in the brittle regime. Shear-enhanced compaction failure mode has been often documented in porous sandstones (*e.g.*, Wong *et al.*, 2001, Mair *et al.*, 2002, Bésuelle *et al.*, 2003, Baud *et al.*, 2004, Baud *et al.*, 2006, Charalampidou, 2011, 2012). High-angle shear compacting bands in the transitional regime are observed also in porous carbonate rocks (Ji *et al.*, 2014, Baud *et al.*, 2009, Baud *et al.*, 2017b). Cilona *et al.* (2012) showed that samples with approximately same porosity (30%) can present conjugate shear bands with a variable forming angles. They also suggest that grain size could be responsible for these variations.

Figure 2.4 shows the different failure modes that are identified as a function of confining pressure (Weinberg *et al.*, 2015). As it is already presented above, shear bands with dilatancy appear under low mean stress, and compaction shear bands under higher mean stress. At even more higher stress (in some cases still in the transitional regime) compaction bands observed in field but also in the laboratory for both sandstones (*e.g.*, Charalampidou, 2011, Wong and Baud, 2012) and carbonate rocks (*e.g.*, Baxevanis *et al.*, 2006, Tembe *et al.*, 2006, Cilona *et al.*, 2012, Vajdova *et al.*, 2012, Baud *et al.*, 2017a). Often, compaction bands referred as the intermediate failure mode between the two end-members of brittle faulting and compactive cataclastic flow. A number of variables influence the formation of deformation bands in general, and compaction bands in particular. These include grain size, shape, mineralogy, cementation, porosity and the

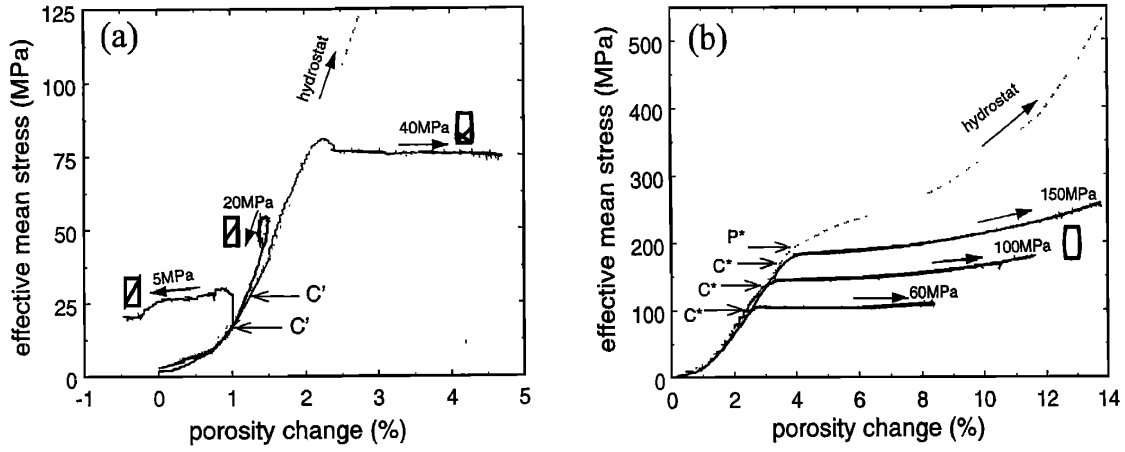

(a) (b)

Figure 2.3: (a)Shear-induced dilation, and (b) compaction in Adamswiller sandstone. The solid curves show the effective mean stress as a function of porosity change for axisymmetric compression tests at fixed effective pressures as indicated. The inflection points are indicated by the arrows. The isotropic compression curve is shown as dashed curves for reference. After Wong *et al.* (1997).

distribution of heterogeneities in the porous rocks (Fossen *et al.*, 2011). Klein *et al.* (2001) proposed that the relatively homogeneous mineralogy and well sorted grains of Bentheim sandstone, both promote the formation of discrete compaction bands. However, Baud *et al.* (2004) have shown that compaction bands can be formed in more complex mineralogy. In addition, two different patterns of localized compaction are reported in the literature, (i) discrete, thin compaction bands of crushed material that are inter-layered with uncrushed material (Klein *et al.*, 2001, Wong *et al.*, 2001), and (ii) one or two compaction bands that appear in the specimen and grow in thickness with increasing loading (Olsson, 1999). This particular failure mode is more extended in the following section (see section 2.2).

At relatively high pressures, Menéndez *et al.* (1996) and Wu *et al.* (2000) reported a damage mechanism that appears to be active in some sandstones, which exhibit localized compaction. They reported uniform cataclastic flow without any indication of strain localization (at high confining pressures), due to the compactive mechanism, grain crushing and pore collapse. In addition, a large number of limestones studied in the laboratory failed by cataclastic flow in the compactive regime (Baud *et al.*, 2000a, Vajdova *et al.*, 2010, 2012). Under high confinement, failure develops by distributed cataclastic flow and except the total porosity, both micropore size and microporosity affect the compactive yield stress (Zhu *et al.*, 2010).

2.2 Compaction bands

Compaction bands are narrow, roughly planar zones of localized deformation, in which shear is less than or comparable to compaction (Rudnicki, 2013). These well-defined zones form at relatively high angles (up to 90°), mainly sub-perpendicular to the maximum compressive stress. The significance of compaction bands is that they reduce the porosity (permeability) and increase the tortuosity relative to the host material (Sun *et al.*, 2011).

The earliest field observation of compaction bands is documented by Hill (1993), who de-

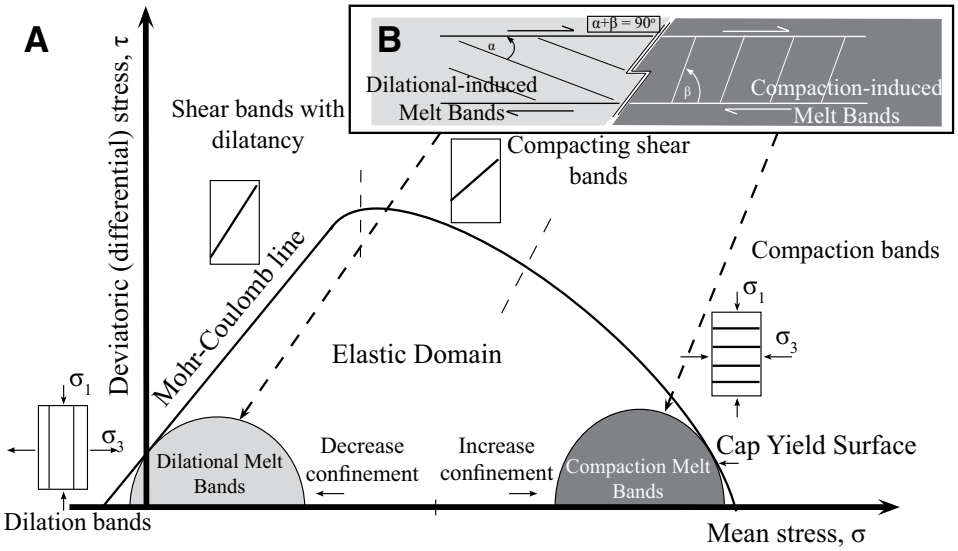

Figure 2.4: Generalized Mohr diagram showing deviatoric stress versus mean stress for failure of porous rocks. Dilation shear bands occur at low confining pressures. Shear bands develop for intermediate pressure conditions. Compaction bands occur at high confining pressure. After Weinberg *et al.* (2015).

scribed multiple sets of deformation bands with reduced porosity and without neither shear displacement nor grain crushing in Aztec Sandstone in Nevada, USA. The term compaction bands was coined by Mollema and Antonellini (1996) to describe thin, tabular zones, approximately 1 cm thick, exhibiting porosity loss in the absence of shear accommodated by granular rearrangement and grain breakage in the eolian Jurassic Navajo Sandstone, Utah, USA. These bands were observed to occur within the compressional quadrants of shear-bands (faults). However, compaction bands do not only localize at the tip of faults Sternlof (2005), and Sternlof *et al.*(2005), (2006) in their extensive analysis of naturally occurring compaction bands, show that compaction bands are not subsidiary structures associated with faults. In addition, field-based studies (Tondi *et al.*, 2006, Cilona *et al.*, 2012, Antonellini *et al.*, 2014) described compaction bands within carbonate rocks as burial-related structures, which accommodate volumetric strain by means of grain rotation/sliding, grain crushing, intergranular solution and pore collapse. The presence of compaction bands in such formations can form impermeable barriers and adversely affect the use of these rocks for a variety of applications such as aquifer management, hydrocarbon recovery and storage, and CO2 sequestration (Aydin and Ahmadov, 2009).

Although the bands are roughly planar, they occur in a variety of configurations with varying thicknesses, spacings, waviness, and orientations (Figure 2.5). Band thicknesses are roughly in the order of 1 mm to 2 cm, and length can range from tens of centimeters to a few meters. In the field, compaction bands appear fairly straight (Mollema and Antonellini, 1996), crooked or wavy or "zig-zag" (Mollema and Antonellini, 1996, Fossen *et al.*, 2011, Deng and Aydin, 2012), as penny-shaped structures (Sternlof *et al.*, 2005), at high-angles, oblique and parallel to bedding (Aydin *et al.*, 2006, Aydin and Ahmadov, 2009, Deng and Aydin, 2012). Compaction bands can be sufficiently identified in the field by their lighter color and positive relief, and by their characteristic echelon and hooking geometry, often described as eye structures, steps or relays (Deng and Aydin, 2012).

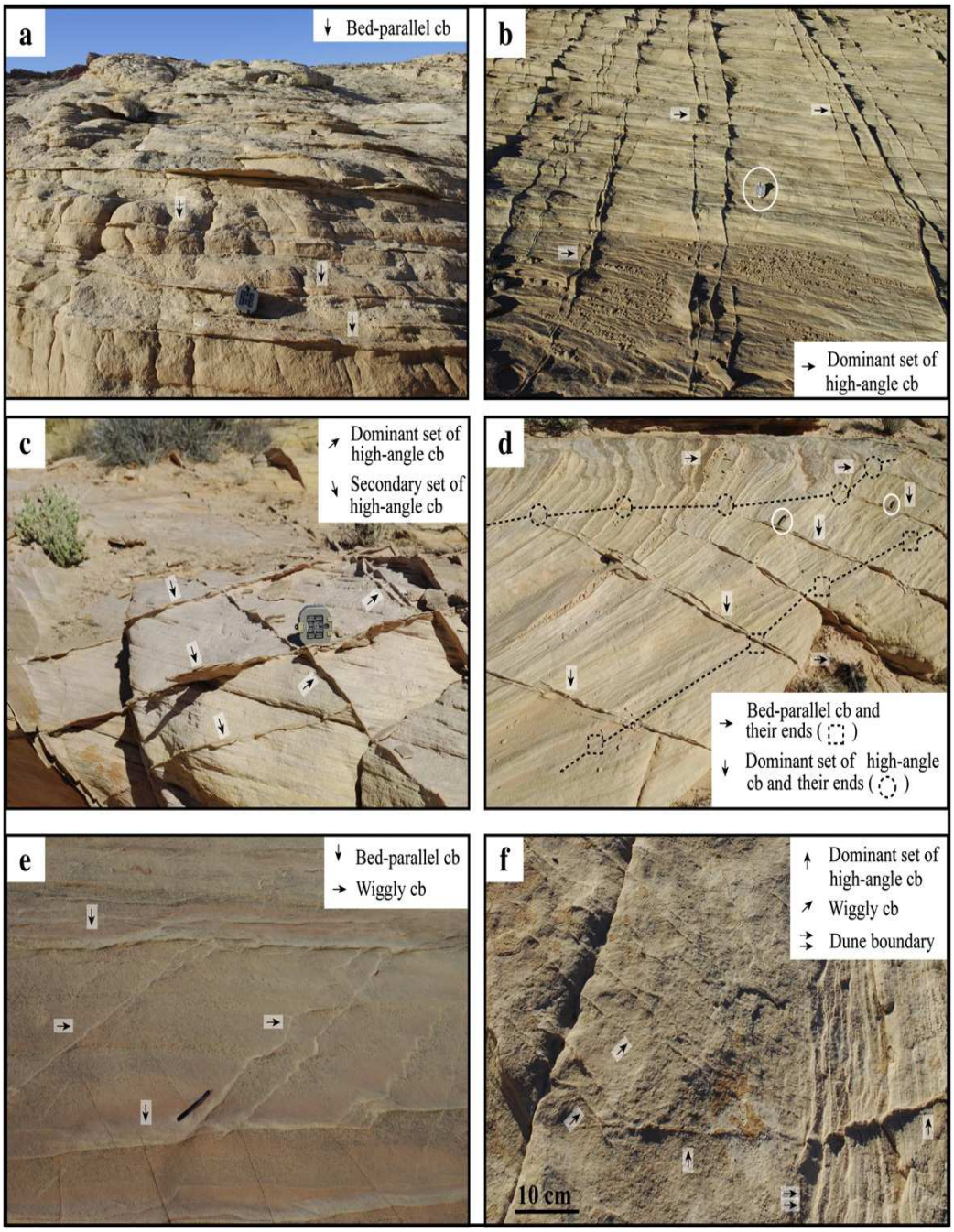

Figure 2.5: Compaction bands (cb) of different orientations. (a) Bed-parallel compaction bands. Compass for scale. (b) High-angle compaction bands. Compass (circled) for scale. (c) Coexistence of dominant set and secondary set of high-angle compaction bands. Compass for scale. (d) Bed-parallel and high-angle compaction bands. The ends of bed-parallel compaction bands and high-angle compaction bands are connected by dashed lines to show the narrow transition zone between them. Pens (circled) for scale. (e) Wiggly compaction bands. Pen for scale. (f) A member of the dominant set of high-angle compaction bands with splays in the form of wiggly bands occurring within a dune. After Deng and Aydin, (2012).

In a porous material, when the rock matrix is compressed, cementation and/or grains may break. Thus grain rearrangement into the open pore space results in a closer packing of the material. This process is called compaction. In porous rocks, in case that the size of the pores is of the same order of magnitude as the size of the grains, pore collapse typically consists in grain reorientation and grain translation to better fill the pore space (Fjar *et al.*, 2008). However, for carbonate rocks with the pore size usually be bigger than the grains this mechanism becomes more important. Mechanical compaction mechanisms in carbonate rocks are affected mainly by stress, grain size and sorting, and clay content (Croize *et al.*, 2013). Microstructural observations on natural deformation bands of Madonna della Mazza quarry (Majella mountain) show a notable pore and grain size reduction inside the compaction bands compare to the surrounding host rock (Cilona *et al.*, 2012). However, studies by Tondi *et al.* (2006) on the same area, showed that the values of the grain-to-matrix ratio inside the deformation bands without cataclasis remained the same than the host rock indicating no grain size reduction. In both studies, pore collapse due to grain rotation and sliding was the earliest deformation micromechanism. Grain crushing and cataclasis in natural deformation bands is usually mediated by pressure solution (Tondi *et al.*, 2006). From the observations in sandstones, compaction band is the result of quartz grain deformation by intense intra-granular fracturing, leading to sharp drop of porosity (Hill, 1993). Microfracture accommodated plastic deformation of quartz grains, however, comprises the dominant microstructural characteristic of the band, and is the obvious mechanism by which granular rearrangement and porosity loss compaction was accommodated (Sternlof *et al.*, 2005). Similar mechanism was detected by Mollema and Antonellini (1996), in Navajo Sandstone, with the intra-granular microfractures slightly curved without intersecting more than one grain.

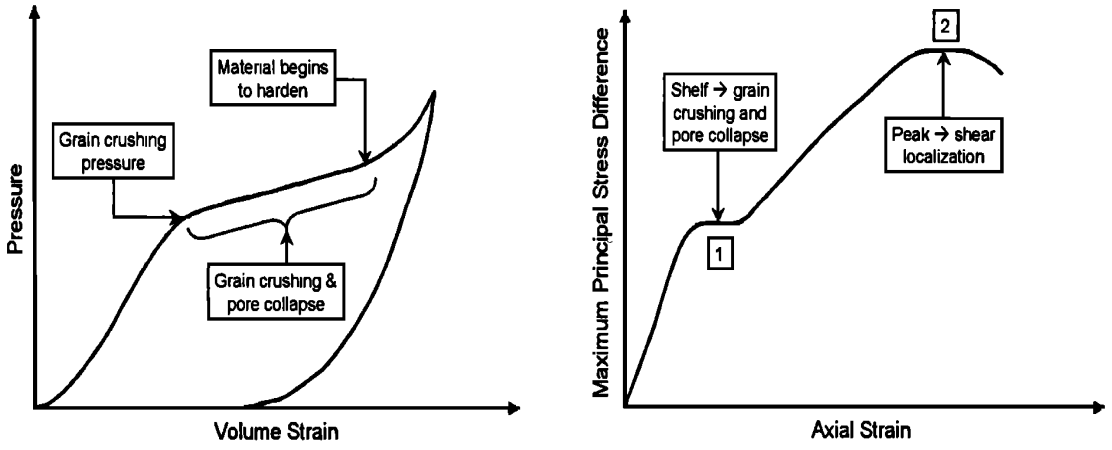

Figure 2.6: (a) Schematic pressure-volumetric strain curve for porous sandstone under hydrostatic conditions, (b) Schematic stress-strain curve for porous sandstone in axisymmetric compression. After Issen and Rudnicki, (2000).

Laboratory studies have shown that discrete compaction bands develop in several sandstones and carbonate rocks. Compaction localization is most likely to occur in clastic sedimentary rocks such as sandstones with porosities over 16% (Holcomb *et al.*, 2007), and in limestones with much lower porosity (Baud *et al.*, 2009). Discrete compaction bands are observed to develop over a wide range of pressures in sandstones and limestones. However, they seem to develop at relatively high confining pressures, beyond the classically defined brittle-ductile transition.

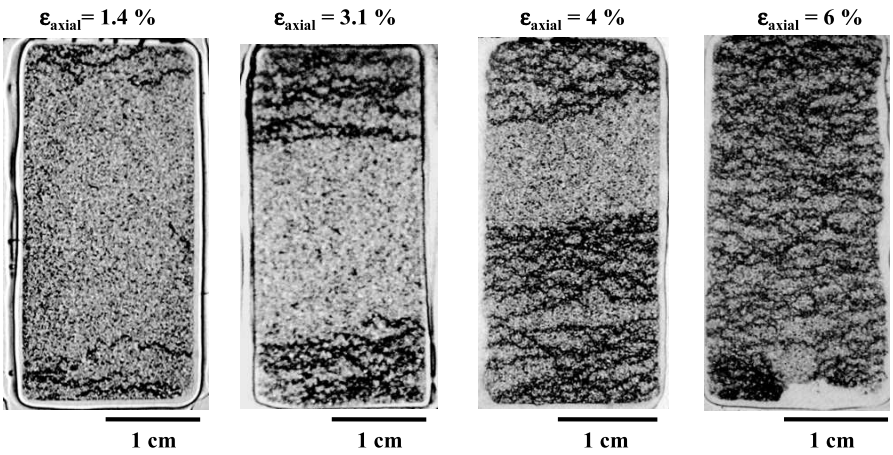

Figure 2.7: Thin-sections of Bentheim sandstone samples deformed at 300MPa confining pressure at different levels of axial strain. After Baud *et al.* (2004).

Systematic studies of mechanical deformation, failure mode and microstructural evolution are conducted to identify the microstructural parameters that influence compaction band formation in porous rocks. These studies investigated compaction band formation, in porous rocks, to different stress conditions such as isotropic (Zhang *et al.*, 1990a) and triaxial compression (Klein *et al.*, 2001, Bésuelle *et al.*, 2003, Baxevanis *et al.*, 2006), and various level of plastic strains.

Porous rocks under increasing confining pressure characterized by a mean stress - volume strain curve which is nonlinear at the lower stress levels, followed by a linear trend up to an inflection point. An accelerated decrease of volume occurs beyond the inflection point, resulting in an appreciable irrecoverable compaction (Zhang *et al.*, 1990a). After this "period" of assumed grain crushing and pore collapse, hardening begins to occur (Figure 2.6a). Several laboratory investigations under axisymmetric compression tests have shown localized compaction in porous rocks with one or more planar bands roughly perpendicular to the maximum compression direction (Figure 2.7). Typically, bands initiate near the ends of specimens, presumably triggered by the inhomogeneity there. As the load increases, bands spread toward the center of the specimen, leaving a laminated structure of very compacted and less compacted material (Baud *et al.*, 2004, Klein *et al.*, 2001). Figure 2.6b shows a representative stress-strain curve for a porous material loaded in axisymmetric conditions at sufficiently high confining pressure. The plateau after the inflection point corresponds to a surge Acoustic Emission (AE) activity, with the implication that pore collapse and grain crushing initiated at this stage (Wong *et al.*, 1992).

In porous sandstones, inelastic compaction in laboratory samples occurs only by grain crushing and pore collapse, that can be either homogeneously distributed and leads macroscopically to cataclastic flow (Menéndez *et al.*, 1996, Wong *et al.*, 1997, Baud *et al.*, 2006), or localized in compaction bands (Bésuelle *et al.*, 2003, Baud *et al.*, 2004). In both cases, significant permeability reduction is associated with inelastic compaction (Zhu and Wong, 1997, Vajdova *et al.*, 2004b). With increasing stress level, inelastic compaction derives from grain crushing initiated by the stress concentrations at grain contacts that induce intragranular cracks (Zhang *et al.*, 1990a, Menéndez *et al.*, 1996, Wu *et al.*, 2000, see Charalampidou, 2011 for an extended review).

A great variety of mechanisms such as pore collapse (Zhu *et al.*, 2010, Vajdova *et al.*, 2012) and grain crushing (Baud *et al.*, 2009, Cilona *et al.*, 2012, Baud *et al.*, 2017a), but also crys-

tal plasticity and pressure-solution (Croize *et al.*, 2013), can potentially play an important role in more complex porous sedimentary rocks, such as limestones. Laboratory-based studies, in addition to the field studies presented previously, have investigated the parameters controlling the mechanics of compaction of porous carbonate rocks. Inelastic compaction in limestones is associated with pore collapse that seems to initiate from stress concentrations at the surface of a pore, which induce a ring of localized damage in its periphery (Zhu *et al.*, 2010). Qualitatively similar behavior to porous limestones is observed also in tuff (Zhu *et al.*, 2011). For carbonate rocks containing both macro and micro-porosity, macropores determine the localization of fractures (Vajdova *et al.*, 2010). Microstructural analysis on carbonate grainstones depicted that at high confining pressures, the intergranular pores tend to collapse by elongating in direction perpendicular to σ_1 (Cilona *et al.*, 2012). On the contrary, intragranular pores appear stiffer and less prone to collapse or be filled by grain spalling. Alike, for specimens with bimodal porosity under isotropic compression tests, the micro-porosity remains almost unaffected by the pore collapse (Dautriat *et al.*, 2011b). In addition, microtomographic images show that microcracking is commonly observed in dense aggregates at contact points whereas the microporous aggregates do not reveal evidence of damage or densification.

However, in Leith limestone (Baud *et al.*, 2017a), the main micromechanism of inelastic compaction is grain crushing in contrast with other limestones with dual porosity. These observations are in agreement with microstructural observations in Saint Maximin limestones (Baud *et al.*, 2009) and in carbonate grainstones (Cilona *et al.*, 2012), where the grain crushing appear to be the dominant deformation micro-processes within the compaction bands. It should be noticed that mechanical twinning is observed in deformed samples of carbonate rocks by a number of researchers. However, because twinning and microcracking tend to be intertwined, it is difficult to characterize quantitatively the twinning activity (Baud *et al.*, 2017a). On the contrary to the twinning activity in field observation, which is due to very low strain-rate, in experimental studies twinning appears pressure dependent and increases with increasing effective pressure (Baud *et al.*, 2009, Vajdova *et al.*, 2010, Cilona *et al.*, 2012, Baud *et al.*, 2017a), and grain size (Vajdova *et al.*, 2012)

Mechanical data shown that the heterogeneity of the host rock (Vajdova and Wong, 2003, Tembe *et al.*, 2006, Charalampidou, 2011), the confining pressure (Mair *et al.*, 2002), the rock mineralogical composition, the grain size distribution (Cheung *et al.*, 2012), sedimentary heterogeneities such as pore and grain orientation, and cement amount (Baud *et al.*, 2017a) can enhance the compaction localization. Particularly, grain size is negatively related to the strength of carbonate rocks. Coarser and more porous samples appear to be also the weakest (Baud *et al.*, 2009, Cilona *et al.*, 2012). Baud *et al.* (2017a) show that compaction bands appear in samples with less cementation in agreement with Menéndez *et al.* (1996) who suggested that high intensity of grain crushing and pore collapse in porous sandstones is associated with weak cementation. In porous limestones though, this is due to fact that cementation creates a more heterogeneous structure in which localized compaction can not develop extensively.

The studies previously discussed shown that field observations and laboratory experiments on compaction bands have comparable characteristics mainly on pore and grain sizes reduction. However, there are still variations among the mechanisms responsible for their development. The main reason for these discrepancies on the failure mechanism, is due to the fact that most of the experimental studies on carbonates have been performed on dry rocks. On the contrary, fluids

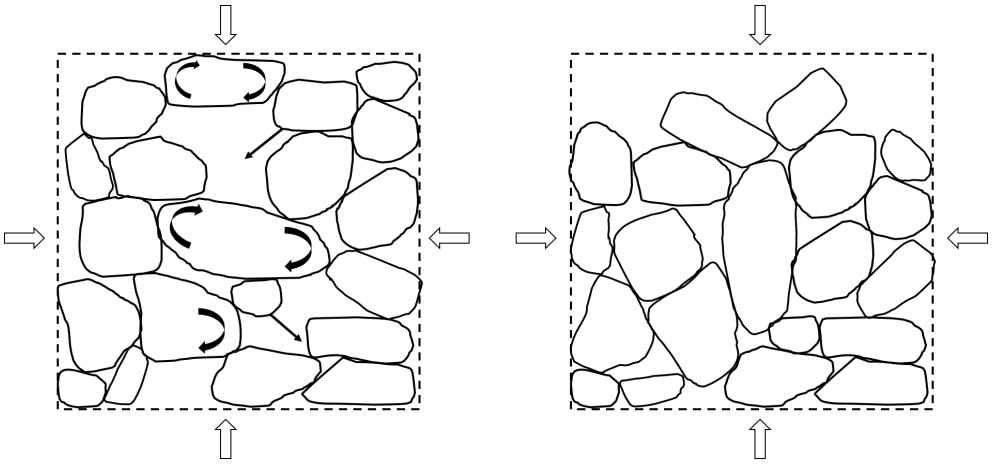

Figure 2.8: Schematic diagram of grain reorientation resulting in closer packing and volume reduction.

are almost always present in natural deformed rocks.

2.3 Pore collapse

In response to an applied stress or pore pressure change, the pore space of a porous rock may either compact or dilate (Zhu *et al.*, 2010). A decrease in the pore fluid pressure results in an increase in the effective stress acting on the rock matrix due to transfer of load from the fluid to the mineral skeleton (Mowar *et al.*, 1996). Under such conditions, certain high-porosity and weakly cemented rocks experience a sudden increase in compressibility (Abdulraheem *et al.*, 1992). This increase in compressibility, coupled with the accompanied irreversible deformation, is often called *pore collapse* (Smits *et al.*, 1988).

Pore collapse is normally observed in high-porosity materials, where the grain skeleton forms a relatively open structure (Figure 2.8). Pore collapse and inelastic deformation of the rock matrix may lead to an abrupt compaction of reservoir rocks. This reduction in bulk volume can propagate to the surface in the form of ground subsidence as well as the subsidence of the sea floor in an offshore environment. In the field, the resultant reservoir compaction and associated surface subsidence can be large, like the well-known subsidence in the Ekofisk field of the North Sea (Geertsma *et al.*, 1973, Johnson *et al.*, 1988, Fredrick *et al.*, 1998, Wong *et al.*, 2004). Reservoir compaction can have catastrophic effects to drilling and producing facilities in addition to inducing damage in the surrounding area. Although the productivity of the carbonate reservoir can seriously decline as a result of any accompanying permeability reduction, pore collapse may also act as a drive mechanism. The collapse of pores is expected to result in significant reduction of permeability even by an order of magnitude as Selvadurai and Głowacki (2008) observed in Indiana limestone.

Laboratory studies have demonstrated that mean stress level, stress ratio (horizontal to vertical), loading rate and pore saturation can influence the occurrence of pore collapse. Several studies were conducted on carbonate rocks both with and without pore pressure (Blanton, 1981), under isotropic and deviatoric loading. The isotropic compression behavior in a porous carbonate rock such as chalk (Blanton, 1981), and limestone (Mowar *et al.*, 1996, Baud *et al.*, 2000a, Dautriat *et al.*, 2011b, Baud *et al.*, 2017a) is primarily elastic up to a critical pressure, beyond

which porosity decreases irreversibly with increasing mean stress (Hamilton and Shafer, 1991). The compaction behavior of carbonate rocks depends strongly on the initial porosity. Experimental data as discussed by Vajdova *et al.* (2004a), indicate an overall trend for the pore collapse pressure to decrease with increasing porosity (Figure 2.9a).

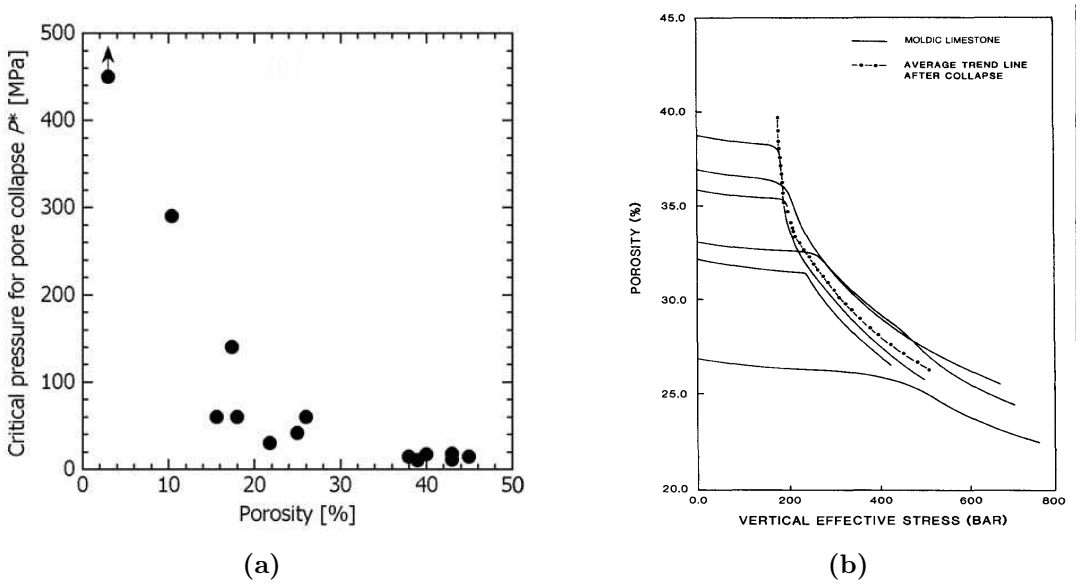

(a) **(b)**

Figure 2.9: Pore collapse is influenced by initial porosity. (a) Critical pore collapse pressure is decreasing with increasing porosity, after Vajdova *et al.* (2004a). (b) Porosity is plotted versus the vertical effective stress for moldic limestone samples. A trend line is proposed to predict pore collapse based on the initial porosity of the intact samples, after Smits *et al.* (1988).

Smits *et al.* (1988) proposed a "trend-line" concept for predicting reservoir compaction caused by pore collapse based on initial porosity measurements. The porosity of a given sample remains more or less constant with increasing stress until the trend-line is reached and pore collapse occurs (Figure 2.9b). However, this trend-line depends on the material and it has to be established each time for the particular sample. Also mineralogy affects the compaction behavior of carbonates. Tests on large number of Ekofisk chalk samples showed that different trend-lines can describe samples even though they are extracted from the same formation (Johnson *et al.*, 1988). Samples with similar initial porosity but different average quartz content experience pore collapse at different stress levels. The higher quartz content corresponds to stronger trend-line.

A number of studies have investigated the micro-mechanisms responsible for pore collapse by means of isotropic and triaxial compression tests on high porosity limestone samples. Mowar *et al.* (1996) recorded and linked the microscopic changes in Cordoba Cream limestone, with 24.5% porosity, at each distinct phase of deformation under isotropic loading. Qualitative and quantitative observations depict a strong preferable orientation of pores and fossil fragments. Both pore fabric and elongate fossil fragments appear almost parallel to the bedding. In addition, in the undeformed Indiana limestone samples (with 17.9% porosity) the allochems include skeletal debris and ooliths (typically elongated features), which are preferentially aligned parallel to the bedding (Vajdova *et al.*, 2012). However, with the progression of pore collapse the pore orientation is totally destroyed for the Cordoba Cream limestone, while rigid body motion of the allochems and of the fossil fragments is observed in Indiana limestone (Vajdova *et al.*, 2012), and in Cordoba Cream limestone (Mowar *et al.*, 1996), respectively.

At low pressures under isotropic compression tests (pre-pore collapse stage) microscopic observations show that a few pores start to collapse in Cordoba Cream limestone. At this stage, collapse within the smaller pores is almost entirely due to grain crushing at the periphery of the pores (cataclastic flow) (Mowar *et al.*, 1996). Although pore collapse initiates by grain boundary spalling into small pores as the process continues, crystal plasticity and larger-scale cataclasis become more important. Microstructural observations in Tavel, Indiana, and Majella limestone show that pore collapse tends to first initiate at the larger pores, accompanied by cataclastis and microcracking (Baud *et al.*, 2009, Vajdova *et al.*, 2010, Vajdova *et al.*, 2012). Specifically, in a Tavel limestone sample (with 10-14% porosity) hydrostatically compressed a halo of cataclastic damage is observed to develop symmetrically around the periphery of a macropore (Figure 2.10a). In Indiana and Majella limestone the cataclastic damage is also localized in the periphery of a macropore, but it is often associated with appreciable spatial heterogeneity. In Indiana limestone pore collapse seems to involve largely the cement, with most of the particles remaining relatively intact. However, in Majella limestone (with 30% porosity), the asymmetry in damage intensity between particles and cement is not as pronounced as in Indiana limestone, possibly because the mechanical contrast between the cements and particles is not as pronounced (Vajdova *et al.*, 2012). In addition, Baud *et al.* (2009) have shown that microcracking becomes the major pore collapse mechanism for high-porosity Majella and Saint Maximin limestones. Motivated by these microstructural observations, Zhu *et al.* (2010) developed a micromechanical model that treats the pore size distribution of a limestone as bimodal, with the total porosity partitioned between the macroporosity and microporosity (Figure 2.10b).

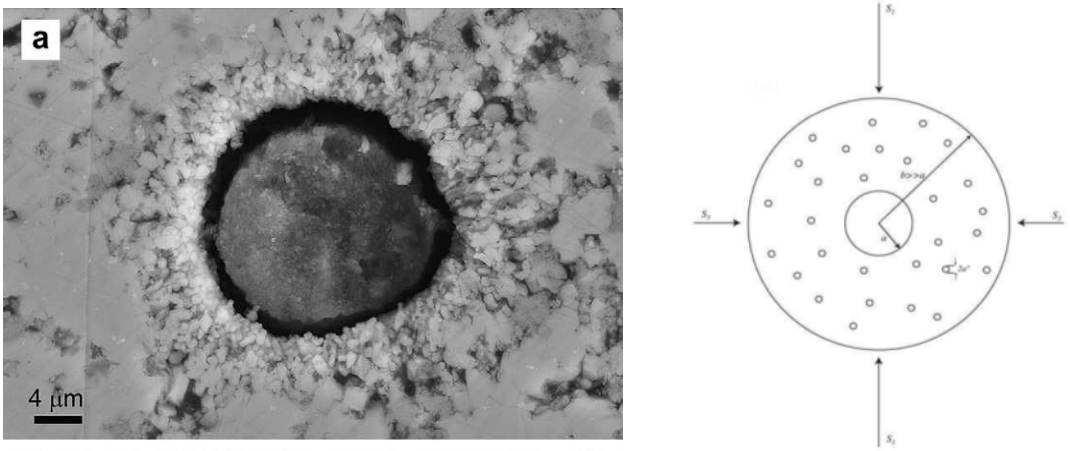

(a) **(b)**

Figure 2.10: (a) SEM image of the isotropically compacted sample of Tavel limestone. A macropore surrounded by a halo of cataclastic damage is observed. The diameter of the macropore is ≈ 20 μm, the concentric rim of particularly intense damage extended over a thickness of ≈ 2 μm, after Vajdova *et al.* (2010). (b) Schematic diagram of a representative element of radius b with dual porosity. A macropore of radius α is surrounded by a medium made of many micropores of radius α^*. Principal stresses are presented by S_1, S_2, and S_3. After Zhu *et al.* (2010)

2.4 Anisotropy

Anisotropy referred as the variation of one or more properties with a direction in which it is measured. Although the term "anisotropy" due to the prefix "an" seems to be a special case of

"isotropy", in fact, the opposite is true, especially for the geomaterials. Thus, anisotropy is one of the fundamental aspects to be taken into account for better understanding of granular materials. Sedimentary rocks like sandstone often display anisotropic behavior due to presence of bedding planes (Nova, 1980). According to Casagrande and Carillo (1944) two significant different forms of anisotropy can be distinguished: (i) inherent, and (ii) induced. Inherent anisotropy is the result of deposition process and grain characteristics (grain size and shape). Mainly, inherent anisotropy is due to a preferred orientation of the long axes of the particles. Whereas, induced anisotropy is caused by the strain associated with an applied stress (Wong and Arthur, 1985).

Studies on porous sandstones demonstrate the effect of the matrix and the voids on the anisotropic behavior of the rocks related to a particular physical property (*e.g.*, Lo *et al.*, 1986, Louis *et al.*, 2003, Baud *et al.*, 2005). Data analysis on the variation of elasticity, permeability, electrical conductivity, magnetic susceptibility and ultrasonic P waves velocities highlights the origins of anisotropy. It should be mentioned that the appearance of bedding planes on visual inspection of the sample cannot be used to presage the existence of anisotropy. Louis *et al.* (2003) in their study on two porous sandstones, show that Bentheim sandstone, which looked very homogeneous from visual examination, is more anisotropic than Rothbach sandstone with visible bedding planes.

Numerous studies on anisotropic rocks shown a remarkable variation of stiffness, strength and of the inclination of the failure plane with the angle, usually named θ, between the cleavage or the bedding plane and the axis of the maximum compressive principal stress. In relatively compact rocks such as slate, and phyllite (Ramamurthy *et al.*, 1993, Kumar, 2006, see Singh *et al.*, 2015 for an extensive review) as well as in porous rocks such as shale (Niandou *et al.*, 1997) the brittle strength is manifested by a minimum in the peak stress at θ = 30-45° and a maxima at $\theta = 0°$ and $\theta = 90°$ (Figure 2.11a). However, Baud *et al.* (2005) demonstrate that the anisotropic behavior of porous sandstones is fundamentally different. The strength attains maximum value in the perpendicular to the bedding samples, *i.e.*, at $\theta = 90°$, and minimum at $\theta = 0°$, in the parallel to the bedding samples (Figure 2.11b). In agreement with (Baud *et al.*, 2005), Louis *et al.* (2007) confirmed that the brittle strength decreases gradually with decreasing angle with maximum and minimum at $\theta = 90°$ and $\theta = 0°$, respectively. Additionally, experiments that performed on "oblique" samples cored at $\theta = 45°$ with respect to the bedding show that the yield stress of these samples is intermediate between those of the perpendicular and the parallel samples (Louis *et al.*, 2007, 2009). In other words, there is an overall trend for the maximum, intermediate and minimum values of both brittle strength and compactive yield stress to be associated with the perpendicular, oblique, and parallel samples, respectively. However, Baud *et al.* (2012) suggest that this trend cannot be generalized for all types of sandstone. For Biemelstadt sandstone, they show that although the brittle strength is higher for samples that deformed normal to bedding, at all higher pressures, the samples parallel to the bedding are systematically stronger and yields at higher deviator stresses. Similar behavior is observed in porous carbonates by Cilona *et al.* (2014)

In addition to the macroscopic variances observed in sandstone samples that cored at different orientations with the respect to the bedding planes, those samples show fundamentally different patterns of strain localization especially in the compactive regime. Several diffuse compaction bands with intense damage subparallel to bedding develop in samples cored perpendicular to bedding (Bésuelle *et al.*, 2003). Compactive shear bands that cut across the sample are observed

in oblique ($\theta = 45°$) samples (Louis *et al.*, 2007, 2009). Whereas in the samples cored parallel to bedding, the strain and damage are smaller and appear to be more diffuse. The overall damage is distributed homogeneously while the localization do not propagate all the way across the sample (Louis *et al.*, 2007).

Thus, it is evident that there are different types of strength anisotropy of localized compaction, which are related to different microstructural origins. Extensive microstructural analysis are performed to provide insights in strength anisotropy observed macroscopically in Rothbach and Diemelstadt sandstones. It can be concluded that non-spherical pore shapes with larger axis along bedding plane, *i.e.*, pore fabric anisotropy, govern anisotropy in Diemelstadt sandstone (Baud *et al.*, 2012, Louis *et al.*, 2005), whereas for Rothbach sandstone, anisotropy is controlled by an orientation-dependent cement radius at the intergranular contacts (Louis *et al.*, 2003, 2005, 2007, 2009).

Recent numerical studies highlight that pore geometry and orientation, with respect to the loading direction, have an important impact on the compressive strength and Young's modulus of porous rocks (Bubeck *et al.*, 2017, Griffiths *et al.*, 2017). It is shown that samples containing elliptical pores are weaker if compression is applied parallel to the short axis, compared to compression applied parallel to the long axis. However, these models are relevant for volcanic rock but not for porous sandstones where the alignment of grains may play a more important role. In addition to that, experimental studies on steel foam demonstrate that strength of localized compaction is ≈ 3 times higher when foam is compressed parallel to the long axis of ellipsoidal cells (Park and Nutt, 2001).

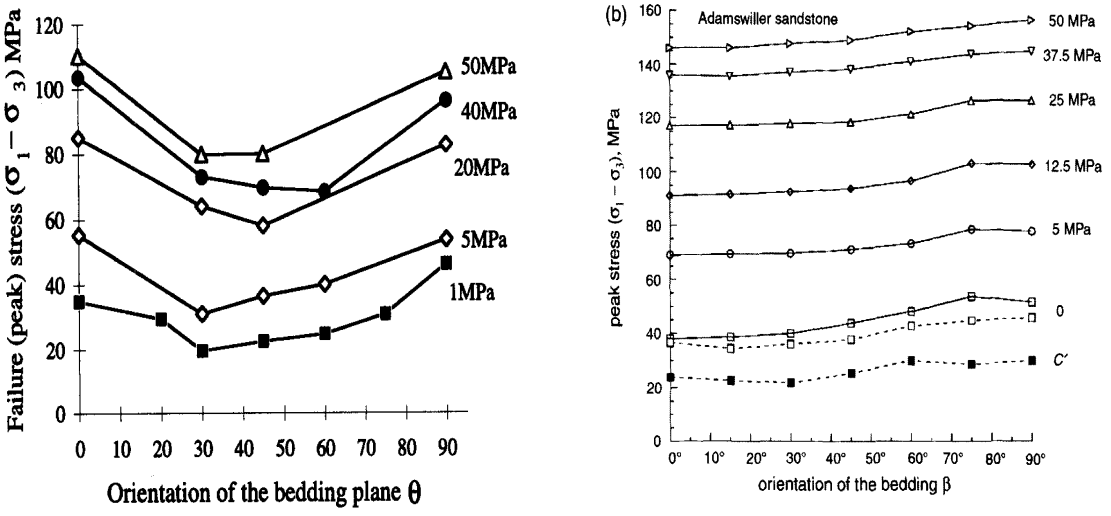

Figure 2.11: Peak stress as a function of bedding angle (a) in Tournemire shale, after Niandou *et al.* (1997), and (b) in Adamswiller sandstone in Baud *et al.* (2005) after Millien *et al.* (1993).

2.5 Full-field measurements in porous rocks

Experimental studies under controlled conditions provide useful insights into the mechanics of strain localization. In section 2.1 it is shown that localization in geomaterials and notably in

porous rocks can take many, and sometimes complex configurations. Thus, understanding the mechanisms of deformation, and in particular strain localization requires the entire deformation process to be followed throughout a test while the sample deforms under load. In conventional material testing, specimen response is characterized only globally and presented as an average material response. Consequently, if deformation is inhomogeneous the traditional boundary measurements of stress and strain have only nominal or conventional meaning. Furthermore, neither the geomaterials are truly homogeneous at the scale of a laboratory specimen, nor the boundary conditions are perfect. Investigating such inhomogeneous behavior requires multiple local measurements.

For more than 30 years, the so-called non-contact measurement techniques are used in material science. Such techniques that follow the golden rule *look but don't touch* are often referred to as full-field measurement techniques. Full-field measurements are increasingly used in experimental geomechanics since they can provide measurements of fields of properties over the entire specimen. Using full-field measurements it is possible to measure the spatial distribution of various types of physical quantities, such as displacements, strains and temperature of samples subjected to loading. They represent a substantial advance over conventional methods in experimental mechanics due to qualitative and quantitative characterization of heterogeneities in both material properties and processes during a test (Viggiani and Hall, 2012). Thus, the development and application of full-field techniques such as ultrasonic tomography, acoustic emission, x-ray computed tomography, neutron tomography, digital image correlation (DIC), optical and electron microscopy have become increasingly common. A rapid overview of some of these techniques and their advantages to detect strain localization in porous rocks (and general in geomaterials) is presented in the following paragraphs. During this study x-ray CT and DIC are used to investigate strain localization in a porous limestone.

2.5.1 Ultrasonic waves

Ultrasonic wave measurements are one of the most widely used non-destructive testing methods in laboratory soil and rock mechanics. The method is based on the generation, transmission and reception of waves and ultrasonic pulse frequencies. Originally, ultrasonic material testing has been used to obtain global elastic or quasi-elastic properties such as Young's modulus and shear modulus at small strains (*e.g.*, Shibuya *et al.*, 2005). The mechanical behavior of porous rocks is highly dependent on the mineralogy, size and shape distribution of voids and grains and their relative arrangements. These microstructural characteristics modify uniquely the frequency of the waves and define the velocities of different propagation modes, *i.e.*, compression and shear. Therefore, except the material's physical and mechanical properties ultrasonic waves are strongly related to the microstructural characteristics. Consequently, this non-destructive technique is used in rock mechanics to characterize fracture damage and its evolution (*e.g.*, Nur and Simmons, 1969, King *et al.*, 1994, Sayers and Kachanov, 1995, Santamarina *et al.*, 2001, Stanchits *et al.*, 2003 Martinez-Martinez *et al.*, 2016, citeriazi2017determination) as well as to detect pore collapse and grain crushing (*e.g.*, Fortin *et al.*, 2007). The ultrasonic test system as a non-destructive tool is also used to investigate the porosity, uniformity and anisotropy of the tested samples by applying a combination of compression (P) and shear (S) waves (*e.g.*, Lo *et al.*, 1986, Louis *et al.*, 2003, Baud *et al.*, 2005, Louis *et al.*, 2005).

However, these standard ultrasonic practices provide measurements on specific directions, which may not be representative of the whole sample, especially in the case of pre-existing heterogeneities or evolving localized deformation. These limitations can be overcome by using ultrasonic tomography, a full-field measurement method that can provide a field of ultrasonic velocity measurements over the whole sample (Hall and Tudisco, 2012). Ultrasonic imaging, also called travel-time tomographic imaging, uses the travel times of ultrasonic waves to locate high and low density inclusions within analyzed samples. Since ultrasonic travel time is density dependent, the travel time map may be interpreted also as a density map. Although the (spatial) resolution of the images is lower than the x-ray images, the cost of ultrasonic testing is much lower. Thus, a (small) number of ultrasonic tomography studies have been done on geomaterials such as: concrete (*e.g.*, Daigle *et al.*, 2005), rocks(*e.g.*, Scott Jr and Abousleiman, 2004, Charalampidou *et al.*, 2011, 2014, Tudisco *et al.*, 2015b), and soils (*e.g.*, Lee *et al.*, 2005).

2.5.2 Acoustic Emissions

In addition to the ultrasonic measurements, another approach based also on waves is used to identify the location, the intensity and the mechanisms of failure in geomaterials. Acoustic emission (AE) measurements are widely known as a non-destructive tool to track and characterize the localization process. AE are waves produced by dislocations, microcracks, friction and other local deformation processes at the grain-scale that release a sufficient amount of energy to generate acoustic pulses. These waves can then be detected by transducers placed at the boundaries of the tested sample. Using multiple transducers, the locations where the AE occur can be pointed out and consequently the spatial origin of the failure can be located and followed during loading. This technique has the advantage of being able to capture the signal generated by the tested sample and not from an external source, as in ultrasonics and radiography, as well as to detect features that have change their original shape/condition by the progressive deformation of the specimen. For these reasons a progressively growing number of experimental studies in rock mechanics are using acoustic emission to study strain localization.

Several studies on porous sandstones shown that the acoustic emission activity combined with the microstructural observations provide information about the localized deformation allowing a better understanding of the micromechanisms (*e.g.*, Zhang *et al.*, 1990b, Wong *et al.*, 1992, David *et al.*, 1994, DiGiovanni *et al.*, 2000). An AE event represents a micromechanical failure event involving particle crushing, debonding and/or pore collapse. This technique has been used to investigate and monitor different failure modes in sandstones such as shear enhanced compaction bands (*e.g.*, Klein *et al.*, 2001, Charalampidou *et al.*, 2011) and compaction bands(*e.g.*, Olsson and Holcomb, 2000, Vajdova and Wong, 2003, Fortin *et al.*, 2006, Holcomb *et al.*, 2007, Stanchits *et al.*, 2009, Heap *et al.*, 2015, Dewers *et al.*, 2017). Baud *et al.* 2004 demonstrated that the various localized modes are manifested by distinct AE activities. In particular, discrete compaction bands are associated with episodic surges in AE. Although acoustic emission is extensively used as a diagnostic tool in laboratory studies on sandstone, relative studies on carbonates did not report any significant AE activity during deformation. Only recently Baud *et al.* 2017c have performed a systematic investigation of localized compaction in limestones using acoustic emissions.

2.5.3 X-ray computed tomography

The use of 2D images as a full-field measurement technique in experimental geomechanics dates back to early 1960s (Roscoe, 1963). These 2D images (radiographs) are produced by x-ray radiation on photographic plates. The radiographs reveal that it is possible to extract qualitative and quantitative information of localized patterns associated with local density changes into the sample. The density variations inside the sample corresponds to different x-ray beam attenuation, which appear in the 2D image with different grey shade. Thus, the x-ray radiography is used as an imaging technique that allows direct observations of the internal structure of the sample with different density. It should be noted though that these images represent the attenuation accumulated through the whole sample. Although this imaging technique provides valuable information about the deformed sample, it still remains in 2D.

This limitation is overcome by x-ray Computed Tomography (CT). Following the same principle with the conventional radiography but in this case acquiring the images at different angular positions, the 3D structure of the sample can be obtained. So, tomography is a method to reconstruct the 3D field of x-ray attenuation from a series of different radiographs. Once the 3D volume of the tested material is obtained qualitative and quantitative measurements can be performed. The pioneering work of Desrues *et al.* (1996) demonstrates that x-ray CT provides valuable 3D information on strain localization but also the potential of this imaging technique as a quantitative measurement tool *e.g.*, for measuring the evolution of void ratio inside a shear band and its relation to critical state. Originally developed for use in healthcare, x-ray CT is now used extensively in field of non-destructive material testing, including geomechanics (*e.g.*, Mees *et al.*, 2003, Desrues *et al.*, 2010, Alshibli and Reed, 2012).

X-ray CT applications can be divided into several major areas. The first and straightforward is sample characterization. CT provides images of the internal structure of the sample, allowing to identify lithology, measure density and local porosity changes, as well as to visualize the 3D distribution of the pores within a volume providing information about their interconnectivity (*e.g.*, Wellington, Vinegar, *et al.*, 1987, Karacan *et al.*, 2003, Van Geet *et al.*, 2003, Cnudde, 2005, Louis *et al.*, 2007, Remeysen and Swennen, 2010, Rozenbaum and Roscoat, 2014, Arzilli *et al.*, 2016). X-ray CT also serves as a powerful tool for fluid flow visualization in rocks. It is used in "coreflooding" tests to quantify multiphase flow behavior, to observe the effect of treatment fluids and to estimate fluid flow properties of porous rocks (*e.g.*, Vinegar and Wellington, 1987, Withjack *et al.*, 1988, Akin and Kovscek, 2003, Ruiz De Argandona *et al.*, 2003). Strain localization is another main application for which x-ray CT is widely used (*e.g.*, Bésuelle *et al.*, 2000, Kodaka *et al.*, 2006, Louis *et al.*, 2006, Charalampidou *et al.*, 2011, Fonseca *et al.*, 2013, Charalampidou *et al.*, 2014, Baud *et al.*, 2015).

2.5.4 Digital Image Correlation

X-ray CT is a powerful tool for imaging the internal structure of the materials as well as providing valuable 3D information on localization patterning both in qualitative and quantitative ways. However, x-ray CT is based on the transmission measurements, hence it is sensible to density variations only. Therefore, if the localized deformation is isochoric, *i.e.*, no volume change, x-ray CT fails to detect the phenomenon by measuring changes in x-ray attenuation (*e.g.*, Lenoir *et al.*,

2007, Viggiani, 2009, Bornert, 2010). Such a limitation can be overcome by using Digital Image Correlation (DIC).

DIC is considered nowadays as one one of the standard full-field measurement techniques in experimental geomechanics. It is a non-destructive technique of relatively easy implementation, based on the comparison of digital images. DIC is essentially a mathematical tool for assessing the spatial transformation (including translations and distortions) between two images. When images of the same rock sample are acquired before and after a loading increment, digital image correlation can be used to obtain the displacement and deformation fields. This can be achieved by comparing the image in the deformed state with the reference image. The matching between the two images is based on the assumption that a material point of an image can be fully identified by its local pattern (*i.e.*, the grey level intensity in a grey-scale image) on the second image. The mapping of the pixel intensity values, and thus the measured displacement is accomplished mathematically through minimization of a normalized cross-correlation coefficient.

Such a method is used in experimental rock mechanics to measure displacement and deformation fields over surfaces (*e.g.*, Hall *et al.*, 2006, Louis *et al.*, 2007, Bésuelle and Lanatà, 2016) or through a volume (*e.g.*, Lenoir *et al.*, 2007, Ji *et al.*, 2014). DIC can provide a better understanding of the material response under loading and allows for characterizing the evolution of the deformation field as well as detecting any localized deformation in the sample. Following the material response under loading it is possible to perform qualitative and quantitative full-field measurements of local responses. This gives the ability to evaluate the internal 3D kinematics due to the applied boundary conditions, and to understand the micro response (only if the spatial resolution is sufficient) to globally imposed deformation (Andò, 2013). Since the pioneering works of Peters and Ranson (1982), and Sutton *et al.* (1983) this powerful technique has been used widely in geomechanics on various materials (*e.g.*, Pan *et al.*, 2009, Dautriat *et al.*, 2011a, and references therein). The quality of the results that can be obtained by digital image correlation crucially depends on the quality of the images. To this end, an increasing number of studies combine the x-ray images with DIC. Louis *et al.* (2007) shown that combining x-ray CT scans with 2D-DIC allows mapping out strain localization as well as associating deformation to local material heterogeneities. Thereafter, pioneer studies such as (*e.g.*, Lenoir *et al.*, 2007) demonstrate the capabilities of combining x-ray tomography and DIC to perform 3D volumetric image correlation, which provides the 3D kinematic measurements.

Chapter 3

Experimental campaign

In this study, experiments are conducted to investigate systematically the macroscopic behavior, and the deformation mechanisms responsible for compaction on a carbonate rock of porosity greater than 45%.

In an attempt to elucidate the mechanisms responsible for the observed macroscopic behavior of the tested material, the majority of the tests are performed *in-situ* inside the x-ray scanner in Laboratoire 3SR (*in-situ* meaning x-ray scanning at the same time as loading). Cylindrical samples perpendicular, oblique (45°), and parallel to the bedding are cored with a diameter of 11.5 mm and length of 22 mm. The response of the material is investigated under three different stress paths. This chapter details the material tested, and the method followed to prepare the samples. Then, the equipment designed for these particular specimen dimensions is described. The experimental campaign is detailed in section 3.5 by describing the set-up and the loading conditions for each test separately.

3.1 Material tested

The material studied in this work is a highly porous limestone from Maastricht region, known as Maastricht limestone or *Tuffeau de Maastricht*. This section describes the material used.

3.1.1 Tuffeau de Maastricht

Maastricht limestone (Tuffeau de Maastricht) is a limestone of the Upper Cretaceous period. During the Upper Cretaceous, widespread deposition of chalk occurred in Northwest Europe. A much coarser-grained than the very fine-grained limestone well know as the white chalk, tuffaceous chalk (*Tuffeau* in French) has been preserved locally. Tuffaceous chalk is a designation for weak, porous limestone which can be characterized according to grain-size as calcarenites and calcisiltites (Bekendam, 1998). This tuffaceous chalk is of Maastrichtian age and occurs in southern Limburg between Belgium and The Netherlands.

The commonly coarser grained limestones of the Formation of Maastricht (of Maastrichtian age) were deposited in a shallow sea and their uniformity is limited. The maximum overall thickness of the formation is about 100 m (Cnudde, 2005). In the outcrop area, the Maastricht

Formation has never been covered by more than about 50m of younger sediments, resulting in only a weak early diagenetic consolidation. Two regional facies types can be recognized in the Maastricht Formation. In the western part of Southern Limburg it is developed as the "Maastricht facies", in the eastern part as the "Kunrade facies". The "Kunrade facies" consists of hard, relatively well cemented limestones alteration with soft limestones with some clay content. All members of the "Maastricht facies" comprise predominantly carbonate bioclasts of sand size. This sequence of calcarenites is also known as the tuffaceous chalk of Maastricht (Tuffeau de Maastricht) (Bekendam, 1998; Dubelaar *et al.*, 2006).

Figure 3.1: Miner in a underground quarry, using a special handsaw to cut a Tuffeau de Maastricht block from the surrounding rock, after Dubelaar *et al.* (2006).

The Tuffeau de Maastricht is a typical building stone that was excavated in the "Maastricht facies" in blocks of about 50 cm wide, 80 cm deep and up to 200 cm high. Coarse toothed handsaws are typically used to cut the stone from the surrounding rock (Figure 3.1). It is a yellow colored soft sedimentary limestone. Tuffeau de Maastricht is formed by sediments transported and deposited in a marine environment, therefore a variable percentage of bioclastic particles can be recognized even with naked eye. It is composed of, among others, echinoids, foraminifera, brachiopods, molluscs and numerous fossil fragments. All these sea skeletons and shell fragments result in a limestone with pure calcium-carbonate grains (see Figure 3.2). The $CaCO_3$ of Tuffeau de Maastricht is high and rarely less than 96% (Figure 3.3).

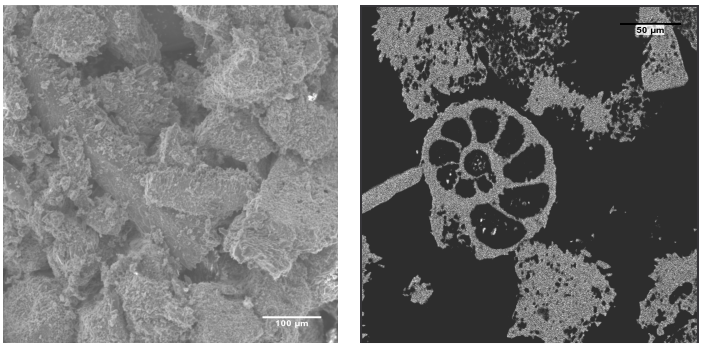

(a) **(b)**

Figure 3.2: SEM images of the Tuffeau de Maastricht (a) rock fragment, (b) thin section, after Cnudde (2005).

The fact that the tuffaceous chalk was deposited at rates of centimeters or decimeters per 1000

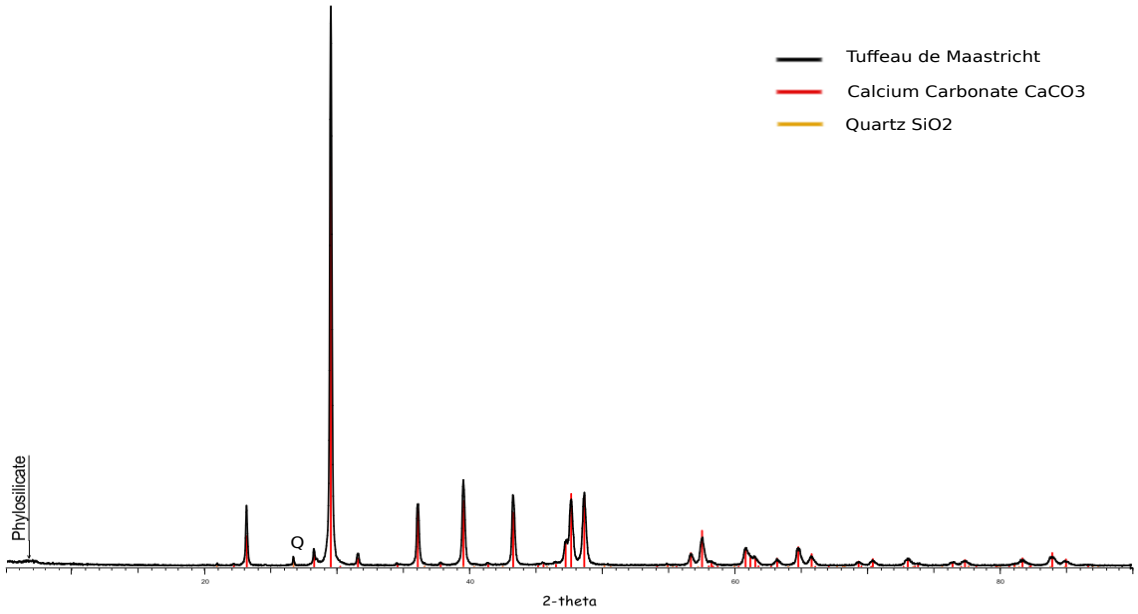

Figure 3.3: Tuffeau de Maastricht diffractogram. This analysis has been performed in ISTerre (Institut des Sciences de la Terre), Grenoble.

years (Zijlstra, 1994) and the lack of lithostatic pressure due to only a few meters of sediments, explain the relative high porosity of Maastricht limestone (up to 52%). Porosity is mainly of the intergranular type (macroporosity) and intragranular porosity due to pores in bioclasts and shell fragments. Apart from the hardgrounds, Tuffeau de Maastricht is weakly cemented: the grains are only loosely bonded at contact points and evidence of pressure-solution or compaction is hardly observed. The weak cementation, combined with the high porosity, result in a relative low strength for the rock, *i.e.*, the unconfined compressive strength is less than 5 MPa (Bekendam, 1998; Ngan-Tillard *et al.*, 2011).

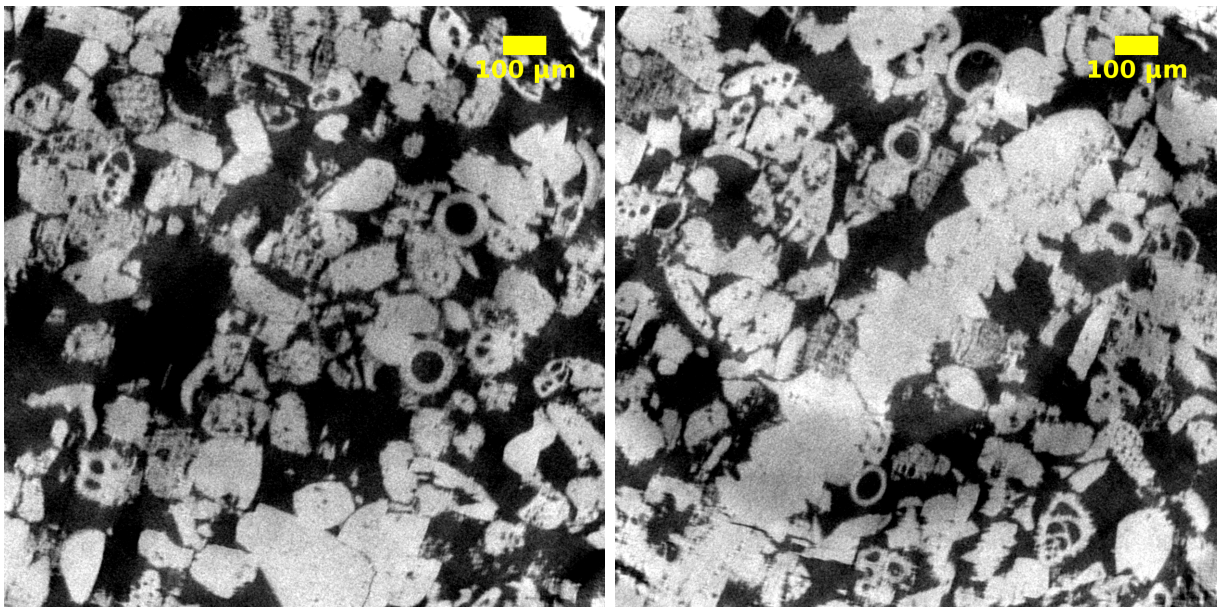

Figure 3.4: Microstructure of Tuffeau de Maastricht. These are x-ray Computed Tomography (CT) scans at a resolution of 1 μm. Note the high porosity and the bioclasts variability.

Figure 3.4 two x-ray tomographic images well portraying the microstructure of Tuffeau de

Maastricht. The material appears as grain supported structure with no mud between grains. A well sorted clastic carbonate rock is to be seen, with an average grain size ranging from 100 to 200 μm. On the basis of the grain supported texture and the absence of mud it can be classified as a grainstone according to the Dunham (1962) classification system. Through x-ray Computed Tomography (CT) scans at a resolution of 1 μm (section 4.1), Figure 3.4 reveals the bioclasts diversity and the intergranular porosity (black color in figure corresponds to pores). Although the average fossil fragments size is similar to grain size, some isolated larger bioclasts occur to a certain layering. The macro pores occupy a variable but large volume and the whole cementation is very poorly developed. Apart from hardgrounds and layers of fossil grit sedimentary bedding is generally not visible, even under the optical microscope or the x-ray scan. However, experiments show that the mechanical properties strongly depend on whether they are measured parallel, oblique or perpendicular to the bedding plane, as shown in chapter 5.

Mercury injection measurements are used to infer the distribution of pore entrance diameter (Figure 3.5). On the contrary to the x-ray scans at high resolution, which show a significant fraction of microporosity, the data show a mono-modal curve with most frequent values between 20 and 70 μm. the MIP (mercury intrusion porosimetry) data indicate that the intergranular porosity is insignificant, or the pores relatively small in diameter with small effect on hydraulic transport.

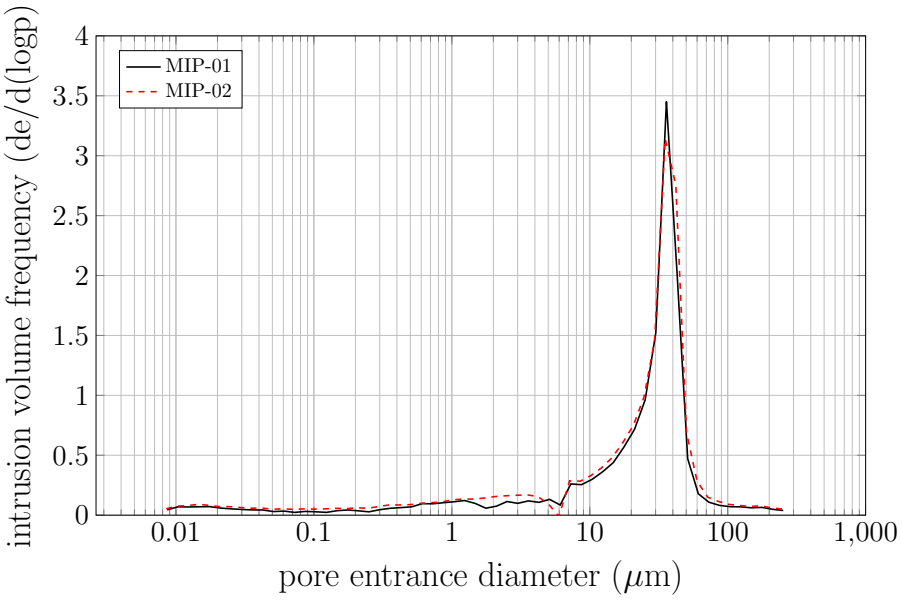

Figure 3.5: Pore throat analysis derived from mercury injection tests on samples of Tuffeau de Maastricht. These analysis is conducted with the help of professor G. Russo and coworkers (University of Cassino and Southern Lazio)

3.1.2 Reference material

In order to understand the behavior of the natural material it is useful to study "destructured" samples, which are formed from the same material by breaking the bonds between the particles. Therefore, to identify the potential degradation mechanisms and study the effects of cementation on the mechanical characteristics of the Tuffeau de Maastricht, destructured samples are prepared (named *reference material* hereafter).

Assuming that the bonding between the particles is weaker than the grains themselves, the *reference material* essentially a non-bonded version of the natural material. The initially natural cemented samples are broken down by two different techniques; by hand and by a plastic hammer. Initially, samples of different size are extracted from the same block and are broken by hand. Then, the same procedure is repeated for more samples but using a plastic hammer. For each of those samples, grain size distribution is measured. Figure 3.6 summarizes these measurements. Both techniques lead to similar results in terms of *reference material*. It can also be seen from the plot, that in agreement with the literature review (subsection 3.1.1), the mean grain size is around 150 μm. In order to assess the objectivity of the results, the whole operation described above was repeated by a second user (a MSc student). It is proved that independently of the user or the technique used, the procedure followed to break down the material yields essentially the same grain size distribution, *i.e.*, it is relatively objective.

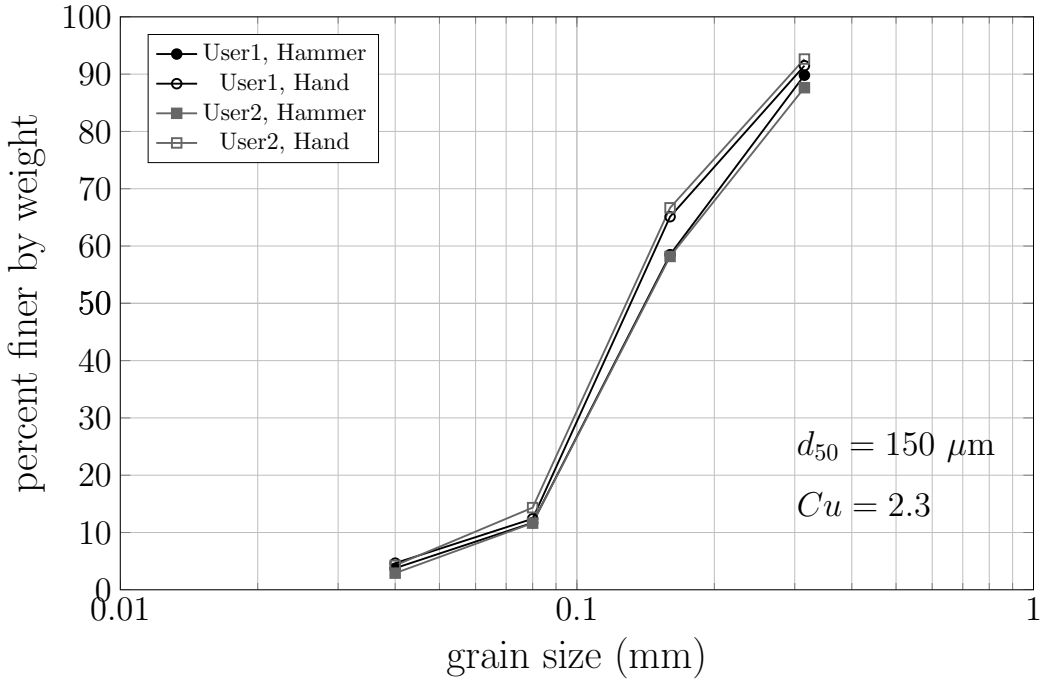

Figure 3.6: Grain size distribution curves for the *reference material*.

3.2 Specimen preparation

A single block of Tuffeau de Maastricht from a quarry in The Netherlands is used for this research project. All the samples tested herein are extracted from the same block to minimize the effects of material variability. The samples are brought to convenient sizes so as to easily fit into the laboratory core drilling machine. The smaller parts are firmly clamped onto the pedestal of drilling machine to facilitate coring at each of the specific orientations. The samples are cored parallel, oblique (at 45 degrees) and perpendicular to the bedding plane. The sampling directions are shown in Figure 3.7. A heavy duty diamond drill assembly, equipped with 11.5 mm internal diameter diamond drill bits, is used for drilling the cores. Due to the unclearness of the bedding planes, it is not easy to judge the orientation angle accurately by eye. So the actual orientations might have possibly deviated by a few degrees from the specified ones. Initially, the specimens

perpendicular to the bedding are cored from the material block. Then, the same block is shifted 90 degrees and new cores are prepared in orthogonal direction with respect to the first ones, *i.e.*, parallel to the bedding. In case of 45 degrees, since the laboratory drilling machine is not equipped with a tilting pedestal, an extra handmade device is used. In order to avoid any variation of the coring orientations among the samples, several cores are prepared at the same time. Once the smaller material block is secured onto the drilling machine, the more possible cores are prepared at once. Figure 3.8 summarizes the steps followed to prepare the samples.

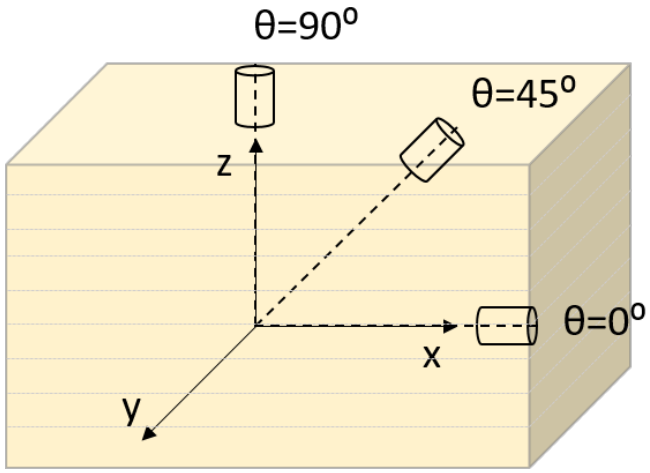

Figure 3.7: Sampling directions for drilling cores

Obtaining good quality cores of the desired size is not an easy task due to the rock's composition. Once the retrieved cores are cut, a great deal of care is taken in removing them from the sample container to reduce the risk of breakage. A proper cutting blade is carefully used to remove the extra material around the cored cylinders. Then, the extracted samples are placed inside an apparatus specially designed for this project with perfect parallel sides, and are polished to ensure parallelism (Figure 3.9a). The end faces of specimens were ground flat and parallel using a fine sandpaper (No. 240). The final cylindrical specimens are prepared to obtain length to diameter (l/d) ratio approximately 2.0 with a diameter of 11.5 mm. This particular geometry is necessary to facilitate the x-ray computed tomography and to allow full-size measurements at a sufficiently high resolution (subsection 4.1.4). Despite the polishing, the surface of the specimen remains relatively rough. To minimize friction on the specimen faces lubricant made of greases based on phenyl methyl silicone oil is smeared on the specimen and the porous stones (see Figure 3.9b). Ceramic porous stones (diameter 12 mm) are selected for their low x-ray attenuation coefficient, which makes it easier to remove them from the acquired images (see section 4.3). Once the specimen is aligned with the top and bottom porous stones, it is enclosed by a membrane, which allows the application of the cell pressure. For this study, a 500 μm thick neoprene membrane with an inner diameter of 10 mm is used, primary to avoid piercing due to the roughness of the specimens surface.

Initially, the membrane is folded around a membrane stretcher with an internal diameter of 14 mm (Figure 3.9c). Through a hole, on the side of the tube, a suction is applied forcing the membrane to adopt its shape. Thereafter, the specimen is inserted into the tube which allows the membrane to enfold it as soon as the vacuum is released. The membrane is unfolded once the whole "system" (specimen and porous stones) is placed on the specimen holder. In this

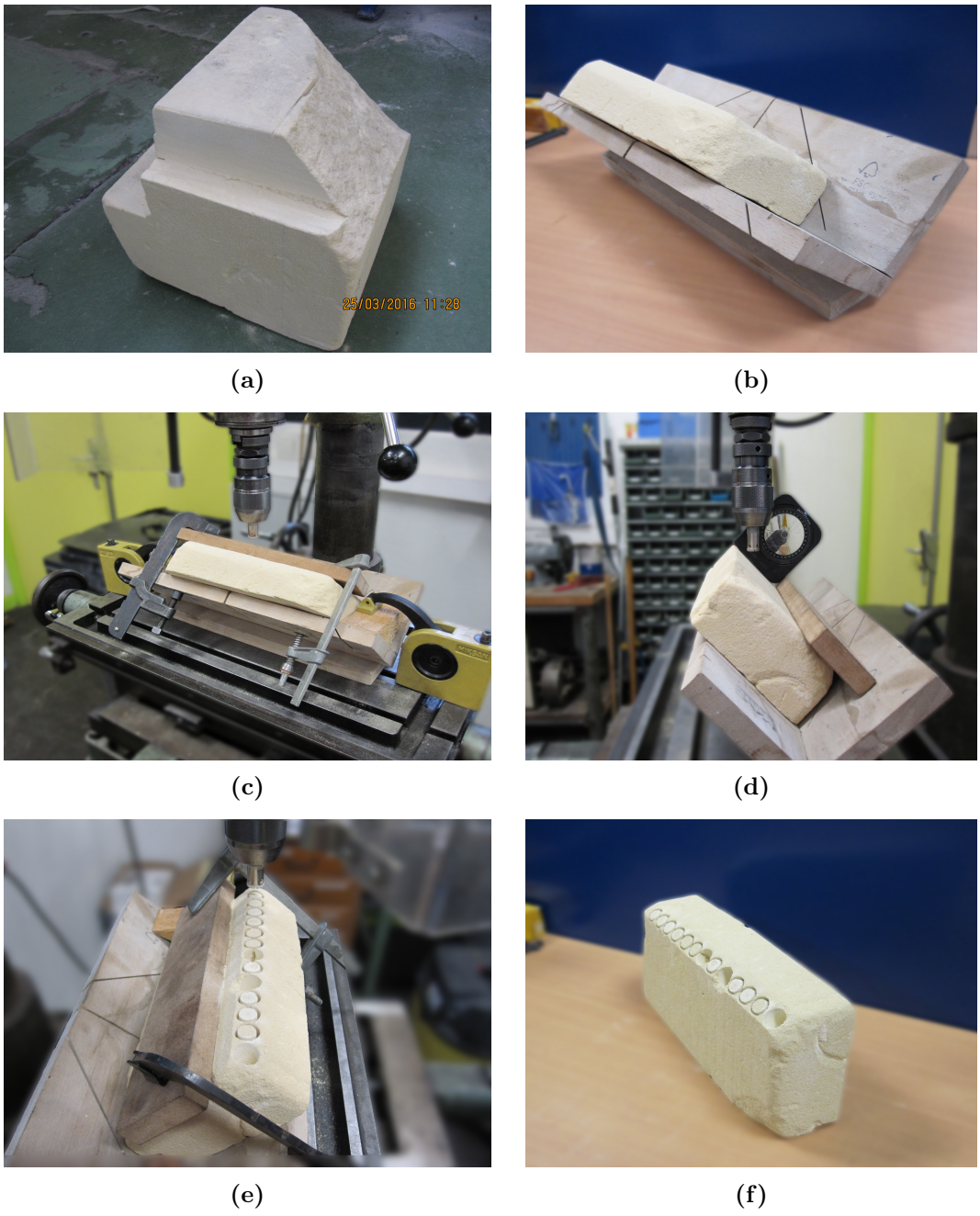

Figure 3.8: Sequence of images illustrating the various steps necessary for specimen preparation, (a) The block of Tuffeau de Maastricht, (b) A smaller part of the material placed on the extra device, necessary for the oblique samples, (c) The material secured onto the pedestal of the drilling machine, (d) Measurement of the actual coring orientation (e) Several cores are prepared at the same time to avoid any deviation from the coring direction among the samples, (f) A number of cores are prepared at 45 degrees with respect to the bedding planes.

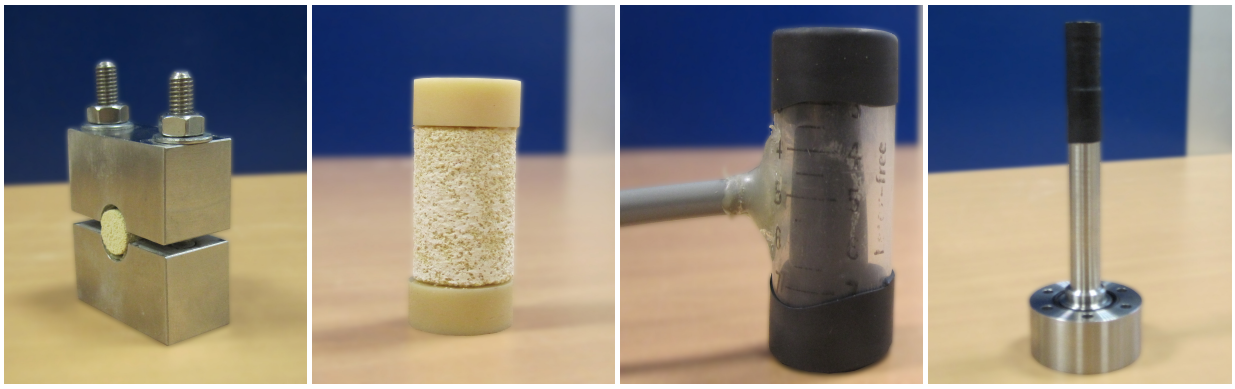

(a) **(b)** **(c)** **(d)**

Figure 3.9: Illustration of the procedure by which the specimen is prepared in this work. (a) The device used to flatten the two specimen's ends and to ensure their parallelism, (b) The lubricated specimen between the two porous stones, (c) The membrane is wrapped around the specimen and the porous stones, (d) Sample placed on the specimen holder.

way the membrane is stretched over the specimen holder, the porous stones and the specimen (Figure 3.9d).

However, in the case of the reference material, a different procedure is followed to prepare the samples (Karatza, 2017). Since the reference material is cohesionless and cannot support its own weight, a mold which maintains the desired specimen shape until the required confinement can be applied, is used.

Initially, the porous stone is placed on the top of the specimen holder. A neoprene membrane is then installed on the lower piston (specimen holder) and the porous stone. Within this membrane the material is later pluviated. In order to ensure that the specimen will be aligned with the porous stone, a great care is taken to place the membrane both vertical, as well as centered with respect to the porous stone. Regulations are done manually when needed. The specimen holder with the membrane is next surrounded by the mold designed for this particular experimental setup. Later the top of the membrane is folded over the mold, allowing access from the top. The sides of the membrane are pushed against the mold by the applied vacuum. Once the membrane is stretched on the mold, the material is pluviated from a varying height, to ensure a constant drop height. When the desirable specimen height is reached, the second porous stone is placed on the top and the specimen is sealed. As soon as all the components of the sample are in place, the vacuum is removed from the mold, and the mold from the specimen. Finally, the specimen is inspected for its verticality and, if not found to be acceptable, the procedure is started again from the beginning (See Andò, 2013, Figure 3.6).

3.3 Experimental apparatus

This section details the experimental apparatus used in this work, in particular the loading system and the triaxial cell.

3.3.1 Loading system

The system used in this research allows performing x-ray Computed Tomography (CT) of the samples under load, *i.e.*, *in-situ*, using the specifically built load frame that can be placed in the x-ray beam. Particularly, the loading system designed in Laboratoire 3SR (Grenoble) is used. The objective of the loading system is to apply and measure the axial load applied on the specimen, as well as the axial displacement.

The axial load is applied by an electric motor which translates the rotation of the motor into a vertical movement of the loading head either upwards or downwards. The speed range for the loading head is from 0.1 μm/min to 1500 μm/min and the maximum axial force that this electric motor can apply is 15 kN (*i.e.*, a normal stress of 144 MPa for a 11.5 mm diameter sample). The speed range considered in this work for the different triaxial tests is 20 μm/min (*i.e.*, strain rate of 0.1% for a specimen of height 20mm). The motor is driven remotely from a laptop used for data acquisition.

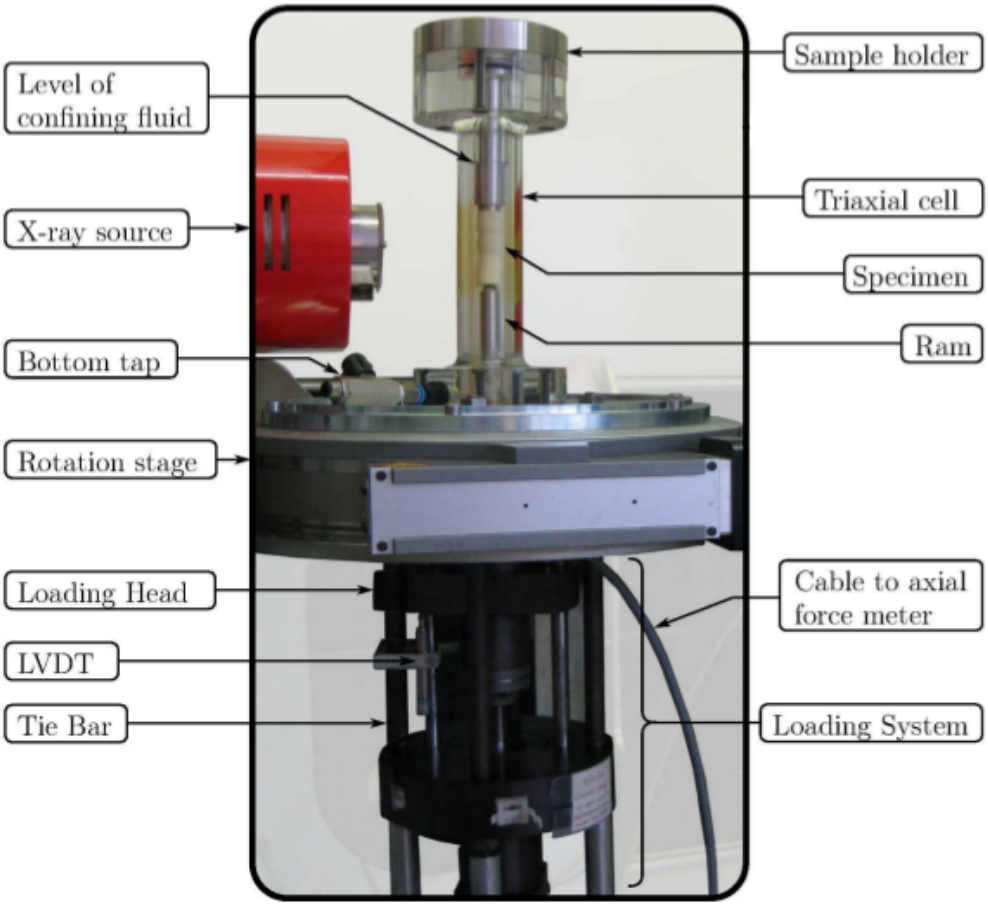

Figure 3.10: The triaxial cell in place in the x-ray tomograph in Laboratoire 3SR, after Andò *et al.* (2013).

Initially and before placing the sample, the entire loading system is installed under the rotation platen inside the x-ray cabin. The loading system, the rotation platen, and the triaxial cell are connected together through four tie bars (Figure 3.10). In order to ensure a seal with the inside of the cell, as well as with the loading ram, a circular plate is placed between the triaxial cell and the rotation stage (Figure 3.10). The ram is pushed progressively through this circular

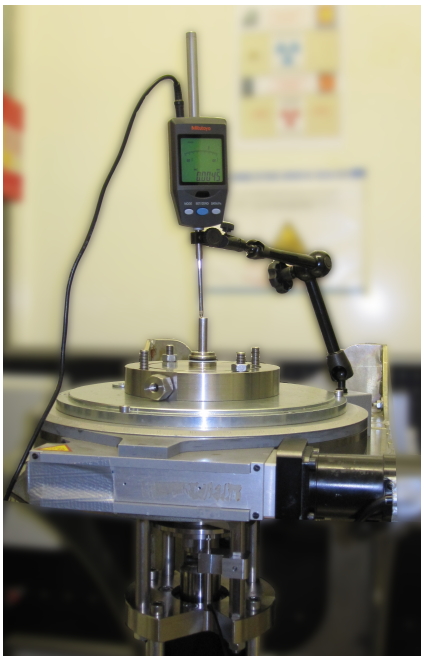

Figure 3.11: LVDT calibration at the beginning of the experiment.

plate by the loading system. The loading ram id a 10 mm diameter steel bar, flat on both ends.

The axial load is measured by a force meter, which is installed onto the loading head, always in contact with the loading ram. The maximum axial force that can be measured by the force meter used is 10kN ($\approx$ 96 MPa for a 11.5 mm diameter sample), with a precision of 0.2%. The measurement of axial displacement is made by an external transducer (LVDT) (shown in Figure 3.10), which is attached to the tie bar and measures the vertical displacement of the loading head. Both pieces of equipment are calibrated at the beginning of the work against a reference force meter and LVDT respectively (Figure 3.11).

3.3.2 Triaxial cell

The triaxial cell used in this work differs from a conventional triaxial cell (Bishop and Henkel, 1957) essentially by its size and by its shape. Since the main objective of this work is to perform *in-situ* x-ray scanning, the cell must be able to be scanned without blocking the x-rays. The vertical steel bars and the tie bars that exist in a conventional apparatus cannot be used due to their high x-ray absorption. Therefore, the triaxial cell used in this study is designed to allow x-ray scanning and to fit the mechanical loading system available at Laboratoire 3SR. The cell, well described in (Lenoir *et al.*, 2007, Hall *et al.*, 2010, (Andò, 2013) is made of Polymethyl methacrylate (PMMA), which makes it very transparent to x-rays but also allows visual monitoring of the test. The 8-mm thick wall allows the cell to sustain the 7 MPa confinement pressure and the tensile reaction force. A comparison between a conventional triaxial cell and the cell used herein is shown in Figure 3.12.

The particular "I" shape of the cell enables the whole set-up, *i.e.*, the sample, to be closer to the x-ray source for higher resolution. The cell has an internal diameter of 20 mm large enough for the specimen dimensions but also the confining fluid. As described above, in subsection 3.3.1, the bottom platen has a hole for the loading ram to pass through and seals the bottom of the

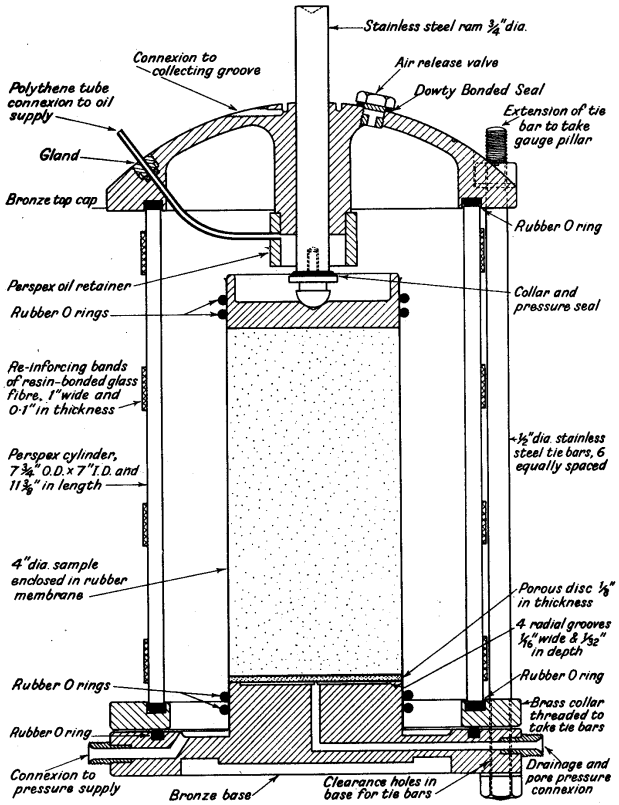

(a)

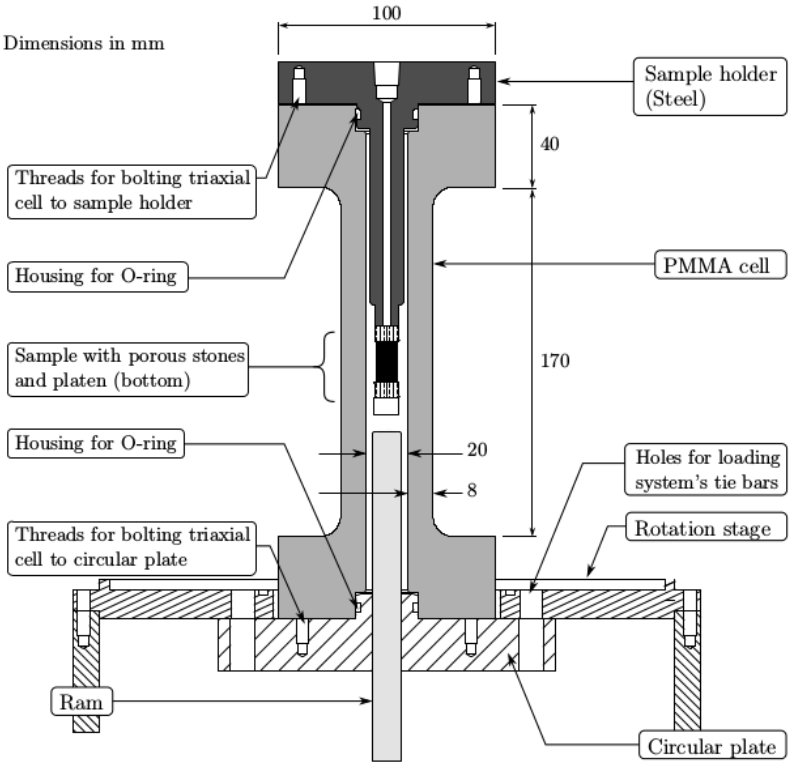

(b)

Figure 3.12: Schematic of (a) conventional triaxial cell after Bishop and Hekel, (1957), (b) triaxial cell of laboratoire 3SR designed by P. Bésuelle and N. Lenoir after Andò (2013). All dimensions are in mm.

cell. The top platen makes a seal with the top part of the cell. Additionally, the upper platen acts as the upper piston with a steel cylinder 10mm in diameter, similar to the loading ram. The upper piston is always in contact with the specimen through the stone at the top of the specimen, thus is also called specimen holder. Both upper and lower platens are connected to drainage lines. The horizontal hole at the bottom part allows filling the cell and the confining pressure to be applied. As for the top platen, the hole is used to apply vacuum to the sample, which is needed to keep the sample standing until it is placed into the cell and the confinement is applied.

3.4 Test setup

The prepared specimen, the triaxial or the oedometer cell (depending on the experiment) and the loading system are assembled altogether before starting the experiment.

The loading system is set up outside the x-ray cabin. The force meter and the LVDT are installed onto the loading head and on the tie bar, respectively. Then, the whole system is installed under the rotation table. On the top of the rotation table, the circular plate, which seals both the bottom of the cell and the ram, is placed. Both the rotation table and the circular plate have four holes through which the four tie bars of the loading system slid. Therefore, all of them are secured by four bolts on the top of the circular plate. Once the system is in place the triaxial cell is screwed on the circular plate. Then, the sample holder, with the desired sample, is pushed down slowly so that the cell can be closed. Both the lower and upper platen are screwed on the cell. At this stage a first tomographic x-ray scan of the specimen is performed. This first scan is labeled as state "00", *i.e.*, initial conditions.

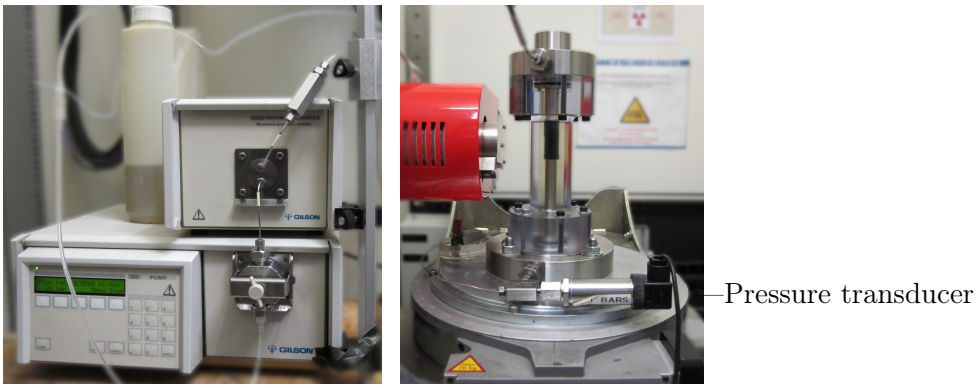

Figure 3.13: (a) The confining pressure is applied by a Gilson pump, (b) The pressure inside the cell is read from a pressure inlet placed on the bottom platen of the cell.

On the lower platen (circular plate) a Gilson 305 Master pump (Figure 3.13a) is connected through a cell pressure inlet (Figure 3.13b). The confining pressure is applied by the pump, using oil as the confining fluid. The flow-rate of the oil inside the cell is controlled by the pump, which allows a fine control of the confining pressure. For each test, the desired confining pressure is set as the threshold value for the pump. This type of pump adjusts automatically the pressure only for values lower than the threshold. However, if and when the pressure exceeds this threshold, then a manual adjustment is needed. In order to avoid adjusting the pressure

manually each time (which would result in a sharp pressure drop), a small, controlled leakage is applied. This technique allows keeping the pressure constant to the desired confining pressure with the fluctuations to be only a few kPa ($\pm 10kPa$). A counterbalance between the leakage and the pump flow-rate must be insured though. The cell pressure is increased to the final desired value gradually with a small flow-rate of 0.05 ml/min. Every 500 kPa the pump is stopped for 1 minute, which is enough to regulate the pressure inside the cell. Once the confining pressure is reached, the loading ram is advanced closer to the specimen. The phase of moving the ram before being in contact with the specimen allows estimating the friction between the loading ram and the bottom platen. In order to get as close to the specimen as possible the x-ray scanner is used (see in Andò, 2013, Figure 3.9). Once the ram is in contact with the specimen, the loading system is stopped, the LVDT is placed in its final position and all the measurements are zeroed.

At this stage the whole system is checked for oil leakage in all the joints but also in the membrane and if none is found, then a second scan, *i.e.*, state "01", is performed. In case that leakage is detected in the membrane, then the test is aborted.

3.5 Experimental campaign

The experimental campaign consists of a number of oedometer, uniaxial, triaxial, and isotropic compression tests on dry samples of Tuffeau de Maastricht. All these tests are performed on the natural cemented material, but also some of them are repeated on the reference material. In total 55 tests have been performed in this study including supplementary backup tests and tests on the reference material.

Table 3.1 summarizes the initial conditions of a collection of specimens tested. Measurements of specimen diameter, height and dry mass are made directly on the specimen before the lubrication as well as sample is wrapped by the membrane. The specimen dimensions have a certain degree of variability. The diameter varies relatively little for the cemented samples since all of them are prepared with the same diamond drill. The height of the specimens however is much more variable and is related to the specimen preparation (section 3.2). The diameter and height are measured three times; values given in Table 3.1 are the mean values

The initial bulk porosity of the samples is obtained using both the specimen bulk volume and the specimen's solid mass for the samples tested outside the x-ray cabin. The equation for total porosity (ϕ) is:

$$\phi = 100\left(1 - \frac{\rho_b}{\rho_g}\right) \tag{3.1}$$

where ρ_b is bulk density and ρ_g is grain density ($2.58g/cm^3$). However, for the *in-situ* experiments porosity is measured from the 3D tomographic images (see chapter 5).

The axial stress is calculated by the axial force measured over the cross-section of the specimen in the initial state, by taking into account the contribution of the cell pressure being exerted on the cross-section of the ram removed (recall – piston's diameter is 10 mm while specimen's is 11.5 mm). The axial strain ϵ_a, *i.e.*, the shortening of the specimen with respect to its initial

height, is monitored with an LVDT.

$$\sigma_1 = \frac{F}{A} + \frac{\sigma_c(A-a)}{A} \tag{3.2}$$

where A is the cross section of the sample, a the cross section of the piston, and σ_c the confining pressure.

3.5.1 Uniaxial compression test

The specimens are compressed axially by the ram driven up by the loading system (section 3.3). Given that the loading system applies and measures the axial force compressing the specimen from below, and the vertical displacement of the lower piston, the specimens have to be attached to the upper piston. A thin latex membrane is applied to the specimens to avoid gravity effects and fix them in place. The membrane is wrapped around the specimen following the same procedure as described in section 3.2.

The specimen is then axially loaded by advancing the ram against one of the loading platen. The ram is advanced under displacement control at a constant rate of axial displacement of 20 μm/min, *i.e.*, a strain rate of $1.5 \times 10^{-5} s^{-1}$. The shortening imposed to the specimen is measured along with the specimen's reaction force. The contact between ram and specimen is made in such a way that the loading platen is always kept horizontal and axially centered.

Despite the fact that the membrane, which is used for this experimental campaign is thin (0.3 mm) and flexible, it applies a mean effective stress to the specimen. Thus, new samples are prepared following a different method. The membrane is cut in smaller pieces and is applied only to the top and the bottom of the specimen. In this way the top of the specimen is placed and fixed on the specimen holder, the porous stone is attached to the bottom end and the rest of the specimen is "free". The mechanical response for both cases with and without membrane is presented in chapter 5. All the uniaxial compression tests are conducted outside the x-ray cabin.

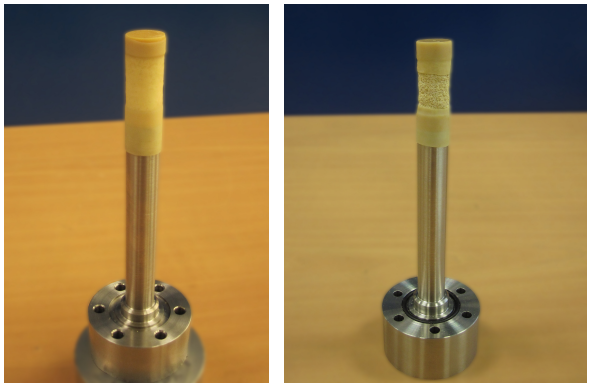

(a) **(b)**

Figure 3.14: Tuffeau de Maastricht specimens placed on the specimen holder before the uniaxial compression test. Two different methods are applied to attach the samples on the upper piston, (a) a thin latex membrane surrounds the whole specimen, (b) the latex membrane is only on the top and the bottom of the specimen.

3.5.2 Isotropic compression test

Both the loading system and the triaxial cell described in section 3.3, are used for the isotropic compression tests. Once the specimen is prepared on the specimen holder, it is installed into the cell with the top of the specimen (as prepared) pointing down. The top of the specimen is always in contact with the upper piston (specimen holder), while the bottom end of the specimen is free. In fact, the loading ram is used for this type of tests with the only purpose to make a seal between the circulate plate and the bottom of the cell.

As far the triaxial compression tests, oil is used as a confining fluid. The isotropic compression tests are conducted by increasing step-by-step the confining pressure, *i.e.*, 0.5 or 1.0 MPa at the time. The confining pressure is applied by a pump with a small flow-rate of 0.05 ml/min. Once the desired pressure is reached the pump is stopped and x-ray scans are performed at each loading step.

Due to the fact that the loading ram is not in contact with the sample during the experiments neither the force nor the axial strain could be acquired from the loading system. Additionally, since the specimens are tested dry, volumetric strain cannot be obtained from the volume of the pore fluid entering or leaving the specimen. The bulk volume, the axial and the volumetric strain of the specimen are instead obtained from the 3D images obtained throughout the tests. The measurements from the 3D images coming from tomography are detailed in section 4.3.

3.5.3 Triaxial compression test

A total of (27) triaxial tests are carried out on Tuffeau de Maastricht samples cored perpendicular, oblique (45°) and parallel to the bedding. Once the sample is placed inside the triaxial cell a first x-ray tomography is performed. The first scan is performed to characterize the initial state of each sample. The samples are then isotropically compressed at different confining pressures ranging from 0 (no confinement) to 5 MPa. Each sample is loaded isotropically (as described above) by pressurizing the cell fluid surrounding the specimen until the desired confining pressure is reached. At this point the second scan is performed.

After the first two scans (state "00" initial conditions, and state "01" end of isotropic compression) have been acquired, the samples are sheared. The deviatoric loading is applied under displacement control by shortening the sample axially using the ram driven up by the loading system at 20 μm/min, as in the uniaxial compression tests. At the point where the axial force starts to climb, *i.e.*, the ram is in contact with the specimen, the axial displacement is recorded and noted as the real zero displacement for each test. Hereafter, loading is continued at 20 μm/min until a decision is made to interrupt loading to scan the sample. When loading, radiographs of the specimen deforming are acquired to record the deformation process during loading. These radiographic scans are acquired under the same conditions as the tomographic scans, except that the rotation stage is kept fixed and that no image averaging is performed (*i.e.*, just one projection is acquired) (see subsection 4.1.4). The acquisition rate for the axial force, axial displacement and cell pressure was one every 2 seconds.

Often in the tests presented in this work, steps of approximately 1.5% axial shortening are aimed for, but every time the macroscopic response suggests significant changes have occurred in

Table 3.1: A collection of tests analyzed in this study: uniaxial compression test (UA), isotropic compression test (ISO), and triaxial compression test (TX)

Test name	Diameter (mm)	Height (mm)	Mass (g)	Porosity (%)	Confining Pressure (MPa)	Coring Direction (°)	Image analysis
Uniaxial compression tests							
UA90-02	11.36	20.34	2.63	50.6	-	90	-
UA90-03	11.31	20.22	2.62	50	-	90	-
UA45-00	11.47	20.46	2.68	50.8	-	45	-
UA45-01	11.46	20.34	2.69	50.3	-	45	-
UA45-02	11.54	20.26	2.66	51.3	-	45	-
UA00-00	11.39	20.62	2.67	50.8	-	0	-
UA00-01	11.37	20.15	2.60	50.7	-	0	-
Isotropic compression tests							
ISO-01	11.31	20.22	2.62	50	-	90	✓
Triaxial compression tests							
TX90-01	11.45	20.23	2.66	50.5	1	90	✓
TX90-04-02	11.45	20.34	2.70	50	4	90	✓
TX90-05	11.48	21.10	2.78	50.7	5	90	✓
TX45-02	11.45	20.97	2.75	49.5	2	45	✓
TX45-03	11.53	21.24	2.74	52.1	3	45	✓
TX45-04	11.45	20.97	2.75	50.6	4	45	✓
TX0-01	11.47	20.43	2.71	50.2	1	0	✓
TX0-03	11.53	20.74	2.75	50.8	3	0	✓

the specimen, scans are performed. While acquiring a full x-ray tomography data (which takes around 1.5 hours), the axial loading system is halted and the piston held in place (the axial displacement is held constant). During the x-ray scan, the force, displacement and confining pressure data acquisition is slowed to once every 30 seconds.

3.6 Summary

The main objective of this to study is to investigate experimentally the mechanisms governing the mechanical behavior and failure mode of high porosity carbonate rocks. In order to achieve this, a highly porous limestone from Maastricht region, known as Tuffeau de Maastricht is chosen. It is a bioclastic calcarenite formed by sediments transported and deposited in a shallow sea during the Upper Cretaceous period. Due to the fact that it was deposited at very slow rate, and the existence of only a few meters of a few meters of sediments, Tuffeau de Maastricht exhibits up to 52% porosity.

A great deal of care is taken in preparing cylindrical samples of Tuffeau de Maastricht cored perpendicular, oblique (45°), and parallel to the sedimentary bedding plane. All the specimens tested in this study are extracted for the same block to minimize the effects of material variability and then ground to diameter of 11.5 mm and length of 22 mm. This particular geometry is necessary to facilitate the x-ray computed tomography (CT) and allows full-size measurements

at a sufficiently high resolution. Thus, the relevant experimental apparatuses for this particular samples dimensions are needed.

This chapter describes the loading system and the triaxial cell used in this study. The loading system is designed in Laboratoire 3SR and allows performing x-ray CT scans, *i.e.*, it can be placed in the x-ray beam. The triaxial cell is accordingly built to be transparent to x-rays allowing the samples to be scanned. Consequently, the triaxial cell used differs from a conventional triaxial cell essentially by its size and shape. Additionally, comprehensive details are given for the final experimental setup adapted for the desired experiments. The experimental procedures are also discussed in this chapter. In particular, details about the isotropic, uniaxial and triaxial compression tests are given.

Chapter 4

Methodology: image and data processing tools

In this study, the development of localized deformation on Tuffeau de Maastricht is investigated quantitatively using x-ray Computed Tomography (CT) and an image analysis of the CT images.

High resolution 3D imaging provides information on the internal degradation as it progresses under loading. All the experiments described above (section 3.5) have been imaged in several different states of increasing axial strain. The 3D images can be analyzed in order to define the solid and void phases of the sample imaged by the x-rays. Continuum porosity measurements are performed on Tuffeau de Maastricht macroscopically as well as at the micro-scale (averaged over a Representative Elementary Volume). Further analysis allows qualitative definition of the complex microstructure of Tuffeau de Maastricht.

Although 3D visualization is a powerful tool to investigate the sample after reconstruction, it has its limitations. Displacement field measurements and subsequent strain field calculations are essential to complete the understanding of the localized deformation throughout an experiment. If the material is followed through the different configurations and images are acquired during deformation, digital image correlation (DIC) can be used to infer the displacement and strain field. In this study, 3D continuum DIC measurements using *TomoWarp2* (Tudisco *et al.*, 2017) code on the gray scale reconstructed images, are performed.

4.1 X-ray computed tomography (CT)

X-ray computed tomography (CT) is a nondestructive technique that allows visualization of the internal structure of objects, determined mainly by variations in density and atomic composition. The principle of CT measurement consists of acquiring x-ray radiographs at many different positions during step-wise rotation around a central axis, whereby either the source and detector or the sample are moved. From these different projections, a 3D image of the object can be reconstructed.

X-ray CT was developed as a medical imaging technique in the early 1970s, and has since found wide applications within the fields of geoscience (Mees *et al.*, 2003). Due to their ability to penetrate certain materials, x-rays are used for a number of non-destructive evaluation and

testing applications. Computed tomography is useful for studying a wide range of materials, *e.g.*, rock, bone, ceramic, metal and soft tissue. Recently, the study of geomaterials (including granulates, soils, rocks and concrete) has become one of the more active and challenging fields of application of x-ray imaging.

Based on computer technology, x-ray CT is developed so efficiently that it can be used to investigate 3D microstructures and discontinuities of geomaterials. It can be applied to obtain either qualitative or quantitative data. Qualitative applications are those that require only a visual assessment of the resulting x-ray image. X-ray CT can be utilized to determine mineralogy, pore characteristics, heterogeneities, multiphase fluid flow, and fracture volume of the rock sample. However, the true power of x-ray tomography lies in the capability to extract quantitative information about internal and external three-dimensional structures. In addition to qualitative assessment of the x-ray images, quantitative information such as density, porosity, and saturation values and distributions can be extracted from CT scan images.

4.1.1 X-ray CT basics

In 1895, Wilhelm Conrad Röentgen noticed a barium platinocyanide screen fluorescing in his laboratory as he generated cathode rays in a Crookes tube some distance away. Even with paper and wood in the way of the beam, the mysterious rays managed to light up the fluorescent screen. Because of their unknown nature, he called them x-rays. Röentgen then replaced the fluorescent screen with photographic paper and took the world's first x-ray, a clear image of the bones and wedding ring on his wife's left hand (Figure 4.1).

X-rays are wavelike forms of electromagnetic energy carried by particles called photons such as visible light rays. The only difference between the various types of electromagnetic radiation is the amount of energy found in the photons, *i.e.*, the wavelength of the rays. Due to their short wavelength, x-rays (and gamma rays) have more energy to pass through matter than the other forms of energy in the electromagnetic spectrum. As they pass through matter, they are scattered and absorbed and the degree of penetration depends on the kind of matter and the energy of the rays. X-rays are divided into "hard" (shorter wavelength, higher energy) and "soft" (longer wavelength, lower energy).

When x-ray photons interact with matter, they may do so through many different mechanisms such as Refraction and Reflection, Pair Production, coherent scattering, Compton scattering, and Photoelectric absorption. The way of interaction depends both on the matter as well as the energy range of the x-ray photons. An important measurement for the different types of interactions is the percent of the energy transferred as a function of x-ray photon energy. At low x-ray energies, the majority of the energy is transferred by the photoelectric process (see Figure 2.11 in Hsieh *et al.*, 2009). In general for geological materials, the photoelectric effect will dominate the attenuation mechanism at low x-ray energies up to approximately 50-100 keV, while Compton scattering is dominant at higher energies up to 5-10 MeV. For the material studied in this work, and the energy of x-ray radiation used, the overcharging mechanism of interaction of x-rays with the material is photoelectric absorption.

The net effect of these interactions is that some of the photons are absorbed or scattered. In other words, x-ray photons are attenuated when they pass through the material. Absorption

is the complete removal of x-ray photons from the x-ray beam due to incident x-ray photons that lose all their energy, while scattering leads to a deflection of x-ray photons after interaction with atoms of matter. Besides absorbed and scattered photons, other photons will simply pass through matter, undergoing transmission. The attenuation can be expressed by an exponential relationship for a monochromatic incident x-ray beam and a material of uniform density and atomic number:

$$I = I_0 e^{-\mu L}, \tag{4.1}$$

where I and I_0 are the transmitted and incident x-ray intensities, L is the thickness of the material, and μ is the linear attenuation coefficient of the material. This is often called the Beer-Lambert law. The linear attenuation coefficient, μ, is correlated to the photon energy E, the density ρ, and the atomic number Z of the investigated material and can be expressed as:

$$\frac{\mu}{\rho} = K\frac{Z^4}{E^3}, \tag{4.2}$$

where K is constant, and (μ/ρ) is the mass attenuation coefficient (Baruchel *et al.*, 2000).

X-rays are produced when fast moving electrons ejected from a heated cathode filament, are retarded by a metal object. More electrons will be released as the temperature of the cathode filament increases. Inside the vacuum tube, which contains the cathode and anode of the x-ray source, an electrical potential forces the electrons to accelerate towards the anode. The vacuum is necessary to prevent early burning of the cathode filament and to make the electrons to reach the anode in an undisturbed way. Generally more than 99% of all kinetic energy is converted into thermal energy, leaving less than 1% available for production of x-rays.

Subtle complications can bias the data obtained by x-ray CT. Beam hardening and ring effect are common features in CT-scans. Beam hardening is the most frequent artifact in CT-scanning. In a polychromatic beam, the x-ray loses first the lower energy parts of its spectrum. This effect causes the edges of an object to appear brighter that the center, even if the material is the same throughout (Mukunoki *et al.*, 2004). On the other hand, a miscalibrated or defective pixel generates, in the reconstructed images, a bright or dark ring centered on the pixel corresponding to the location of the rotation axis, usually called the ring effect. Often these artifacts can be reduced during acquisition, although during reconstruction additional corrections might be necessary.

Radiography The radiography in Figure 4.1 shows details of the bones inside the hand. The bones and the ring are distinguishable in the image because they absorb more radiation that the surrounding flesh and therefore result darker in the image. Since x-rays penetrate solid objects, but are weakened by them depending on the object's composition, the resulting picture reveals the internal structure of the object.

X-ray radiography is therefore an imaging technique that allows viewing the internal structure of materials with different density. It is a two-dimensional measurement of the amount of x-ray photons arriving at each point on a detector during a given exposure time, which is an integration of the x-ray attenuation of the matter being traversed along the path of the x-rays.

Figure 4.1: "*Hand mit ringen*" - First radiography, showing Anna Röntgen's left hand with a ring, by Wilhelm Conrad Röentgen (Wikimedia Commons).

Nevertheless, the internal structure of a more complex material cannot be adequately described by a 2D image. An x-ray image from only one location provides a two dimensional look into an object, but the internal structures are stacked on top of each other in the image. A dark spot in the radiography indicates a dense material due to low x-ray penetration. However, it is not easily detected if this is the result from a single region within an object, or from multiple dense regions that are in alignment with the x-ray trajectory. On the contrary, x-ray images taken at different angles around the object will show different alignments of the same dense regions, and a sufficient description of the regions' location can be made.

Tomography X-ray Computed Tomography (CT) scanning overcomes the obvious main limitation of conventional radiography which measures a projection of any three-dimensional object onto a two-dimensional plane with a concomitant loss of spatial information. It was developed as a medical imaging technique in the early 1970s invented by Godfrey Hounsfield. The possibility of its use in engineering was soon recognized, resulting in large number of publications from the early 1980s onward.

In traditional two-dimensional CT scanning, the object is scanned through a single "slice" and each of the individual images consists of the object's x-ray penetration pattern through the location of the slice. When performed from several angles across a single plane, the collected attenuation data may be transformed into a two-dimensional density map, thus reconstructing a slice image of the specimen's internal structure. When combined with data from adjacent slices, a 3D map is obtained. So, tomography is a method for reconstructing a 3D field of x-ray attenuation coefficients from a series of different radiographs. The different projections (radiographs) are in general acquired by a relative rotation of object and image acquisition system.

4.1.2 X-ray scanner in Laboratoire 3SR

The majority of the *in-situ* experiments during this study are conducted in a specialized lab x-ray scanner in Laboratoire 3SR in Grenoble. The x-ray scanner in Laboratoire 3SR (Grenoble) is a built-to-specification laboratory x-ray tomograph supplied by RX-Solution (Annecy), which

was bought in 2007 with funds from ANR Project MicroModEx as well as Laboratoire 3SR. The x-ray scanner is housed inside a lead-lined cabin and includes a Hamamatsu Corporation L8121-03 micro-focus x-ray source emitting a cone beam, as well as a 1920 by 1536 pixel x-ray flat panel detector (Varian PaxScan 2520V).

The range of the x-ray energy of the source is 40 to 150 keV, and can supply currents between 0 and 500 μA, allowing a range of different sample sizes and densities to be imaged. The source operates in three different "spot size" modes: small, medium and large. In the work presented here, 100 kV are selected in order to have the best contrast between pore and grain when imaging the materials studied. The highest current allowed for this voltage setting while remaining in small spot-size mode is selected as the tube current, *i.e.*, 100 μA. The detector, which measures the intensity of "incident" x-ray photons can be put either in portrait or landscape mode (portrait mode is used in this work). Each pixel measuring 0.127×0.127 mm that gives a detector size of 243.84×195.072 mm, which is a bit smaller than a A4 page. This type of detector uses a scintillator (Caesium Iodide, CsI, in this case) to convert x-rays into visible light (Andò, 2013). The "exposure time" is chosen depending on the x-ray attenuation of the sample and the power used. It is adjusted in such a way to use as much of the dynamic range as possible (without saturating any pixels) in order to increase the signal to noise ratio of the images acquired, while also trying to keep the time small, to shorten the total scan time. For the work presented here, the Frames Per Second (FPS), which corresponds to an exposure time of 0.71 seconds, is set to 1.4.

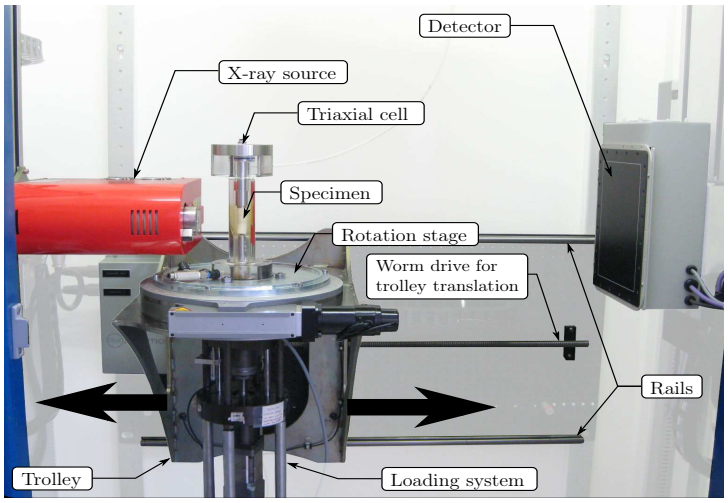

Figure 4.2: Labeled photography of the Laboratoire 3SR x-ray scanner, after Andò, 2013.

The sample to be scanned is placed between the source and the detector on a translation and rotation stage. Rotation is necessary for the specimen to be imaged at different angular positions while translation allows control of the distance between the sample and the source, which in turn controls the size of the image that is projected onto the detector. The spatial resolution (expressed in terms of voxel size) depends on the "zoom" level, *i.e.*, the distance between the sample and the source; it cannot be smaller that the smallest spot size (5 μm in low-power mode), and is limited upward by the physical size of the detector (Viggiani *et al.*, 2014). The source and detector can be driven simultaneously remaining in the plane of the detector. They can be translated in the two directions normal to the axis of the beam, which allows specimens of different heights to be conceived and scanned.

Figure 4.2 illustrates the 3SR x-ray scanner and its main parts that make it different from the standard laboratory scanners. The rotation stage is a hollow ring that rotates and allows the experimental devices to be placed onto, as described in section 3.4. Also, the rotation table acts as a link between the cell and the loading device placed below it. The rotation stage is placed onto the trolley which allows easy control of the zoom level for the specimen being scanned. In other words, all the experimental equipment is attached on the trolley which can move closer or further the x-ray source, depending on the experimental campaign each time. Furthermore, the trolley made by steel is able to carry considerable load (up to 75 kg), which means that massive experimental equipment can be mounted onto the trolley and kept in place during an x-ray scan. One of the main advantages of the 3SR scanner is the room space inside the cabin, so that experimental equipment can be mounted on around the specimen being scanned.

4.1.3 X-ray reconstruction

The purpose of a computed tomography system is to build a 2D or 3D representation of the inner structure of an object. A regular single x-ray image produces a representation of the interior features of an object, but the accurate locations of these features cannot be determined from a single view. However, this limitation can be overcome by a set of projection measurements, acquired from a number of points of view.

Converting recorded x-ray data into a digital image is one of the primary functions of computed tomography. A reconstructed tomographic data file provides a quantifiable description of solid particles and void spaces in a series of two-dimensional cross-sectional images, which also can be combined together to create a three dimensional volume of the scanned object. Reconstruction essentially builds the CT image from the data collected and represents a cross-section of the object. Each of those tomographic slices consists of discrete units known as voxels (3D pixels), the size of which reflects the spatial resolution of the scans. The parameter that is reconstructed is the linear attenuation coefficient μ of the object. In most of the non-destructive testing applications, this is assumed to be proportional to the mass density ρ of the object. Consequently, each voxel of a scanned image represents the average density of a voxel at a particular (x,y,z) location.

Image reconstruction from projections is the process of producing an image of a two dimensional distribution (usually of some physical property) from estimates of its line integrals along a finite number of lines of known locations (Herman, 1980). Reconstruction is achieved with the use of a mathematical tool, the Radon transform, whose mathematical formulation can be traced back to 1917 when J. Radon first developed a solution for the reconstruction of a function from its line integrals. A number of techniques have been proposed that try to deal with computational complexity, spatial resolution, temporal resolution, noise, flexibility, and artifacts. One important family of reconstruction algorithms are the so-called iterative ones, such as ART (Algebraic Reconstruction Technique). Each projected density is thrown back across the reconstruction space in which the densities are iteratively modified to bring each reconstructed projection into agreement with the measured projection. Although conceptually simple, this approach is computationally intensive (in general the iterative reconstruction methods) because forward projections must be performed repeatedly.

The most commonly used algorithm for tomographic reconstruction is the filtered backpro-

jection (FBP). It consists in assigning to each point of the object the average value of all the projections at the corresponding location based on the assumption that the intensity of the object is uniform along the ray path.

A simple case in which the object of interest is an isolated point can be used to explain this method (Figure 4.3). Similar to the ART method, there is no a priory knowledge of the object. Therefore, a uniform probability distribution for its location have to be assumed. So, the entire ray path has the same intensity as the measured projection. The procedure remains the same for the next projection with the difference that the ray path is rotated relative to the previous because of difference in projection angles. This process, repeated for all the projections, formulates a 2D object from a set of 1D line integrals, and is called backprojection. The backprojected image, when compared with the real object is highly blurred. However, an mathematical correction can be done by an appropriate pre-filtering of the projections as in the Filtered Backprojection (FBP).

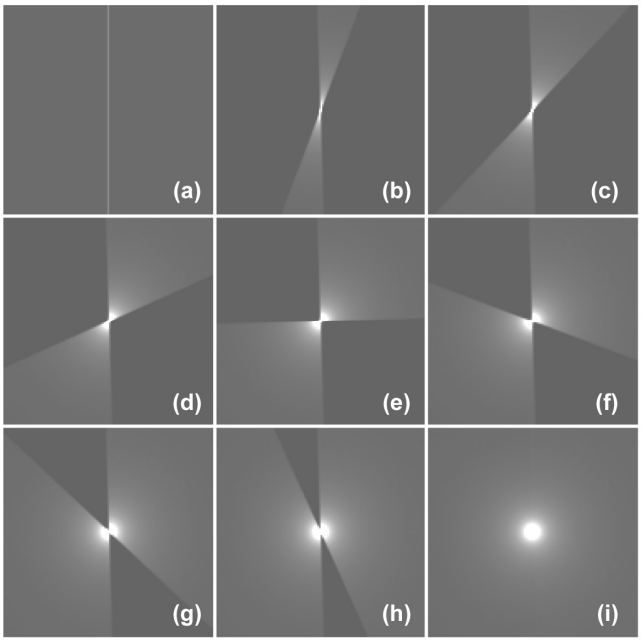

Figure 4.3: Backprojection process of a single point. (a) Backprojected image of a single projection. (b)-(i) Backprojection of views covering: (b) 0 to 22.5°; (c) 0 to 45°; (d) 0 to 67.5°; (e) 0 to 90°; (f) 0 to 112.5°; (g) 0 to 135°; (h) 0 to 135°; and (i) 0 to 180°. After Hsieh *et al.*, 2009.

In this work, the reconstruction software DigiCT from Digisens is used. Since the x-ray source emitting a cone beam, DigiCT uses a reconstruction algorithm based on the FDK algorithm provided by Feldkamp (Feldkamp *et al.*, 1984). More practical information about the reconstruction technique used in Laboratoire 3SR are provided in Andò, 2013 (see Subsection 2.2.3). Once all the parameters are fixed and the initial scan of the specimen is reconstructed satisfactorily, a fixed volume to be reconstructed is defined and fixed for the entire test, *i.e.*, all the scans. At first, the initial and the last scan of each test are reconstructed. This method helps to define the height and the width of the reconstructed volume. In the initial configuration the specimen is at its maximum height. The last scan is used to define the width since the specimen is expected to expand in diameter. In this way, a fixed reconstruction area which includes the whole specimen is imposed for all the reconstructions of a given test. Furthermore, the fact that all the reconstructed volumes have the same size simplifies the data analysis.

4.1.4 X-ray to study localisation on Tuffeau de Maastricht

Before starting a scan, all acquisition parameters need to be optimized in order to obtain images of the highest possible quality. The acquisition parameters have to be chosen in such a way that a high signal-to-noise ratio can be achieved in a relatively limited scanning time.

The first parameters to be set are the x-ray energy and current, that both depend on the density and composition of the sample. In order to study high-density materials such as natural building stones, high x-ray energies can be used (Cnudde, 2005). There are no general rules for the acquisitions, however it is clear that x-rays should not be completely absorbed by the object and those that pass through the sample have to be fully detected. In this work, 100 kV and 100 μA are selected as the x-ray energy and tube current, respectively. Once the tube settings are defined, a good exposure time has to be selected. The exposure time controls saturation and blooming, affecting both detector's quantitative and qualitative imaging characteristics. If the exposure time is too short, the result is a very dark image. On the other hand, if it is too long, each pixel approaches its saturation limit, which means that the pixel loses its ability to accommodate additional charge. As it is already mentioned above, the exposure time for this work is 0.71 seconds, which corresponds to 1.4 Frames Per Second (FPS).

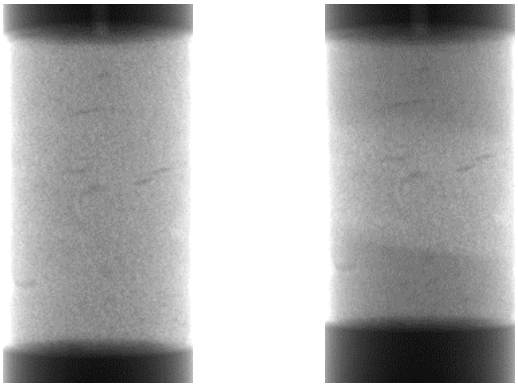

(a) **(b)**

Figure 4.4: A radiograph of Tuffeau de Maastricht where the sample appears between the ceramic porous platens on the top and the bottom (a) at initial conditions, and (b) after deformation is applied.

During the acquisition it is recommended to minimize noise. This noise can be reduced by averaging several projections taken at the same angle. So, at each angular position 4 radiographs are acquired and averaged. A radiograph of Tuffeau de Maastricht scanned during this research, is shown in Figure 4.4. The regions that appear darker mean that fewer x-ray photons interact with the detector because an amount of photons has been adsorbed by the scanned objects. In other words, the darker color corresponds to denser material. An additional improvement is applied before start scanning, whereby images are corrected with dark and flat-field image. An number of images are acquired and averaged with no incident x-rays to capture the dark current, and the procedure is repeated with x-rays "on" but with no specimen in the x-ray beam.

Finally, the amount of data needed to be acquired is defined. Multiple radiographs are acquired over a range of angular orientations (a few tenths of a degree) as the specimen rotates over 360°. A full 360° rotation is required due to the conical beam (Feldkamp *et al.*, 1984). Figure 4.5 demonstrates that the acquired images with only 180° are noisy compared to the ones at 360°. The number of the acquired radiographs defines the rotation angle of the platen.

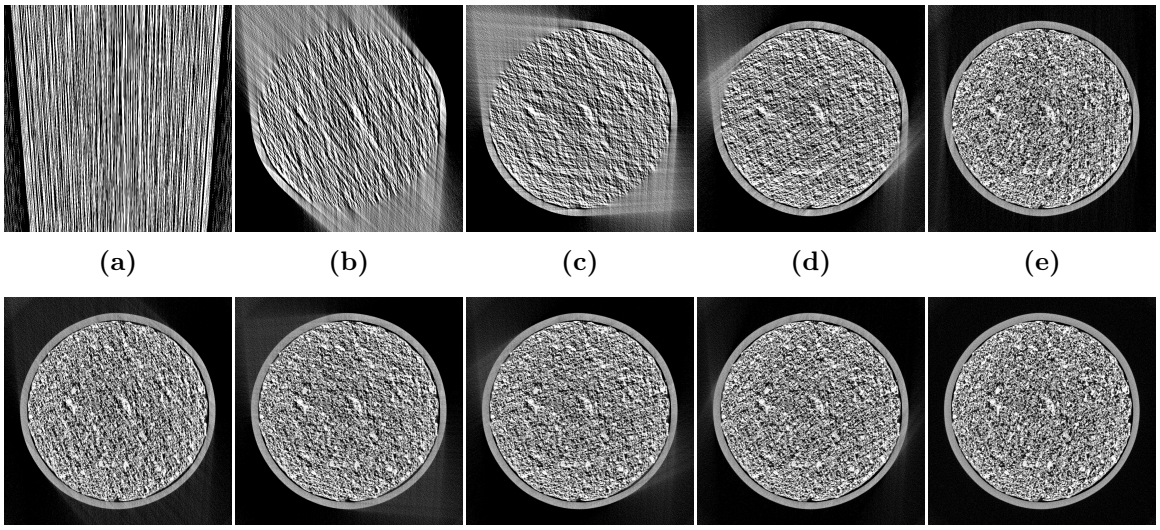

Figure 4.5: Horizontal slices of the 3D reconstructed volume of Tuffeau de Maastricht. In order to reconstruct the CT images, radiographs are acquired at (a) only 1°, (b) 0 to 45°, (c) 0 to 90°, (d) o to 135°, (e) 0 to 180°, (f) 0 to 225°, (g) 0 to 270°, (h) 0 to 300°, (i) 0 to 330°, and (j) 0 to 360°. Note that all the radiographs are acquired at regular spaced intervals of 0.32°.

The tomographic scans performed in this work consist in acquiring 1120 or 1200 radiographs as the specimen is rotated at regular spaced intervals of 0.32° or 0.30° respectively. Increasing the value of the rotation step size will not only decrease the corresponding number of views (radiographs) during acquisition and consequently lower the signal-to-noise ratio, but will also decrease the acquisition and reconstruction time. Figure 4.6 depicts the level of noise for the same reconstructed image but with different rotation step size. The higher the angular step the lower the signal-to-noise ratio. A complete tomographic scan with the settings used in this work and described above takes 1 hour and 33 minutes.

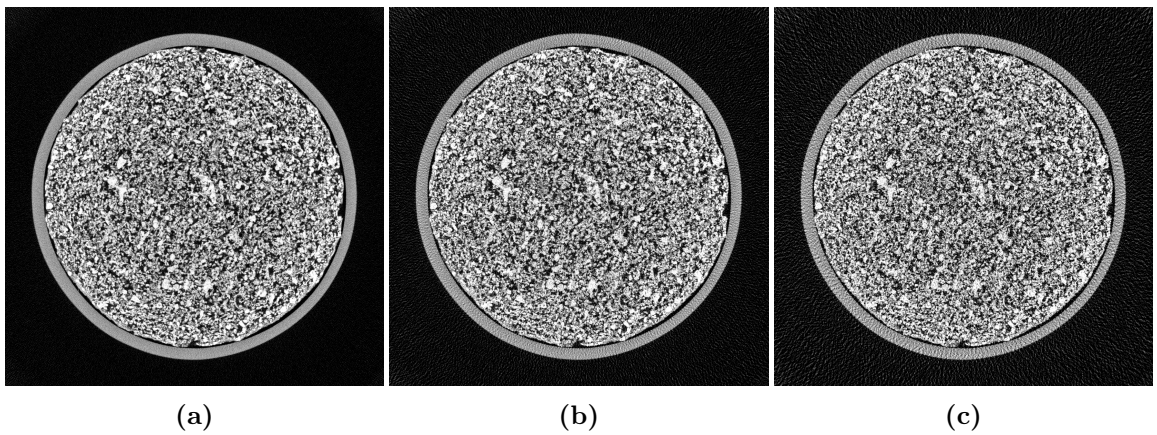

Figure 4.6: Horizontal slices of the same 3D reconstructed volume. A full 360° rotation applied to the sample with different angular steps: (a) every 0.32° (1120 radiographs), (b) every 0.34° (560 radiographs) (c) 0.96° (374 radiographs).

The detector used in this study works in a similar way to a typical Charge-Couple Device (CCD). Therefore, much like the human eye reading a book, the detector is able to discern small features when they are closer. In case someone tries to read the book from across the room, large letters or headers may be clear, but the small text letters will likely be blurry. As the book is

getting closer to the eye, it's possible to distinguish even the small dots. The same analogy can be applied to CT scans of Tuffeau de Maastricht. So either small volumes can be scanned at a high spatial resolution, or large ones can be scanned at lower spatial resolution. Figure 4.7 shows 2D cross sections of Tuffeau de Maastricht, which come from tomographic scans at different levels of zoom. In this study, the zoom level is selected so that the whole specimen fits comfortably inside the field of view. In particular a voxel size of 13 μm is selected in order to best image the specimen. As a result, there are about 11 pixels across a mean particle of Tuffeau de Maastricht (D_{50} =150 μm).

Once all the parameters are optimized for this particular study on Tuffeau de Maastricht, they are fixed and kept constant during all the experimental campaign. After completing the CT scan, the x-ray images are compiled into a quality two-dimensional view of the interior of the scanned sample. Then, the 3D volume is reconstructed as a series of slices that are aligned and laid on top of each other. These 2D slices stacked together form the 3D volume that can be sliced in any orientation. Note that these slices are equally spaced with a unit thickness of only one voxel, *i.e.*, 13 μm.

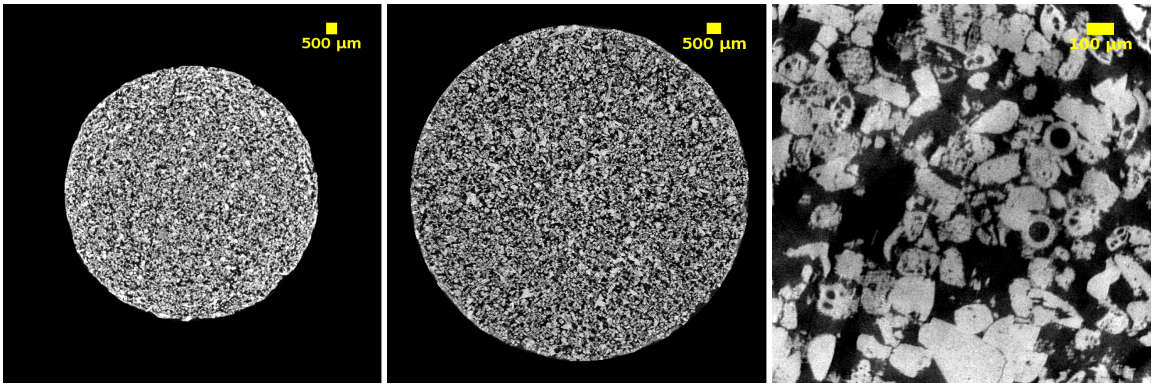

(a) **(b)** **(c)**

Figure 4.7: Cross-section of Tuffeau de Maastricht at different zoom level: voxel size of (a) 13 μm, (b) 7 μm, and (c) 1 μm. The x-ray CT images at high resolution are not obtained in Laboratoire 3SR.

It is very important to note that a CT scan image is not only a cross-section of the specimen as a whole , but it also contains images of cross-section of the individual particles. Some of the particles may have been sectioned through their thickest portion and others in less-thick portions or near their edge. So they appear as larger or smaller (respectively) in a particular 2D slice. A typical cross-sectional image of Tuffeau de Maastricht with the corresponding histogram is shown in Figure 4.8. The gray-scale values vary from white to dark gray and the pixel values range from 0 (black) to 65535 (white), *i.e.*, 16 bits image. These grey levels represent the range of x-ray attenuation through the sample, with black pixels representing the voids and the light-gray/gray pixels representing the solid phase.

Due to the image resolution chosen for this study, the solid phase has to be considered as a single portion, *i.e.*, grains are not seen individually (see section 4.2 and section 4.4). Additionally, since Tuffeau de Maastricht is a 96% calcite rock, the bonds between the particles and the grains have the same x-ray attenuation value, and this makes any separation very difficult (Figure 4.7a). However, these digital images are ideal for collecting information about the internal structure of the material and can be used for quantifiable measurements of basic properties such as void

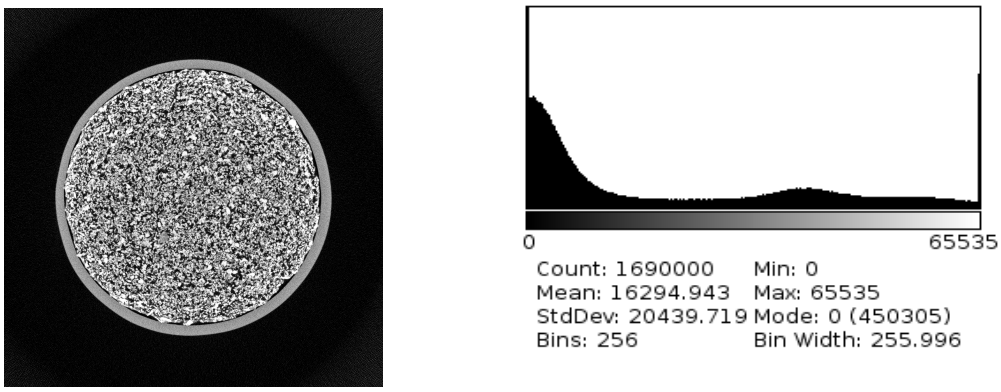

Figure 4.8: A cross-section of Tuffeau de Maastricht with the corresponding histogram.

ratio, porosity and grain size. Figure 4.9 presents a schematic diagram of x-ray imaging procedure followed during this study.

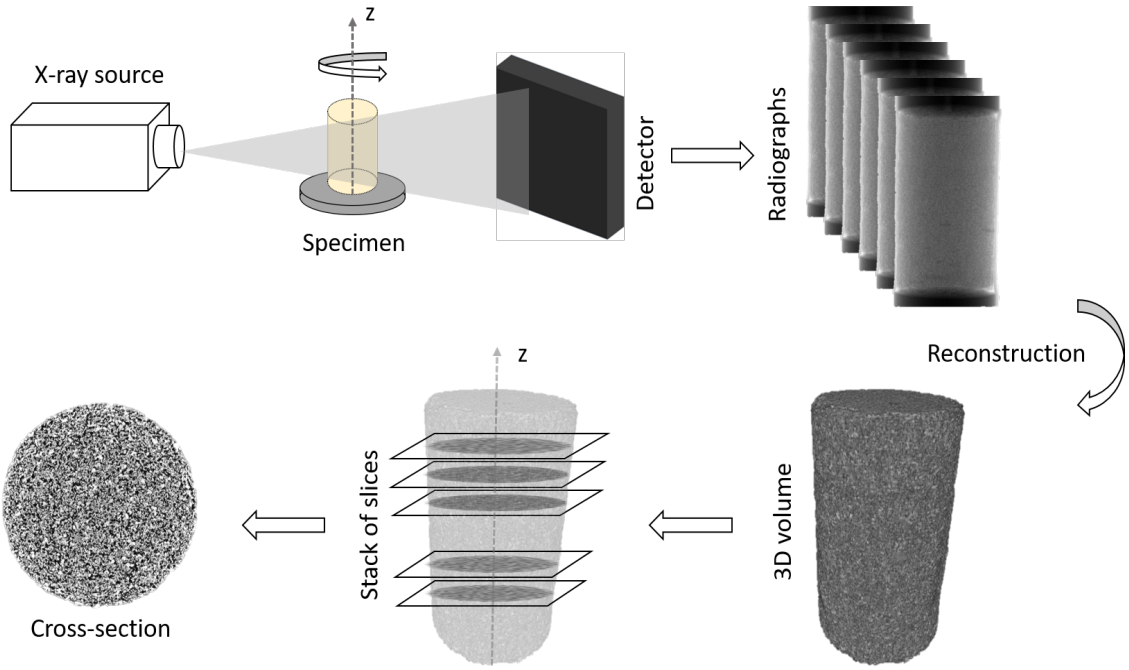

Figure 4.9: Schematic description of image acquisition with x-ray computed tomography.

4.2 Porosity measurements

In this study, x-ray CT is used as a tool to determine porosity based on the information of the reconstructed images. The CT images produced through *in-situ* x-ray tomography, especially the one at high resolution (Figure 4.7c), reveal that Tuffeau de Maastricht is highly porous, but they remain just images. However, when porosity needs to be quantified further data analysis is required. The first and most straightforward quantification of these images involves determining the measurements of a 3D field of porosity, and its evolution through the test. Since the linear attenuation coefficient depends on density and atomic number (Equation 4.1), mineralogical constituents as well as pores inside the material can be differentiated. The fact that Tuffeau

de Maastricht is in general a mono-mineralic rock (more than 96% is calcite) makes porosity measurements less complicated than for other types of rock.

By definition, porosity is defined as the ratio of the volume of pores (voids) over the total volume of the specimen, $\phi = V_V/V_t$. In this work, the macroscopic initial porosity is measured following three methods: i) the standard method (described in section 3.5), ii) MIP, and iii) using the x-ray reconstructed images, which also allows tracking the evolution of the porosity.

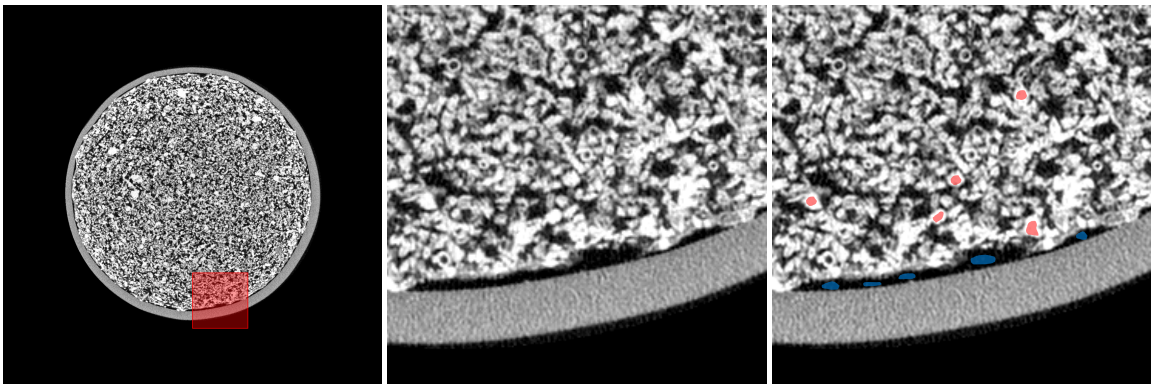

(a) **(b)** **(c)**

Figure 4.10: The threshold values that separate the voids from the grains are defined manually in small selected regions. This schematic diagram shows how these measurements are collected. In red are the measurements for the solid phase while in blue are the ones for the void.

The CT scans provide a description of the solid and void spaces shown in cross-sections through the samples. So, it is possible to obtain the macroscopic porosity from binarized images where the number of void and solid pixels can be counted. Each voxel is characterized by its gray level that ranges for 0 to 65535 for a 16 bit image. The pores are rather in black and the particles in light gray. The particles appear in the CT scan as many different shades of gray that correspond to each particle's density (Figure 4.7). In order to calculate porosity from the images, the gray values of the solid must be distinguished from darker values of the voids, by setting a threshold value. Since porosity calculation depends on the threshold values used, great care is taken to choose this value. An efficient algorithm is built to quantify and separate the main solid phases from the voids in the original gray-scale image. The two threshold values (one for the void and the other for the solid) have to be defined and given as an input to the algorithm. These values are measured manually on a small selection of pores and grains throughout the specimen. In particular, for each tomographic x-ray scan a number of measurements, large enough to guarantee objectivity (more than 50), is taken and the mean value is used as the threshold. Especially for the voids, these measurements are taken in small regions between the membrane and the sample at the initial conditions (state "00"). This assures that only void is selected and measured (Figure 4.10). Finally, all the voxels with values less than the threshold value for voids are changed to "0" (black), and the voxels with values above the threshold for solid phase are converted to "1" (white). Porosity is then calculated by dividing the total number of voxels representing pores by the total number of voxels representing the whole sample.

The non-destructive nature of CT scanning allows the same rock sample to be scanned multiple times. Particles and pore characteristics can be studied at any time during the experiment and at any location within the sample. Thus, another attempt to use these "rich" x-ray reconstructed images is to perform local measurements of porosity. As it is described above, due to

the spatial resolution of the images the solid phase of Tuffeau de Maastricht is considered as a continuum. So, a continuum approach is used for making local measurements of porosity on the gray-scale images within a small cubic subvolume at regular intervals. This subvolume needs to be sufficiently small in order to make a proper local measurement of porosity, (*i.e.*, a subvolume occupying most of the specimen is not describing local measurement). The subvolume also needs to be sufficiently large in order not to be a simple manifestation of noise (Andò, 2013). Once the size of the subvolume is chosen, then it defines the size of a Representative Elementary Volume (REV). The determination of REV size is by no means a trivial task as it is a function of the nature of the material being considered, and the micro-scale parameter being looked for (see subsection 4.2.1).

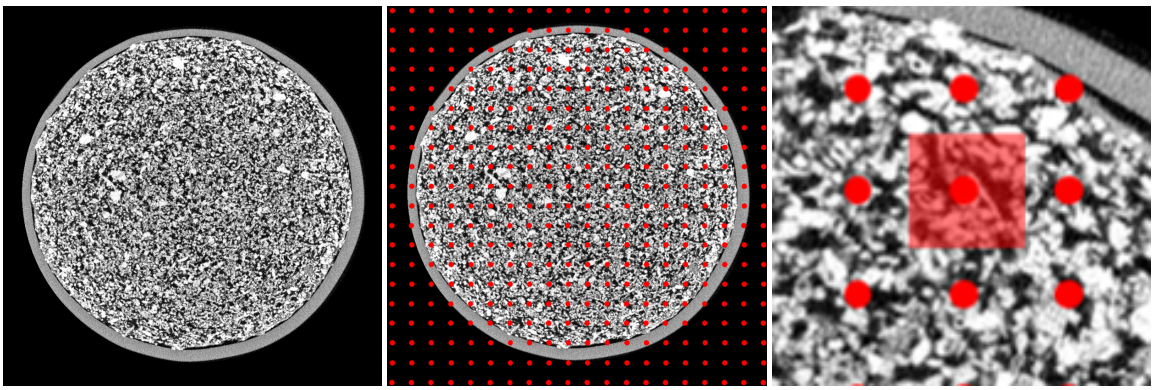

(a) **(b)** **(c)**

Figure 4.11: Schematic 2D diagram of local porosity measurements. Porosity is measured for each node within a predefined subvolume the REV. In this diagram a non overlapping subvolume example is presented.

In the 3D reconstructed images a set of equally spaced nodes, is defined. The 3D mesh of nodes is defined with respect to the image's coordinate system, so the nodes are an Eulerian reference frame with respect to specimen's micro-structure that is changing (moving). Once the REV size is defined, the local porosity measurements are made inside the subvolume (REV), centered at each node. The porosity is calculated by summing the number of void pixels inside the cube and dividing this by the known cube volume (the total number of pixels included inside the REV). Thus, for each node, with known coordinates (x,y,z) inside the image (sample), the corresponding porosity is assigned. Note that in this study, the measurements are performed on the gray-scale 3D images. Except for the REV size, similar to the macroscopic measurements of porosity, the threshold value should be given in the beginning as an input to the code. The corresponding threshold values for the pores and the solid phase used for the macroscopic measurements of porosity for each x-ray scan (for each experiment), are used also for the local porosity analysis. Thereafter, any voxel that has a gray-scale value equal to, or higher than, the grain gray-scale value is identified as 100% solid, and any voxel that has a gray-scale value equal to, or lower than, the void gray-scale value is identified as 100% pore. Gray-scale values between these two thresholds are interpolated with a linear relationship.

The code used for the local measurements of porosity is specifically written in Python, by Edward Andò, in Laboratoire 3SR. It gives, for a chosen REV size, a value of porosity in percentage for every point in the defined node grid. The code is written in such a way to allow easy modification of the node spacing. Node spacing can be set equal to REV size, or it can be

smaller than REV size and thus overlapping measurements are allowed. In this study, the local measurements of porosity are done within overlapping subvolumes with node spacing 10 pixels. The results of mapping the porosity are presented as 3D images formed by a number of voxels, where each voxel represents a node. Results of porosity are shown in chapter 5. Figure 4.11 shows a 2D section of the local porosity measurements procedure.

4.2.1 Representative Elementary Volume (REV)

In order to make measurements of porosity at a given node, the size of the REV needs to be defined. However, there is no explicit formula for the REV size. The main indication being is that it has to respect the separation scale $l_{micro} << l_{REV} << l_{macro}$, where l_{micro}, l_{REV}, and l_{macro} denote respectively, the characteristic length at the microscale, the representative, and the macroscale (Baruchel *et al.*, 2000, Rozenbaum and Roscoat, 2014). The separation scale means that the volume has to be large enough compared to the local scale characteristic length, and small enough compared to the large scale characteristic length. In other words, REV has to be much larger than heterogeneities such as grains or pores but should be smaller than the macroscopic structural dimensions. In this study two independent methods are followed to define the size of the REV. The first and more "standard" method is to evaluate the REV size by measuring the porosity inside randomly chosen elements of a given size and to analyze its fluctuations as a function of this size. This technique, and the code are successfully used in the past to measure the porosity on bio-cemented sand (Tagliaferri *et al.*, 2011), on granular media such as Zeolite, Hostun, Caicos, and Ottawa sands (Viggiani *et al.*, 2010, Soriano *et al.*, 2017, Alikarami *et al.*, 2015, Desrues and Andò, 2015, Karatza, 2017) as well as the degree of saturation for unsaturated media (Kaddhour *et al.*, 2013).

For each node, the program placed a cube centered on the node. The cube is then increased in size step by step by shifting the corners progressively away from the node, checking that the corners did not move outside the 3D image. As the cube is growing, the porosity is calculated withing the subvolume as it is described above. This process generates, for each node, an array of cube dimensions and their corresponding porosity. These measurements necessarily start from a cube (volume) of 1 voxel up to a predefined value depending on the material tested. In this case the maximum size of the subvolume is 100 voxels. For the volume of 1 voxel the porosity measurement is either 0% (*i.e.*, solid voxel), or 100% (*i.e.*, void voxel) and that only depends on where the node is placed. As the subvolume is increasing in size, the calculated value of porosity is changing. For nodes where the increasing subvolume does not go out of the domain of the specimen, the porosity reading is expected to tend towards the macroscopic porosity. For nodes where the subvolume eventually goes out of the domain of the specimen into the void on the outside of the specimen, the values tend to show higher porosity. On the contrary, if the subvolume includes the loading platens, porosity measurements appear lower that the macroscopic one. This is illustrated in Figure 4.12 for chosen nodes far from the boundaries of the specimen.

Figure 4.12 shows the evolution of the void volume fraction (porosity) computed in 20 non overlapping cubes vertically distributed along the axis of the sample. The position of the nodes within the specimen can be estimated from the graph. The nodes that are located in a void voxel, start from 100% of porosity, which decreases gradually as the size of the cube is increasing, and

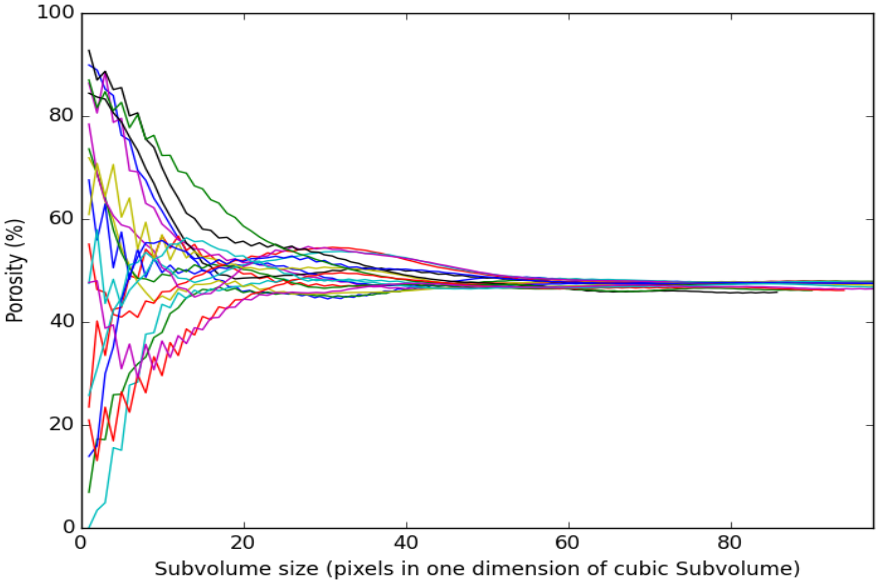

Figure 4.12: Evolution of the measurement of porosity as the cubic subvolume of on which it is calculated increases from 1 pixel to 100 pixels. As the subvolume increases in size, the calculated value of porosity tends towards a value representative of specimen's overall porosity.

grains start to be involved in the measurement. On the contrary, porosity is 0% for the nodes that are located inside a solid and remains low until the size of the subvolume becomes bigger than the grain itself, and pores start to be involved. Porosity measurements are very sensitive to the subvolume size up to around 40 pixels. The measurements become less sensitive to the cube size and converge to the macroscopic porosity of the specimen as the size of the subvolume increases. It is clear from the graph that a value of $30 \times 30 \times 30$ pixels for the subvolume is too small, and that $70 \times 70 \times 70$ pixels would be sufficient. Therefore, a subvolume with 55 pixels is chosen as as representative elementary volume (REV) for the porosity measurements.

Given that this choice relies on visual inspection, it may introduce a high degree of subjectivity. Therefore, an additional objective criterion is used to evaluate the size of the REV. Statistical tools can be used to evaluate the representativeness of the subvolume. REV often refers to a sample size sufficiently large to provide statistical robustness to an averaging procedure (Bear, 1972). This assumes that the material is homogeneous when viewed at a sufficiently large scale, or at least that a physical property of interest becomes independent of the size of the specimen. In such case, statistics generated by sub-sampling a large domain are enough to determine variance reduction as function of size (Yuan *et al.*, 2016). These statistical approaches start from the assumption that the tested sample comes from an underlying random process. However, in order to perform any statistical analysis, the double assumption of stationarity and ergodicity of the underlying random process has to be fulfilled. As a consequence, if the image is not stationary, the estimated statistical features are useless and irrelevant. On the contrary, statistical features estimated on a stationary region are representative and can be used for comparing textures (Blanc *et al.*, 2008). Based on a framework developed by Matheron (1963), an image can be considered as homogeneous if the variance of the empirical mean of a parameter of interest (porosity) decreases asymptotically as fast as or faster than the inverse of the image size. It is also possible to define a range which gives information on the volume size of the structure

for which the parameter measured (porosity in this case) in this volume has a good statistical representativity (Kanit *et al.*, 2003). This range is called the integral range (Matheron, 1989) and is defined as:

$$A = \lim_{V \to \infty} |V| \frac{var\{Z(V)\}}{\sigma^2}, \tag{4.3}$$

where $|V|$ is the size of the sample, $Z(V)$ the property of interest computed over the sample volume, $var\{Z(V)\}$ the variance of the property in all the samples at each specific size $|V|$. This inverse proportionality for homogenous images proposed by Matheron (1963), has been confirmed on real specimens by (Lantuejoul, 1991, Blanc *et al.*, 2008). In addition, Lantuéjoul (1991) shows that for a large specimen ($V \gg A$), the variance of the parameter of interest can be expressed as a function of the integral range A, by:

$$var\{Z(V)\} = \frac{\alpha}{|V|^b} = \frac{A\sigma^2}{|V|^b} = \frac{AP(1-P)}{|V|^b}, \tag{4.4}$$

where α and b are fitting parameters and $\sigma^2 = P(1-P)$ is the point variance with P the property of interest obtained from the image analysis over the whole specimen. Parameter α quantifies the scale of microscopic fluctuation, while b controls how fast the variance is reduced as a function of the subvolume. The results on the real specimens (Lantuejoul, 1991, Blanc *et al.*, 2008) shown that for a homogeneous image in the log-log plot of the variance versus the subvolume area, the experimental points tend to be aligned along a straight line with slope $b = -1$. Instead, for heterogeneous media $b < 1$. Therefore, in this study the homogeneity of the sample (volume) is verified by using the parameter b (Bruchon *et al.*, 2013a, Shahin *et al.*, 2018).

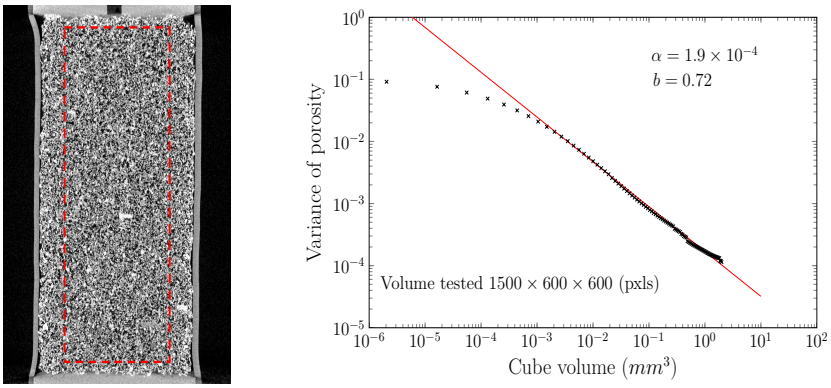

(a) **(b)**

Figure 4.13: Variance of porosity versus the subvolume size. The measurements are performed on a smaller volume extracted from the whole specimen. (a) Vertical slice of the global CT scan where the extracted volume is delimited with dashed red lines. (b) The effect of the size of the subvolume on the variance of the porosity for the extracted volume (1500 × 600 × 600 pixels).

In order to limit the effect of the membrane, and the porous platens, as well as the artifacts near to the edge, a smaller volume is extracted from the center of the total 3D volume (Fig-

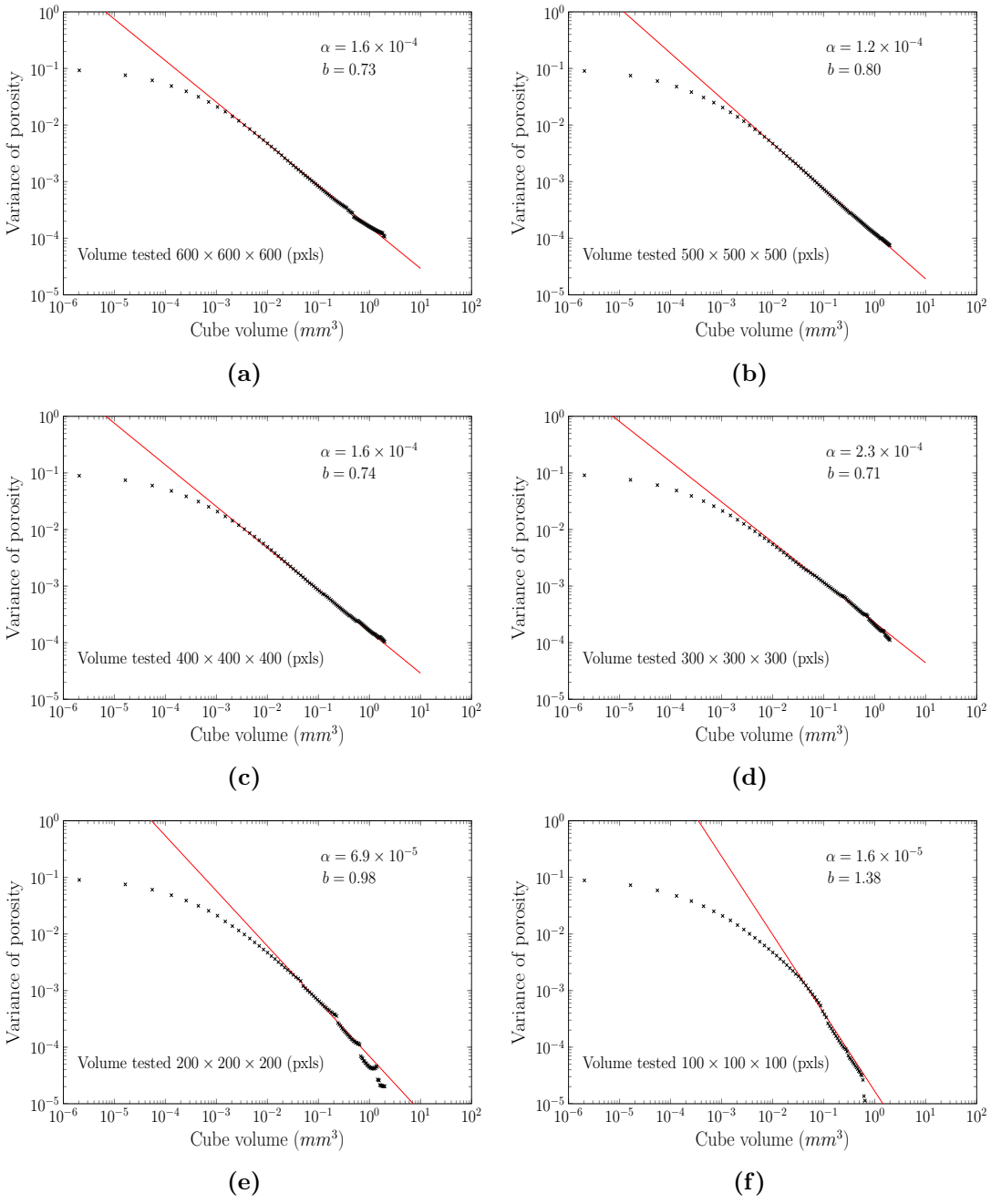

Figure 4.14: Variograms of porosity measured for an increasing size subvolume at different extracted volume (a) $600 \times 600 \times 600$ pixels, (b) $500 \times 500 \times 500$ pixels, (c) $400 \times 400 \times 400$ pixels, (d) $300 \times 300 \times 300$ pixels, (e) $200 \times 200 \times 200$ pixels, (f) $100 \times 100 \times 100$ pixels.

ure 4.13a). The extracted volume is divided into a regular grid with a fairly large number of nodes (approximately 30.000). The porosity is then evaluated at each node through a subvolume, which is increasing in size. To verify the homogeneity of the sample the variance of the porosity of each node is plotted versus the subvolume size. Equation 4.4 is then fitted on the data and the parameters a and b are obtained for the best fit.

Figure 4.13 illustrates the outcome of the fitting procedure for the extracted volume. It should be mentioned that the fitting procedure is carried out manually. This analysis shows that $b < 1$, indicating that the sample is heterogeneous. Therefore, the procedure is repeated for smaller volume each time (always in the center of the sample) until Matheron's criterion is fulfilled. Figure 4.14 summarizes the variograms (*i.e.*, plot of the variance associated with each subvolume size) at different sample sizes. It can be observed that there is no significant change for the parameter b (still $b < 1$) for smaller volumes until a sample size of $300 \times 300 \times 300$ pixels. So, also these samples cannot be considered as homogeneous. Similar trend can be observed for the parameter α, which quantifies the scale of microscopic fluctuation. The parameter b is ≥ 1 only for volume of $200 \times 200 \times 200$ pixels or smaller, indicating homogeneity of the sample. Therefore for a cubic volume of side length equal to 200 pixels the criterion is verified with $\alpha = 6.9 \times 10^{-5}$ and $b = 0.98$. Note that the volume with side length 100 pixels is equal to the maximum size of the subvolume, thus was considered very small. Consequently the volume with 200 voxels (2.6 mm) is used in this study.

Therefore, the volume of 200 voxels is considered as the scale of observation and the integral range A (Equation 4.4) as the scale of the phenomenon. Since the image fulfills the two criteria of ergodicity and stationarity, the integral range is a convenient measurement of the size of the REV. From the variance (Figure 4.14e) it is easy to define the confidence interval of the volume considered, as a function of the integral range (Bruchon *et al.*, 2013b, Kanit *et al.*, 2003). Assuming a Gaussian distribution, the 95% confidence interval is $P \pm 2\sigma(V)$, where $\sigma(V) = \sqrt{\frac{\alpha}{V^b}}$ (Equation 4.4) with $b \approx 1$ and $P = 44.6\%$. For instance, if the volume fraction is estimated on a volume with side length 55 pixels, *i.e.*, 0.715 mm (the value estimated for the previous method), the volume fraction of porosity is in the interval $44.6 \pm 2.74\%$ and the relative uncertainty is $\frac{2\sigma(V)}{P} = 6\%$ with a 95% of confidence. The advantage of this method is that allows to find the REV size for a given confidence. Thus, in case of the relative uncertainty is limited by 1% the side length of the REV should be greater bigger than 185 pixels (2.4 mm).

This second approach gives a relatively bigger REV than the first for 5% relative uncertainty. Therefore, a REV of side length 55 pixels is used in this study with the second method mainly used to estimate the relative uncertainty with 95% confidence.

4.3 Measurement of specimen volume

In this study, the bulk volume of the specimen is calculated from the 3D images obtained throughout the tests. Additionally, the non-destructive nature of x-rays gives the ability to follow the volume change during a test.

Herein, the bulk volume is defined as the volume of the pores and the solid within the membrane surrounding the specimen and between the porous stones. However, the membrane and the porous stones almost always appear in the 3D images of the specimen. So, to define

only the specimen volume, the first, essential step is to remove those objects.

The first objects that are removed for the images are the top and bottom platens. This is done on the gray-scale 3D reconstructed images. The 3D volume of the specimen is divided in equally spaced horizontal slices, (with thickness of 13 μm), and each slice including the porous stone is removed from the total final volume. This technique of porous platens removal from the images is relatively subjective. When the two end surfaces of the specimen are not perfectly horizontal then, a few grains of the specimen are also removed from the total volume. Figure 4.15 shows the horizontal slices on top of the sample, where the porous plate "disappears" gradually and the specimen starts to emerge. The fact that the thickness of the slices is a single pixel gives flexibility to the final choice. One more or one less slice does not affect the total volume measurement.

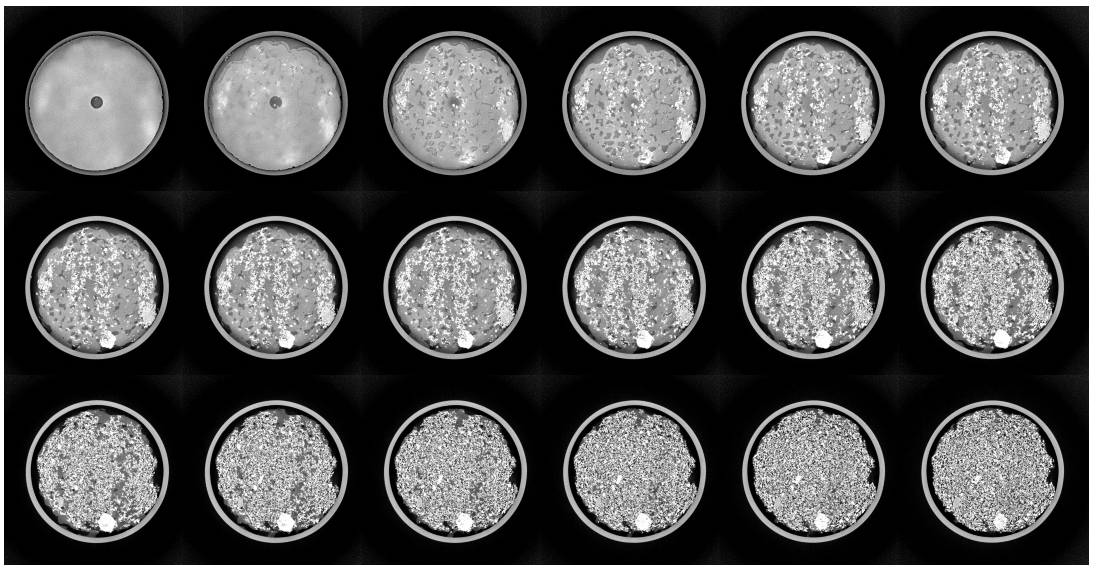

Figure 4.15: Sequential horizontal slices of the 3D reconstructed volume of Tuffeau de Maastricht. On the left top the surrounding membrane and the top porous platen can be detected. As the images are moving in $i-1$ slice towards the bottom of the sample, the porous platen disappears and the top of the specimen emerges.

Previous studies have shown that it is not always possible to reliably remove the membrane from the 3D tomographic images (Andò, 2013, Alikarami *et al.*, 2015, Tengattini, 2015, Karatza, 2017). In this study, a thick neoprene membrane is used to withstand the pressure applied to the specimen. The x-ray absorption of this membrane is high, thus it appears clearly in the reconstructed images. As it can be observed in Figure 4.16 the membrane has a gray value similar to Tuffeau de Maastricht, it is therefore impossible to remove it from the images based only on its gray value. Additionally, the shape of the membrane is not constantly cylindrical during the experiments, especially when the samples start to deform. An algorithm is therefore designed to delete the membrane based on its peripheral position in the sample. The python based algorithm is built using the open source Computer Vision Library (OpenCV) (Bradski, 2000).

The first step for the algorithm is to find the outer surface of the membrane, called hereafter "contour". Such a "contour" is considered a curve that joins all the points along a continuous boundary with the same intensity. The inner surface of the membrane cannot be defined with this algorithm due to the fact that some grains touch the membrane so, the boundary is not

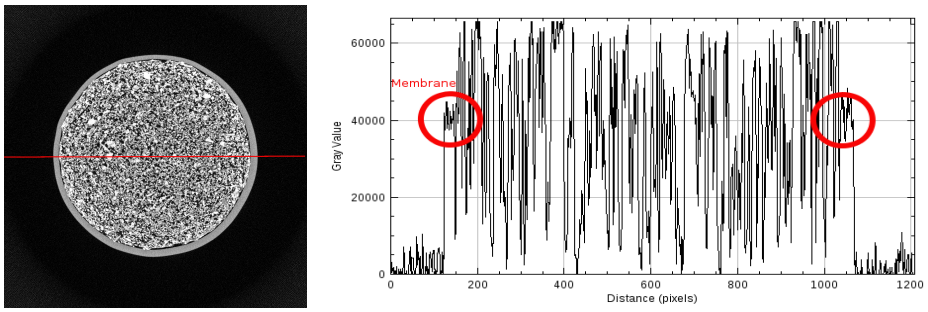

Figure 4.16: A two-dimensional plot of pixel's intensity along a line plotted on the horizontal slice. The gray value of the neoprene membrane is similar to gray value of the material.

continuous. Consequently, the biggest contour is determined for each horizontal slice of the 3D volume. Then a mask is applied to the area within the contour. The result is a binary image where everything surrounding by the membrane including the membrane are in white while the rest blacked out. In order to separate the sample from the membrane an erosion function is applied. A specified structural element, designed for this study, is used to erode the initial images. This element determines the shape of a pixel neighborhood over which the minimum is taken, (*i.e.*, a pixel in the initial image, either white or black, will be considered white only if all the pixels under the structural element are white, otherwise it is eroded) (Bradski, 2000). Assuming that the external and internal surfaces of the membrane deform uniformly, it is then possible to isolate the specimen only. The number of the erosion steps, and the shape of the structural element are adapted to each specimen separately after a trial and error method. In some particular cases, such as in areas where the membrane is folded, the erosion phase is applied twice. Finally, the total volume is measured simply by counting the voxels within the Region Of Interest (ROI), *i.e.*, inside the membrane. The procedure is illustrated in Figure 4.17, while Figure 4.18 proves the reliability of the method to determine the ROI for different loading stages.

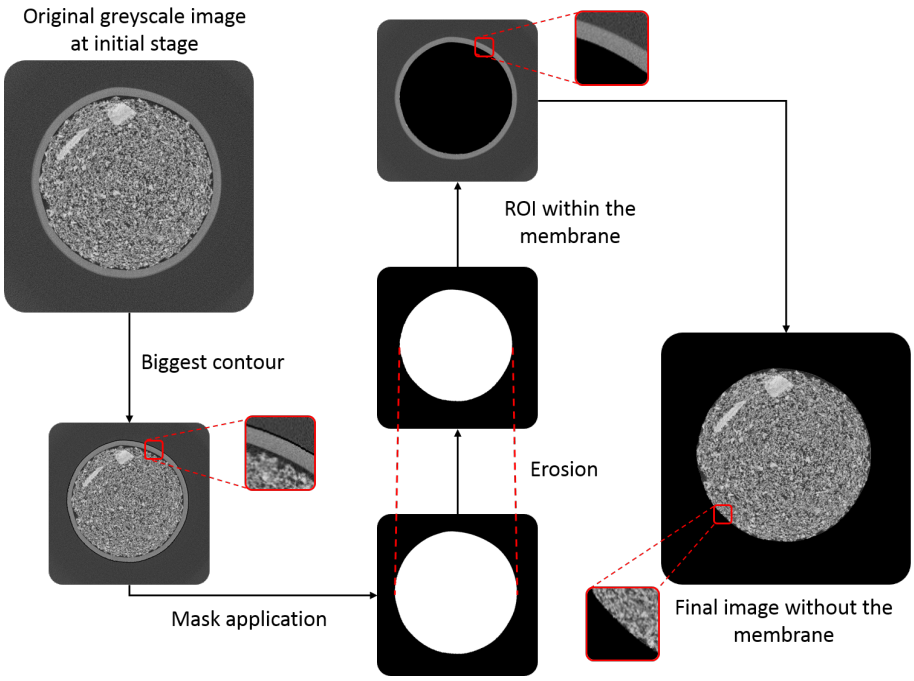

Figure 4.17: Schematic diagram of the technique developed for the removal of the membrane from the 3D images.

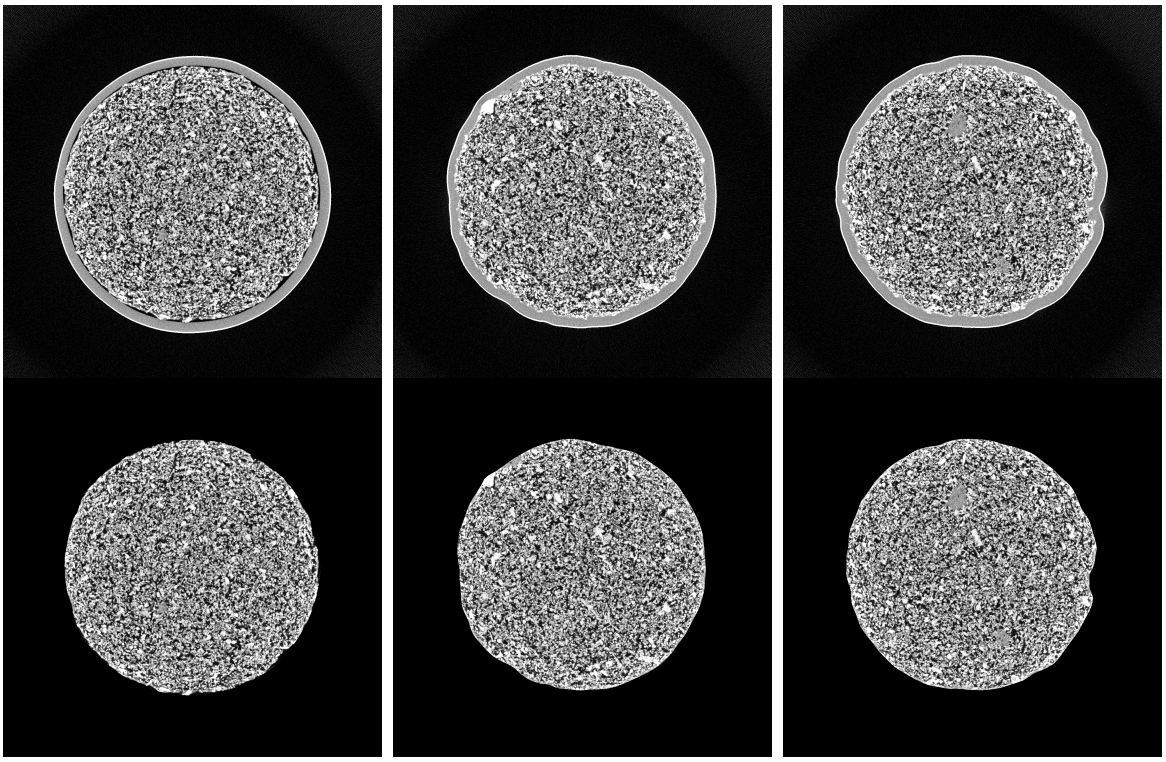

(a) **(b)** **(c)**

Figure 4.18: Horizontal slices of the same sample at different loading stages. The top images illustrate the sample and the surrounding membrane without any image processing. The corresponding images after the removal of the membrane is applied are presented in the bottom.

4.4 Digital Image Correlation (DIC)

In this study "continuum" 3D-volumetric DIC is carried out incrementally (between sequential loading stages), to obtain the shear and volumetric strain field for Tuffeau de Maastricht. It is called "continuum" because displacement is calculated at nodes (called also reference points) which are laid out on a regular grid. The analysis is performed using the *TomoWarp2* algorithm (Tudisco *et al.*, 2015a, Tudisco *et al.*, 2017), a code based on the work of (Hall, 2006), which is initially developed for time-lapse analysis of hydrocarbon reservoirs under production, based on 3D seismic images.

Continuum DIC is performed on the gray-scale reconstructed images. A grid pattern is applied on the two volumes: the reference image and the deformed image. The grid is defined in both images in the same place with respect to the coordinate system. The locations of the reference points (x, y, z) at which the displacements are calculated are placed on the grid pattern in the reference images. Then the algorithm looked for the corresponding points in the deformed image. A subvolume, referred as the "correlation window" of $(2n+1) \times (2n+1) \times (2n+1)$ voxels centered at each reference point (node) from the reference image, is chosen and used to track its corresponding location in the deformed image. The size of the correlation window is typically an input to *TomoWarp2* and it should be big enough to capture the different features of the material. In this study, it is chosen to be 41 pixels roughly 3.5 times bigger than the average grain size of Tuffeau de Maastricht ($D_{50} = 150$ μm).

In order to find the best matching pattern for each node between the reference and the deformed image , the Normalized Cross-Correlation (NCC) is used. The normalized cross-correlation between two 3D images is typically defined as:

$$NCC(u,v,w) = \frac{\Sigma_{x,y,z} I_1(x,y,z) I2(x+u, y+v, z+w)}{\sqrt{\Sigma_{x,y,z} I_1(x,y,z)^2 \Sigma_{x,y,z} I_2(x+u, y+v, z+w)^2}} \tag{4.5}$$

where I_1 and I_2 denote the local gray value in the 3D images reference and deformed images, x, y, z are the coordinates of the nodes of the images, while u, v, z are integer displacements applied to the second image in the x, y, z directions, respectively. The 3D image correlation is typically performed by scanning all the combinations of u, v, and w in a predefined area (*search window* called hereafter), and for each combination the NCC is calculated. The result of this process is a set of u, v, and w values which yield the highest NCC for each node. The correlation coefficient ranges from 0 to +1, in which +1 shows 100% similarity between the two images, or part of the images. Several other types of cross-correlation have been developed (Pan *et al.*, 2009) although the NCC is one of the most widely accepted.

Since the image is a matrix of discrete numbers (pixels), the process described above is able only to measure displacements in the direction of u, v, and w to nearest pixel, *i.e.*, the displacement of the correlation window can be only in integer numbers, and is not able to measure rotation. In this study, only sub-pixel displacements are desired, without taking rotations into account, so the interpolation of the correlation coefficient is used. This method involves the interpolation of a set of correlation coefficients corresponding to integer displacements by a mathematical function. The maximum of this function gives the sub-pixel resolution displacement (see Tudisco *et al.*, 2015a for details). This is an essential step in DIC, especially when strains are calculated from displacements. Without sub-pixel refinement only integer number of pixel displacements can be resolved, and this has as a consequence of "stepped" displacement fields and strain maps with very large strains (Viggiani, 2009).

The results of the continuum DIC technique is the 3D displacement field for every node laid out on the regular grid. By deriving this displacement field, the 3D strain tensor can be obtained. Therefore, the output of the *TomoWarp2* is the 3D field of each component of the strain tensor, as well as the first and second invariants. In this work the results are presented in terms of incremental volumetric strain and the incremental maximum deviatoric (shear) strain, shown in the following equations:

$$\epsilon_v = \epsilon_1 + \epsilon_2 + \epsilon_3 \tag{4.6}$$

$$\epsilon_s = \frac{\sqrt{2}}{3} \sqrt{(\epsilon_1 - \epsilon_2)^2 + (\epsilon_2 - \epsilon_3)^2 + (\epsilon_3 - \epsilon_1)^2} \tag{4.7}$$

where ϵ_1, ϵ_2, and ϵ_3 are the major, intermediate and minor principal strains respectively. Results of the 3D DIC on Tuffeau de Maastricht are discussed in chapter 5.

4.5 Summary

In this chapter the image processing methods and tools used to investigate the onset and evolution of strain localization in Tuffeau de Maastricht are presented. The basics of x-ray computed tomography and the main advantages to be used as a non-destructive technique to study porous rocks are discussed. Details are given for the lab scanner in Laboratoire 3SR, in which the majority of the *in-situ* experiments of this study are conducted. The choice of the necessary acquisition parameters to obtain images of the highest possible quality is further explained in this chapter. It is also shown that the higher spatial resolution reveals valuable information about the material tested such as the high percentage of intragranular porosity and the grain-supported structure with the grains loosely bonded at contact points.

Porosity measurements are of great importance in this study. Thus, the procedure to perform porosity measurements macroscopically as well as locally is detailed. An efficient method to separate the main solid phase from the voids in the original (not binarized) reconstructed images is presented. A continuum approach is selected for making local porosity measurements within a small cubic subvolume at regular intervals. The importance of the size of the REV is discussed and two independent methods to define its size are developed. The comparison of the two method based on (i) visual inspections, and (ii) statistical tools, demonstrates that the size of the REV can be estimated for a given confidence.

An original tool, developed during this study, to delete the membrane from the 3D reconstructed images is presented. The new method is based on the membrane's peripheral position in the sample, and not on its x-ray attenuation values. Images at several loading stages depict the capability of this tool to delete the membrane even from highly deformed samples.

This chapter also introduces digital image correlation as a full-field measurement technique between images acquired at sequential loading stages. The continuum image correlation code *TomoWarp2* that is used to obtain shear and volumetric strain field for Tuffeau de Maastricht is briefly described.

Chapter 5

Results

In this chapter the macroscopic mechanical behavior of Tuffeau de Maastricht as well as the results from the full-filed measurements are presented. All the experiments presented herein, are performed using the loading devices and the experimental setup described in chapter 3. Cylindrical samples of 11.5 mm diameter and 22 mm height are tested under isotropic, triaxial, and uniaxial compression conditions.

The isotropic compression tests are conducted in the triaxial compression cell. The confining pressure is increased by step of 0.5 or 1 MPa up to 8 MPa (cell's maximum pressure) with a pressurization pump. At the end of each step, confining pressure is kept constant and x-ray CT is performed. The triaxial tests are performed at confining pressures ranging from 1 to 5 MPa in nominally dry condition at room temperature. Several of the triaxial tests are duplicated and the samples deformed up to much higher axial strain. For both uniaxial and triaxial compression tests, additional experiments are performed for samples cored perpendicular, oblique (45°), and parallel to the bedding plane. The deviatoric loading is applied under displacement control mode at a constant axial displacement rate of 20 μm/min, *i.e.*, a strain rate of $1.5 \times 10^{-5} s^{-1}$. The axial displacement is measured outside of the cell with an external transducer (LVDT). At different axial strain levels, the loading is halted and x-ray CT scans are acquired. In each test an average number of 15 scans are performed. The acquired images are processed and the full-filed measurement techniques that are discussed in chapter 4 are used. Macroscopic and local measurements are made on porosity variations, volumetric and maximum shear strain fields.

In this study the convention is adopted that compressive stress and compactive strains, *i.e.*, shortening and porosity decrease are considered positive. The maximum and the minimum principal stresses are denoted by σ_1 and σ_3, respectively. The deviator stress is computed as the major principal stress minus the minor principal stress $(\sigma_1 - \sigma_3)$ hereafter denoted by q, and the mean stress $(\sigma_1 + 2\sigma_3)/3$ by p.

5.1 Isotropic compression test

Two isotropic compression tests are conducted both on intact samples, and on the reference material (see subsection 3.1.2). The experimental data of the three samples are compiled in Table 5.1. Two nominal "identical" tests are conducted on intact cylindrical samples to check

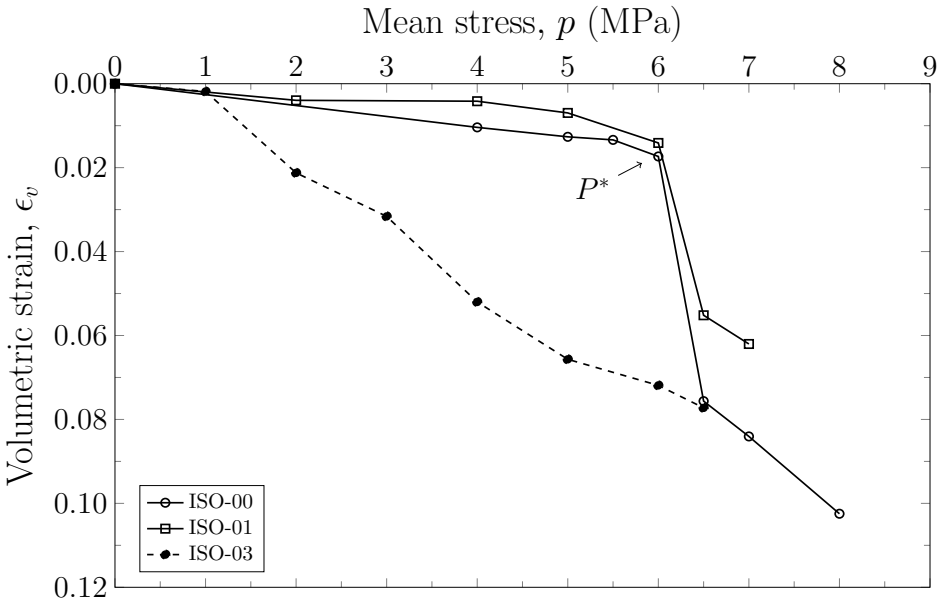

Figure 5.1: Curves of volumetric strain versus mean stress obtained from isotropic compression tests for intact samples (solid line), and the reference material (dashed line) samples. The arrow indicates the critical pressure P^* for the onset of pore collapse.

Table 5.1: Summary of isotropic compression tests.

Test	Porosity (%)	Porosity* (%)	Critical Pressure P^* (MPa)	Analysis	Comments
ISO-00	-	44	6	x-ray CT/DIC/Porosity	Intact sample
ISO-01	50	46	6	x-ray CT/DIC/Porosity	Intact sample
ISO-03	48.8	-	-	x-ray CT	Reference material

* Porosity obtained through image analysis

reproducibility. Sample volume reduction is measured through x-ray CT as the isotropic confining pressure increases (see section 4.3 for details). The volumetric strain versus mean stress is plotted in Figure 5.1. Data from these two tests are found reasonably reproducible. The two curves are almost parallel with each other, showing that the behavior under isotropic conditions are basically identical. The isotropic compression curves for the intact samples (solid lines) have a sigmoidal shape, with an inflection point at a given pressure called hereafter the *critical pressure* P^*. Three distinct regions with different slopes along the curves are defined, indicating three distinct phases of deformation. The first segment is quasi-linear where the samples deform with moderate compaction. In the second stage the behavior becomes nonlinear at pressures above the critical value P^* marked in Figure 5.1. This second segment is characterized by sudden reduction in volume with large volumetric strains occurring at roughly constant isotropic pressure. The value of the critical pressure can be estimated with good accuracy from the inflection point on the curve that occurs at a confining pressure of 6 MPa. Table 5.1 compiles the critical pressure for Tuffeau de Maastricht. This value appears to be identical for the two intact samples of Tuffeau de Maastricht. At confining pressure of 6.5 MPa, the isotropic compression curves present a second inflection point.

In addition, Figure 5.1 also shows the isotropic compression curve of the reference material (dashed line). The porosity of the reference material, as measured before loading, is about 48.8%,

close to the porosity of the intact (natural) samples. In the first stage, the curve is relatively linear, up to 1 MPa, and basically coincides with the isotropic compression curves of the intact material. In the second stage, there is an accelerated decrease in volume with increasing pressure. However, the volume reduction is much less sharp for the reference material than for the other two experiments beyond the critical pressure P^*. Furthermore, it appears to coincide with the post-pore collapse (hardening) stage.

For the intact samples, the pore collapse induces an increase in the contact surface between grains, leading to the decrease of the volumetric strain rate at the third phase. Thereafter, work-hardening takes place and the material regains stiffness. The comparison of the two curves (intact and reference samples), helps to quantify the influence of cementation on the material's strength, and qualitatively associate pore collapse with cement breakage, grain rearrangement, and grain breakage. The visual inspection of the intact samples deformed isotropically revealed in all cases a sand-like (cohesionless) samples that enhance the first hypothesis of bond breakage.

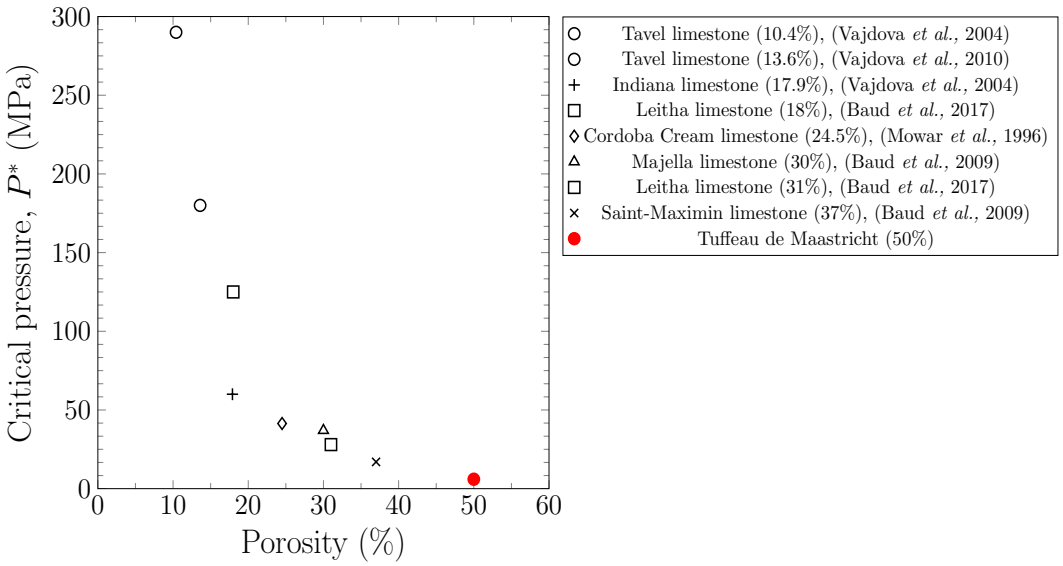

Figure 5.2: Compilation of critical pressure for porous limestones. Pore collapse pressure P^* is decreasing with increasing porosity. The material tested in this study (Tuffeau de Maastricht) is presented in red color.

The isotropic compression behavior of Tuffeau de Maastricht is qualitatively similar to that observed for other porous sandstones (Bésuelle *et al.*, 2003, Menéndez *et al.*, 1996, Zhang *et al.*, 1990a) and porous carbonate rocks (Baud *et al.*, 2000a, 2017a, Dautriat *et al.*, 2011b, Mowar *et al.*, 1996, Vajdova *et al.*, 2004a). However, at relatively low confining pressures the nonlinear "toe" in the curve, observed in sandstones (Vajdova *et al.*, 2004a), and limestone (Baud *et al.*, 2000a), is not very pronounced in Tuffeau de Maastricht. This nonlinear behavior is related to the elastic closure of microcrack porosity (Brace, 1978). The initial quasi-linear response for Tuffeau de Maastricht might confirm the absence of microcracks in this type of rock. Nevertheless, the volumetric measurements in this study are performed through image analysis, *i.e.*, incrementally, and not continuously. Beyond the critical pressure P^*, the acceleration of the compaction corresponds to the onset of pore collapse and grain crushing. Zhang *et al.* (1990a) show that for porous sandstones, the critical pressure P^* at the onset of pore collapse decreases with increasing porosity and increasing grain size. Figure 5.2 summarizes the critical pressure for limestones from previous studies and for Tuffeau de Maastricht. There is an overall trend for

the critical pressure to decreases with increasing porosity.

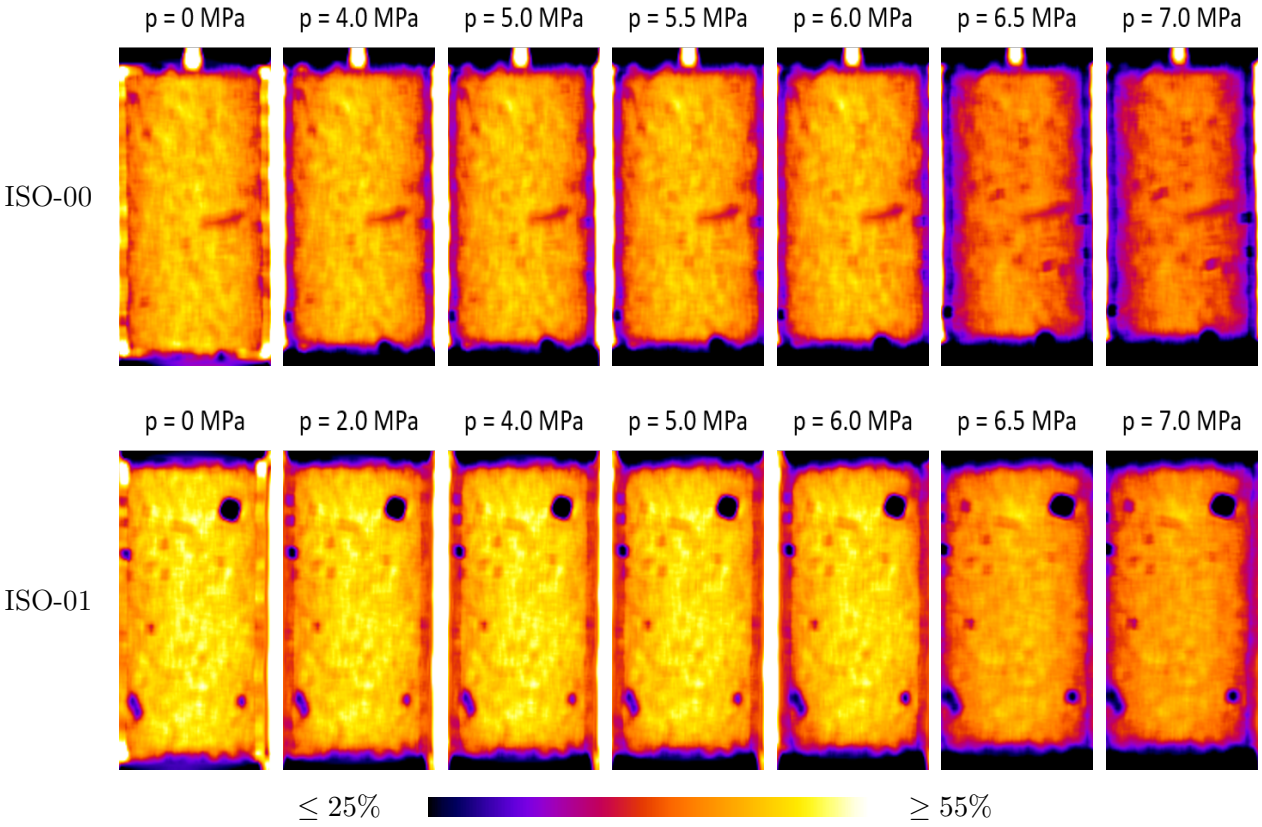

Figure 5.3: Vertical slices through the measured 3D field of porosity in different configurations for the isotropic compression tests ISO-00 and ISO-01. On the top of each figure is marked the mean stress at which the measurement is taken.

Under isotropic loading, the onset of inelastic compaction reflects on the volume reduction. This volume reduction is commonly "translated" to porosity change with increasing confining pressure. The local measurements of porosity are performed for all loading steps, in order to characterize its evolution under isotropic compression condition. The optimal REV size, over which the local porosity is measured, is defined following the methods presented in subsection 4.2.1. More specifically, the value of porosity is calculated on a REV with side size measuring 54 pixels. It should be also mentioned that the spacing between calculation nodes is 10 pixels, which means that there is considerable overlap of measured volumes.

Figure 5.3 shows central vertical slices in the porosity map for the two intact samples of Tuffeau de Maastricht. All the measurements presented herein are 3D in nature, but for illustration purposes, 2D images are presented. The confining pressure at which the local porosity measurements are performed, is marked on the top of the relevant image. The threshold applied to these porosity maps is chosen in such a way to easily separate the porous platens from the samples. The platens appear with very dark color in images. In addition, several inclusions with porosity much lower that the surrounding material appear in darker color, especially for test ISO-01.

At zero confining pressure, the porosity map shows that the porosity of the specimens is relatively uniform, with a mean value of 44% and 46% for tests ISO-00 and ISO-01, respectively. Figure 5.3 illustrates that almost no changes in the distribution of porosity can be detected

until 6 MPa of confining pressure for both samples. Between these loading stages, which are different for each sample, the specimens have slightly shortened and compacted. This can be seen in the images from the movement of the porous platen on the bottom of the samples, and the change of color on the boundaries, respectively. These changes in porosity maps correspond to the relatively small volumetric strain reduction depicted in Figure 5.1. Thereafter, from 6 to 6.5 MPa mean stress, a considerable difference can be noticed, with a significant porosity reduction in the whole sample at 6.5 MPa confinement. This porosity reduction corresponds to the sharp volumetric collapse that both samples shown for pressures beyond the critical pressure, *i.e.*, $P^* = 6MPa$. In particular, porosity is reduced from 40.7% to 36.3%, and from 43.3% to 39.8% for tests ISO-00 and ISO-01, respectively.

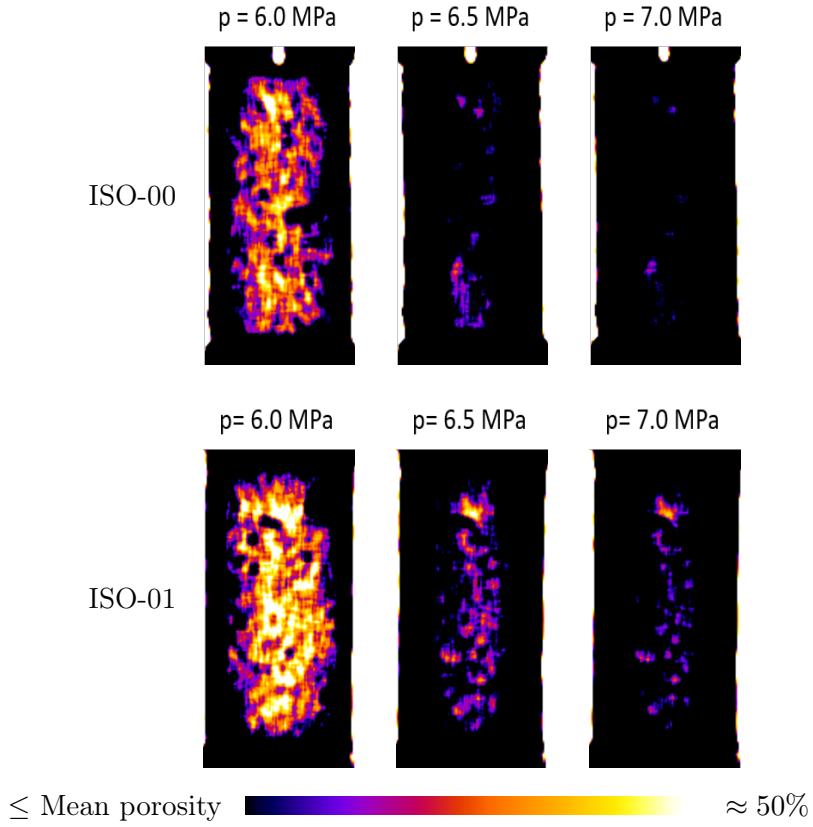

Figure 5.4: Vertical slices through the measured 3D field of porosity in different configurations for the isotropic compression tests ISO-00 and ISO-01. The initial mean porosity of each sample is subtracted from the porosity maps. On the top of each figure is marked the mean stress at which the measurement is taken.

Referring back to Figure 5.1, although the two intact samples of Tuffeau de Maastricht have different initial porosity, they present pore collapse at the same critical pressure. However, they show a different volumetric collapse. This difference in the volumetric strain might be due to differences in their initial porosity. In this direction, a further analysis of the porosity field is performed. The initial mean porosity of each sample is subtracted from the porosity maps for every loading stage. Figure 5.4 presents the $\phi_n - \phi_0$ maps (porosity at the loading stage - initial porosity) for three confinements: (i) at 5 MPa, just before the critical pressure, (ii) at the critical pressure, 6 MPa, and (iii) at 6.5 MPa, just after the critical pressure. At 5 MPa confinement, both samples appears to have still high porosity. Except from the boundaries of the specimens where the porosity is lower than the mean (black color), the main core of the samples

has porosity above the mean value. At pressures beyond the critical pressure, in the case of test ISO-01, a region in the middle of the specimen is characterized by high porosity indicating that pore collapse did not cover the whole sample.

5.2 Triaxial compression tests

The main experimental campaign of this study consists of triaxial compression tests. In this section only a selection of results is presented. The triaxial compression tests are performed at confining pressures ranging for 0 to 5 MPa on dry specimens. Table 5.2 summarizes the triaxial compression tests discussed in this section. Coring and sample preparation procedures are performed as described in section 3.2. The cylindrical samples that are discussed particularly in this section, are prepared by coring perpendicular to the bedding plane and grinding to a nominal 11.5 mm diameter by 22 mm length. All samples are cored from the same block of Tuffeau de Maastricht in an attempt to minimize sample-to-sample variability. Each sample is jacketed in a neoprene membrane and placed between two porous lubricated end platens.

The macroscopic responses are presented in Figure 5.5. The deviator stress ($q = \sigma_1 - \sigma_3$) is plotted against the axial strain (ϵ_a). Both these measurements come from direct recordings from the load device (force meter) and an external displacement gauge (LVDT). Note that the membrane correction has not been applied to these data due to the fact that the experiments are performed at relatively high pressures compared to the membrane's stiffness. In addition, the total volumetric strain (ϵ_v) is plotted against the axial strain (ϵ_a). Since the specimens are tested dry, the volumetric strain is calculated from the x-ray images. Thus, the curves are not continuous, and there are no volumetric strain measurements for test TX90-07, because it was not x-ray scanned. For these measurements the membrane is removed from the images using the method described in section 4.3. A uniaxial compression test is added in Figure 5.5 for the purpose of comparison with the triaxial compression tests. The corresponding analysis to this test is presented in the following section (section 5.3). Note that the axial stress relaxations correspond to the moments during the tests at which loading has been interrupted in order to scan the samples.

Table 5.2: Summary of triaxial compression tests on Tuffeau de Maastricht.

Confining pressure (MPa)	Test	Initial Porosity(%)	Peak stress q (MPa)	Axial strain ϵ_a (%)	Analysis
0.5	TX90-07	-	3.9	14	-
1	TX90-01	50.5	4.2	20	x-ray CT/DIC
2	TX90-02	53	4.5	12.4	x-ray CT/DIC/Porosity
3	TX90-03	50.6	4.25	15	x-ray CT/DIC/Porosity
4	TX90-04	49	3.6	14	x-ray CT/DIC/Porosity
5	TX90-05	50.7	2.5	11	x-ray CT/DIC/Porosity

At low confining pressures (0.5 and 1 MPa), the response is brittle, *i.e.*, the deviator stress attains a peak beyond which strain softening is observed. Particularly, the stress drop is higher at the lowest pressures (0-0.5 MPa) and decreases with increasing pressure, *i.e.*, the response becomes more ductile. The value of peak deviator stress increases with increasing confining

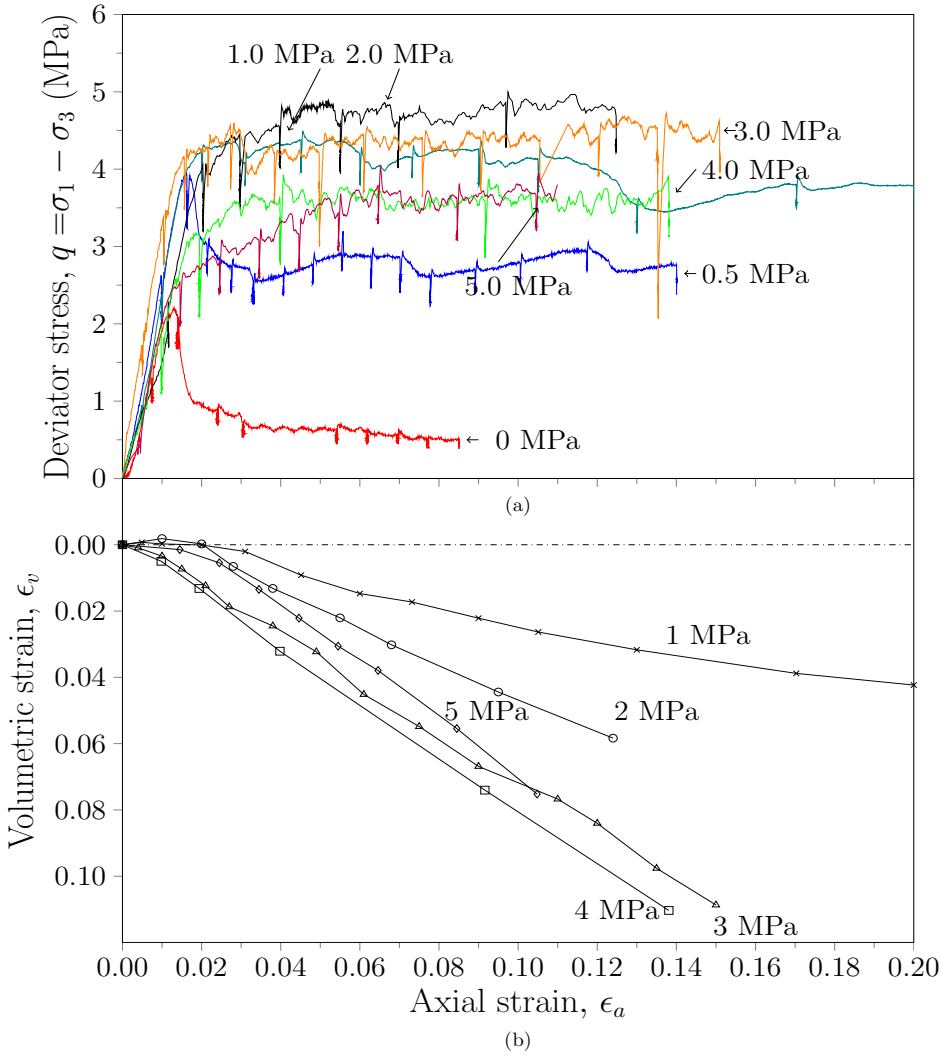

Figure 5.5: (a) Stress-strain curves for triaxial compression test at confining pressures ranging from 0.5 to 5 MPa. The uniaxial compression test is plotted as a reference. (b) The corresponding volumetric strain versus axial strain curves (please note that volumetric strain is obtained by image analysis; no x-ray scans are performed for the test at 0.5 MPa confinement, and thus no volumetric data are available for this test).

pressure. Visual inspection of the samples after testing confirms the development of shear bands. Image analysis is not performed for the lowest confining pressure (0.5 MPa) and therefore the volumetric strain measurement is missing. However, at 1 MPa confinement the volumetric strain increases throughout the test, indicating a compactive behavior (Figure 5.5b).

In Figure 5.6 the stress-strain curves are split into two figures for better visualization (brittle and ductile behavior). At confining pressures between 2 and 4 MPa, the stress-strain curves do not show any stress peak, but rather a stress plateau. At the highest confining pressure (5 MPa) the relative plateau is almost absent and appreciable hardening is observed. There is an overall trend for the "post-yield" slope to increase with increasing confining pressure, *i.e.*, a transition from strain softening to hardening. In this range of confining pressures, $\sigma_3 \geq 2MPa$, the maximum value of the deviator stress decreases with increasing confinement (see Figure 5.6b).

Volumetric strain curves (Figure 5.5b) for high confining pressures (higher than 2 MPa) show compaction until high axial strain. Note that at very low axial strains the specimen sheared

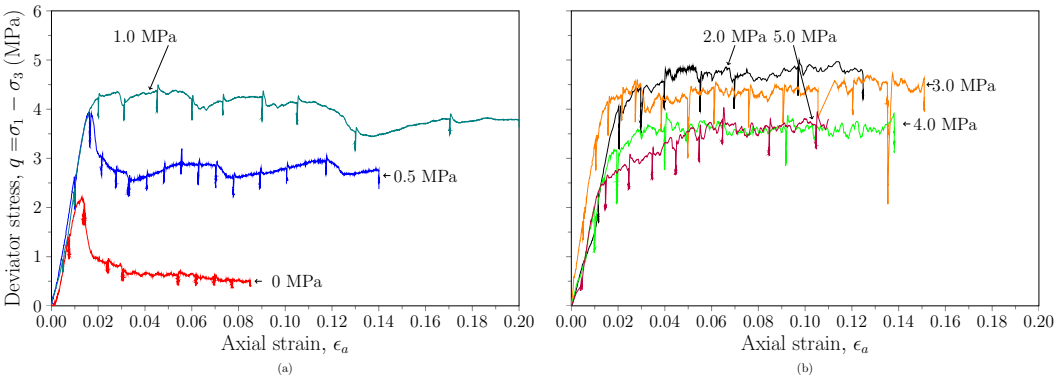

Figure 5.6: Stress-strain curves for the triaxial tests that are performed at (a) in the brittle regime, (b) in the ductile regime.

at 2 MPa confinement shows negative volumetric strains (dilation), followed by a change to compressive behavior. For all tests the stress-strain curves are punctuated by episodic stress drops. There is an overall trend for these stress drops to appear more often and be more pronounced with increasing confining pressure. Previous studies on sandstones (Baud *et al.*, 2004) as well as on carbonate rocks (Baud *et al.*, 2009) showed that these episodic stress drops are accompanied by upsurges in Acoustic Emission (AE) activity. This behavior is usually indicating individual increments of compaction bands propagation.

The macroscopic behavior of Tuffeau de Maastricht presented herein, is qualitatively and quantitatively similar to the one presented by Baxevanis *et al.* (2006). In their case though, the stress drops during the relative plateau of deviator stress are less pronounced. In general, the overall behavior of Tuffeau de Maastricht in the brittle and ductile regime is qualitatively similar to earlier studies in porous (Baxevanis *et al.*, 2006, Baud *et al.*, 2009, 2017a, Vajdova *et al.*, 2004a, 2012) and less porous (Baud *et al.*, 2000a, Zhu *et al.*, 2010) limestones. In the present study, the volume change and the global compactive behavior (even at low confining pressures) are qualitatively similar to highly porous limestones such as: (i) Saint-Maxim limestone (Baud *et al.*, 2009), (ii) Leitha limestone (Baud *et al.*, 2017a, (iii) Majella limestone (Baud *et al.*, 2009, Vajdova *et al.*, 2012) with porosity $\phi = 37\%$, $\phi = 31\%$, and $\phi = 30\%$, respectively.

In order to underline the influence of non-isotropic (deviatoric) loading on the behavior of Tuffeau de Maastricht, data for the mean stress p as a function of volumetric strain ϵ_v is presented in Figure 5.7. The isotropic compression curve is also shown for reference. During triaxial compression at constant confining pressure, an increase $\Delta\sigma_1$ for the axial stress, corresponds to an increase $\Delta\sigma_1$ and $\Delta\sigma_1/3$ for the deviator and mean stress, respectively. For elastic deformation the volumetric strain is controlled only by the isotropic compression and it is independent of the deviatoric stress. Therefore, the data from the triaxial compression tests in Figure 5.7 (solid curves) should coincide with the isotropic data (dashed curve). Any deviation from the isotropic compression curve would imply that the volume change is induced by the deviator stress in the axisymmetric conditions (Brace, 1978). In all experiments shown in Figure 5.7, the triaxial curve for a given confining pressure follows the same trend with the isotropic compression curve up to a critical stress state, indicated by C^* in the figure. Beyond C^*, there is an accelerated decrease in volumetric strain in comparison to the isotropic. At stress levels beyond C^* the deviator stress provides an significant contribution to the compactive strain and this phenomenon is referred

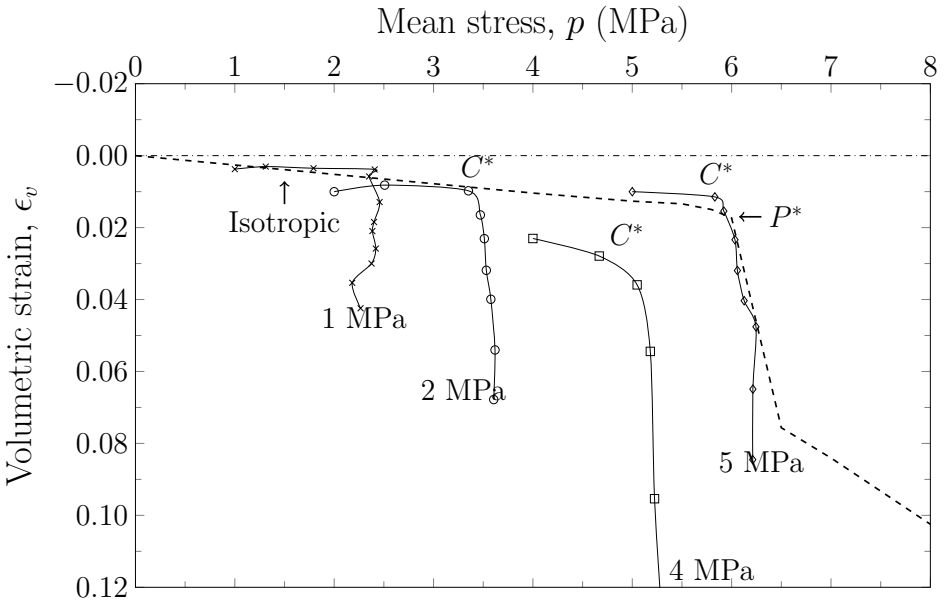

Figure 5.7: The volumetric strain is plotted versus the mean stress and for reference the isotropic data is shown (the dashed line). P^* indicates the critical pressure for pore collapse, C^* indicate the stress state of accelerated compaction.

as "shear-enhanced compaction" (Wong *et al.*, 1997). For the experiments at confining pressure between 2 and 5 MPa, the stress remains relatively constant, *i.e.*, the curves have a slope of 1, after the inflection point (C^*). This behavior is in agreement with prior observations in porous limestones (Baud *et al.*, 2009, 2017a). Additionally, the curve for the triaxial compression test at 5 MPa confinement almost coincide with the isotropic compression curve, indicating that this experiment is performed close to the critical pressure P^*. Note that the triaxial curves do not coincide with the isotropic as it is expected and presented in previous studies (Baud *et al.*, 2004, Tembe *et al.*, 2006, Wong *et al.*, 1997, Wong and Baud, 2012). This is related to the approach used to do the measurements. The volumetric strain for the triaxial compression tests is measured through the image analysis since the specimens are tested dry. Thus, a variation in the measurements is expected.

The critical stress state C^* for the onset of localized compaction also marks the initial yield stress, which decreases with increasing confining pressure. In Figure 5.8a, the data on brittle strength and the critical stress values C^* of Tuffeau de Maastricht are compiled in the $p - q$ space. Since no dilatancy is observed in the experiments previously presented, the data maps a single failure envelope for Tuffeau de Maastricht. Figure 5.8a summarizes the peak stress for the experiments presented in Figure 5.5, as well as the data from Baxevanis *et al.* (Baxevanis *et al.*, 2006). Except from the critical pressure P^* that is significant higher for their case, the rest of the data presented in this work are qualitatively and quantitatively in good agreement with the preliminary data of Baxevanis *et al.* (2006). It is obvious that this material undergoes the brittle to plastic transition at room temperature at very low confining pressures, easily accessible in the laboratory. Figure 5.8b summarizes representative data for the yield caps of five porous carbonate rocks (including Tuffeau de Maastricht). It shows that porosity clearly affects the size of the yield surface, which decreases with increasing porosity.

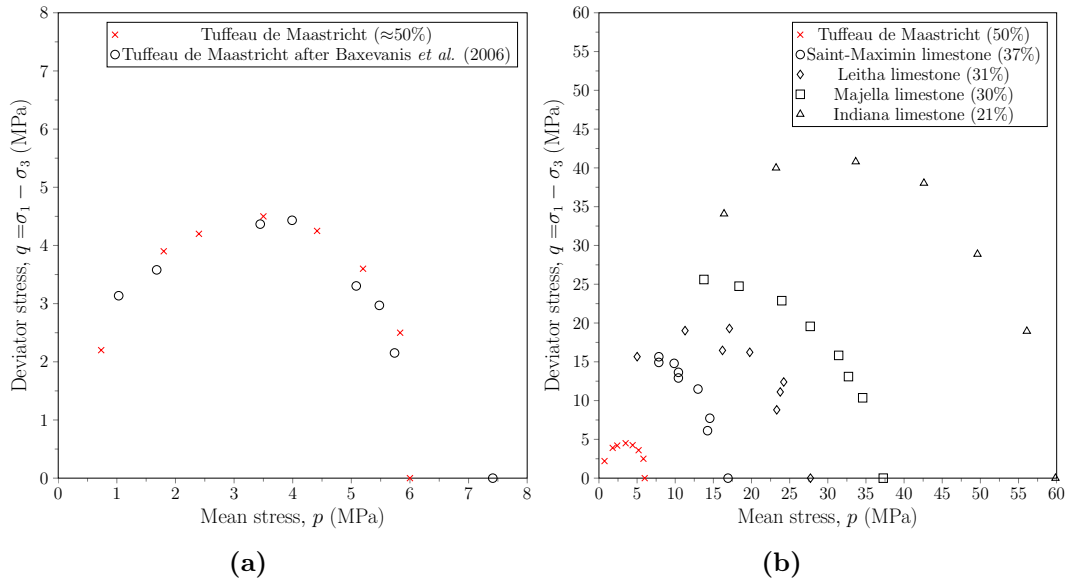

Figure 5.8: (a) Peak stresses that map the yield surface for Tuffeau de Maastricht plotted in p-q plane, compared with prior results from Baxevanis *et al.* (Baxevanis *et al.*, 2006) (b) Comparison of Tuffeau de Maastricht yield surface with other porous limestones.

5.2.1 Full-field measurements: failure mode and localized compaction

As it is already mentioned before, most of the experiments presented in this study are performed *in-situ*, using the x-ray scanner in laboratoire 3SR. At first, the x-ray images are used to measure each specimen's initial conditions and help to distinguish the "good" samples to be tested. Then, they are elaborated to perform specimen-scale measurements such as total initial porosity, specimen's bulk volume and volumetric strain. However, the main advantage of x-ray CT is that allows continuous non-destructive observations of the sample during deformation.

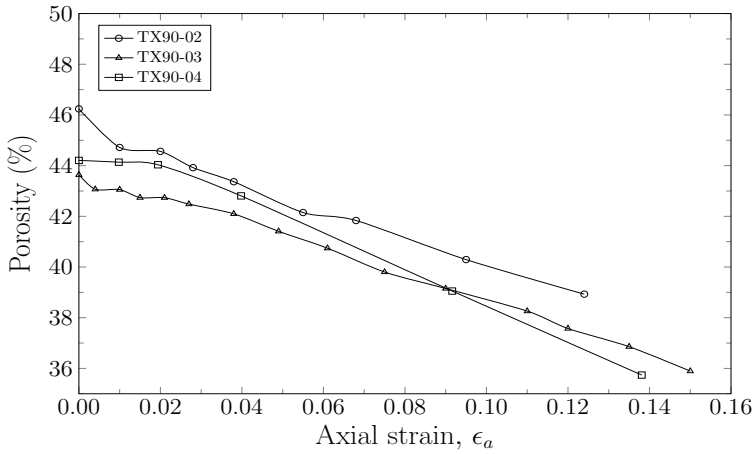

Figure 5.9: The evolution of macroscopic porosity with loading for the triaxial tests performed at confining pressure from 2 to 4 MPa.

The macroscopic specimens response in Figure 5.5b clearly shows a decrease of the specimen volume during these tests, which means that porosity must also be decreasing. Figure 5.9 presents the mean porosity measured macroscopically for three tests using the method described in section 4.2 and its evolution during loading.

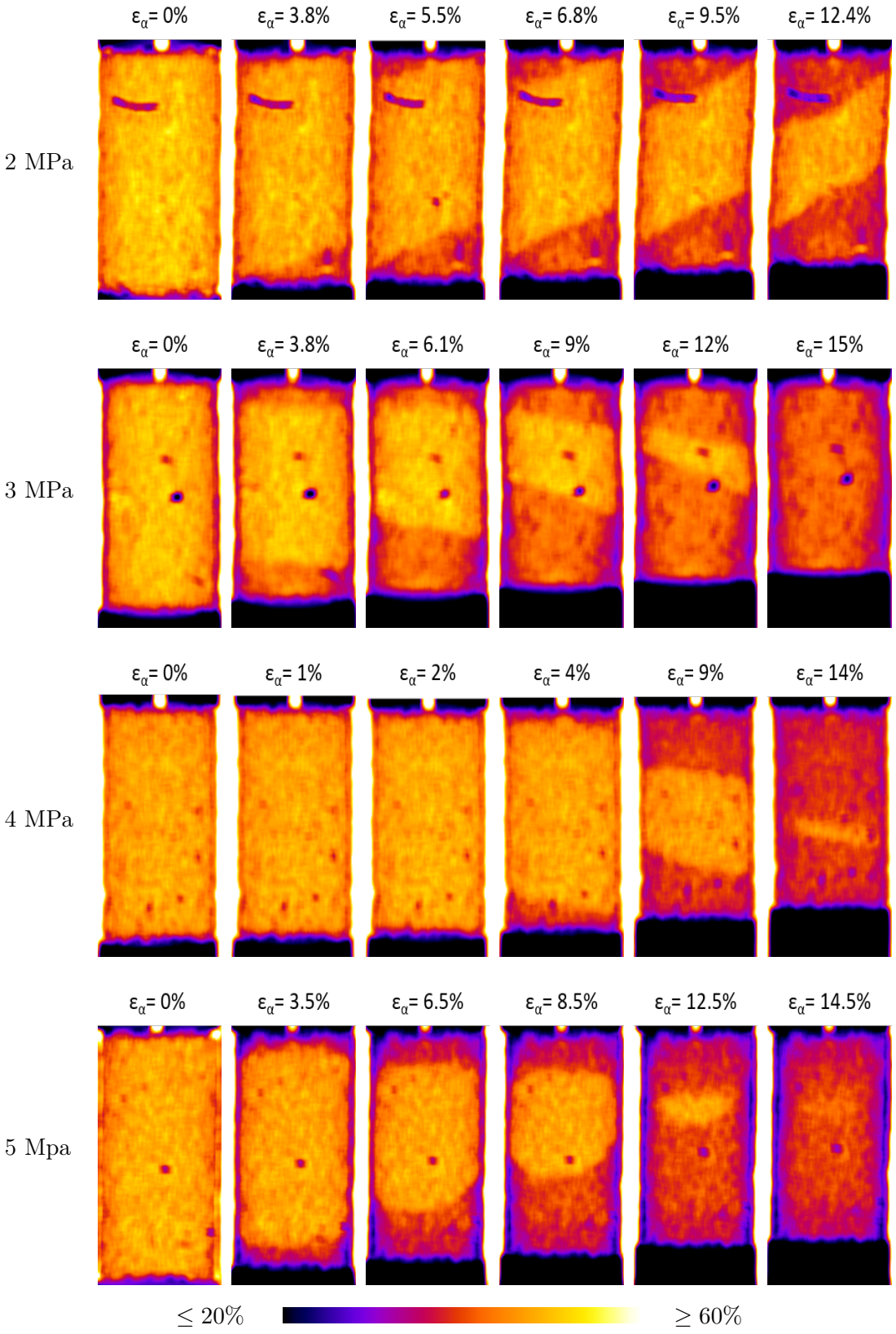

Figure 5.10: Vertical slices of the 3D field of porosity of some selected loading stages for test (a) TX90-02, (b) TX90-03, (c) TX90-04, and (d) TX90-05.

In addition to the specimen-scale porosity measurements, the 3D porosity field is obtained. Figure 5.10 shows slices taken through the porosity field, where each pixel represents the value of porosity calculated on overlapped subvolume (REV) of 54 voxels. This figure presents a selection of porosity measurements for triaxial compression experiments with confining pressure ranging from 2 to 5 MPa. At the top of each slice is marked the axial strain at which the specimen loading is interrupted and the x-ray CT is performed. The threshold value applied to the porosity maps is selected in such a way to maintain the same convention with the radiographs, *i.e.*, the denser the material, the darker the color. It should also be mentioned that the porous platens and the membrane are not deleted from the images, thus they appear in the slices. It is more straightforward to identify the porous platens, which are the black areas on the top and bottom on the slices, while deleting the membranes is less easy. In addition, an number of inclusions with much lower porosity than the surrounding material can be seen in the slices.

For all the triaxial compression tests, the porosity maps indicate the initial high porosity of Tuffeau de Maastricht and its evolution during the loading. Prior to shearing, all the specimens have a relatively uniform distribution of porosity and no clear change occurred until the yield stress, in terms of absolute value and distribution. Thus, most of the slices presented in Figure 5.10, are after the yield stress, mainly during the plateau of deviator stress.For all samples (and for all confining pressures), the first changes in porosity always appear at the top and at the bottom of the specimen. With further increase in axial strain, porosity continues to decrease and the densified zones appear to propagate towards the middle of the sample. For the rest of the material, outside of these densified zones, there is no change in porosity. This can be confirmed by Figure 5.11 where the porosity is plotted versus the length of the sample at the initial state, *i.e.*, $\epsilon_a = 0\%$, and at $\epsilon_a = 8.5\%$. The two ends of the sample present much lower porosity than the initial values while in the middle of the sample the porosity is still equal to the initial value.

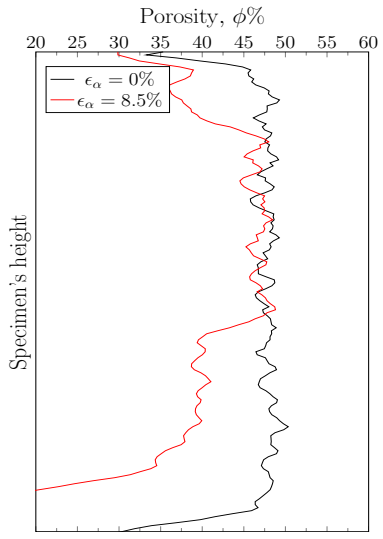

Figure 5.11: Porosity profile along the specimen axis before any load applied to the sample and for loading step $\epsilon_a = 8.5\%$ in the triaxial compression test at 5 MPa (TX90-05).

The porosity map in Figure 5.10 show that all the specimens undergo a decrease of porosity. However, at low confining pressure (2 MPa) the densified regions appear inclined to the maximum compressive stress, and the inclination keeps increasing with increasing confining pressure. For the specimen tested at confining pressures, $\sigma_3 \geq 3MPa$, the regions of compaction continue to

propagate until they "cover" the whole sample at $\epsilon_a \approx 15\%$. At this axial strain level, the entire specimen has reached a much lower (and essentially uniform) porosity. Visual inspection of the samples after the test revealed the absence of any cementation among the particles.

In the following all the results of DIC are presented for the triaxial compression test TX90-04, which will be used as a reference test hereafter. Figure 5.12a shows the vertical slices of the 3D reconstructed volume of the samples and the corresponding axial strain at which the x-ray CT images are acquired. The solid light-grey areas that appear at the bottom and top of the samples are the two porous platens. From those slices, it is not easy to identify any deformation process. At axial strain of $\epsilon_a = 9\%$, only someone with trained eyes can recognize that the top and the bottom part of the sample are denser that the rest of the specimen. This is easier to be identified when looking at the voids (darker areas), which are present in the middle of the sample but not at the two ends of the sample.

Figure 5.12b summarizes the incremental z displacement fields for all the loading stages in the test TX90-04. The vertical slices of the samples are colored by the measured displacement over each increment. The z coordinate direction coincides with specimen's axis, *i.e.*, it is parallel to the loading axis. Thus, the z displacement field corresponds to the vertical incremental displacement of the sample. In the first increment, the distribution of the vertical displacement shows that the specimen is deforming homogeneously. Since the same color maps is used for all the slices, the color representing the values in the first increments indicates that they are very small on that scale. In the following increment, the vertical displacement field loses its homogeneity and higher values appear at the bottom, this is expected since the samples are loaded from the bottom. As the test develops, the gradient of the displacement field starts showing a discontinuity with the higher values always at the bottom and almost zero values at the top, respectively. It should be noted that the gradient of the vertical displacement does not remain constant throughout the different increments, evidence that there is no a single failure zone. A comparison of the horizontal displacement, *i.e.*, x and y displacement field, with the vertical for the same increment of loading is presented in Figure 5.13. The slices showing components of displacement in three direction, reveal that there is very little displacement, almost zero, in the x and y direction (horizontally) compare to the vertical direction. Hence, only the vertical displacement field is presented hereafter.

The full strain tensor that maps the deformation between two increments, is obtained by 3D DIC using the *TomoWarp2* code. It should be reminded that the volumetric and the shear strain are calculated in terms of the principal values of the strain tensor and positive volumetric strain corresponds to compaction (see Equation 4.6 and Equation 4.7). In addition, it is worth noting that the DIC strain analysis provides an incremental analysis, *i.e.*, it indicates the deformation active in each strain increment. Figure 5.14 shows the evolution of incremental maximum shear and volumetric strains obtained from DIC for the test TX90-04. As it can be seen from these incremental maps there is no clear concentration of strains in the earlier increments of loading, at the specimen scale. However, at the local scale, the localization initiates at low axial strain, well before the stress plateau. Shear and volumetric strain concentration appears to the top and the bottom of the sample, something that is not that clear in the porosity map. Furthermore, in the next increment the localization gets more pronounced and starts as two thin horizontal bands. These localized zones become thicker and propagate towards the middle of the sample with increasing loading. At higher axial strain, the two distinct bands at the two ends of the

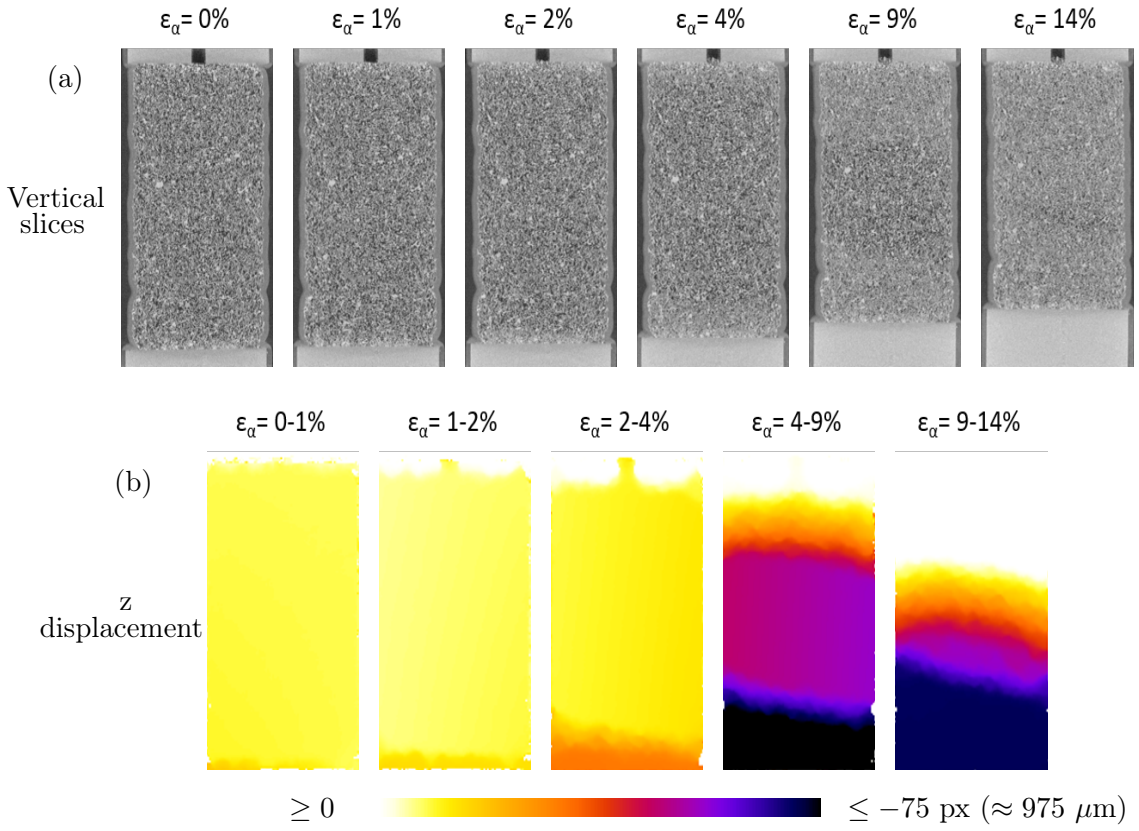

Figure 5.12: (a)Vertical slices from the 3D reconstructed volume of the sample compressed at 4 MPa confining pressure (TX90-04). The loading step at which the x-ray CT is performed is noted on the top of each slice. (b) Vertical slices of the displacement field measured over increments during the test. The slices are colored by the value of the measured vertical incremental displacement (negative values mean upwards).

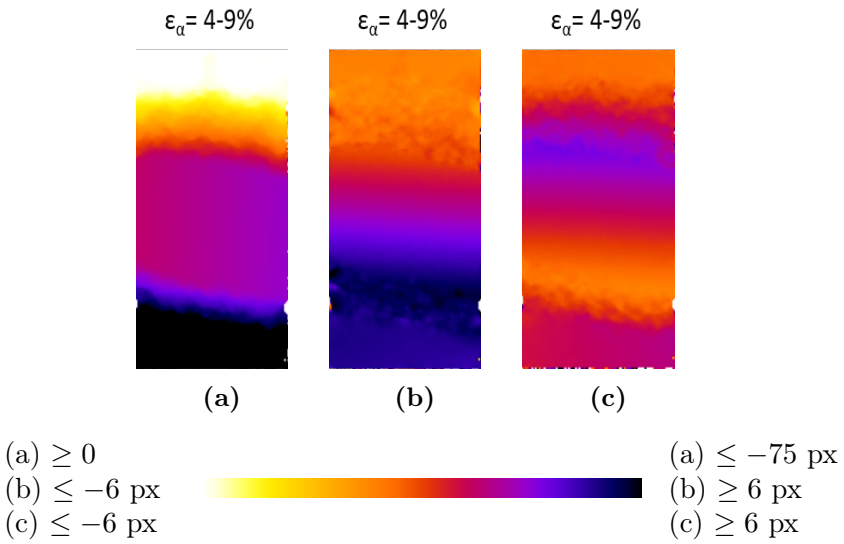

Figure 5.13: Vertical slices of the displacement fields for a selected increment of $\epsilon_a = 4 - 9\%$ for test TX90-04. (a) Vertical displacement, (b) X displacement, and (c) Y displacement.

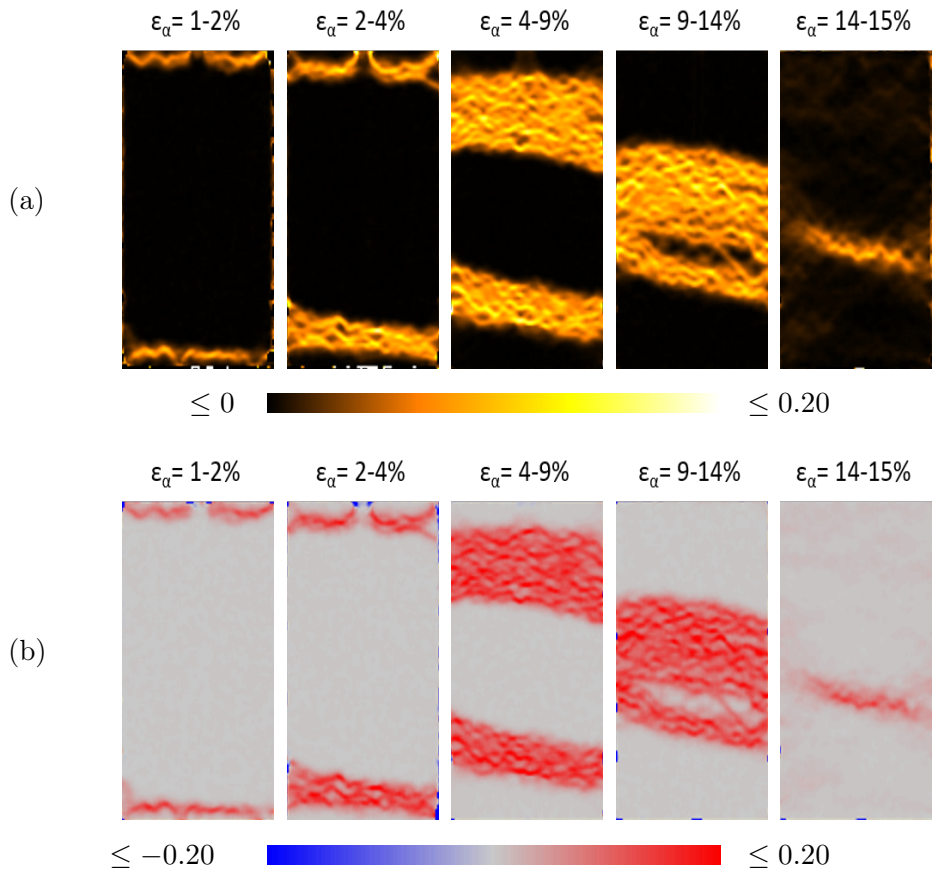

Figure 5.14: Vertical slices of the 3D strain field for test TX90-04. (a) Deviatoric strain, and (b) maximum volumetric strain measured by Digital Image Correlation.

sample become one thicker band in the middle. The increase of shear strain is associated to a corresponding increase in compaction, as indicated from the volumetric strain field. The volumetric strain field indicates that there is no dilation throughout the whole sample. The zones with high shear strain are associated with very high localized compaction, whilst the rest of the specimen remains essentially undeformed. The orientation of these compactive zones is almost perpendicular to the maximum compressive stress, indicating the formation of compaction bands. Both shear and volumetric strain fields illustrate that there is an internal more complex structure inside these thick localized zones. Each zone consists of thinner warm-like (crooked) compaction bands with higher strain values (brighter color).

In order to investigate the localization pattern in the brittle as well as in the compactive regime, image analysis is also performed for triaxial compression experiments with confining pressure ranging from 1 to 5 MPa. A detailed inspection of local deformation processes is carried out on the high-resolution digital images that are acquired at various loading stages. DIC is used to infer the displacement field and the corresponding incremental strain maps. Figure 5.15 and Figure 5.16 present slices through the field of deviatoric and volumetric strain in selected increments, respectively. Strain distribution in the five samples show significant heterogeneity. At low axial strain, each test shows a small strain concentration near the two ends of the samples, before the peak load. The sample tested at confining pressure of 1 MPa shows a global stress-strain response with strain softening. Two inclined bands associated with enhanced shear strain can easily be identified. Similar strain localization is observed for the sample tested at 2 MPa

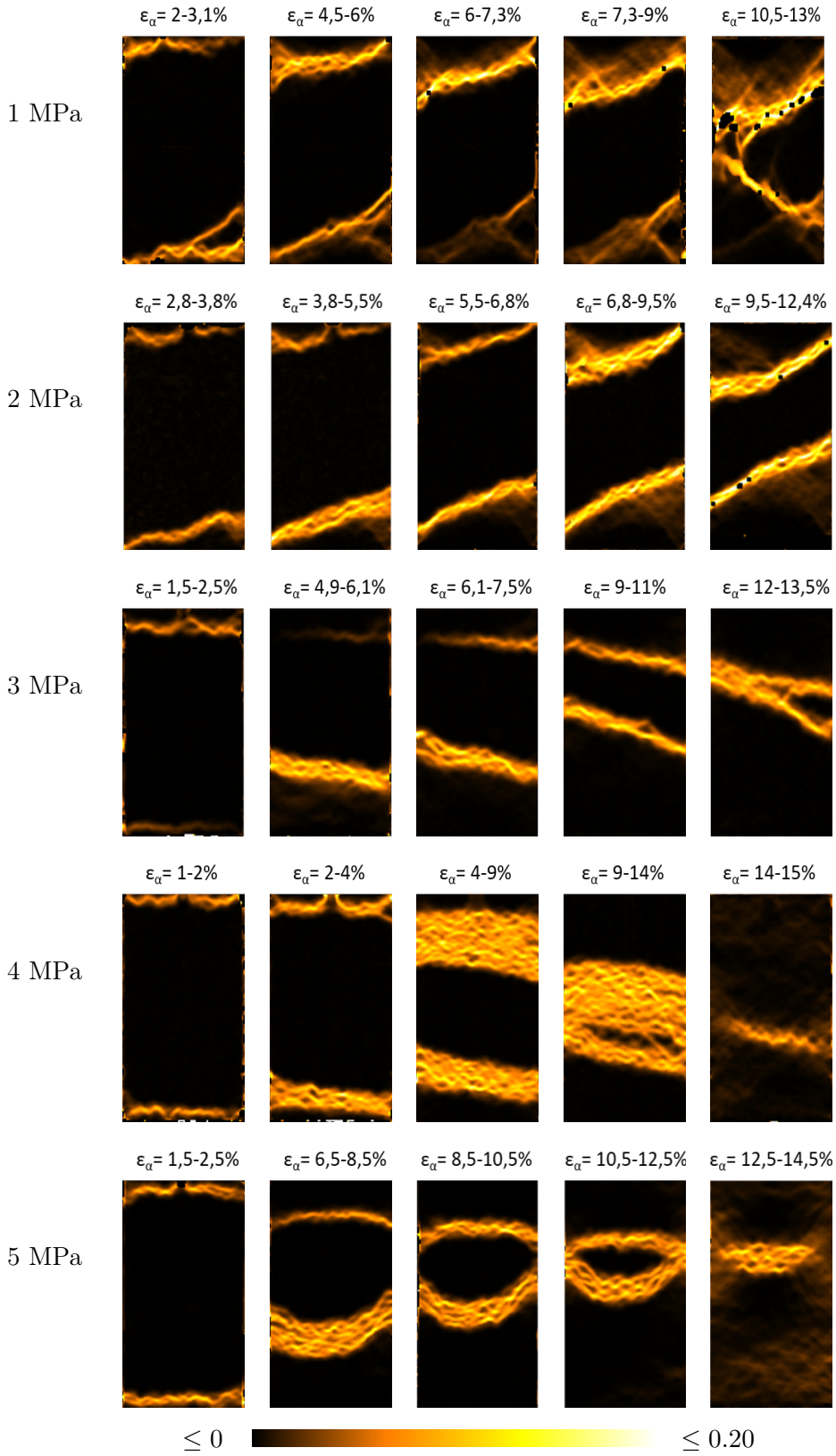

Figure 5.15: Vertical slices in selected loading stages, measured by DIC in terms of maximum shear strain at different confining pressures for test (a) TX90-01, (b) TX90-02, (c) TX90-03, (d) TX90-04, and (e) TX90-05.

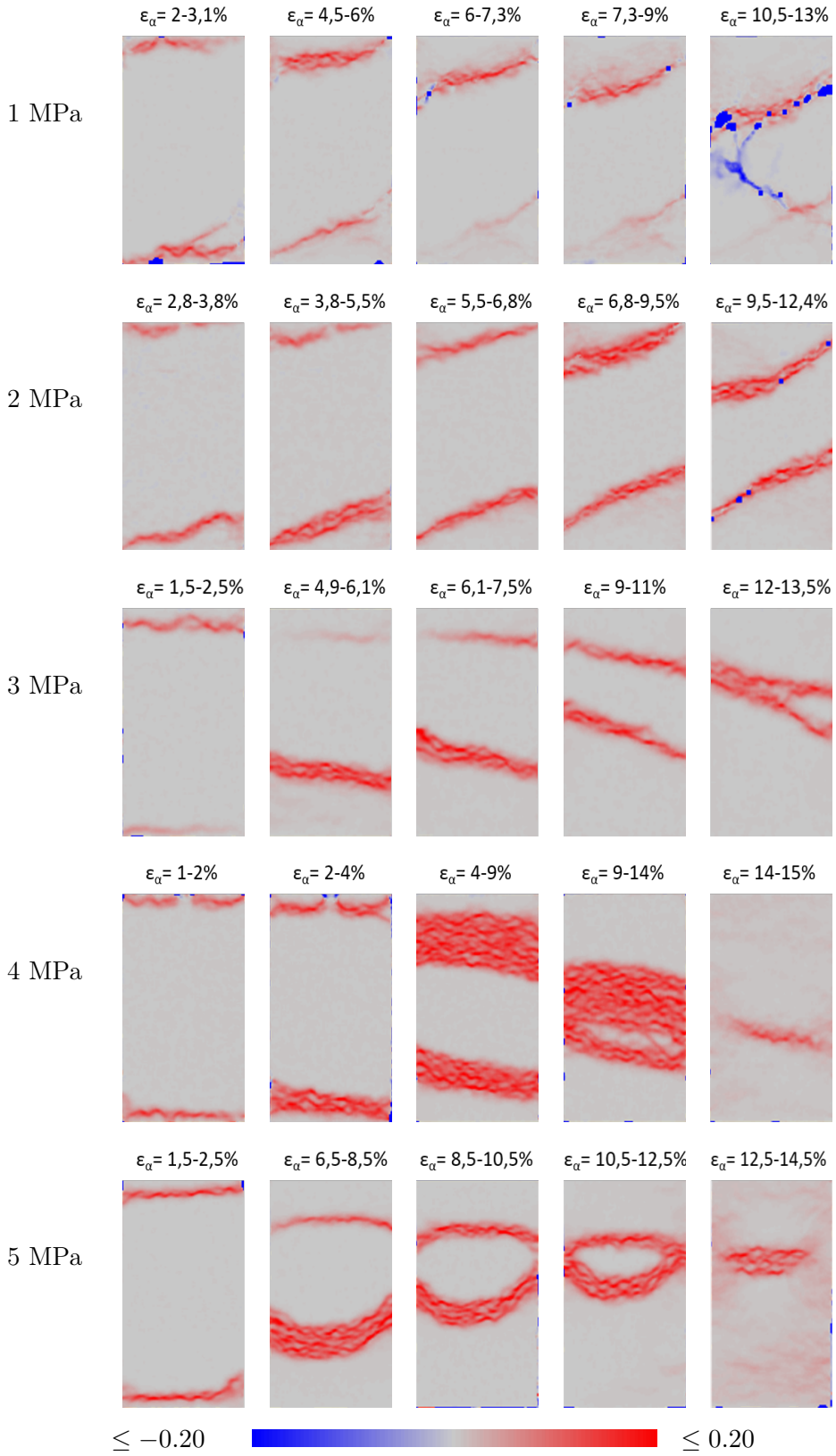

Figure 5.16: Vertical slices in selected loading stages, measured by DIC in terms of volumetric strain at different confining pressures for test (a) TX90-01, (b) TX90-02, (c) TX90-03, (d) TX90-04, and (e) TX90-05.

confinement, although its behavior is more ductile. The band orientations for both samples, are at high angles with respect to the maximum compression direction. Given these observations, the mode of localization in these two samples can be categorized as high-angle compactive shear bands. In particular, these compactive shear bands nucleate at an angle of about 60° to 70° which stays constant for all the increments. With increasing loading these bands propagate from the two ends towards the middle of the sample.

In the other three samples tested at pressures from 3 to 5 MPa shear strain concentration increases at the boundaries of the samples and propagates with increasing applied deformation until both shear enhanced compaction bands meet in the middle of the specimen. The experiment performed at 4 MPa confinement is included for comparison. The band angle (defined as the angle between the band and the direction of maximum compression) increases with increasing mean stress. At 3 MPa confinement the shear enhanced compaction bands tilt at an angle of 80° while for the TX90-04 the bands are inclined sub-perpendicular with respect to the major principal stress direction. For the TX90-05 a different localization pattern is observed though. Although the localized zones appear tabular at low axial strain, as the loading increases they become curved close to the boundaries of the sample. For all the experiments, regardless of the confining pressure, the localized zones are made up of multiple strands of closely spaced tortuous bands with enhanced volumetric strain. The thickness of the localized zones appears to depend on the number of these crooked compaction bands, which increases as the loading step gets bigger. In other words, for bigger loading step the localized zone appears thicker than in the case of a smaller increment of axial strain (for comparison reason see the TX90-04 experiment at $\epsilon_a = 2-4\%$ and $\epsilon_a = 4-9\%$). Therefore, the thickness of the localized zones as it appears in these DIC-based strain fields depends on the size of the strain increment considered. Comparison of the deviatoric and volumetric strain fields shows a general compactive behavior as well as indicates a shear component to the localized deformation, higher at the lower confining pressures. This is in agreement with the porosity maps and the macroscopic behavior previously presented. Intense shear and volumetric strain is identified inside the localized zones (bright colors), whereas strains in the rest of the specimen are rather negligible compared to those inside the bands.

5.2.2 Triaxial compression tests up to high axial strain

Previous experimental studies on sandstone (Baud *et al.*, 2006, Heap *et al.*, 2015), limestone (Baud *et al.*, 2017a), and foam (Park and Nutt, 2001) show that in triaxial compression there is considerable strain hardening after the plateau of deviator stress. In order to investigate this phenomenon some additional triaxial compression tests were conducted on Tuffeau de Maastricht for high confining pressures (4 and 5 MPa) until high axial strain (more that 50%).

Figure 5.17a presents the stress-strain curves of tests TX90-04 and TX90-05. For the sample deformed at 4 MPa pressure, the stress-strain curve is characterized by three stages. A roughly linear initial trend (with a stiffness of about 0.18 GPa) followed by a curvature to the peak load at around 1.5% nominal axial strain. A nearly constant plateau of deviator stress with fluctuations follows, without any decrease in stress observed after the peak value. At about 14% axial strain, the deviator stress starts to increase again; almost linearly, with a stiffness of about 0.03GPa. TX90-05 test at 5 MPa shows a similar response: after attaining an initial peak the deviator

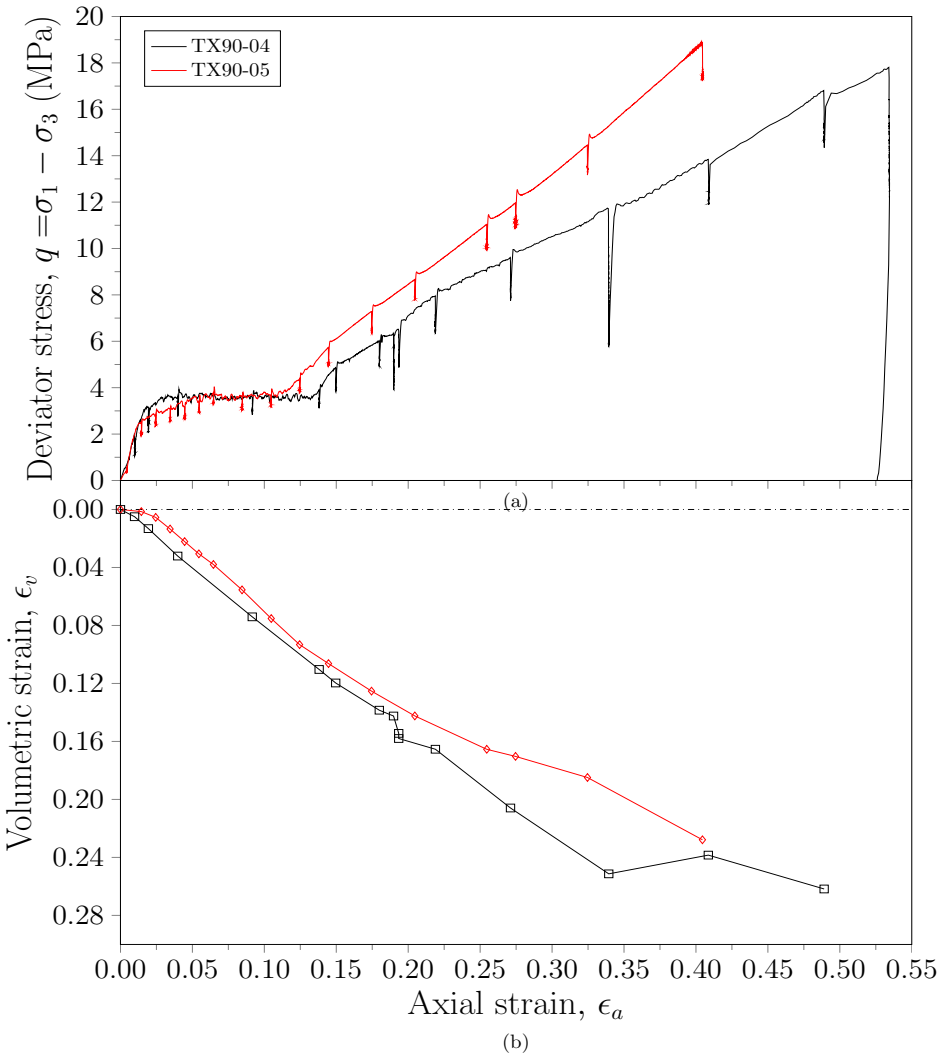

Figure 5.17: (a) Stress-strain curves for triaxial compression tests at 4 and 5 MPa confining pressure. (b) Volumetric strain versus axial strain for test TX90-04 and TX90-05.

stress remains relatively constant with an overall strain hardening trend but only after an axial strain of $\approx 12\%$ is strain hardening appreciable. In both samples the plateau is punctuated by episodic stress drops, which are generally absent afterwards.

The volumetric strain - axial strain ($\epsilon_v - \epsilon_a$) curves show a contractant behavior throughout (Figure 5.17b). For the sample tested at 4 MPa, the strain maps that obtained from DIC and presented in Figure 5.13 illustrate that the first compaction bands initiate during the strain interval 1-2%, *i.e.*, at the beginning of the deviator stress plateau (Figure 5.17). These bands grow and propagate across the sample at essentially constant deviator stress (except for the episodic stress drops). At 14% axial strain the region of compaction coincides with the entire specimen. This can be observed also in the porosity map (Figure 5.10). At this stage, the sample presents a relatively uniform distribution of porosity, much lower than the initial though (from 50% to 40% approximately). The macroscopic behavior of the specimen (Figure 5.17) indicates that this stage corresponds to the end of the stress plateau and the beginning of the hardening phase. Visual inspection of the samples at the end of the plateau (before the hardening phase) revealed substantial debonding. It seems therefore that hardening starts when the whole sample

has become debonded. Hence, the development of compaction bands in Tuffeau de Maastricht seems to reduce the porosity and break the cementation which decrease porosity promoting strain hardening. However, further investigation is needed to corroborate this interpretation, with observations at a smaller scale.

Microstructural observations on natural deformation bands show a notable pore and grain size reduction inside the compaction bands compared to the surrounding host rock (Mollema and Antonellini, 1996,Cilona *et al.*, 2012, Tondi *et al.*, 2006). Additional experimental microstructural analysis on porous carbonates points out that pore collapse and intra-granular microfractures are the dominant mechanisms (Baud *et al.*, 2009, Vajdova *et al.*, 2012, Zhang *et al.*, 1990a). Furthermore, prior studies shown that the plateau of deviator stress combined with the episodic stress drops, corresponds to a surge of AE activity indicating that pore collapse and grain breakage initiated at this stage. In order to further investigate the micromechanisms responsible for the macroscopic behavior two additional triaxial compression tests at 4 MPa confinement are conducted. Figure 5.18 presents the stress-strain curves from these two experiments. The samples are monotonically loaded, without x-ray CT images acquired, up to the end of the plateau, and stopped before the hardening phase, *i.e.*, at 14% of axial strain. Then, grain size distribution is performed for the tested samples and compared with the measurements acquired for the reference material (Figure 3.6). The grain size distribution curves show a notable reduction of grain size occurring during the compaction band formation and propagation (Figure 5.19). These results strongly suggest that grain breakage is an important deformation microprocess within the compaction bands. Although it is not adequate to characterize grain crushing as a dominant mechanism. Furthermore, image analysis of samples that deformed in axisymmetric conditions at 4 MPa confining pressure at high resolution (4 μm pixel size) shows intragranular microfractures mainly at the contact point without extensive grain crushing. Unfortunately, these images are lost due to a malfunction of the server so they are not available for this report.

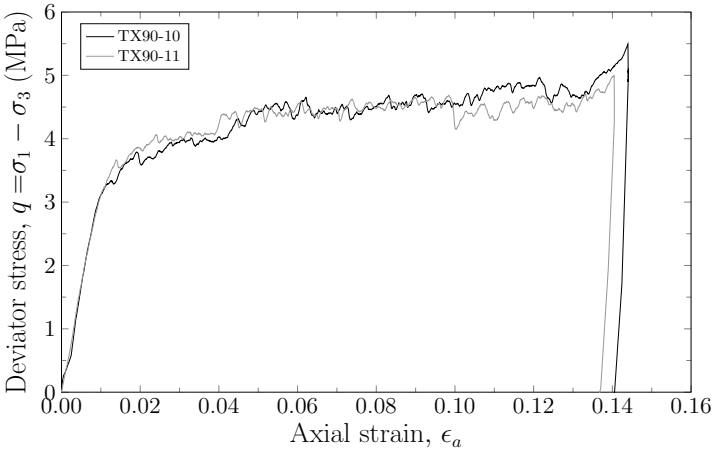

Figure 5.18: Stress-strain curves for triaxial compression tests at 4 MPa confinement stopped right before the hardening phase.

In an attempt to determine the main micromechanisms leading to failure, a new series of triaxial compression tests is conducted. Unlike the previous ones, these tests are carried out on the reference material. Specifically, three additional triaxial compression tests are performed on destructured samples (subsection 3.1.2) of Tuffeau de Maastricht at 4 MPa confining pressure. Initially loose specimens of reference material with porosity values similar to the intact samples,

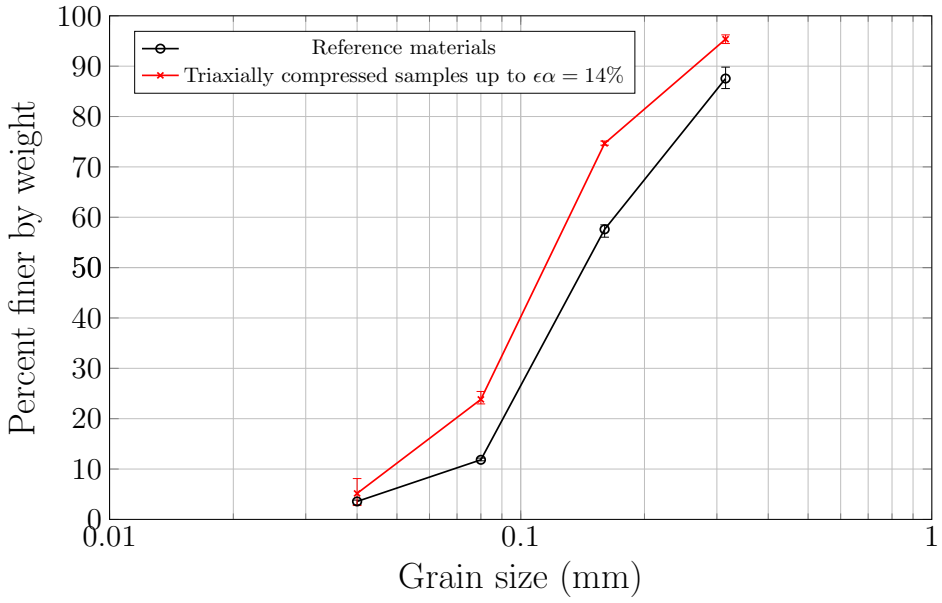

Figure 5.19: Grain size distribution curve for the samples tested at 4 MPa confinement and loaded up to 14% axial strain (end of the plateau). The grain size distribution curve for the reference material is added as a reference (black color).

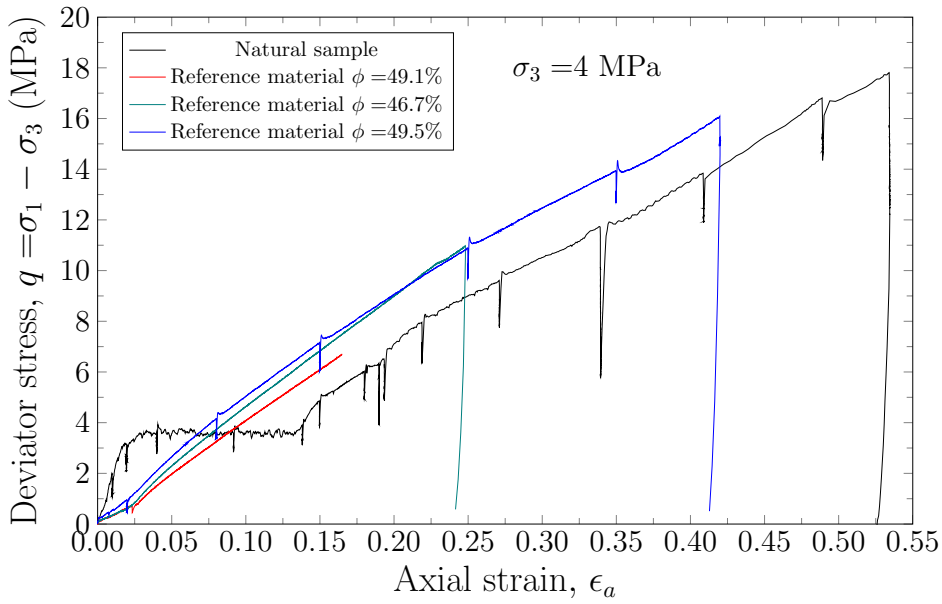

Figure 5.20: Mechanical response for three samples of reference material that deformed under axisymmetric conditions at 4 MPa confinement. The stress-strain curve for test TX90-04 is plotted as a reference.

are obtained as described in section 3.2. Table 5.3 presents the characteristics of the specimens tested. The stress-strain diagrams of these samples and for the intact sample tested at the same confinement are plotted in Figure 5.20. For the two tests TXref-01 and TXref-02, the samples are loaded monotonically up to $\epsilon_a = 16.5\%$ and $\epsilon_a = 24.8\%$, respectively. While the test TXref-03 is performed *in-situ* until much higher axial strain $\epsilon_a = 42\%$. The three samples show similar macroscopic behavior: the deviator stress increases with increasing loading without attaining a peak value even at higher axial strain. Due to the absence of cementation among the grains, the reference material is weaker and less stiff than the intact one. However, Figure 5.20 reveals

that the stress-strain curves for the reference material coincide with the post-plateau behavior obtained from the TX90-04 experiment. This means that at the end of the plateau, the material converts into a new one, very similar to the reference material. Such a behavior confirms the hypothesis that the relative plateau of deviator stress is associated with debonding and it is in good agreement with the findings from previous studies on calcarenite (Lagioia and Nova, 1995).

Table 5.3: Summary of mechanical data from triaxial compression tests up to high axial strain on Tuffeau de Maastricht

Test	Porosity (%)	Peak stress q (MPa)	Axial strain ϵ_a (%)	Analysis	Comments
Confining pressure: 4 MPa					
TX90-04	49	3.6	52.5	x-ray CT/DIC/Porosity	-
TX90-05	50.7	2.5	40.4	x-ray CT/DIC/Porosity	-
TX90-10	49.8	3.5	14.4	Grain size distribution	-
TX90-11	49.9	3.6	14	Grain size distribution	-
TXref-01	49.1	-	16.5	-	Reference material
TXref-02	46.7	-	24.8	-	Reference material
TXref-03	49.5	-	42	-	Reference material
TX90-04-2	50	3.9	60.1	x-ray CT/DIC/Porosity	-

The 3D porosity field for test TX90-04 elucidates even more this phenomenon. Figure 5.10 indicates that at $\epsilon_a = 14\%$, which corresponds to the end of the plateau, the densified zones have covered the whole sample. The entire sample has been compressed and converted into a new, denser material, with homogeneous distribution of porosity. Figure 5.21 presents the porosity field for the same sample at higher axial strain. As the loading continues further, shear strain localization, typical of dense sand, is visible in the sample. Two conjugate bands of reduced porosity develop at 35% axial strain and become more pronounced by the end of the test. At this stage, the porosity inside the contractant bands is 40% less.

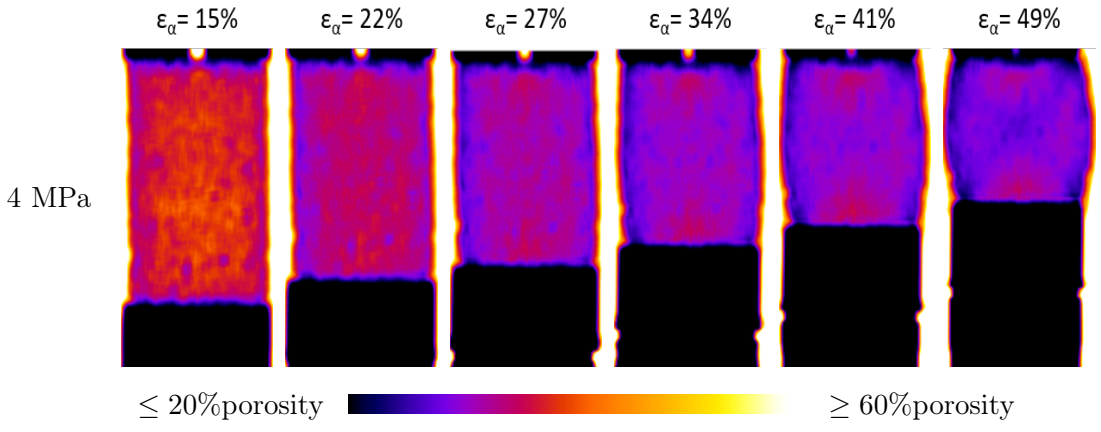

Figure 5.21: Vertical slices of the 3D porosity field in the post plateau loading stage for test TX90-04. Two conjugate shear bands are evident at the end of the experiment up to high axial strain.

In order to ascertain reproducibility, test TX90-04 was duplicated. However, for this backup test, steps of approximately 0.5% axial strain are aimed for scans to be performed. In total 42 scans with most of them during the plateau of deviator stress, are performed for this test, which which lasted 7 days. Porosity maps and strain fields through DIC, are obtained for all

the loading steps but for obvious reasons only a selection of them are presented in this study. The mechanical response of the sample is shown in Figure 5.22. It should be noted that there is high repeatability of the tests. Although the specimen present different initial conditions (variations in size and porosity) the mechanical response is practically identical (see Figure 5.17 for comparison). After a quasi-linear stress-strain relationship, a curvature at peak load follows at 1.5% nominal axial strain. Then, axial strain steadily increases at constant deviator stress. After considerable straining, hardening takes place. In all the four triaxial compression tests at 4 MPa confinement presented in this section, the post-plateau hardening takes place at the same axial strain, *i.e.*, $\epsilon_a = 14\%$.

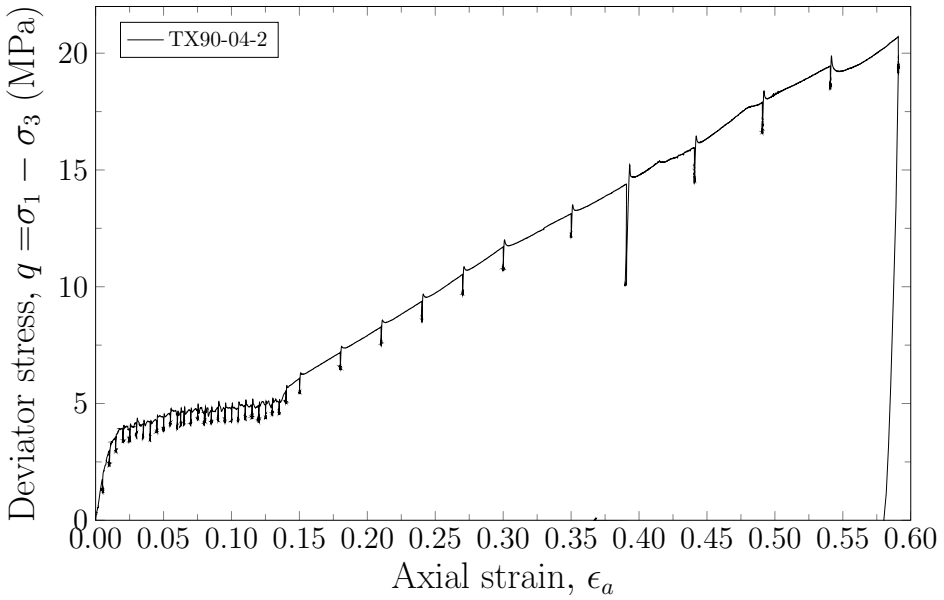

Figure 5.22: Stress-strain curve for the additional triaxial compression test at 4 MPa confinement. In total, 42 x-ray CT scans are performed for this particular test with most of them at constant deviator strain (plateau).

Figure 5.23a presents the volumetric strain for very small axial strain increments (0.5% and 0.25%). The increments presented in this figure are purposely chosen at constant deviator stress (plateau) to capture the propagation of the compaction bands. The strain field shows two localized zones close to the ends of the sample. Due to the very small loading step the localization seems to be in the exact same place for all the increments. However, plotting the difference of the consecutive increments it turns out that there is a small offset between the localized zones. This offset emerges even for smaller strain increments ($\epsilon_a = 0.25\%$). Recalling the incremental nature of DIC, Figure 5.23b indicates that different localized zones are active in each loading stage. Further analysis is though required to determine if this deformation is only one compaction band that propagates or if it is developed due to two different bands. These images also confirm that the thickness of the localized zones in these DIC strain fields depends on the size of the strain increment. Thus, the smaller the loading step, the thinner the localized zone appears. The 3D map of the volumetric strain is further analyzed and sliced vertically for each 10° increment in azimuth angle. Figure 5.24 shows the vertical slices each 10° increment for the loading increment 5.5-6% for test TX90-04-2. The volumetric maps shows localized compaction at the top and bottom of the sample. This representation clearly shows that these localized zones are formed perpendicular to the maximum compressive stress.

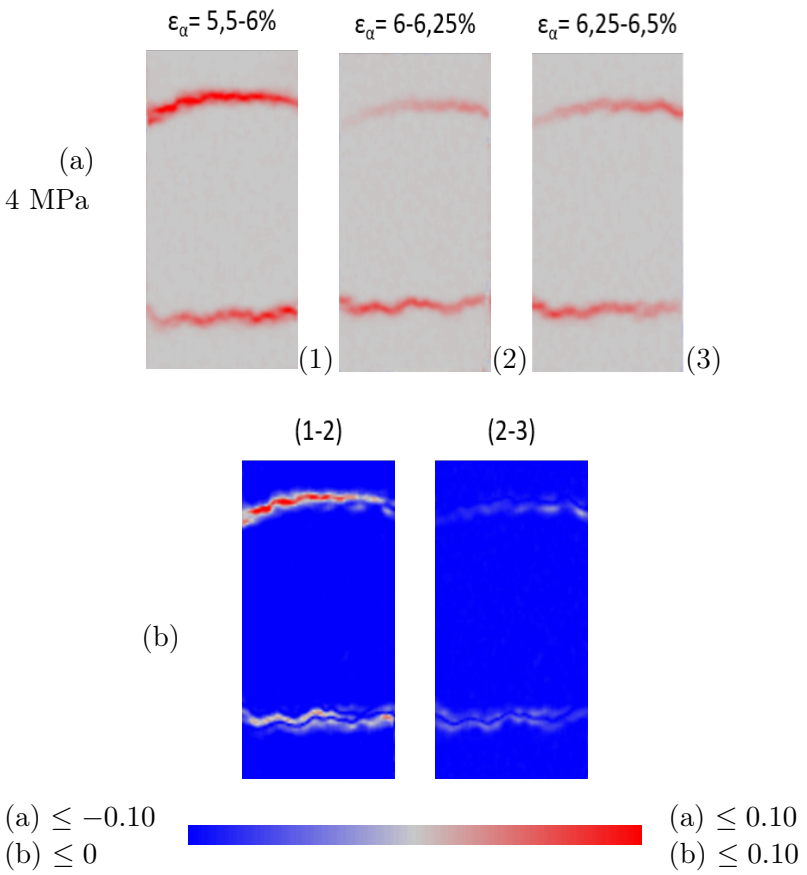

Figure 5.23: Vertical slices of the 3D volumetric strain field for test TX90-04-2 at 4 MPa confinement. (a) Small loading increments are shown here of 0.5% and 0.25% of axial strain. (b) The difference between the slices of the volumetric strain, shows that the regions of localized strain are not fixed in space.

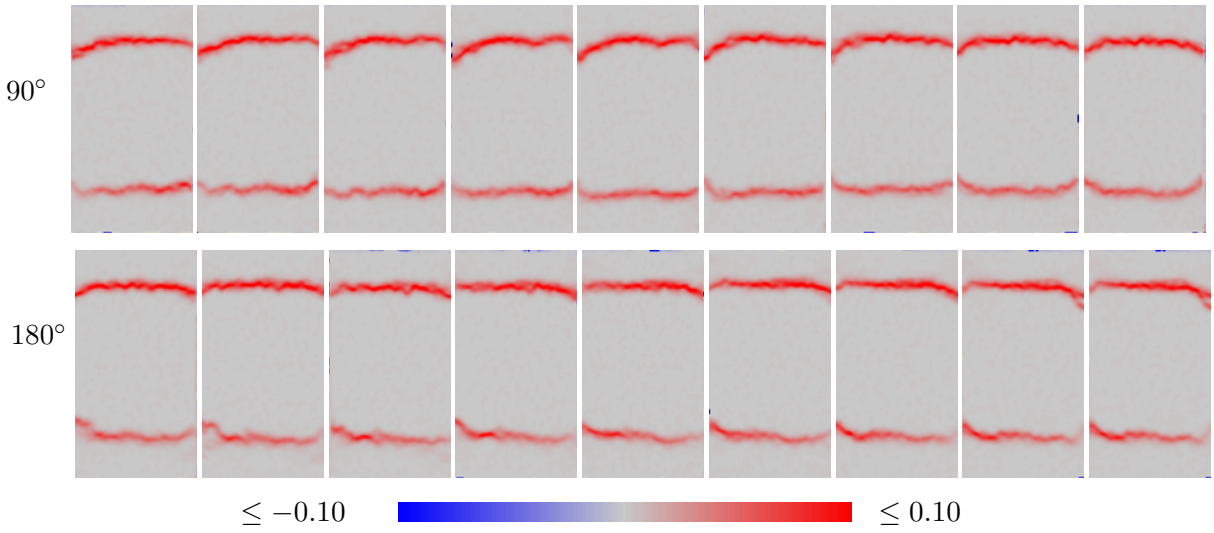

Figure 5.24: Vertical slices each 10° increment, in the volumetric strain map of the increment 5.5-6% for test TX90-04-2.

5.2.3 Anisotropy

Although Tuffeau de Maastricht is a sedimentary rock, it is almost impossible (with naked eye) to see any bedding plane in the block from which the specimens are cored. However, sedimentary

rocks may present significant anisotropy in mechanical behavior and failure strength without any visible bedding planes. Louis *et al.* (2003) in their study on two porous sandstones, shown that Bentheim sandstone, with no visible plane, is actually more anisotropic than Rohtbach sandstone with a visible bedding plane. In addition, Baud *et al.* (2005) indicate that bedding represents one type of planar anisotropy, nevertheless, anisotropy may derive from preferred alignment of irregular voids in a sedimentary rock. For these reasons, an experimental campaign on samples cored at different orientations is performed to investigate the mechanical response of the material as well as the development of strain localization. Due to the unclearness of the bedding planes orientation, the samples for this set of experiments are cored along directions 90° and 45° with respect to the specimens tested in the previous section, *i.e.*, parallel and oblique to the bedding plane, respectively (Figure 3.7). Table 5.4 compiles the mechanical data for the samples cored in both directions.

Table 5.4: Summary of mechanical data for Tuffeau de Maastricht from triaxial compression tests for samples cored parallel and oblique (45°) to the bedding.

Confining pressure (MPa)	Test	Porosity (%)	Peak stress q (MPa)	Axial strain ϵ_a (%)	Analysis
Specimens cored at 0° to the bedding					
1	TX0-01	50.2	1.82	8.6	x-ray CT/DIC/Porosity
3	TX0-03	50.8	2.3	9.0	x-ray CT/DIC/Porosity
4	TX0-04	49.4	2.0	50.2	x-ray CT/DIC/Porosity
5	TX0-05	50.8	1.4	4.5	x-ray CT/DIC/Porosity
Specimens cored at 45° to the bedding					
1	TX45-01	49.8	3.1	9.5	x-ray CT/DIC
2	TX45-02	49.5	3.28	9.0	x-ray CT/DIC
3	TX45-03	52.1	3.13	8.0	x-ray CT/DIC
4	TX45-04	50.6	2.6	17.0	x-ray CT/DIC
5	TX45-05	51.7	2.0	8.0	x-ray CT

Figure 5.25 shows the stress-strain responses obtained from the tests for the two orientations and various confining pressures. The uniaxial compression test is also plotted in both figures for comparison reasons. It is obvious that the behavior of Tuffeau de Maastricht is pressure dependent. The mechanical response of specimens that were cored parallel and oblique (45°) to the bedding is similar to the ones at 90° (perpendicular). Under low confining pressure (1 MPa), Tuffeau de Maastricht exhibits a behavior characterized by a peak deviator stress and a strain-softening phase. The peak stress increases with confining pressure up to 2 MPa confinement. However, as σ_3 level increases beyond 2 MPa, the maximum deviator stress decreases. At confining pressures of 2, 3 and 4 MPa the deviator stress increases until it reaches a plateau punctuated by episodic stress drops, while the sample at 3 MPa confinement, parallel to the bedding, at higher axial strain undergoes a second stage of strain hardening. When the confining pressure becomes high, for instance 5 MPa, an elastic-plastic response is observed with more and more important strain hardening phase, *i.e.*, the deviator stress continues to increase with increasing axial strain.

Figure 5.26 summarizes triaxial compression tests for samples cored perpendicular, oblique (45°), and parallel to the bedding plane at the same confining pressure. Each figure corresponds

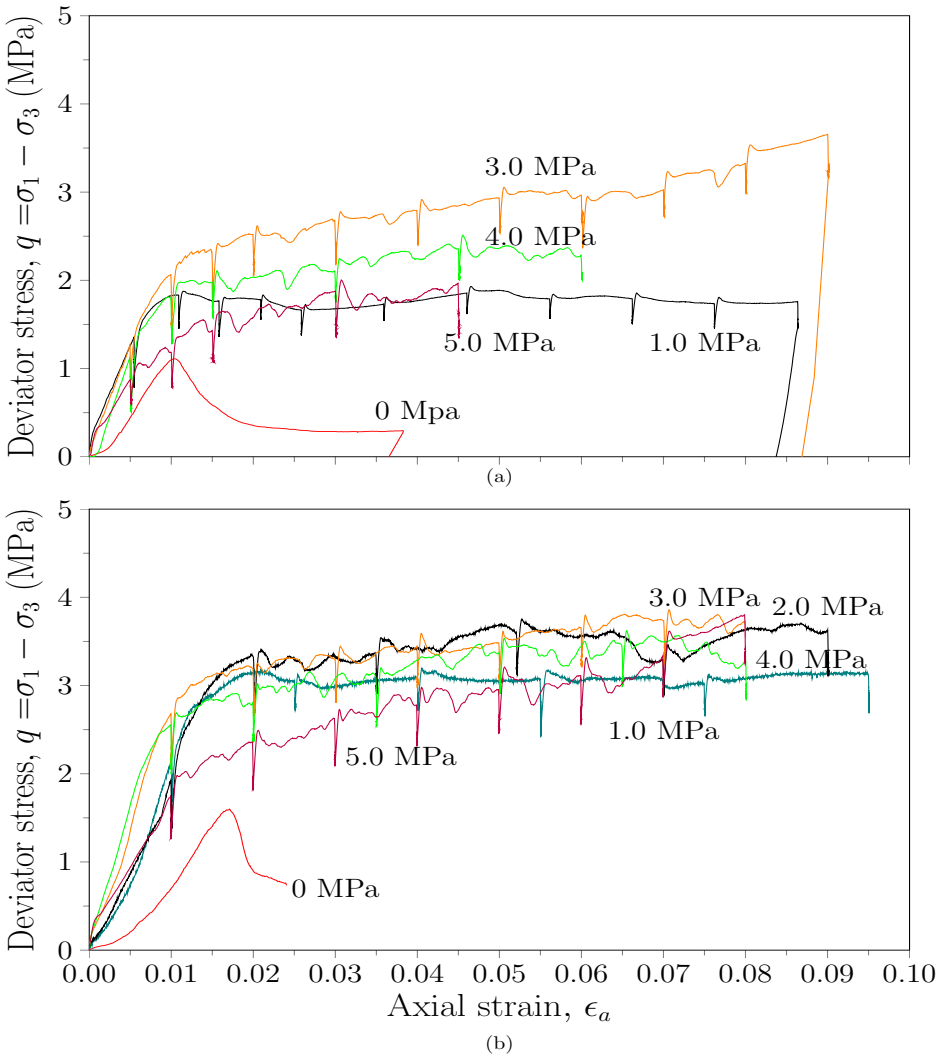

Figure 5.25: Stress-strain curves for triaxial compression tests at confining pressures ranging for 1-5 MPa for samples cored at (a) 0°, (b) 45°

to a different confining pressure. The stress-strain curves for the samples cored perpendicular to the bedding is plotted with black color, in blue samples at (45°), and in red at (0°). The first straightforward observation, is the order at which the "colors" appear in the figures. The mechanical data indicate that the maximum, intermediate and minimum values of peak stress are associated with the perpendicular, oblique and parallel samples, respectively. At low confining pressure (1 MPa), the peak stress for the perpendicular samples is twice higher than the parallel ones. In addition, the stress drop after the peak value decreases with increasing the bedding orientation, *i.e.*, it is higher at 0°. As the confinement increases, the difference between the peak stress values among the samples cored at different angles decreases. For the samples loaded perpendicular at confining pressures 3 and 4 MPa, axial strain is increasing at constant deviator stress after the peak value. However, for the samples cored in the other two directions the relative plateau is less pronounced. Inline with the analysis of the samples loaded perpendicular to the bedding presented in section 5.2, Figure 5.26 shows that the episodic stress drops indicating compaction band propagation, are more pronounced with increasing confining pressure for parallel and oblique samples as well.

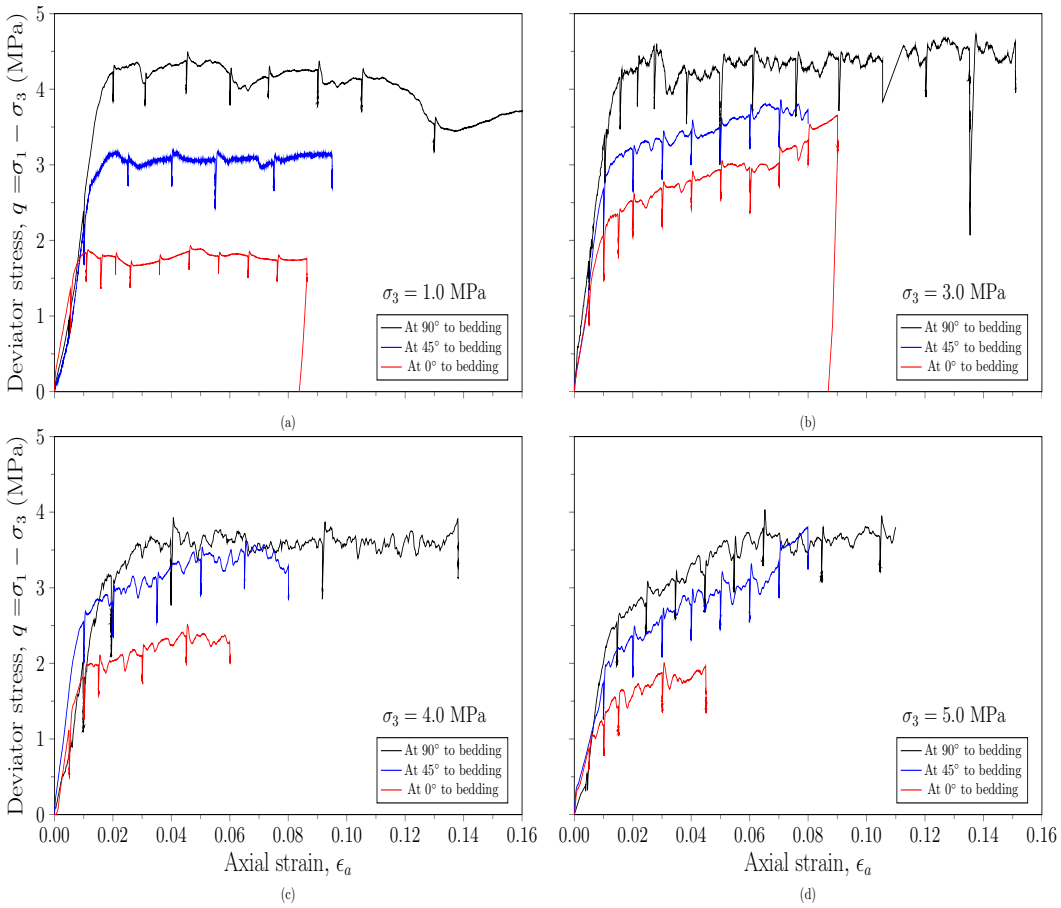

Figure 5.26: Collection of mechanical data of Tuffeau de Maastricht for samples cored at different directions at (a) 1 MPa, (b) 3 MPa, (c) 4MPa, and (d) 5 MPa confinement. The black color corresponds to perpendicular samples, the blue to oblique, and the red to parallel.

Figure 5.27a compiles the failure data obtained over a wide range of confining pressure conditions (from 0 to 5 MPa) in series of samples cored perpendicular, oblique (45°), and parallel to the bedding plane. Three independent yield surfaces as they come from three different materials describe the peak stress values. It can be easily noticed that the failure stress of Tuffeau de Maastricht depends on the loading orientation, hereafter called θ (is the angle between the loading direction and the bedding plane). Additionally, the bedding surface does not constitute a plane of weakness and the samples cored at 45° fail at intermediate level of deviator stress between the ones for perpendicular and parallel samples. The three yield surfaces present the same shape and critical pressure $P^* = 6$ MPa. Note that the critical pressure P^* is identical regardless of the coring direction.

The deviator stress at failure as a function of the confining pressure and the specimen orientation is presented in Figure 5.27b. The figure illustrates the anisotropic strength behavior of Tuffeau de Maastricht. There is a consistent trend in strength anisotropy at each confining pressure investigated, with a gradual decrease from a maximum for σ_1 normal to bedding to a minimum for σ_1 parallel to bedding. The maximum values in the anisotropic curves are located at $\theta = 90°$ orientation, *i.e.*, perpendicular to maximum compressive stress, throughout the investigated range of confining pressures. Anisotropic behavior of Tuffeau de Maastricht is in basic agreement with systematic investigation on sandstones (Baud *et al.*, 2005, Millien,

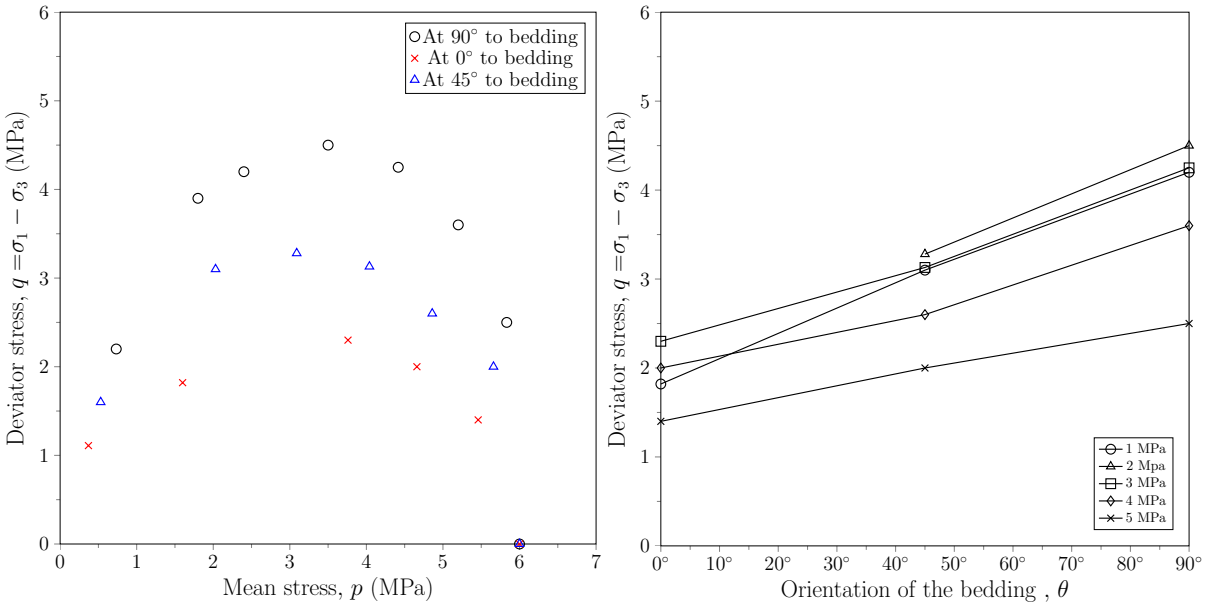

Figure 5.27: (a)Peak stresses that map the yield surface for samples that cored perpendicular, oblique (45°), and parallel to the bedding plane. (b) Peak stress as a function of bedding plane orientation from triaxial compression tests with confining pressure ranging from 1-5 MPa.

1993, Louis *et al.*, 2009). Prior studies present a general trend for both brittle strength and compactive yield stress showing a progressive decrease with decreasing angle, from a maximum for the perpendicular sample (90°) to a minimum for the parallel sample (90°).

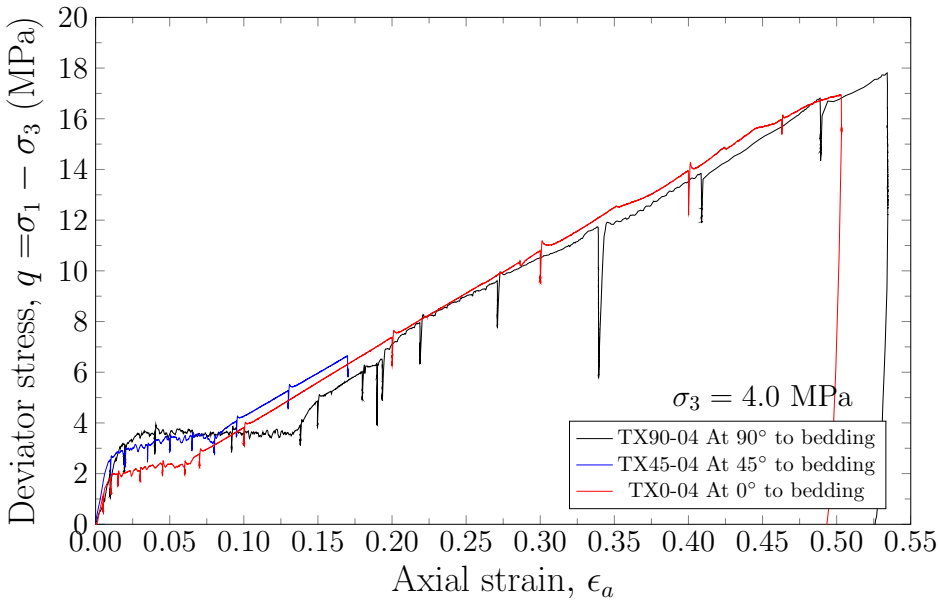

Figure 5.28: Stress-strain curves for triaxial compression tests at 4 MPa confinement up to high axial strain. A collection of mechanical data for samples cored at different directions. The black color corresponds to the perpendicular sample, the blue to oblique and the red to parallel, respectively.

In addition to the tests reported in Figure 5.25, further experiments at 4 MPa confinement are conducted for parallel and oblique samples, up to a much higher axial strain. Figure 5.28 shows the deviator stress versus axial strain for the two tests TX45-04 and TX0-04 oblique and parallel

to the bedding, respectively. The response from test TX90-04 on the perpendicular sample is plotted as well for comparison. Post-plateau hardening is observed in all tests. As it is already shown in Figure 5.26, the parallel sample exhibits the minimum yield stress while the oblique and perpendicular samples the intermediate and maximum stress, respectively. Figure 5.28 provides further insights into the mechanical behavior of Tuffeau de Maastricht. In all of the three specimens the deviator stress starts to increase (hardening phase) at different level of axial strain. Thus, the length of the plateau of deviator stress is not identical in all tests. The mechanical data from these experiments indicate that the maximum, intermediate and minimum length of the plateau correspond to the perpendicular, oblique and parallel samples, respectively, similarly to the trend observed for the yield stress. These observations combined with the analysis discussed in subsection 5.2.2 demonstrate that in the perpendicular samples the compaction bands cover the whole sample at much higher axial strain compared to the parallel ones. To the best of our knowledge, such a behavior is for the first time observed in porous carbonate rocks.

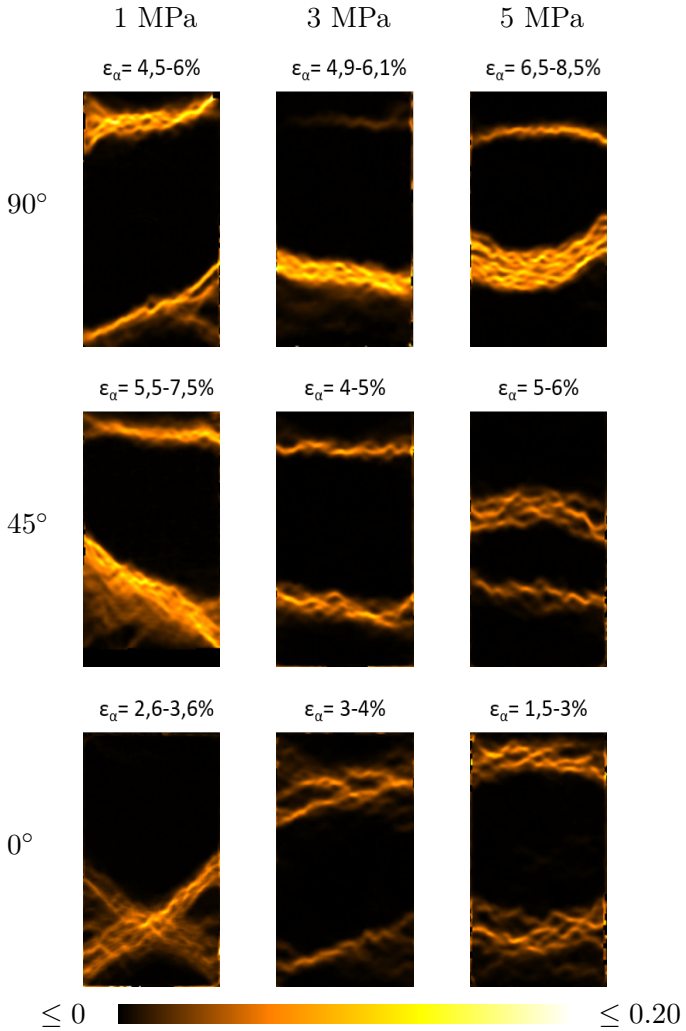

Figure 5.29: Vertical slices of the 3D shear strain field at one selected increment, for samples cored at 90, 45 and 0° and tested at 1, 3 and 5 MPa confinement. The selected increment is noted at the top of each slice.

Interestingly, although the stress-strain curves for tests TX90-04, TX45-04 and TX0-04 show different values for the yield stress and the length of the plateau, the post-plateau behavior is the essentially the same for the three samples. The specimens, regardless of their coring direction with

respect to the bedding plane, and the amount of axial strain that it takes to compact the whole sample, exhibit the same post-plateau response. This result corroborates with the hypothesis that the relative plateau is mainly associated with debonding, the intergranular bonds being the main reason for the observed anisotropy.

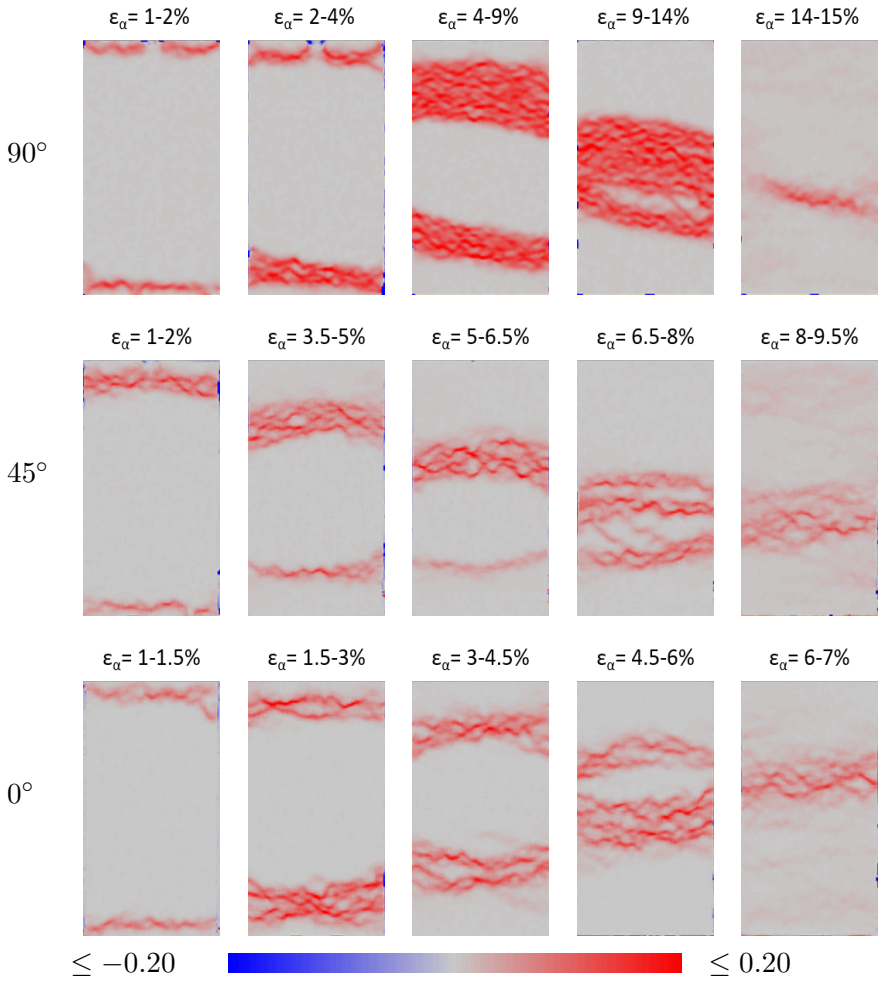

Figure 5.30: Vertical slices of the 3D volumetric strain field for samples cored perpendicular, oblique,and parallel to the bedding plane. A collection of selected loading steps during a triaxial compression test performed at 4 MPa confining pressure.

In order to investigate the influence of the bedding orientation on the failure mode, DIC is performed for the samples cored perpendicular, oblique and parallel to the bedding plane. Figure 5.29 presents the incremental shear strain at one selected loading step, for samples cored at different orientations (90, 45 and 0°) and confining pressures (1, 3 and 5 MPa). At low confining pressure (1 MPa), shear bands are observed to develop inclined to the major compressive stress for all the three orientations. The angle of the shear band with respect to σ_1 for the perpendicular sample is $\sim 60°$, which is higher that the $\sim 50°$ angle for the oblique sample. Despite the variation in the inclination, the localization pattern is qualitatively similar for both orientation. On the contrary, strain localization developed by conjugate shear bands at high angles (45°) for the parallel sample. For higher confining pressures (3 and 5 MPa) strain localization seems to be less affected by the bedding orientation. The strain fields reveal similar spatial pattern of localization for all the samples, regardless of the bedding orientation. For the 3 MPa confinement, two localized zones develop at the two ends of the samples almost perpendicular ($\sim 80°$) to the loading

direction. These bands can be classified as shear enhanced compaction bands. Additionally, the DIC indicates two localized zones with relatively high strain in all the samples tested at 5 MPa confining pressure. However, in this case the bands are less planar, especially close to the boundaries of the samples.

Figure 5.30 presents vertical slices of the 3D volumetric strain field for the experiments presented in Figure 5.28. It is already demonstrated that the bedding orientation affects the mechanical response of Tuffeau de Maastricht. Even though the peak stress and the length of the plateau depend on the bedding orientation, the failure mode and the inclination of the localized zones with respect to the major compressive stress, seem to be the same for the tests at 4 MPa confinement. No systematic difference can be observed in the localization pattern for samples perpendicular, oblique and parallel to the bedding plane. Two localized zones perpendicular to the major compressive stress, form at the bottom and the top of the samples and propagate towards the middle with increasing loading. This localized compaction covers the whole sample at the end of the plateau at different axial strain for each sample.

5.3 Uniaxial compression tests

In addition to the experiments discussed previously, a series of uniaxial compression tests are performed on Tuffeau de Maastricht in order to complete the mechanical response of the material under compression. The purpose of these tests is to determine the uniaxial compressive strength and to investigate the effect of the bedding on the elastic properties such as Young's modulus of the material. Details about the sample preparation and the experimental set-up are presented in subsection 3.5.1. The tests are carried out on samples cored perpendicular, oblique (45°), and parallel to the bedding plane. At least two experiments are carried out for each coring direction to assess the repeatability of the tests.

A thin latex membrane is wrapped around the specimens in order to keep them attached to the specimen holder. Two different techniques are followed to keep the samples in place: (i) the whole samples is jacketed in the membrane, and (ii) membrane is applied only to the two ends of the samples (subsection 3.5.1). Figure 5.31a shows a comparison of these two methods for samples cored perpendicular to the bedding. Despite the fact that the membrane used is thin (0.3 mm) and flexible, it affects the mechanical response of the material. The samples that are fully wrapped by the membrane (blue lines), present higher values for UCS (unconfined compressive strength) as well as for Young's modulus (E). Thereafter, the rest of the tests are performed with the minimum possible membrane around the samples.

Figure 5.31 presents the uniaxial compression tests for the three coring directions. The curves after an initial non-linear behavior, exhibit a linear stress-strain relationship up to about 90% of peak stress. Beyond 90% of the unconfined compression strength, a non linear relationship between stress and strain occurs. At peak stress, the samples fail by brittle faulting. Visual inspection of the samples cored perpendicular reveals that the failure mode of these samples is axial splitting with a small angle between the fracture and the main stress direction (Figure 5.32). Figure 5.31d summarizes the mechanical response of the samples cored perpendicular (black color), oblique (blue color) and parallel (red color) to the bedding plane. It is obvious that the perpendicular samples show the highest value for UCS as well as for the Young's modulus.

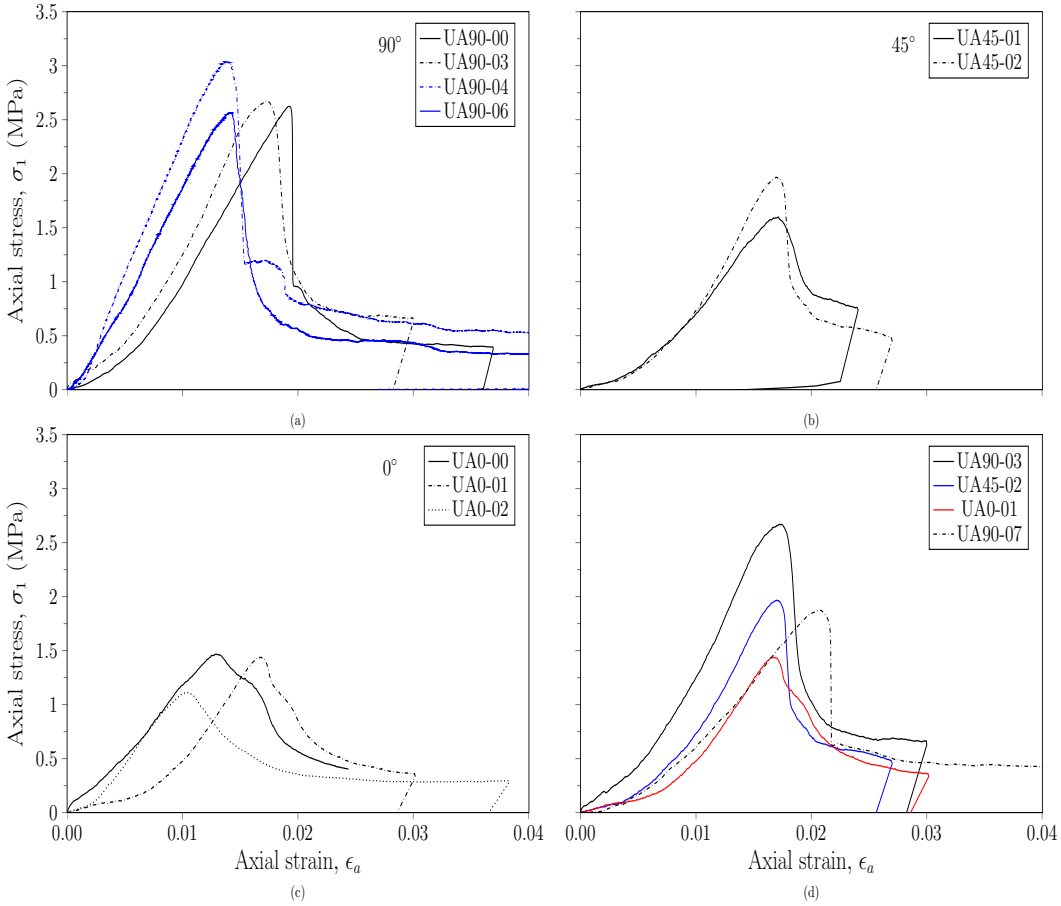

Figure 5.31: Mechanical data of samples tested under uniaxial compression conditions. (a) A comparison of samples that are cored perpendicular to the bedding. The blue color corresponds to the samples that are fully wrapped by a membrane, while in black are samples with almost no membrane. Samples that are cored (b) oblique (45°), and (c) parallel to the bedding plane. (d) The mechanical response of a wet sample (dashed line) is compared with dry samples cored at three different orientations.

In particular, these values are almost twice as high as the ones for the parallel samples. It is also observed that the post-peak behavior is less abrupt for the sample cored at 0°. In Figure 5.31d, an additional experiment on a wet sample cored perpendicular to the bedding is presented (dashed line). The comparison reveals a significant weakening effect of water on Tuffeau de Maastricht. Table 5.5 summarized the mechanical response of the material under uniaxial compression conditions.

Figure 5.33a shows the obtained uniaxial compressive strength values as a function of orientation angle. This plot shows that Tuffeau de Maastricht presents pronounced anisotropy in strength. Similarly to the triaxial compression tests, the maximum, intermediate and minimum values of UCS are associated with the perpendicular, intermediate and parallel samples, respectively. Young's modulus are estimated from the stress-strain data for each test over the linear part of the unconfined compression strength. These values are shown as a function of bedding orientation in Figure 5.33b. In general, the moduli vary between 0.1 and 0.25 GPa. Even though there is a scatter between the values, there is a trend to decrease with decreasing θ (from 90 to 0°). However, this trend is less pronounced for the ratio between the UCS and the Young's modulus (UCS/E).

(a) **(b)** **(c)**

Figure 5.32: Axial splitting of samples that are tested under uniaxial compression conditions. (a) and (b) are photos of dry samples while (c) presents a wet sample.

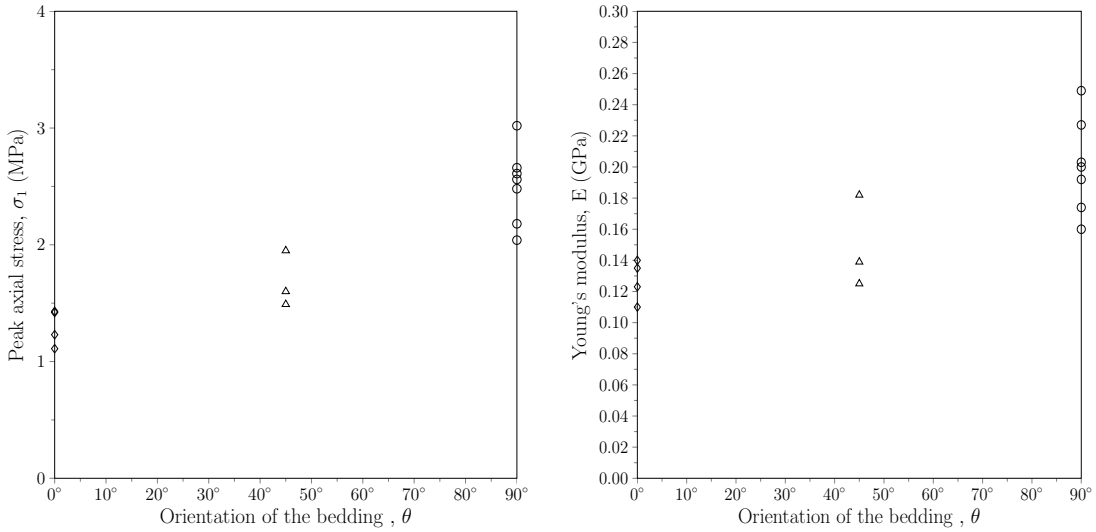

(a) **(b)**

Figure 5.33: (a) Unconfined Compressive Strength (UCS), and (b) Young's modulus as a function of bedding plane orientation for uniaxial compression tests.

5.4 Summary

In this chapter the mechanical behavior of Tuffeau de Maastricht is presented. An extensive experimental campaign is performed to characterize the inelastic behavior and failure mode from brittle to ductile transition in high porosity rocks. Full-filed measurement techniques are also conducted to investigate the onset and evolution of localized compaction during loading. To this end, the response of the material has been investigated under three different stress paths.

The isotropic compression tests show a distinct inflection point at a given pressure called the critical pressure P^*. For pressures beyond the critical pressure sudden volumetric collapse occurs associated with pore collapse and cement breakage. Local porosity variations enhance the macroscopic observations showing significant porosity reduction that propagates from the boundaries to the middle of the sample.

The triaxial compression tests at confining pressures ranging from 1 to 5 MPa reveal two

Table 5.5: Summary of mechanical data from uniaxial compression tests for samples that cored perpendicular, oblique (45°) and parallel to the bedding plane.

Test	Porosity (%)	UCS (MPa)	E (GPa)	UCS/E	Details
Specimens cored at 90° to the bedding					
UA90-00	-	2.6	0.17	0.015	-
UA90-01	-	2.2	0.16	0.0137	-
UA90-02	50.6	2.5	0.19	0.0131	-
UA90-03	50	2.7	0.2	0.0135	-
UA90-04	-	3.2	0.25	0.0128	Membrane
UA90-05	-	2.1	0.23	0.009	Membrane
UA90-06	-	2.6	0.2	0.013	Membrane
UA90-07	-	1.9	0.12	0.0158	Wet sample
Specimens cored at 45° to the bedding					
UA45-00	50.8	1.5	0.14	0.0107	-
UA45-01	50.3	1.6	0.13	0.0123	-
UA45-02	51.3	1.9	0.18	0.0105	-
Specimens cored at 0° to the bedding					
UA0-00	50.8	1.4	0.12	0.0116	-
UA0-01	50.7	1.4	0.135	0.0103	-
UA0-02	-	1.1	0.14	0.0078	-
UA0-03	-	1.2	0.11	0.0109	-

failure modes developed in Tuffeau de Maastricht. Shear enhanced compactive bands observed at low confining pressures, while compaction bands that are formed perpendicular to the major principal stress are detected at higher confinement. The additional triaxial tests up to very high axial strain combined with advanced image analysis are used to assess the micromechanisms associated with the destructuration of the samples during the the plateau of deviator stress. This result corroborates with the mechanical response of the artificially destructurated material. Thus, at the end of this phase (plateau), the entire specimen has been compressed and converted into a new dense sand-like sample with homogenous distribution of porosity.

The experimental results of Tuffeau de Maastricht on samples cored at different orientations, underline that the mechanical response of the material is strongly dependent on the loading direction with respect to the bedding plane. Similarly to prior studies on porous sandstones, the maximum and minimum peak stresses are observed in the perpendicular and parallel to the bedding samples, respectively. Even though the peak stress depends on the bedding bedding orientation, digital image correlation shown that the failure mode and the inclination of the localized zones seem to be the same with respect to the major compressive stress.

Chapter 6

Simulation of localized compaction in Tuffeau de Maastricht based on evidence from X-ray tomography

One of the most remarkable features of porous rocks is their marked pressure-sensitivity, which allows them to transition from a brittle-like response characterized by fracture and dilative slip to a plastic behavior displaying pore collapse, macroscopic hardening, and homogeneous deformation (Wong and Baud, 2012). Porous rocks are known to exhibit elusive forms of localized deformation referred to as compaction bands (Olsson, 1999). Despite being a form of strain localization which bears similarity with shear bands, compaction localization takes place at stress levels typical of cap plasticity and is characterized by the appearance of multiple bands which may spread across the volume until covering the whole sample (Olsson and Holcomb, 2000, Olsson, 2001). As a result, deformation in the compaction banding regime involves considerable porosity loss and may lead to a deviatoric stress plateau during the propagation of compaction fronts, followed by stages of re-hardening (Wong *et al.*, 1997).

To understand the mechanisms underlying this variety of behaviors, extensive suites of deformation tests are conducted on porous rock samples (Baud *et al.*, 2004, Wong and Baud, 2012). In most cases, such experiments result in the quantification of elastic (e.g., bulk and shear stiffness) and plastic (e.g., yield surface, plastic flow direction, hardening modulus) properties. In this context, the majority of parameter calibration efforts takes a macroscopic stance in modeling the sample behavior, often treating the measurements as if they corresponded to a homogeneous response reflective of the intrinsic material behavior. Although convenient, such methodology fails to take into account strain localization processes (Issen and Rudnicki, 2000, 2001), thus ignoring that macroscopic measurements reflect in fact a structural response of the sample rather than a true material response. In fact, while the strain localization theory can be an asset to infer the connection between material properties and expected deformation patterns (e.g., the stress state at the onset of strain localization and the inclination of the ensuing bands), most existing studies tend to ignore the representation of both pre- and post-localization deformations, resulting in a disconnection between the properties that reflect the onset of deformation bands and those that are associated with the inelastic deformation during the stages of band propagation. Efforts in this direction have been made by several authors by using a range of modeling platforms, such

as elastoplasticity (Grueschow and Rudnicki, 2005), Breakage Mechanics (Das *et al.*, 2011), or continuum thermodynamics (Nguyen *et al.*, 2016). To address this problem, this chapter illustrates numerical analysis based on an elastoplastic constitutive law for porous rocks (Lagioia and Nova, 1995, Nova *et al.*, 2003). In analogy with recent studies for the same class of geomaterials (Buscarnera and Laverack, 2014, Das and Buscarnera, 2014, Marinelli and Buscarnera, 2015), it is shown that deformation response and strain localization patterns can be used synergistically to constrain the model parameters and achieve a satisfactory representation of most behavioral properties, including the onset and propagation of compaction zones. At variance with previous analysis, the simulations focus on a rich dataset for Tuffeau de Maastricht presented in chapter 5. Such detailed information is used for model calibration purposes, by identifying a set of model parameters able to capture satisfactorily the pressure dependence of the inelasticity of Tuffeau de Maastricht through Finite Element (FE) simulations.

6.1 Constitutive model

Reproducing the mechanics of high-porosity rocks often requires sophisticated constitutive laws, in that geomaterials display the tendency to dilate or contract depending on the loading path (Menéndez *et al.*, 1996, Wong *et al.*, 1997, Wong and Baud, 2012). This rich variety of deformation responses derives from the competition between numerous inelastic processes that lead to material softening or hardening, depending on the dominant mechanism (Bésuelle *et al.*, 2000, Bésuelle and Rudnicki, 2004).

Typical frameworks used to replicate the deformation behavior of porous rocks include cap plasticity (DiMaggio and Sandler, 1971,Fossum, Fredrich, *et al.*, 2000, Rudnicki, 2004, Grueschow and Rudnicki, 2005) and critical state plasticity (Wood, 1990, Carroll, 1991, Cuss *et al.*, 2003). This class of models, however, often lacked the ability to simultaneously inspect the deformation response and the formation of compaction bands (Issen and Rudnicki, 2000, Issen, 2002). In this context, improvements are proposed by Challa and Issen (Challa and Issen, 2004) who used multiple yield surfaces to capture this variability. The approach is proved effective in capturing the onset and inclination of the compaction band, yet clear evidences on rheological characteristics have never been demonstrated.

The strain-hardening plasticity model adopted in the current study aims to accurately reproduce pre- and post-localization deformations, while enabling the representation of pressure-dependent strain localization patterns. The model is developed in a series of contributions by Nova and coworkers (Gens and Nova, 1993, Lagioia and Nova, 1995, Nova *et al.*, 2003), and is selected by virtue of its proven success in capturing the inception and development of plastic compaction under different stress paths and for a variety of boundary conditions (Arroyo *et al.*, 2005, Buscarnera and Laverack, 2014, Das and Buscarnera, 2014).

6.1.1 Model Formulation

The selected constitutive law is developed in the framework of elastoplasticity and is inspired by the classical theory of critical state plasticity (Wood, 1990). It adopts a single yield surface evolving homothetically with plastic strains. The expression proposed by Lagioia et al. 1996

is here used to describe both yield surface and plastic potential, and is characterized by the following expression:

$$\left.\begin{matrix} f \\ g \end{matrix}\right\} = A_h^{K_{1h}/C_h} * B_h^{-K_{2h}/C_h} * P^\star - P_c^\star = 0 \tag{6.1a}$$

$$K_{1h/2h} = \frac{\mu_h\,(1-\alpha_h)}{2\,(1-\mu_h)}\left(1 \pm \sqrt{1 - \frac{4\alpha_h\,(1-\mu_h)}{\mu_h\,(1-\alpha_h)^2}}\right) \tag{6.1b}$$

$$A_h = 1 + \frac{\eta^\star}{K_{1h}M_h} \tag{6.1c}$$

$$B_h = 1 + \frac{\eta^\star}{K_{2h}M_h} \tag{6.1d}$$

$$C_h = (1-\mu_h)(K_{1h} - K_{2h}) \tag{6.1e}$$

$$\tag{6.1f}$$

Where p and q are the mean and deviator stresses, respectively, $\eta^\star$ is the corresponding stress ratio, defined as follows:

$$p = \frac{1}{3}\sigma_{ij}\delta_{ij} \quad q = \sqrt{\frac{3}{2}s_{ij}s_{ij}} \quad \eta^\star = \frac{q}{p+p_t} \tag{6.2}$$

in which $s_{ij} = \sigma_{ij} - p\delta_{ij}$, δ_{ij} is Kronecker delta. Under axisymmetric stress conditions, p and q can be specified as:

$$p = \frac{\sigma_1 + 2\sigma_3}{3} \quad q = \sigma_1 - \sigma_3 \tag{6.3}$$

where σ_1 and σ_3 are the maximum and minimal principal stress, respectively. The yield surface, $\mathfrak{f}$, intersects the hydrostatic compression axis at, P_c, which represents the yielding stress under pure compression. This parameter is defined by an additive combination of the variables, P_s and P_m, representing the effect of porosity hardening and interparticle bonding, respectively. The hydrostatic yield threshold in the tensile stress regime is defined by P_t, and is assumed to be a proportion of P_m (*i.e.*, $P_t = kP_m$). The sum of these variables defines $P_c^\star$ ($P_c^\star = P_s + P_m + P_t$), which is the total extent of the yield surface along the hydrostatic axis. The geometry of the surface is controlled by a set of shape parameters, M_h, μ_h, and α_h, which provide considerable flexibility to fit experimental data. While the same expression is used to characterize the plastic potential, g, non-associativity is incorporated in the model by means of distinct values of shape parameters (*i.e.*, the subscript h in the symbols above makes reference to either yield surface ($h = f$) or plastic potential ($h = g$)). Plastic processes in porous rocks involve simultaneous pore-collapse and solid phase destructuration (*i.e.*, cement softening and grain breakage). Plastic volumetric strains are here considered responsible for the former, whereas the latter derives from a combination of volumetric and deviator strain. These mechanisms are introduced through hardening rules defined for both P_s and P_m, as follows:

$$\dot{P}_s = \frac{P_s}{B_p}\dot{\epsilon}_v^p \tag{6.4}$$

$$\dot{P}_m = -\rho_m P_m(|\dot{\epsilon}_v^p| + \xi_m\dot{\epsilon}_s^p) \tag{6.5}$$

Where B_p, ρ_m and ξ_m are constitutive parameters. These rules are formulated such that P_s can exhibit hardening and softening depending on the sign of the volumetric strain, whereas P_m contributes only to softening effects. The rationale for this choice derives from the evidence that geomaterials such as lightly cemented porous rocks undergo loss of structure upon straining, which typically manifests in the form of macroscopic strain-softening (Leroueil and Vaughan, 1990). The interplay between these competing mechanisms leads to a homothetic contraction/-expansion of the yield surface, capturing subsequently the post-yielding stress-strain behavior. The plastic strains are obtained by substituting the constitutive functions in the plastic flow rule, as follows:

$$\dot{\epsilon}^p_{ij} = \Lambda \frac{\partial g}{\partial \sigma_{ij}} \tag{6.6}$$

in which Λ is a non-negative multiplier. In this model, for sake of simplicity, linear elasticity is incorporated through the following relation:

$$\sigma_{ij} = D_{ijkl}\epsilon^e_{kl} \tag{6.7}$$

where σ_{ij} is the Cauchy stress tensor, ϵ^e_{kl} is the elastic strain tensor, and D_{ijkl} is the linear elastic tangential stiffness tensor. This tensor can be defined in terms of bulk, K_o, and shear, G_o, moduli, as $D_{ijkl} = G(\delta_{ik}\delta_{jl}) + (K - 2G/3)\delta_{ij}\delta kl$.

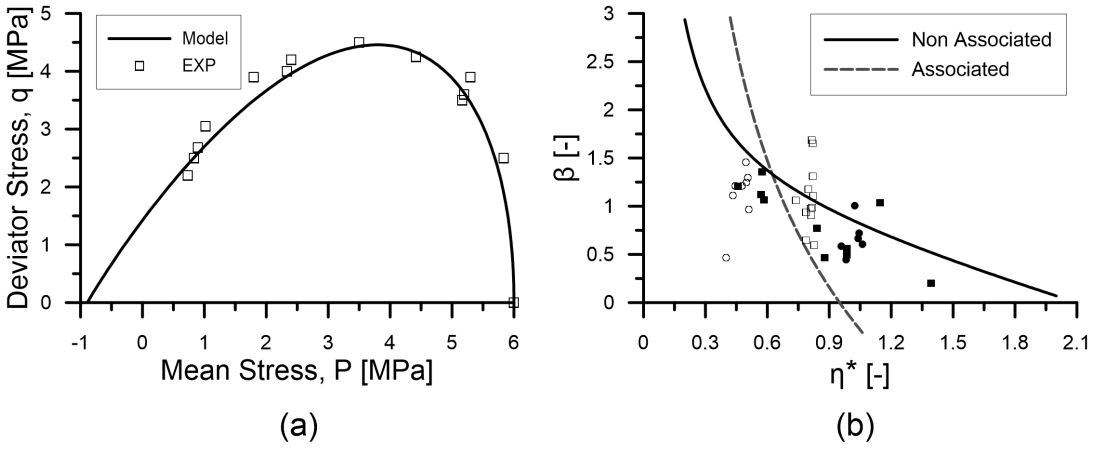

Figure 6.1: Calibration of the shape-parameters of the yield surface and plastic potential from (a) yield points and (b) relation between dilatancy and stress-ratio obtained from triaxial compression data.

6.1.2 Model Calibration

The selected constitutive model is calibrated by following the procedure proposed by Buscarnera and coworkers (Das and Buscarnera, 2014, Marinelli and Buscarnera, 2015). A preliminary calibration is first conducted on the grounds of the macroscopic material rheology emerging from different stress probes. The calibration is then enhanced on the basis of strain localization analysis guided by the bifurcation theory (Rudnicki and Rice, 1975). The measurements presented in Figure 5.5 and Figure 5.10, provide considerable insight for a preliminary model calibration. The wide range of confinement pressures covered by the triaxial tests, in fact, readily allows for the determination of the yield surface. The material response in $\epsilon_a - q$ space, see Figure 6.1a, is inspected to determine the yield threshold, which is then plotted also in the $p-q$ stress space. By

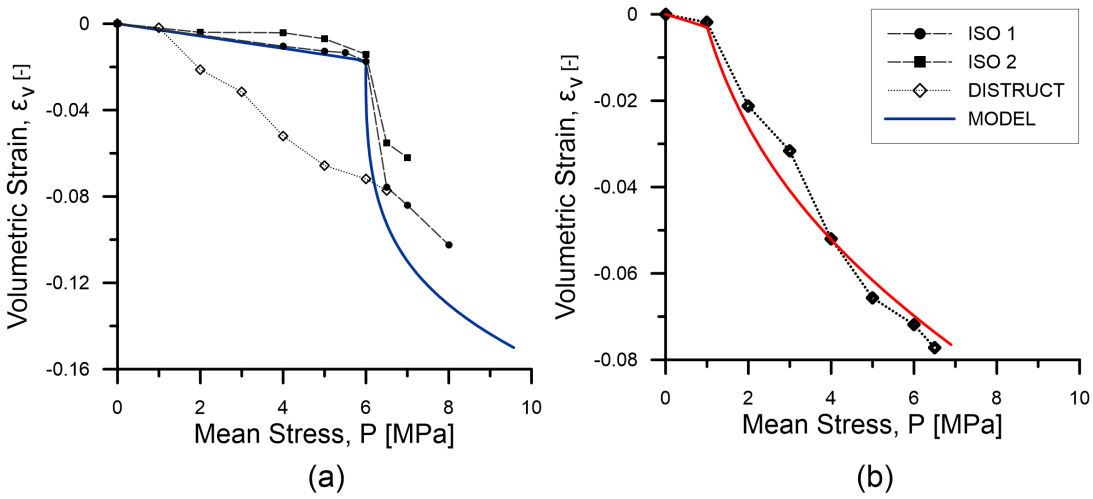

Figure 6.2: Isotropic compression tests used to calibrate the compressibility parameters (i.e., B_p, ρ_m, and the ratio P_{so}/P_{mo}): (a) is the intact sample and (b) the destructured material.

adjusting the shape parameters, M_f, μ_f, and α_f, the mathematical expression of yield surface is defined, as shown in Figure 6.1a. The parameters of the plastic potential, M_g, μ_g, and α_g, can instead be defined on the basis of the underlying stress-dilatancy relationship, which in this model is given as follows:

$$d = \frac{\dot{\epsilon}_v^p}{\dot{\epsilon}_d^p} = \frac{\partial g/\partial p}{\partial g/\partial q} = \mu_g(M_g - \eta^\star)(\frac{\alpha_g M_g}{\eta^\star} + 1) \tag{6.8}$$

This function defines the ratio of volumetric and deviatoric plastic strains computed for a given imposed stress level (e.g., in correspondence of the plastic flow plateau). These ratios can be reported in the $\eta^\star - d$ space, as shown in Figure 6.1b, and are used to calibrate the shape parameters. Although this procedure relies on global measurements taken in the post-yielding regime (*i.e.*, where the specimen exhibits a structural response with heterogeneous deformation patterns), since they are expressed in the form of a normalized strain ratio they can be regarded as representative of the material behavior inside the active zone, thus providing a first-order insight on the expected plastic flow characteristics, which will be later further assessed through full-field simulations. The hydrostatic compression behavior is used to calibrate most of the model parameters controlling the hardening/softening response, namely, ρ_m, B_p, and the initial values of the internal variables, P_{so} and P_{mo}. The yielding stress upon hydrostatic loading, $P_{co} = P_{so} + P_{mo}$, can be assumed to coincide with the stress at which the hydrostatic compressibility sharply increases. The ratio P_{so}/P_{mo} governs the rate of destructuration occurs upon volumetric loading. This rate appears in the form of a magnified plastic volumetric deformation taking place upon yielding. On the other hand, ρ_m controls the amount of softening during this stage of enhanced plastic deformation. B_p, in turn, defines the rate of plastic hardening in the post-plateau region, where inter-particle bonds are fully destructured. As a result, this constant regulates the porosity hardening emerging upon volumetric deformation in a completely reconstituted material. The experimental dataset obtained from hydrostatic compression on destructured material is used to calibrate B_p. The calibration of B_p is reported in Figure 6.2b, while the overall hydrostatic compression behaviour reproduced by the model is depicted in Figure 6.2a. It can be noted that the model overestimates the compressiblilty in the plastic regime. In fact, as it will be shown

in the subsequent sections, higher volumetric softening is necessary to augment the porosity loss during shearing and match the elongation of the deviatoric stress plateau exhibited by Tuffeau de Maastricht during triaxial compression tests. As a consequence, the final set of hydrostatic compression parameters is a compromise aimed at obtaining a reasonable match with the measured hydrostatic response, while prioritizing the model performance in the compaction localization regime.

6.1.3 Strain localization analysis

The data used in the calibration above are derived from global measurements of specimens deformed in localization regime. During this phase, strain localization promotes a transition from homogeneous to heterogeneous responses. Measurements performed in the localization regime might have considerable deviations from the material point behavior, thus not being able to solely provide reliable information for model calibration. To overcome this obstacle, enhancements are possible by using evidence about the onset and pressure-dependence of strain localization modes, as recently proposed by Marinelli and Buscarnera, (2015). This procedure is based on the modes of strain localization predicted by the model for a given set of parameters, which can be optimized in order to match the evidence of pressure-dependent compaction banding. With reference to the model used in this work, M_g and ξ_m are used for such optimization. By controlling these parameters, the material rheology, as well as the strain localization characteristics, can be successfully captured. For this purpose, the strain localization theory (Rudnicki and Rice, 1975) represents the main reference to identify the conditions at which bifurcated solutions emerge leading to narrow deformation bands. Chambon, (1986) combined this criterion with the elastoplasticity theory, suggesting that the bifurcation criterion can be written as follows:

$$A(\theta) = det[n_j(\theta)(C^{ep}_{ijkl})n_l(\theta)] \leq 0 \tag{6.9}$$

Where θ is the angle of unit vector, n_j, normal to the band, and C^{ep}_{jjkl} is the elastoplastic constitutive tensor. The expression above enables the computation of a "*localization profile*", *i.e.*, a representation of the determinant of the acoustic tensor $A(\theta)$ as a function of the band angle θ for a given stress state. An illustration of this analysis is reported in Figure 6.3, where the localization profile is computed for triaxial stress paths at varying confinements. This plot depicts the pressure dependence of the strain localization potential of the selected material. In particular, a transition from the development of conjugate shear-enhanced compaction bands at lower confinements (*i.e.*, state I, II, III) to the potential formation of pure compaction bands at high pressure (*i.e.*, state IV) is readily apparent. Locating these results in the stress space provides information about the strain localization modes predicted by the model for varying stress conditions (see upper-left chart in Figure 6.3). The transition between these two end-members takes place smoothly, thus providing opportunities to calibrate the relevant model parameters by adjusting their values to cover the entire range of expected strain localization. As shown by Marinelli and Buscarnera, (2015), M_g and ξ_m play a significant role on the prediction of strain localizations. Thus, their calibration can be further elaborated based on information from tomographic imaging. In particular, full-field measurements enabled the distinction between stress states resulting into pure compaction bands from those associated with shear-enhanced compaction bands. As a result, the optimization of the model parameters in light of these findings

resulted into model computations able to reflect the evidence (see data points in Figure 6.3a).

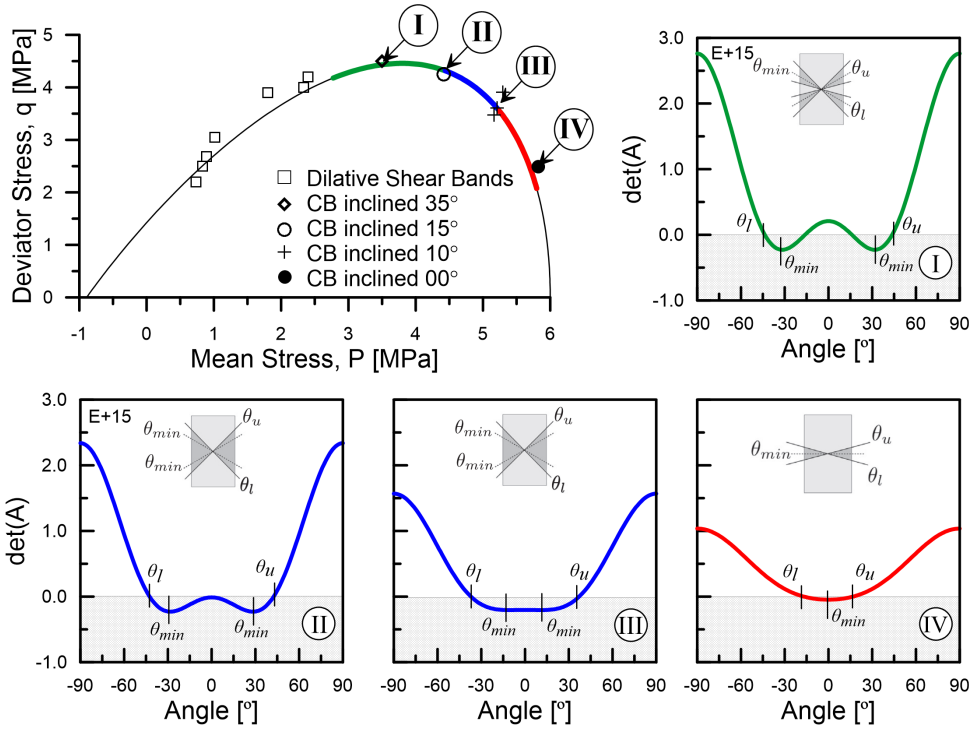

Figure 6.3: Strain localization characteristics of Tuffeau de Maastricht predicted with the selected constitutive model. The localization domain in stress space is superposed to the yield surface (thick line) and the associated inclination of the deformation band predicted by a bifurcation analysis. The theory defines different modes of strain localization. Zone 1 (green line), implies two distinct cones of localization, each with a non-zero preferable angle of localization. Zone 2 (blue line), involves a single cone of localization potential with two non-zero preferential angles of strain localization. Both zones represent shear-enhanced compaction bands. By contrast, Zone 3 (red line) involves a single cone of expected strain localization with a unique angle of preferential band formation which is perpendicular to the maximum principal stress (pure compaction band). The localization profiles at the points I, II, III, and IV are presented with the same color convention. This points represent the intersection point of triaxial paths under 2.0, 3.0, 4.0, and 5.0 MPa confinement, thus providing information about the predicted localization model.

6.1.4 Upper and Lower bounds calibration

Based on this calibration, Figure 6.4 illustrates a simulation of triaxial test at a confinement pressure (4.0 MPa) displaying transition from localized to homogeneous compaction. The same figure reports similar computations based on a different calibration strategy discussed in (Papazoglou *et al.*, 2017). These two sets of computations are herein referred to as a *"lower bound"* and an *"upper bound"*, respectively. While the upper bound calibration focuses on the representation of the post-localization re-hardening emerging from the tests conducted at higher confinements (*e.g.*, 4.0 MPa), the lower bound calibration is instead aimed at capturing the localization potential and the rate of compaction band propagation over a wider range of confinements (*i.e.*, from 2.0 to 5.0 MPa). Achieving this goal, however, has required the use of marked strain softening to prevent early delocalization (see at this reference the full-field numerical simulations discussed in the next sections). This trade off between different macroscopic signatures of the Tuffeau de Maastricht behavior implied a remarkable drop in resistance along the post-yielding response for the lower bound calibration. Although a compromise between these end members of simulated

Table 6.1: Constitutive parameters and internal variables for Tuffeau de Maastricht, including the upper and the lower bounds.

	Definition	Lower Bound	Upper Bound
K [MPa]	Bulk modulus	350	350
G [MPa]	Shear modulus	78	80
ρ_m	Parameter governing volumetric destructuration	0.45	0.7
ξ_m	Parameter governing deviatoric destructuration	12.5	2
B_p	Isotropic plastic compressibility	0.03	0.034
μ_f	Shape parameter of the yield surface	1.01	1.01
α_f	Shape parameter of the yield surface	2.0	2.0
M_f	Shape parameter of the yield surface	0.95	0.88
μ_g	Shape parameter of the plastic potential	0.6	0.65
α_g	Shape parameter of the plastic potential	0.15	0.15
M_g	Shape parameter of the plastic potential	2.1	2.1
κ	Expansion of the yield surface in the tensile stress domain	0.15	0.20
P_{so} [MPa]	Initial size of the elastic domain (cohesionless medium)	0.06	0.09
P_{mo} [MPa]	Lithification-induced expansion of the initial elastic domain	5.94	5.91

behavior could in principle be achieved by further adjusting the competition between P_s and P_m embedded in the hardening rule in light of micromechanical considerations (Barthélémy and Dormieux, 2004), this task is considered beyond the scope of this work. As a result, unless otherwise stated, in the following sections the lower bound calibration will be used to simulate numerically the propagation of localized compaction zones.

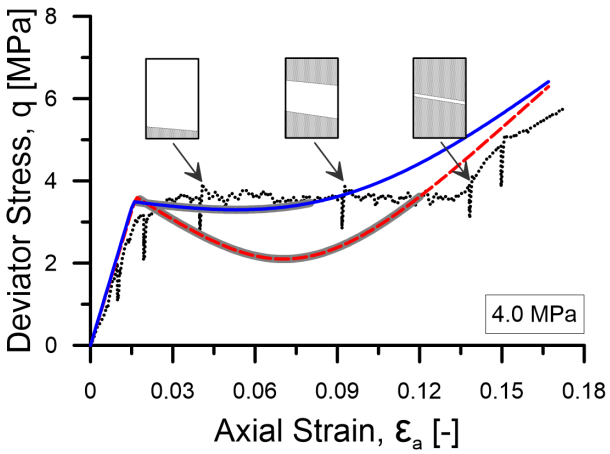

Figure 6.4: Comparison of material point analysis conduced on the basis of two different sets of model parameters (upper bound and lower bound). The upper bound calibration matches the post-yielding stress plateau and the re-hardening process, while the lower bound computations exploit the large drop in the post-yielding resistance to ensure that the deformation regime of active localized compaction matches the measurements (*i.e.*, the strain level at which the stress goes back to pre-yielding values corresponds to the extent of the strain plateau). The measured zone of compaction propagation is depicted on the measured response.

6.2 Full-Field Analysis

The use of conventional continuum models in full-field simulations affected by strain localization are typically hampered by the lack of objective results and pathological mesh dependence. To address this problem, continuum models can be enriched with an internal length scale reflecting the material microstructure (Needleman, 1988, Schreyer and Neilsen, 1996). Usual choices made for this purpose include second gradient continua (De Borst and Muhlhaus, 1992), nonlocal models (Bazant and Jirasek, 2002, Liu *et al.*, 2016), and rate-dependent models (Perzyna, 1966).

6.2.1 Rate-dependent regularization

A Perzyna-type generalization (Perzyna, 1966) of the selected constitutive law is used in this study to suppress mesh-dependent solutions in Finite Element computations. This approach is selected by virtue of its simplicity, ease of implementation and computational efficiency (Wang *et al.*, 1997). Furthermore, it is successfully used for a variety of materials (Das *et al.*, 2013, Etse and Willam, 1999, Carosio *et al.*, 2000, Heeres *et al.*, 2002). In overstress viscoplastic models, the material viscosity is introduced through a modification of the flow rule, as follows:

$$\dot{\epsilon}^p_{ij} = \frac{\langle \phi(\mathfrak{f}) \rangle}{\omega} \frac{\partial \mathfrak{g}}{\partial \sigma_{ij}}, \quad \phi(\mathfrak{f}) = \frac{\mathfrak{f}}{P_{co}} \tag{6.10}$$

where $\langle \bullet \rangle$ indicate the McCauley brackets, ϕ is the viscous nucleus which depends on the current value of the yield surface, $\mathfrak{f}$, and ω is a viscosity parameter.

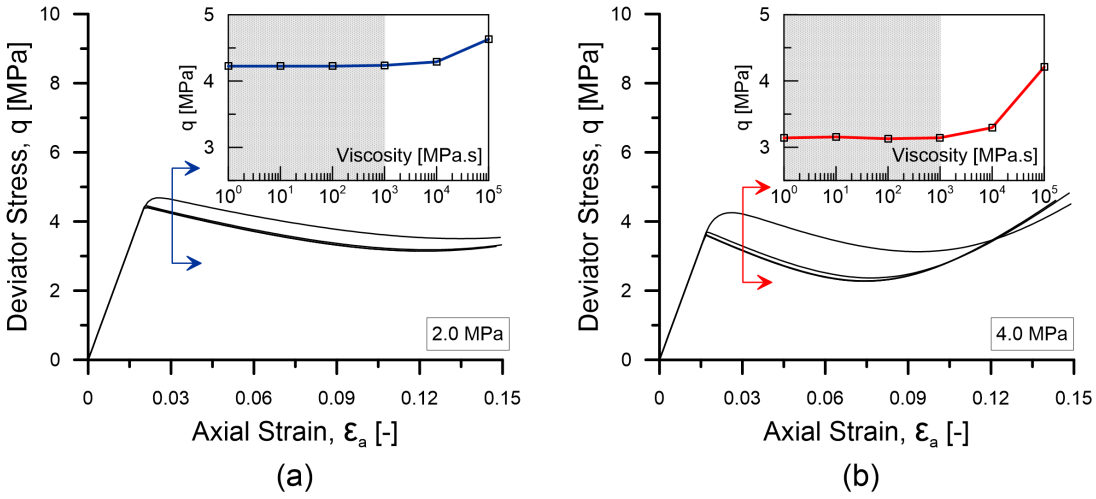

Figure 6.5: Sensitivity analysis of viscosity effects on the material point response at different confinements (a) 2.0 MPa and (b) 4.0 MPa. The inset shows the value of deviatoric stress computed for each value of viscosity at a fixed strain level (3.0%). Simulations conducted with a strain rate of $\dot{\epsilon}_a = d\epsilon_a/dt \leq 1.0E-5\ sec^{-1}$, and viscosity varying from 1.0 to $10.0E+5\ MPaS$.

In the laboratory, Tuffeau de Maastricht was tested under quasi-static conditions by imposing a nominal axial strain rate $d\epsilon_a/dt \leq 1.0E-5\ MPa.s$, in which dt is the time increment during which a loading step is imposed. The use of viscoplasticity for regularization purposes is achieved by pursuing a quasi-rate-independent behavior, *i.e.*, by introducing minimal deviations between the regularized material behavior and the underlying rate-independent calibration discussed in the previous section. The range of viscosity that guarantees quasi-rate-independent response is identified through a sensitivity analysis of the model performance during triaxial compression tests at two confinements ($2.0MPa$ and $4.0MPa$), through which the viscosity is varied from $1.0E-2$ to $1.0E+5\ MPaS$. The results are reported in Figure 6.5 a and b, respectively. The inset shows the variation of the computed deviatoric stress at $\epsilon_a = 0.03$ as a function of viscosity. It can be readily seen that in both cases a viscosity threshold of 1000 $MPaS$ can be identified (shaded area within the inset) below which the model displays a stable stress response and therefore a limited role of the rate-dependent effects introduced by the viscoplastic extension.

6.2.2 Triaxial test simulations

The proposed calibration is validated through numerical analysis of the response of Tuffeau de Maastricht samples treated as boundary value problems. The assessment of the performance of the simulations is focused on various features of the macroscopic response, such as global deformability in the post-yielding stage (*i.e.*, elongation of the plateau), as well as the geometrical characteristics of the persistent bands, the spatial evolution of the zone of compaction and its dependency on the confinement pressure.

A finite element model of cylindrical specimens with aspect ratio 1 : 2 is considered to reproduce a laboratory specimen of diameter 11 mm and height 22 mm. The simulated specimens are discretized into more than 75,000 4-node linear tetrahedral ($C4D4$) elements. The initial confinement is applied through an internal stress state in equilibrium with the external pressure applied at all boundaries. Essential boundary conditions are then introduced in the form of fixed vertical displacements on the bottom of the specimen and single fixed node at the center of the base preventing horizontal movement. Shearing is finally applied by moving downwards a roller support located at the upper boundary. An illustration of the specimen and its boundary conditions is given in Figure 6.6a.

A homogeneous distribution of material properties is assigned throughout the simulated mesh, in accordance with the model calibration discussed in the previous sections. To trigger strain localization, however, a weak element with 2% reduced yielding strength (i.e., lower P_{co}) has been introduced at the middle of the specimen, as shown in Figure 6.6b.

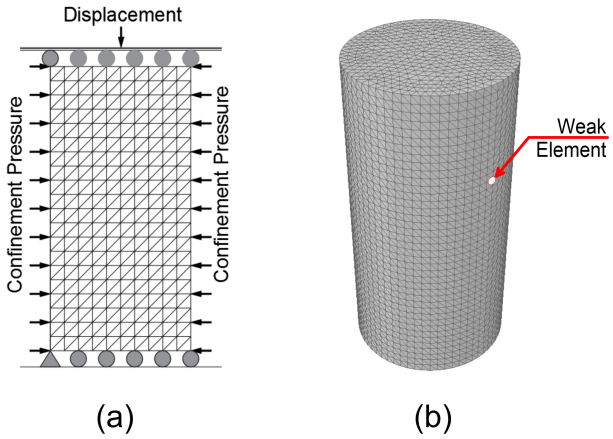

Figure 6.6: Illustration of the finite element model used for triaxial test simulations. (a) Specimen section showing the finite element mesh and the boundary conditions; (b) Location of the weak element in a 3D cylindrical sample.

An essential step before proceeding with the numerical analysis is to set the parameters that will control the computed thickness of the deformation bands and identify an optimal finite element mesh. Although the precise determination of the band thickness heavily depends on the frequency with which CT scans are conducted, thus representing a major challenge, an indirect estimate of the thickness of successively formed compaction zones can be gained from the inspection of DIC measurements associated with relatively small strain increments. From a modeling standpoint, the thickness of the resulting compaction zone will be controlled by the viscosity parameter, which is here constrained by the upper bound of quasi-rate-independent threshold (*i.e.*, $\omega = 1000\ MPaS$) identified in the previous section. The value of ω is therefore

defined with the goal to match the size of the compacted zone detected by the kinematic field upon the application of 2% global deformation (Figure 6.7a). In this context, Figure 6.7b shows the thickness of the computed compaction zone for the same value of viscosity for three different meshes. In this figure, it can be seen that the thickness of the band becomes almost unaffected between the second and the third mesh refitment. Figure 6.7c reports the computed responses up to 5% nominal axial strain (at which the strain field in (b) is illustrated) where it can be readily seen that the computed response becomes mesh-independent for the last two simulations which provide nearly identical results. The good agreement between the simulations confirms the effectiveness of a viscosity factor of $\omega = 650$ MPaS in replicating the measurements of spatially propagating compaction, as well as in suppressing mesh-dependent solutions.

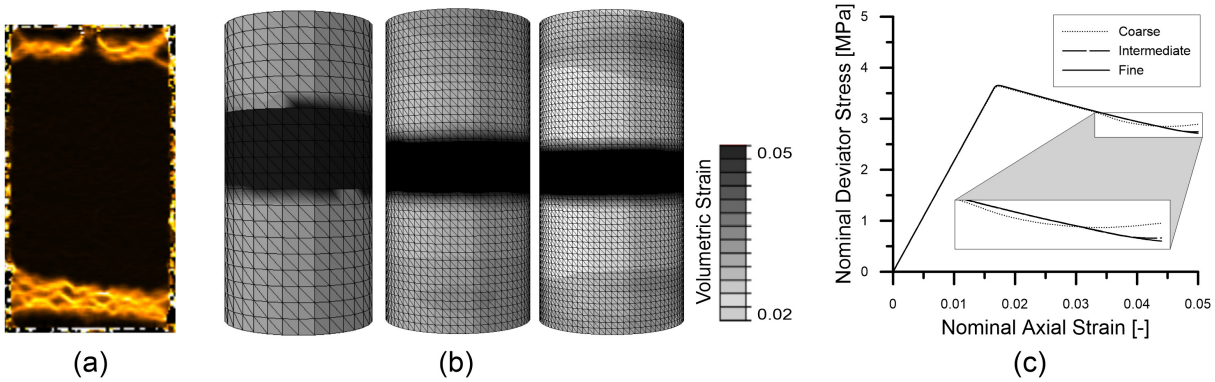

Figure 6.7: Assessment of mesh-sensitivity and thickness of the simulated compaction zone. (a) A vertical slice of 3D volumetric strain field obtained through DIC for incremental loading of 2% axial strain in a triaxial compression test performed at 4 MPa confinement. (b) the volumetric strain field resulting from finite element analysis with different mesh size, namely with more than 12000, 75,000, and 170000-element mesh. The comparison shows that the FE simulations capture satisfactorily the thickness of the compaction zone with $\omega = 650$ MPaS. Furthermore, they confirm the successful regularization of the computations by suppressing mesh dependence, as is readily apparent from the nearly identical global responses computed for the three simulations (c).

Based on this optimal value of viscosity, four simulations are run under confinement pressures of 2.0, 3.0, 4.0, and 5.0 MPa. The vertical displacement is applied at a rate of nominal axial strain $\dot{\epsilon}_a = 1.0E-5\ s^{-1}$, in agreement with the conditions imposed in the laboratory. The resulting simulated response is depicted in Figure 6.8, where the deviator stress is plotted as a function of the normalized vertical displacement. It can be seen that, in all cases, yielding is triggered at stress levels comparable to those observed in the experimental data. The post-yielding behavior tends to be characterized by more intense softening than the measurements, with a sharp drop of resistance shortly after yielding, after which a stress plateau is achieved for a sustained amount of axial deformation. This tendency is found to be more pronounced at the highest confinement level. As mentioned earlier, the lower bound calibration conducted in this work has focused on deformation characteristics, thus this tendency can be attributed to the exponential expression of the hardening laws, which requires a steeper loss of strength to guarantee a quantitatively accurate length of the deformation plateau. Indeed, despite their limitations, the choice of the hardening parameters can be considered satisfactory to capture the volume change taking place during plastic compaction (*i.e.*, something which is directly associated with the extension of the deformation plateau). The advantages of this choice become more readily apparent by comparing full-field simulations obtained with the upper bound and

the lower bound calibrations. This comparison is illustrated in Figure 6.9, with reference to the experiment conducted at 4.0 MPa confinement. It is readily apparent that, although the upper bound calibration satisfactory replicated the reaction force provided by the specimen, it severely underestimate the nominal axial deformation during which localized compaction is active (*i.e.*, the simulated response transitions to homogeneous compaction approximately half-way along the deviatoric stress plateau measured in the experiment). This shortcoming is not present in the lower bound calibration, which accurately predicts the transition from localized compaction to homogeneous re-hardening. It can be therefore concluded that the former set of parameters (upper bound calibration) is preferable if the focus is on force calculation, while the latter (lower bound calibration) is the optimal choice if the goal of the analysis is to replicate the propagation of compaction zones at similar deformation levels.

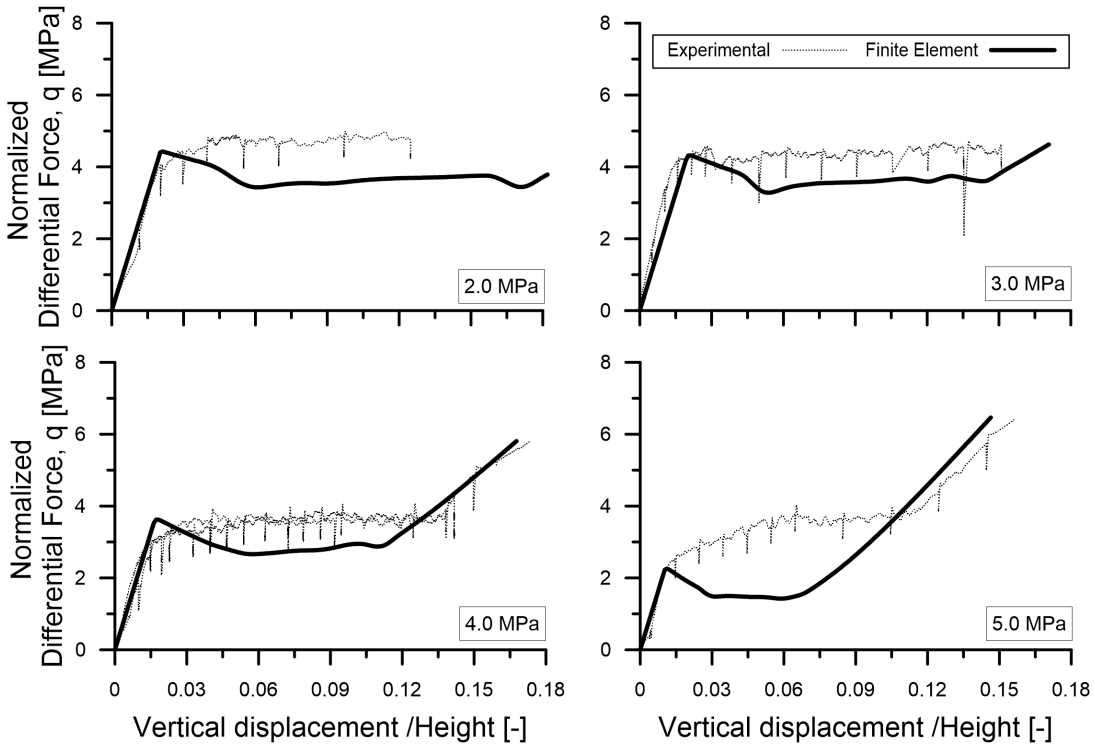

Figure 6.8: Comparison between finite element simulations and measurements of deformation tests on samples of Tuffeau de Maastricht at varying confinement pressures.

This point is further highlighted by Figure 6.10, which illustrates the evolution of the nominal volumetric strain versus the axial strain simulated at 4.0 MPa with the upper and the lower bound calibration. These computations are displayed along with the measured data. It can be readily seen that the FE analysis are capable of reproducing with a remarkable accuracy the overall deformation characteristics. The range of compaction propagation as a function of the axial strain is displayed through solid symbols, emphasizing again the satisfactory match with the measurements obtained with the lower bound calibration.

A closer inspection on the strain field predicted by the lower bound calibration is shown in Figure 6.11, revealing the development of deformation bands in all simulations. The figure displays the experimental counterpart obtained by DIC, which indicates good agreement in terms of measured and computed band angle. Specifically, simulations run for 2.0, 3.0, 4.0, and 5.0 MPa confinement displayed strain localization at band angles of 35°, 20°, 12°, and 0°, respectively,

which match satisfactorily the laboratory evidence (measured angles of 35°, 15°, 10°, and 0°, respectively). It is worth mentioning that these results are also consistent with the predicted angles obtained from the bifurcation analysis reported in Section 6.1.3, which predicted higher localization potential (*i.e.*, minimum acoustic tensor determinant for each localization profile) at 32°, 28°, 11°, and 0°, respectively. This comparison confirms the adequacy of the calibration in replicating the pressure-dependency of the strain localization mechanisms.

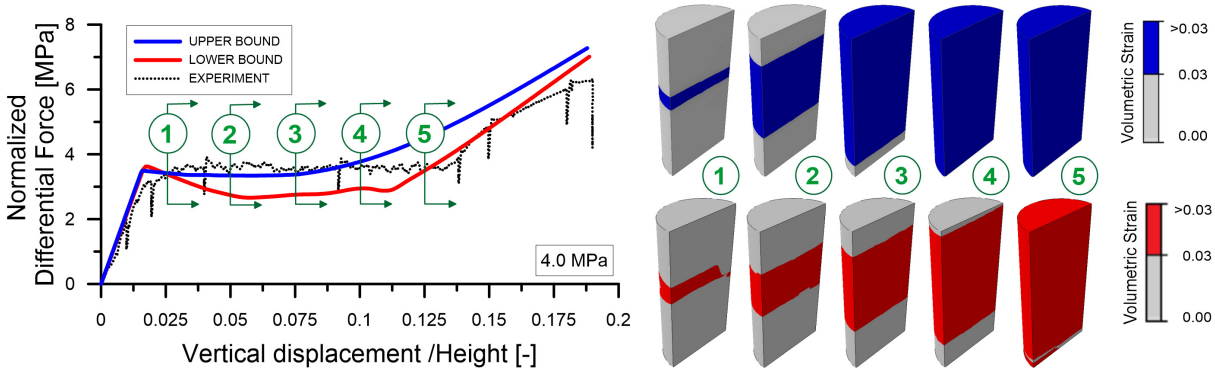

Figure 6.9: Comparison between the full-field response with an upper-bound and lower-bound calibration. The propagation of compaction zone is illustrated at various intervals over loading path. This comparison illustrates the pros and cons of each calibration, in that, the upper-bound calibration reproduces satisfactorily the stress levels, while the lower-bound maintains a better performance on the pace of compaction propagation.

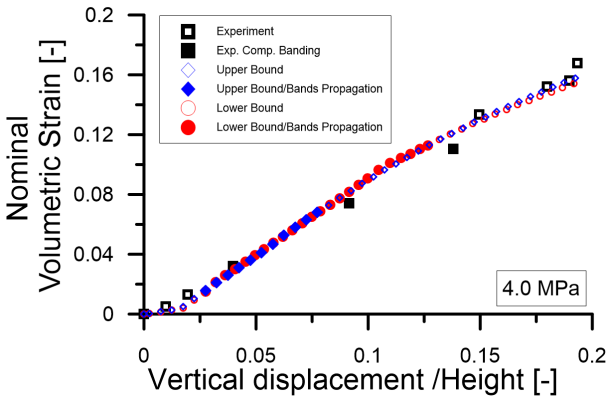

Figure 6.10: Nominal volumetric strain associated with the upper bound and lower bound calibration compared with the measured experimental data. The solid symbols indicate the range of compaction propagation.

The simulations are then examined to assess their ability to replicate the rate at which localized compaction propagates across the sample with imposed increments of global deformation. The cumulative volumetric strain field is therefore compared with measured porosity maps. Figure 6.12 shows a qualitative comparison between these variables at different levels of global axial strain along the plateau. For instance, Figure 6.12a, shows the data corresponding to the test at 2.0 MPa of confinement, where volumetric strain field and porosity map at 6.8%, 9.5%, and 12.4% axial strain are presented. Visual inspection indicates good agreement between simulations and experiments in terms of the volume of compacted sample, which approximately propagated over 20%, 40%, and 60% of the specimen. Similar conclusions can be drawn from the simulations run at 3.0 and 4.0 MPa confinement, while a less satisfactory agreement is obtained at 5.0 MPa (Figure 6.12d). In the latter case, the simulations overestimated the extent of plastically compacted

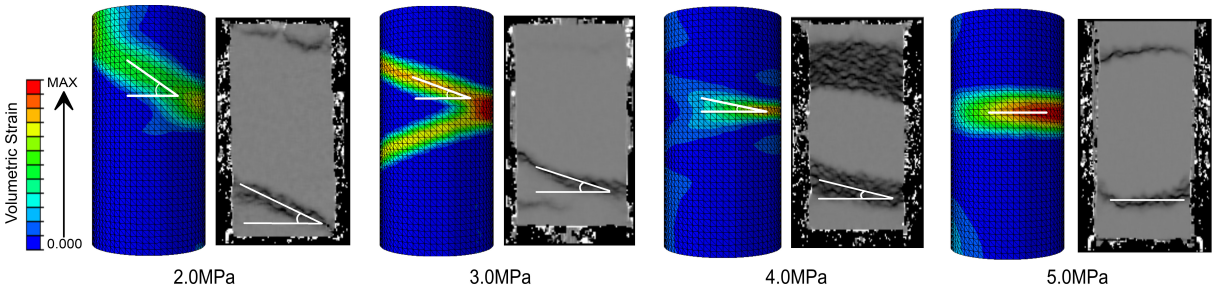

Figure 6.11: Comparison between finite element simulations and DIC computations for laboratory tests on samples of Tuffeau de Maastricht deformed under triaxial compression conditions at various confinement pressures. The comparison was conducted with reference to the incremental volumetric strain field at the inception of localization.

sample volume (*i.e.*, while at 7.0% axial strain the laboratory tests displayed major compaction only over 40% of the sample volume, the numerical analysis reached almost full compaction at the same global strain level). This can be considered as an outcome of the high amount of softening incorporated into the analysis and, as previously mentioned, can be mitigated by employing augmented hardening rules with a more flexible analytical expression.

Despite these limitations, the overall performance of the model can be considered satisfactory, in that it succeeds in reproducing most of the evidence measured at laboratory scale, most notably the pace and spatial extent of localized compaction. Nevertheless, it is worth remarking that the analysis was unable to reproduce the exact spatial patterns of strain localization. In fact, since a weak element is used to trigger localization, the onset and propagation is always controlled by this element. Given the important role of spatial variations in material properties on the triggering of strain localization (Borja *et al.*, 2013, Shahin *et al.*, 2016), future analysis should be conducted to gain even greater benefits from full-field measurements of initial and emerging heterogeneity. This step would require the incorporation of more accurate spatially-distributed information about the local material conditions, as well as about properties and boundary conditions.

6.3 Conclusions

The rich dataset is used to calibrate an elastoplastic constitutive model, employing synergistically data about macroscopic deformation and spatially-varying strain localization to enable the simulation of the full-field sample response. First global measurements are used to obtain a preliminary model calibration, which is then further elaborated based on the insight from digital image analysis. The competition between porosity hardening and cement destructuration is discussed with reference to two end-members of calibrations (here referred to as upper and lower bound, respectively). It is shown that while the former is more accurate to simulate stress plateau and re-hardening, the latter is better suited to match the rate of compaction propagation. With reference to the lower bound calibration, it is also shown that guidance from bifurcation analysis can be used to constrain the material constants and capture pressure-dependent strain localization patterns.

The second part of the chapter provides a validation of the selected model calibration procedure on the basis of full-field finite element analysis. A rate-dependent enhancement of the constitutive law is used to suppress mesh dependence, while maintaining an accurate representa-

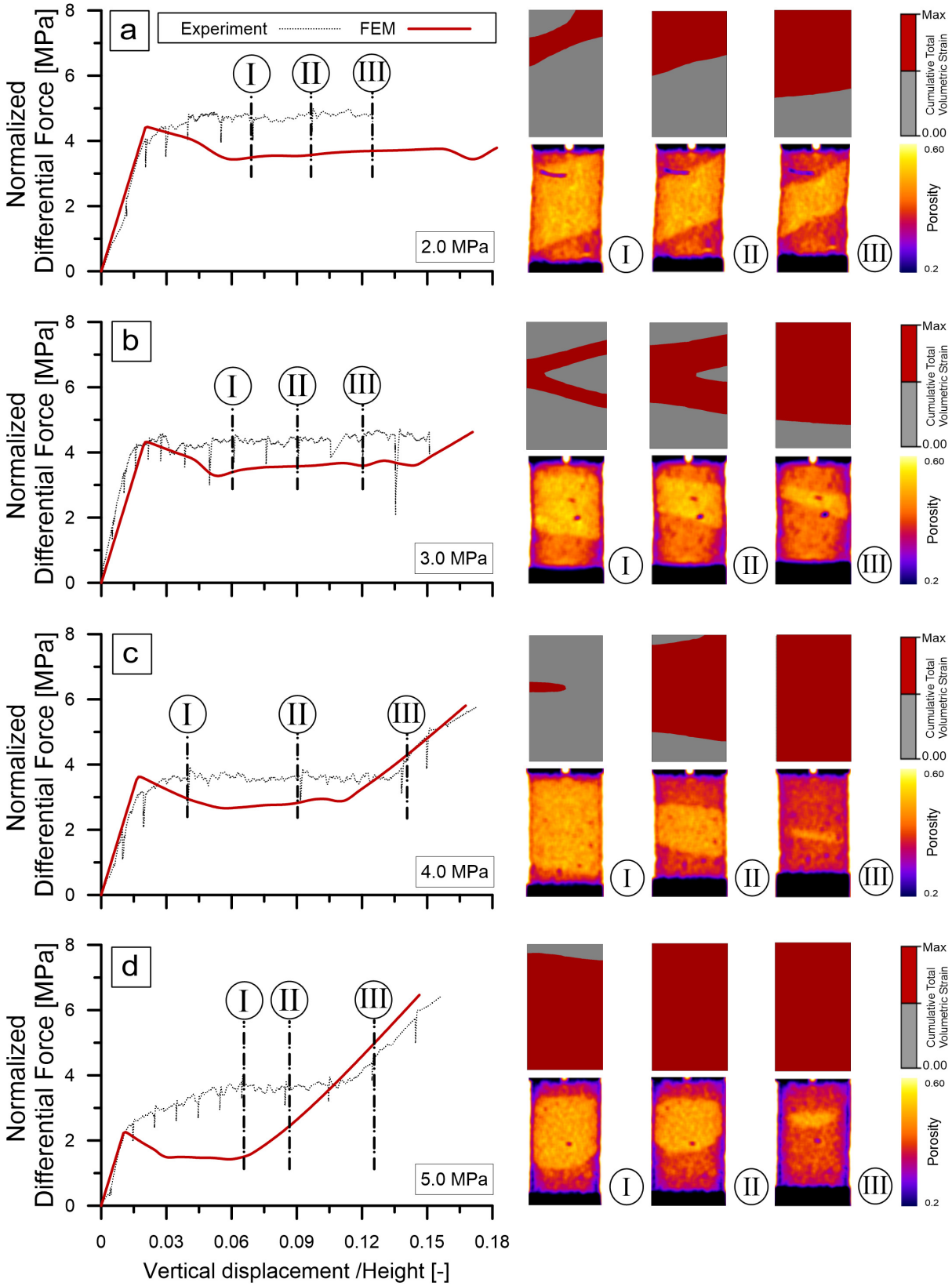

Figure 6.12: Triaxial test simulations with confinement pressures ranging from 2.0 MPa to 5.0 MPa. The propagation of compaction along loading path is illustrated in terms of cumulative volumetric strain field. Comparing these results with their counterparts obtained through X-ray tomography demonstrates the capabilities of the numerical model in reproducing the pace of propagation as a function of the imposed global deformation.

tion of the stress-strain behavior calibrated in light of the bifurcation theory. Triaxial compression tests are then simulated as boundary value problems, illustrating the ability of the calibrated model to capture satisfactorily a wide range of macroscopic attributes of the compaction process, such as the elongation of the post-yielding plateau, the inclination of the deformation bands and the spatial propagation of compaction across the specimen. Despite the inevitable approximations related with the use of a relatively simple constitutive law, the satisfactory agreement between numerical results and laboratory measurements point out the benefits of parameter optimization strategies accounting synergistically for global measurements and spatially-distributed deformations, especially in the presence of compaction localization processes. Future analysis may benefit from these results to incorporate the effect of spatially distributed heterogeneity on the propagation of compaction zone or to enhance the competition between hardening and softening effects through micro-mechanical considerations.

Chapter 7

Conclusions and Perspectives

7.1 Conclusions

An extensive experimental study has been presented on localized compaction in a high porosity bioclastic sedimentary limestone, with the main objective of better understanding the micro mechanisms of deformation that are responsible for localized compaction.

The experimental campaigns consist of: (i) uniaxial compression, (ii) isotropic compression, and (iii) triaxial compression tests at confining pressures ranging from 1 to 5 MPa on natural as well as on artificially debonded specimens. For this purpose, cylindrical specimens of 2:1 height-diameter ratio and 11.5 mm in diameter are cored perpendicular, oblique (45°), and parallel to the bedding plane. Full-field non-destructive techniques are used during this doctoral work to elucidate the mechanics of initiation and propagation of localized deformation during the loading process. With the use of x-ray computed tomography, 3D images of the specimens are obtained at different loading stages and advanced image analysis methods are applied to process the reconstructed images. Porosity variations during loading are measured macroscopically as well as locally. Local porosity measurements are performed over a REV, which is defined with the use of statistical tools. Digital image correlation is applied to the 3D images to obtain the shear and volumetric strain field evolution in the specimens throughout the tests. Strain fields provide quantitative 3D information about the shear and compaction bands formation in Tuffeau de Maastricht and its evolution with increasing deformation. The key finding of the thesis are summarized below.

The mechanical behavior of the material under **isotropic compression** conditions is characterized by the typical sigmoidal shape with an inflection point at the "critical pressure" P^*. The initial quasi-linear phase at low mean stress is less pronounced than in other porous rocks, confirming the almost total absence of microcracks in Tuffeau de Maastricht. This is also confirmed by the local porosity measurements, which show almost no changes in the distribution of porosity until the critical pressure. Beyond P^*, a sharp volumetric collapse occurs at roughly constant mean stress, with the porosity reducing from 40% to 36%. The comparison with the compression curve for the destructured material suggests that this volumetric collapse is essentially due to the destructuration of the intergranular bonds, which is also confirmed by the visual inspection of the tested samples. At higher mean stress, pore collapse induces an increase in the contact surface between the particles, which results in decrease of the volumetric strain rate. Thus, the

third phase is characterized by hardening.

The **triaxial compression** tests show that the mechanical behavior of Tuffeau de Maastricht is strongly pressure-dependent. Under low confining pressure the material exhibits a behavior characterized by a peak deviator stress and a strain-softening phase. The initial failure envelope is consistent with a Mohr-Coulomb frictional behavior, *i.e.*, the peak stress increases with increasing confining pressure. At higher confining pressure a transition from brittle to ductile behavior is observed. There is an overall trend for the "post-yield" slope to increase with increasing confining pressure while the maximum value of the deviator stress decreases. The yield surface confirms that porous carbonate rocks undergo the brittle to plastic transition at relatively low confining pressures. Two modes of failure are identified: shear localization and compaction localization at low and high confinement, respectively. The local porosity measurements as well as the volumetric strain indicate compactive behavior for all the tests even at low confining pressures. The use of 3D digital image correlation allows to map out the two failure modes and to track their evolution during loading. Strain concentration starts at the two ends of the samples and propagates with increasing applied deformation towards the middle of the specimens. The 3D strain fields obtained from DIC reveal a gradual progression for the localized bands as a function of increasing confining pressure, from high angle compactive shear bands to sub-perpendicular compaction bands with respect to the maximum compressive stress.

Triaxial compression tests up to much higher axial strain indicate that the mechanical behavior can be divided in three distinct phases: (1) an initial quasi-linear increase of deviator stress, followed by (2) a plateau and (3) a post plateau hardening. The 3D porosity fields show that there is a plausible relation between the end of the plateau and the stage at which the compaction bands "cover" the whole sample. At this stage the entire sample has been compressed and converted into a new, denser material, with homogeneous distribution of porosity –much lower than the initial. A further localization, typical of dense sand eventually occurs for very high axial strain. Additional experiments on the destructured material associate the development of compaction bands in Tuffeau de Maastricht (during the plateau) with porosity reduction and breakage of the bonds between the particles.

This doctoral work highlights the strong anisotropy of Tuffeau de Maastricht. The mechanical response is strongly dependent on the loading direction with respect to the bedding plane. As already observed for other porous sandstones, the bedding plane does not represent a plane of weakness and the samples cored at 45° fail at intermediate level of deviator stress between the ones for perpendicular and parallel cored samples. The experimental data show a consistent trend in strength anisotropy with a gradual decrease from maximum for σ_1 normal to bedding to a minimum for σ_1 parallel to bedding. Therefore, the maximum, intermediate and minimum values of the yield surface in the p-q plane are associated with the perpendicular, oblique and parallel samples, respectively. The results from triaxial compression up to very high axial strain suggest that the intergranular bonds are the main reason for the observed anisotropy. Even though the mechanical response of the material depends on the bedding orientation, strain localization seems not to be affected, *i.e.*, 3D strain field does not show any systematic difference in the localization pattern among the samples cored in different direction.

7.2 Perspectives

7.2.1 Further experimental studies

1D (oedometer) compression

A first attempt to perform oedometer tests on Tuffeau de Maastricht was done during this study. A small oedometer cell based on the design by Karatza (2017) was built for weak rocks using PolyEther Ether Ketone (PEEK). This material was selected mainly due to the fact that it is relatively transparent to x-rays, very smooth (which results in small friction during loading) and stiff enough (E $\approx$ 3.8 GPa) for the applied forces. Similarly to the triaxial cell used in this study, the oedometer cell was designed with an "I" shape to minimize the distance between the specimen and the x-ray source (Figure 7.1). In order for the specimen to be under oedometric conditions, the internal diameter of the cell is designed to be equal to the specimen's diameter, *i.e.*, 11.5 mm. The wall thickness is such that the wall stands the lateral stresses and attenuates the least x-rays.

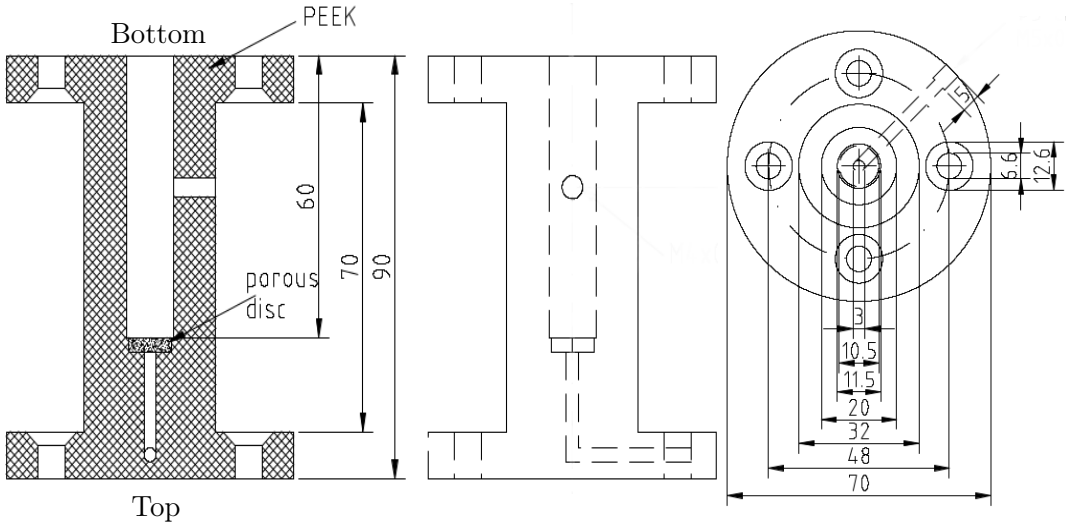

Figure 7.1: Schematic of oedometer cell designed for this doctoral work. All dimensions are in mm.

A few oedometer tests were carried out on Tuffeau de Maastricht. Once prepared, the samples were simply pushed down manually into the cell. The specimens were then loaded vertically, under a constant strain rate of $1.5 \times 10^{-5} s^{-1}$. Like the other experiments (section 3.5), the axial displacement is measured using an external transducer (LVDT). The cell walls are thick enough to prevent significant radial deformation of the specimen, however the whole system (cell and circular base, Figure 7.2) turns out not to be stiff enough to withstand the load. Therefore, the LVTD measurement included the displacement (in the vertical direction) of the whole system, *i.e.*, the specimen, the cell, and the circular base. Additionally, despite the fact that all the samples were cored with the same diamond drill, the diameter of the specimen varies from one test to another. This means that in some cases the sample is not completely in contact with the cell walls. Consequently, these samples are not initially deforming in oedometric conditions. For those reasons this experimental campaign is not presented in this work, and will be repeated in the future.

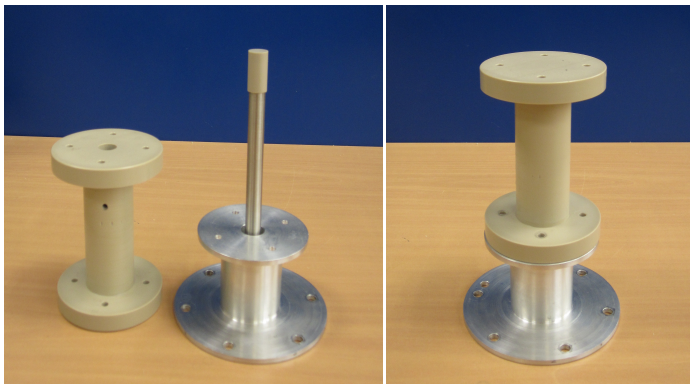

Figure 7.2: The "small" oedometer cell made by PEEK, specifically designed for this Ph.D. project.

True triaxial loading conditions

In addition to the "conventional" triaxial tests, an attempt to perform triaxial compression using a true triaxial apparatus has been made. The experiments are conducted using the true triaxial apparatus developed at Laboratoire 3SR by Pierre Bésuelle (Bésuelle and Lanatà, 2016). This device can independently apply the three principal stresses to a prismatic rock sample. In addition, it allows the visualization of one of the sample sides under loading. The prismatic samples are 50 mm in size in the direction of the major principal stress, 30 mm in the direction of the intermediate stress, and 25 mm in the direction of minor stress. Each pair of surfaces are made parallel, with a maximum offset of 100 micron (less than the average grain size $d_{50} = 150\mu$m), using a vertical-spindle surface grinder. A high resolution camera is used to obtain photographs of the visible surface of the sample throughout the loading every 30 seconds. The experiments are performed under strain control at constant vertical displacement rate of 50 μm/min, *i.e.*, at a strain rate of $1.5 \times 10^{-5} s^{-1}$.

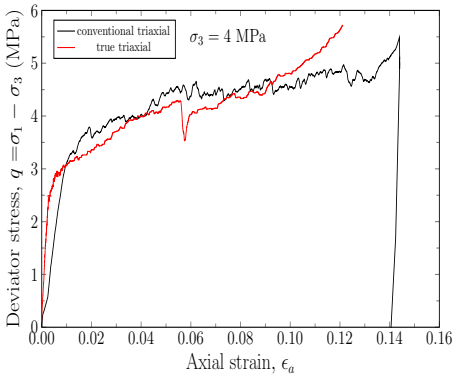

Figure 7.3: Comparison of mechanical data from triaxial compression tests at 4 MPa confinement performed in (i) conventional triaxial configuration (dark line), and (ii) true triaxial device (red line).

With the objective of comparing these results with those obtained from triaxial compression, the experiments are performed in axisymmetric conditions (*i.e.*, $\sigma_2 = \sigma_3$). After two different attempts only one can be considered as a successful experiment. Figure 7.3 shows the mechanical response of the material while Figure 7.4 shows the vertical incremental displacement for three different loading stages. After all, these results are promising to provide valuable information about the localized compaction in porous rocks, as well as to detect compaction band propagation. The main advantage of these experiments is that the temporal resolution is substantially

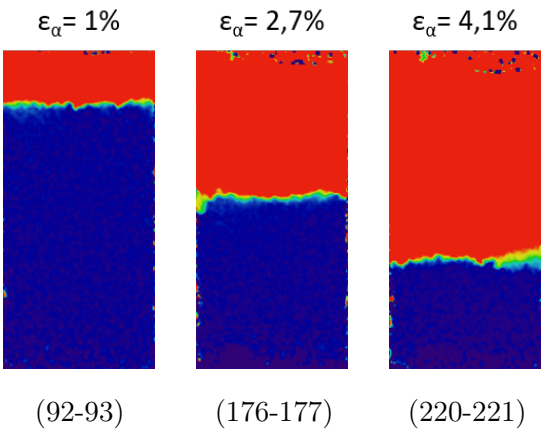

Figure 7.4: Incremental vertical displacement obtained from 2D-DIC of the sample tested with the true triaxial device. The 2D-DIC is performed between two images taken with 30 seconds difference, which are noted at the bottom of each figure. The blue color corresponds to zero displacement and the red to 15 μm approximately.

increased. However, the field measurements are taken only at the surface (2D).

Fluid effects

Previous experimental studies (*e.g.*, Baud *et al.*, 2000b) on porous sandstone indicate that although localized compaction is similar qualitatively in dry and saturated samples, the yield stresses are lower in the presence of water. A weakening effect of water is also observed in tuffs (*e.g.*, Zhu *et al.*, 2010), limestones (*e.g.*, Baud *et al.*, 2009) and grainstones (*e.g.*, Cilona *et al.*, 2012). A preliminary test on a wet sample was performed during this study under uniaxial compression conditions. Figure 7.5 shows that the Unconfined Compressive Strength (UCS) of the wet sample is almost half than the value obtained on the dry samples. The origin of the detrimental effect of a fluid is still not well understood. Further research is required on the hydro-mechanical behavior of porous carbonates to complete the picture of localized compaction.

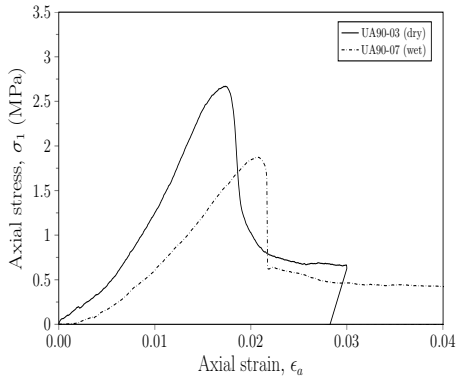

Figure 7.5: Uniaxial compression tests on a nominal dry (solid line) and a wet (dashed line) sample.

Chemical effects

For many years in the past Tuffeau de Maastricht was used as a durable building stone in the construction of historical monuments (Dreesen and Dusar, 2004, Dubelaar *et al.*, 2006). However,

soft porous carbonate rocks, such as calcarenites, due to their microstructure and chemical composition, are prone to water induced weathering mechanisms. Generally, chemical degradation of the solid skeleton is an important factor that may trigger instabilities in the form of compaction bands (Stefanou and Sulem, 2014). Xie *et al.* (2011) show that the chemical effects may significantly influence the mechanical responses of limestones resulting in much lower pore collapse critical stress, elastic modulus and material cohesion. So, the influence of chemical degradation on the mechanical behavior of porous rocks requires further investigation.

Full-field measurements

In this work a combination of two full-field measurement techniques (x-ray CT and 3D-DIC) are applied to study the localized deformation in the Tuffeau de Maastricht limestone. However, all the measurements are performed at the "macro" and "meso" scale. With the resolution chosen for the x-ray CT (13 μm pixel size) and the microstructure of the material, it is not possible to characterize any mechanisms at the grain scale. However, in this doctoral work similarly to prior studies on porous carbonates it is shown that a variety of micromechanisms can potentially play an important role on deformation. Acoustic emission (AE) measurements, a non-destructive measurement technique capable of detecting the dynamic processes associated with the damage of the microstructure, have not been used in this study. The combination of the tools used so far with acoustic emission and/or other full-field techniques is clearly a perspective of interest; each technique being sensitive to different processes (*e.g.*, Charalampidou, 2011, Viggiani and Hall, 2012).

7.2.2 Modeling

A large set of experimental data has been obtained during this dissertation, including the macroscopic mechanical responses in triaxial and isotropic compression tests, as well as the characterization of localized compaction through full-field measurements. A further straightforward perspective of this study would be to use this set of data in order to formulate, calibrate and/or validate mechanical models describing inelastic compaction in porous rocks. These models should be able to capture the complex mechanical behavior of high porous rocks that derives from the development of multiple inelastic softening and hardening mechanisms.

Based on the experimental results, an elasto-plastic model is used to reproduce material behavior (see chapter 6). The selected model includes two independent internal variables simulating the competition between the brittle breakage of the microstructure and the macroscopic strain hardening due to inelastic compaction and pore collapse (Buscarnera and Laverack, 2014). The global mechanical behavior of the material is used to conduct a preliminary calibration of the model that is further refined based on the obtained data from image analysis and DIC conducted on x-ray CT images. Although material behavior is captured successfully by the model, the numerical analysis is not able to reproduce the exact spatial aspects of localized compaction. This might be due to the weak element used to trigger the localization. Therefore, in order for the model to provide a better control of the localization mode, a further enhancement about material properties and microstructure, as well as about the boundary conditions is needed.

It is interesting to mention that in the framework of this doctoral work, a cooperative project

has also started with Prof. Jidong Zhao and Dr. Huanran Wu, in which their FEMxDEm approach (Zhao *et al.*, 2016, Wu *et al.*, 2018b) has been calibrated using the experimental data from the tests on Tuffeau de Maastricht. Interestingly, preliminary FEMxDEM simulations of the present triaxial compression tests show that compaction bands patterns in the triaxial compression simulation match amazingly well with the experimental observations in terms of porosity field, incremental volumetric and deviatoric strain (Wu *et al.*, 2018a). Although the global mechanical response is qualitatively similar to the experimental results, some discrepancies are also noted because of the spherical shape of the particles used to define the microstructure (DEM component of the model) and the absence of grain breakage. Grain breakage appears to be an important mechanism in granular rocks and the implementation of appropriate constitutive equations into the constitutive model needs further investigation.

Microstructural heterogeneity and material anisotropy are two complex and important aspects of porous sedimentary rocks which are not investigated in both numerical models described above. The anisotropic behavior of the material is also studied experimentally during this doctoral work providing comprehensive mechanical data. Therefore, it seems important to properly embody these effects in a constitutive framework in order to arrive at a more accurate and rational description of the mechanical response.

Bibliography

Abdulraheem, A., Roegiers, J.-C., Zaman, M., *et al.* (1992), "Mechanics of pore collapse and compaction in weak porous rocks", in: *The 33th US Symposium on Rock Mechanics (USRMS)*, American Rock Mechanics Association (cit. on p. 14).

Akin, S. and Kovscek, A. (2003), "Computed tomography in petroleum engineering research", in: *Geological Society, London, Special Publications*, Vol. 215, No. 1, pp. 23–38 (cit. on p. 21).

Alikarami, R., Andò, E., Gkiousas-Kapnisis, M., Torabi, A., and Viggiani, G. (2015), "Strain localisation and grain breakage in sand under shearing at high mean stress: insights from in situ X-ray tomography", in: *Acta Geotechnica*, Vol. 10, No. 1, pp. 15–30 (cit. on pp. 54, 59).

Alshibli, K. A. and Reed, A. H. (2012), *Advances in computed tomography for geomaterials: GeoX 2010*, John Wiley & Sons (cit. on p. 21).

Andò, E. (2013), "Experimental investigation of microstructural changes in deforming granular media using x-ray tomography", PhD thesis, Université de Grenoble (cit. on pp. 22, 30–33, 35, 45, 47, 53, 59).

Antonellini, M., Petracchini, L., Billi, A., and Scrocca, D. (2014), "First reported occurrence of deformation bands in a platform limestone, the Jurassic Calcare Massiccio Fm., northern Apennines, Italy", in: *Tectonophysics*, Vol. 628, pp. 85–104 (cit. on p. 9).

Arroyo, M., Castellanza, R., and Nova, R. (2005), "Compaction bands and oedometric testing in cemented soils", in: *Soils and foundations*, Vol. 45, No. 2, pp. 181–194 (cit. on p. 100).

Arzilli, F., Cilona, A., Mancini, L., and Tondi, E. (2016), "Using synchrotron X-ray microtomography to characterize the pore network of reservoir rocks: A case study on carbonates", in: *Advances in water resources*, Vol. 95, pp. 254–263 (cit. on p. 21).

Aydin, A. and Ahmadov, R. (2009), "Bed-parallel compaction bands in aeolian sandstone: their identification, characterization and implications", in: *Tectonophysics*, Vol. 479, No. 3-4, pp. 277–284 (cit. on p. 9).

Aydin, A., Borja, R. I., and Eichhubl, P. (2006), "Geological and mathematical framework for failure modes in granular rock", in: *Journal of Structural Geology*, Vol. 28, No. 1, pp. 83–98 (cit. on pp. 2, 5, 6, 9).

Barthélémy, J.-F. and Dormieux, L. (2004), "A micromechanical approach to the strength criterion of Drucker-Prager materials reinforced by rigid inclusions", in: *International Journal for Numerical and Analytical Methods in Geomechanics*, Vol. 28, No. 7-8, pp. 565–582 (cit. on p. 106).

Baruchel, J., Buffiere, J.-Y., and Maire, E. (2000), "X-ray tomography in material science", in: (cit. on pp. 43, 54).

Baud, P., Vinciguerra, S., David, C., Cavallo, A., Walker, E., and Reuschlé, T. (2009), "Compaction and failure in high porosity carbonates: Mechanical data and microstructural obser-

vations", in: *Pure and Applied Geophysics*, Vol. 166, No. 5-7, pp. 869–898 (cit. on pp. 2, 7, 11–13, 16, 72, 73, 84, 119).

Baud, P., Exner, U., Lommatzsch, M., Reuschlé, T., and Wong, T.-f. (2017a), "Mechanical behavior, failure mode, and transport properties in a porous carbonate", in: *Journal of Geophysical Research: Solid Earth*, Vol. 122, No. 9, pp. 7363–7387 (cit. on pp. 2, 7, 12–14, 67, 72, 73, 82).

Baud, P., Hall, S., Ji, Y., Wong, T.-F., and Heap, M. J. (2017b), "The Brittle-Ductile Transition in Porous Limestone Imaged by X-Ray Computed Tomography and Digital Image Correlation", in: *Poromechanics VI*, pp. 1782–1788 (cit. on p. 7).

Baud, P., Klein, E., and Wong, T.-f. (2004), "Compaction localization in porous sandstones: spatial evolution of damage and acoustic emission activity", in: *Journal of Structural Geology*, Vol. 26, No. 4, pp. 603–624 (cit. on pp. 1, 7, 8, 12, 20, 72, 73, 99).

Baud, P., Louis, L., David, C., Rawling, G. C., and Wong, T.-F. (2005), "Effects of bedding and foliation on mechanical anisotropy, damage evolution and failure mode", in: *Geological Society, London, Special Publications*, Vol. 245, No. 1, pp. 223–249 (cit. on pp. 17–19, 89, 91).

Baud, P., Meredith, P., and Townend, E. (2012), "Permeability evolution during triaxial compaction of an anisotropic porous sandstone", in: *Journal of Geophysical Research: Solid Earth*, Vol. 117, No. B5 (cit. on pp. 2, 17, 18).

Baud, P., Reuschlé, T., Ji, Y., Cheung, C. S., and Wong, T.-f. (2015), "Mechanical compaction and strain localization in Bleurswiller sandstone", in: *Journal of Geophysical Research: Solid Earth*, Vol. 120, No. 9, pp. 6501–6522 (cit. on p. 21).

Baud, P., Schubnel, A., Heap, M., and Rolland, A. (2017c), "Inelastic Compaction in High-Porosity Limestone Monitored Using Acoustic Emissions", in: *Journal of Geophysical Research: Solid Earth*, Vol. 122, No. 12, p. 9989 (cit. on p. 20).

Baud, P., Schubnel, A., and Wong, T.-f. (2000a), "Dilatancy, compaction, and failure mode in Solnhofen limestone", in: *Journal of Geophysical Research: Solid Earth*, Vol. 105, No. B8, pp. 19289–19303 (cit. on pp. 8, 14, 67, 72).

Baud, P., Vajdova, V., and Wong, T.-f. (2006), "Shear-enhanced compaction and strain localization: Inelastic deformation and constitutive modeling of four porous sandstones", in: *Journal of Geophysical Research: Solid Earth*, Vol. 111, No. B12 (cit. on pp. 7, 12, 82).

Baud, P., Zhu, W., and Wong, T.-f. (2000b), "Failure mode and weakening effect of water on sandstone", in: *Journal of Geophysical Research: Solid Earth*, Vol. 105, No. B7, pp. 16371–16389 (cit. on p. 119).

Baxevanis, T., Papamichos, E., Flornes, O., and Larsen, I. (2006), "Compaction bands and induced permeability reduction in Tuffeau de Maastricht calcarenite", in: *Acta Geotechnica*, Vol. 1, No. 2, pp. 123–135 (cit. on pp. 1, 7, 12, 72–74).

Bazant, Z. P. and Jirasek, M. (2002), "Nonlocal integral formulations of plasticity and damage: survey of progress", in: *Journal of Engineering Mechanics*, Vol. 128, No. 11, pp. 1119–1149 (cit. on p. 106).

Bear, J. (1972), "Dynamics of fluids in porous media", in: *American Else-vier, New York* (cit. on p. 55).

Bekendam, R. F. (1998), *Pillar stability and large-sacle collapse of abandoned room and pillar limestone mines in South-Limburg, the Netherlands*, TU Delft, Delft University of Technology (cit. on pp. 23–25).

Bésuelle, P. (2001a), "Evolution of strain localisation with stress in a sandstone: brittle and semi-brittle regimes", in: *Physics and Chemistry of the Earth, Part A: Solid Earth and Geodesy*, Vol. 26, No. 1-2, pp. 101–106 (cit. on p. 7).

Bésuelle, P., Desrues, J., and Raynaud, S. (2000), "Experimental characterisation of the localisation phenomenon inside a Vosges sandstone in a triaxial cell", in: *International Journal of Rock Mechanics and Mining Sciences*, Vol. 37, No. 8, pp. 1223–1237 (cit. on pp. 1, 7, 21, 100).

Bésuelle, P. and Lanatà, P. (2016), "A new true triaxial cell for field measurements on rock specimens and its use in the characterization of strain localization on a Vosges sandstone during a plane strain compression test", in: *Geotechnical Testing Journal*, Vol. 39, No. 5, pp. 879–890 (cit. on pp. 22, 118).

Bésuelle, P. (2001b), "Compacting and dilating shear bands in porous rock: Theoretical and experimental conditions", in: *Journal of Geophysical Research: Solid Earth*, Vol. 106, No. B7, pp. 13435–13442 (cit. on p. 1).

Bésuelle, P., Baud, P., and Wong, T.-F. (2003), "Failure mode and spatial distribution of damage in Rothbach sandstone in the brittle-ductile transition", in: *Thermo-Hydro-Mechanical Coupling in Fractured Rock*, Springer, pp. 851–868 (cit. on pp. 1, 7, 12, 17, 67).

Bésuelle, P. and Rudnicki, J. W. (2004), "Localization: shear bands and compaction bands", in: *INTERNATIONAL GEOPHYSICS SERIES*. Vol. 89, pp. 219–322 (cit. on p. 100).

Bishop, A. W. and Henkel, D. J. (1957), *The measurement of soil properties in the triaxial test*, Edward Arnold (Publishers) Ltd; London (cit. on pp. 32, 33).

Blanc, R., Da Costa, J.-P., Stitou, Y., Baylou, P., and Germain, C. (2008), "Assessment of texture stationarity using the asymptotic behavior of the empirical mean and variance", in: *IEEE Transactions on Image Processing*, Vol. 17, No. 9, pp. 1481–1490 (cit. on pp. 55, 56).

Blanton, T. L. (1981), "Deformation of chalk under confining pressure and pore pressure", in: *Society of Petroleum Engineers Journal*, Vol. 21, No. 01, pp. 43–50 (cit. on p. 14).

Borja, R. I., Song, X., Rechenmacher, A. L., Abedi, S., and Wu, W. (2013), "Shear band in sand with spatially varying density", in: *Journal of the Mechanics and Physics of Solids*, Vol. 61, No. 1, pp. 219–234 (cit. on p. 112).

Bornert, M. (2010), "X-ray micro CT for studying strain localization in clay rocks under triaxial compression", in: *Advances in X-ray Tomography for Geomaterials*, Vol. 118, p. 35 (cit. on p. 22).

Brace, W. (1978), "Volume changes during fracture and frictional sliding: a review", in: *Pure and Applied Geophysics*, Vol. 116, No. 4-5, pp. 603–614 (cit. on pp. 7, 67, 72).

Bradski, G. (2000), "The OpenCV Library", in: *Dr. Dobb's Journal of Software Tools* (cit. on pp. 59, 60).

Bruchon, J.-F., Pereira, J.-M., Vandamme, M., Lenoir, N., Delage, P., and Bornert, M. (2013a), "Full 3D investigation and characterisation of capillary collapse of a loose unsaturated sand using X-ray CT", in: *Granular Matter*, Vol. 15, No. 6, pp. 783–800 (cit. on p. 56).

Bruchon, J.-F., Pereira, J.-M., Vandamme, M., Lenoir, N., Delage, P., and Bornert, M. (2013b), "X-ray microtomography characterisation of the changes in statistical homogeneity of an unsaturated sand during imbibition", in: *Géotechnique Letters*, Vol. 3, No. 2, pp. 84–88 (cit. on p. 58).

Bubeck, A., Walker, R., Healy, D., Dobbs, M., and Holwell, D. (2017), "Pore geometry as a control on rock strength", in: *Earth and Planetary Science Letters*, Vol. 457, pp. 38–48 (cit. on p. 18).

Buscarnera, G. and Laverack, R. T. (2014), "Path dependence of the potential for compaction banding: Theoretical predictions based on a plasticity model for porous rocks", in: *Journal of Geophysical Research: Solid Earth*, Vol. 119, No. 3, pp. 1882–1903 (cit. on pp. 4, 100, 120).

Carosio, A., Willam, K., and Etse, G. (2000), "On the consistency of viscoplastic formulations", in: *International Journal of Solids and Structures*, Vol. 37, No. 48, pp. 7349–7369 (cit. on p. 107).

Carroll, M. (1991), "A critical state plasticity theory for porous reservoir rock", in: *Recent Advances in Mechanics of Structured Continua*, Vol. 117, pp. 1–8 (cit. on p. 100).

Casagrande, A. (1944), "Shear failure of anisotropic materials", in: *Proc. Boston Soc. Civ. Engrs*, Vol. 31, pp. 74–87 (cit. on p. 17).

Challa, V. and Issen, K. A. (2004), "Conditions for compaction band formation in porous rock using a two-yield surface model", in: *Journal of engineering mechanics*, Vol. 130, No. 9, pp. 1089–1097 (cit. on p. 100).

Chambon, R. (1986), "Bifurcation par localisation en bande de cisaillement, une approche avec des lois incrementalement non linéaires", in: *Journal de Mécanique théorique et appliquée*, Vol. 5, No. 2, pp. 277–298 (cit. on p. 104).

Charalampidou, E. M. (2011), "Etude expérimentale sur la localisation des déformations dans les grès poreux", PhD thesis, Grenoble (cit. on pp. 2, 7, 12, 13, 120).

Charalampidou, E.-M., Hall, S. A., Stanchits, S., Lewis, H., and Viggiani, G. (2011), "Characterization of shear and compaction bands in a porous sandstone deformed under triaxial compression", in: *Tectonophysics*, Vol. 503, No. 1-2, pp. 8–17 (cit. on pp. 1, 20, 21).

Charalampidou, E.-M., Hall, S. A., Stanchits, S., Viggiani, G., and Lewis, H. (2014), "Shear-enhanced compaction band identification at the laboratory scale using acoustic and full-field methods", in: *International Journal of Rock Mechanics and Mining Sciences*, Vol. 67, pp. 240–252 (cit. on pp. 1, 20, 21).

Cheung, C. S., Baud, P., and Wong, T.-f. (2012), "Effect of grain size distribution on the development of compaction localization in porous sandstone", in: *Geophysical Research Letters*, Vol. 39, No. 21 (cit. on pp. 2, 13).

Cilona, A., Baud, P., Tondi, E., Agosta, F., Vinciguerra, S., Rustichelli, A., and Spiers, C. J. (2012), "Deformation bands in porous carbonate grainstones: Field and laboratory observations", in: *Journal of Structural Geology*, Vol. 45, pp. 137–157 (cit. on pp. 2, 7, 9, 11–13, 84, 119).

Cilona, A., Faulkner, D. R., Tondi, E., Agosta, F., Mancini, L., Rustichelli, A., Baud, P., and Vinciguerra, S. (2014), "The effects of rock heterogeneity on compaction localization in porous carbonates", in: *Journal of Structural Geology*, Vol. 67, pp. 75–93 (cit. on p. 17).

Cnudde, V. (2005), "Exploring the potential of X-ray tomography as a new non-destructive research tool in conservation studies of natural building stones", PhD thesis, Ghent University (cit. on pp. 21, 23, 24, 48).

Croize, D., Renard, F., and Gratier, J.-P. (2013), "Compaction and porosity reduction in carbonates: A review of observations, theory, and experiments", in: *Advances in Geophysics*, vol. 54, Elsevier, pp. 181–238 (cit. on pp. 2, 11, 13).

Cuss, R., Rutter, E., and Holloway, R. (2003), "The application of critical state soil mechanics to the mechanical behaviour of porous sandstones", in: *International Journal of Rock Mechanics and Mining Sciences*, Vol. 40, No. 6, pp. 847–862 (cit. on p. 100).

Daigle, M., Fratta, D., and Wang, L. (2005), "Ultrasonic and X-ray tomographic imaging of highly contrasting inclusions in concrete specimens", in: *Site Characterization and Modeling*, pp. 1–12 (cit. on p. 20).

Das, A. and Buscarnera, G. (2014), "Simulation of localized compaction in high-porosity calcarenite subjected to boundary constraints", in: *International Journal of Rock Mechanics and Mining Sciences*, Vol. 71, pp. 91–104 (cit. on pp. 100, 102).

Das, A., Nguyen, G. D., and Einav, I. (2011), "Compaction bands due to grain crushing in porous rocks: a theoretical approach based on breakage mechanics", in: *Journal of Geophysical Research: Solid Earth*, Vol. 116, No. B8 (cit. on p. 100).

Das, A., Nguyen, G. D., and Einav, I. (2013), "The propagation of compaction bands in porous rocks based on breakage mechanics", in: *Journal of Geophysical Research: Solid Earth*, Vol. 118, No. 5, pp. 2049–2066 (cit. on p. 107).

Dautriat, J., Bornert, M., Gland, N., Dimanov, A., and Raphanel, J. (2011a), "Localized deformation induced by heterogeneities in porous carbonate analysed by multi-scale digital image correlation", in: *Tectonophysics*, Vol. 503, No. 1-2, pp. 100–116 (cit. on p. 22).

Dautriat, J., Gland, N., Dimanov, A., and Raphanel, J. (2011b), "Hydromechanical behavior of heterogeneous carbonate rock under proportional triaxial loadings", in: *Journal of Geophysical Research: Solid Earth*, Vol. 116, No. B1 (cit. on pp. 13, 14, 67).

David, C., Wong, T.-F., Zhu, W., and Zhang, J. (1994), "Laboratory measurement of compaction-induced permeability change in porous rocks: Implications for the generation and maintenance of pore pressure excess in the crust", in: *Pure and Applied Geophysics*, Vol. 143, No. 1-3, pp. 425–456 (cit. on p. 20).

De Borst, R. and Muhlhaus, H.-B. (1992), "Gradient-dependent plasticity: formulation and algorithmic aspects", in: *International Journal for Numerical Methods in Engineering*, Vol. 35, No. 3, pp. 521–539 (cit. on p. 106).

Deng, S. and Aydin, A. (2012), "Distribution of compaction bands in 3D in an aeolian sandstone: The role of cross-bed orientation", in: *Tectonophysics*, Vol. 574, pp. 204–218 (cit. on pp. 9, 10).

Desrues, J., Chambon, R., Mokni, M., and Mazerolle, F. (1996), "Void ratio evolution inside shear bands in triaxial sand specimens studied by computed tomography", in: *Géotechnique*, Vol. 46, No. 3, pp. 529–546 (cit. on p. 21).

Desrues, J. and Andò, E. (2015), "Strain localisation in granular media", in: *Comptes Rendus Physique*, Vol. 16, No. 1, pp. 26–36 (cit. on p. 54).

Desrues, J. and Réthoré, J. (2013), "Characterization of Localized Phenomena", in: *Full-Field Measurements and Identification in Solid Mechanics*, pp. 379–410 (cit. on p. 5).

Desrues, J., Viggiani, G., and Besuelle, P. (2010), *Advances in X-ray Tomography for Geomaterials*, vol. 118, John Wiley & Sons (cit. on p. 21).

Dewers, T. A., Issen, K. A., Holcomb, D. J., Olsson, W. A., and Ingraham, M. D. (2017), "Strain localization and elastic-plastic coupling during deformation of porous sandstone", in: *International Journal of Rock Mechanics and Mining Sciences*, Vol. 98, pp. 167–180 (cit. on p. 20).

DiGiovanni, A. A., Fredrich, J. T., Holcomb, D. J., Olsson, W. A., *et al.* (2000), "Micromechanics of compaction in an analogue reservoir sandstone", in: *4th North American Rock Mechanics Symposium*, American Rock Mechanics Association (cit. on p. 20).

DiMaggio, F. L. and Sandler, I. S. (1971), "Material model for granular soils", in: *Journal of Engineering Mechanics* (cit. on p. 100).

Dreesen, R. and Dusar, M. (2004), "Historical building stones in the province of Limburg (NE Belgium): role of petrography in provenance and durability assessment", in: *Materials Characterization*, Vol. 53, No. 2, pp. 273–287 (cit. on p. 119).

Dubelaar, C., Dusar, M., Dreesen, R., Felder, W., and Nijland, T. (2006), "Maastricht limestone: a regionally significant building stone in Belgium and the Netherlands. Extremely weak yet time-resistant", in: *Proceedings of the international heritage weathering and conservation conference. Taylor & Francis Group, London*, pp. 9–14 (cit. on pp. 24, 119).

Dunham, R. J. (1962), "Classification of carbonate rocks according to depositional textures", in: (cit. on p. 26).

Etse, G. and Willam, K. (1999), "Failure analysis of elastoviscoplastic material models", in: *Journal of engineering mechanics*, Vol. 125, No. 1, pp. 60–69 (cit. on p. 107).

Feldkamp, L., Davis, L., and Kress, J. (1984), "Practical cone-beam algorithm", in: *JOSA A*, Vol. 1, No. 6, pp. 612–619 (cit. on pp. 47, 48).

Fjar, E., Holt, R. M., Raaen, A., Risnes, R., and Horsrud, P. (2008), *Petroleum related rock mechanics*, vol. 53, Elsevier (cit. on p. 11).

Fonseca, J., Bésuelle, P., and Viggiani, G. (2013), "Micromechanisms of inelastic deformation in sandstones: an insight using x-ray micro-tomography", in: *Géotechnique Letters*, Vol. 3, pp. 78–83 (cit. on p. 21).

Fortin, J., Guéguen, Y., and Schubnel, A. (2007), "Effects of pore collapse and grain crushing on ultrasonic velocities and Vp/Vs", in: *Journal of Geophysical Research: Solid Earth*, Vol. 112, No. B8 (cit. on p. 19).

Fortin, J., Stanchits, S., Dresen, G., and Guéguen, Y. (2006), "Acoustic emission and velocities associated with the formation of compaction bands in sandstone", in: *Journal of Geophysical Research: Solid Earth*, Vol. 111, No. B10 (cit. on p. 20).

Fossen, H., Schultz, R. A., Shipton, Z. K., and Mair, K. (2007), "Deformation bands in sandstone: a review", in: *Journal of the Geological Society*, Vol. 164, No. 4, pp. 755–769 (cit. on p. 5).

Fossen, H., Schultz, R. A., and Torabi, A. (2011), "Conditions and implications for compaction band formation in the Navajo Sandstone, Utah", in: *Journal of Structural Geology*, Vol. 33, No. 10, pp. 1477–1490 (cit. on pp. 8, 9).

Fossen, H., Soliva, R., Ballas, G., Trzaskos, B., Cavalcante, C., and Schultz, R. A. (2017), "A review of deformation bands in reservoir sandstones: geometries, mechanisms and distribution", in: *Geological Society, London, Special Publications*, Vol. 459, SP459–4 (cit. on pp. 1, 5, 6).

Fossum, A. F., Fredrich, J. T., *et al.* (2000), "Cap plasticity models and compactive and dilatant pre-failure deformation", in: *4th North American Rock Mechanics Symposium*, American Rock Mechanics Association (cit. on p. 100).

Fredrick, J., Deitrick, G., Arguello, J., DeRouffignac, E., *et al.* (1998), "Reservoir compaction, surface subsidence, and casing damage: a geomechanics approach to mitigation and reservoir management", in: *SPE/ISRM Rock Mechanics in Petroleum Engineering*, Society of Petroleum Engineers (cit. on pp. 1, 14).

Geertsma, J. *et al.* (1973), "Land subsidence above compacting oil and gas reservoirs", in: *Journal of Petroleum Technology*, Vol. 25, No. 06, pp. 734–744 (cit. on pp. 1, 14).

Gens, A. and Nova, R. (1993), "Conceptual bases for a constitutive model for bonded soils and weak rocks", in: *Geotechnical engineering of hard soils-soft rocks*, Vol. 1, No. 1, pp. 485–494 (cit. on p. 100).

Grédiac, M. and Hild, F. (2012), *Full-field measurements and identification in solid mechanics*, John Wiley & Sons (cit. on p. 5).

Griffiths, L., Heap, M. J., Xu, T., Chen, C.-f., and Baud, P. (2017), "The influence of pore geometry and orientation on the strength and stiffness of porous rock", in: *Journal of Structural Geology*, Vol. 96, pp. 149–160 (cit. on p. 18).

Grueschow, E. and Rudnicki, J. W. (2005), "Elliptic yield cap constitutive modeling for high porosity sandstone", in: *International Journal of Solids and Structures*, Vol. 42, No. 16, pp. 4574–4587 (cit. on p. 100).

Hall, S., Bornert, M., Desrues, J., Pannier, Y., Lenoir, N., Viggiani, G., and Bésuelle, P. (2010), "Discrete and continuum analysis of localised deformation in sand using X-ray μCT and volumetric digital image correlation", in: *Géotechnique*, Vol. 60, No. 5, pp. 315–322 (cit. on p. 32).

Hall, S. A. (2006), "A methodology for 7D warping and deformation monitoring using time-lapse seismic data", in: *Geophysics*, Vol. 71, No. 4, O21–O31 (cit. on p. 61).

Hall, S. A., De Sanctis, F., and Viggiani, G. (2006), "Monitoring fracture propagation in a soft rock (Neapolitan Tuff) using acoustic emissions and digital images", in: *Pure and Applied Geophysics*, Vol. 163, No. 10, pp. 2171–2204 (cit. on p. 22).

Hall, S. A. and Tudisco, E. (2012), "Full-field ultrasonic measurement (ultrasonic tomography) in experimental geomechanics", in: *ALERT Doctoral School 2012: Advanced experimental techniques in geomechanics*, ALERT Geomaterials, pp. 103–123 (cit. on p. 20).

Hamilton, J. and Shafer, J. (1991), "Measurement of pore compressibility characteristics in rock exhibiting pore collapse and volumetric creep", in: *Society of Core Analysts Conference*, Citeseer, pp. 273–282 (cit. on p. 15).

Heap, M. J., Brantut, N., Baud, P., and Meredith, P. G. (2015), "Time-dependent compaction band formation in sandstone", in: *Journal of Geophysical Research: Solid Earth*, Vol. 120, No. 7, pp. 4808–4830 (cit. on pp. 20, 82).

Heeres, O. M., Suiker, A. S., and Borst, R. de (2002), "A comparison between the Perzyna viscoplastic model and the consistency viscoplastic model", in: *European Journal of Mechanics-A/Solids*, Vol. 21, No. 1, pp. 1–12 (cit. on p. 107).

Herman, G. T. (1980), "Image Reconstruction from Projections: The Fundamentals of Computerized Tomography (Computer Science Applied Mathematics)", in: *image*, Vol. 10, p. 03 (cit. on p. 46).

Hill, R. E. (1993), "Analysis of deformation bands in the Aztec sandstone, Valley of Fire State Park, Nevada", in: *Geological Society of America, Abstracts with Programs;(United States)*, Vol. 25, No. CONF-9305259– (cit. on pp. 2, 8, 11).

Holcomb, D., Rudnicki, J. W., Issen, K. A., and Sternlof, K. (2007), "Compaction localization in the Earth and the laboratory: state of the research and research directions", in: *Acta Geotechnica*, Vol. 2, No. 1, pp. 1–15 (cit. on pp. 2, 11, 20).

Hsieh, J. *et al.* (2009), "Computed tomography: principles, design, artifacts, and recent advances", in: SPIE Bellingham, WA (cit. on pp. 42, 47).

Issen, K. and Rudnicki, J. (2000), "Conditions for compaction bands in porous rock", in: *Journal of Geophysical Research: Solid Earth*, Vol. 105, No. B9, pp. 21529–21536 (cit. on pp. 11, 99, 100).

Issen, K. and Rudnicki, J. (2001), "Theory of compaction bands in porous rock", in: *Physics and Chemistry of the Earth, Part A: Solid Earth and Geodesy*, Vol. 26, No. 1-2, pp. 95–100 (cit. on p. 99).

Issen, K. A. (2002), "The influence of constitutive models on localization conditions for porous rock", in: *Engineering Fracture Mechanics*, Vol. 69, No. 17, pp. 1891–1906 (cit. on p. 100).

Ji, Y., Hall, S. A., Baud, P., and Wong, T.-f. (2014), "Characterization of pore structure and strain localization in Majella limestone by X-ray computed tomography and digital image correlation", in: *Geophysical Journal International*, Vol. 200, No. 2, pp. 701–719 (cit. on pp. 1, 7, 22).

Johnson, J., Rhett, D., Siemers, W., *et al.* (1988), "Rock mechanics of the Ekofisk reservoir in the evaluation of subsidence", in: *Offshore Technology Conference*, Offshore Technology Conference (cit. on pp. 1, 14, 15).

Kaddhour, G., Andò, E., Salager, S., Bésuelle, P., Viggiani, C., Hall, S., and Desrues, J. (2013), "Application of X-ray Tomography to the Characterisation of Grain-Scale Mechanisms in Sand", in: *Multiphysical Testing of Soils and Shales*, Springer, pp. 195–200 (cit. on p. 54).

Kanit, T., Forest, S., Galliet, I., Mounoury, V., and Jeulin, D. (2003), "Determination of the size of the representative volume element for random composites: statistical and numerical approach", in: *International Journal of solids and structures*, Vol. 40, No. 13-14, pp. 3647–3679 (cit. on pp. 56, 58).

Karacan, C., Grader, A., and Halleck, P. (2003), "Evaluation of local porosity changes in limestone samples under triaxial stress field by using X-ray computed tomography", in: *Geological Society, London, Special Publications*, Vol. 215, No. 1, pp. 177–189 (cit. on p. 21).

Karatza, Z. (2017), "Study of temporal and spatial evolution of deformation and breakage of dry granular materials using x-ray computed tomography and the discrete element method", in: (cit. on pp. 30, 54, 59, 117).

King, M., Chaudry, N., and Ahmed, S. (1994), "Experimental ultrasonic velocities and permeability of sandstones with aligned cracks", in: *56th EAEG Meeting* (cit. on p. 19).

Klein, E., Baud, P., Reuschlé, T., and Wong, T. (2001), "Mechanical behaviour and failure mode of Bentheim sandstone under triaxial compression", in: *Physics and Chemistry of the Earth, Part A: Solid Earth and Geodesy*, Vol. 26, No. 1-2, pp. 21–25 (cit. on pp. 7, 8, 12, 20).

Kodaka, T., Oka, F., Otani, J., Kitahara, H., and Ohta, H. (2006), "Experimental study of compaction bands in diatomaceous porous rock", in: *Advances in X-ray Tomography for Geomaterials*, pp. 185–191 (cit. on p. 21).

Kumar, A. (2006), "Engineering Behaviour of anisotropic rocks", in: (cit. on p. 17).

Lagioia, R. and Nova, R. (1995), "An experimental and theoretical study of the behaviour of a calcarenite in triaxial compression", in: *Géotechnique*, Vol. 45, No. 4, pp. 633–648 (cit. on pp. 86, 100).

Lagioia, R., Puzrin, A., and Potts, D. (1996), "A new versatile expression for yield and plastic potential surfaces", in: *Computers and Geotechnics*, Vol. 19, No. 3, pp. 171–191 (cit. on p. 100).

Lantuejoul, C. (1991), "Ergodicity and integral range", in: *Journal of Microscopy*, Vol. 161, No. 3, pp. 387–403 (cit. on p. 56).

Lee, J.-S., Fernandez, A. L., and Santamarina, J. C. (2005), "S-wave velocity tomography: Small-scale laboratory application", in: *Geotechnical Testing Journal*, Vol. 28, No. 4, pp. 336–344 (cit. on p. 20).

Lenoir, N., Bornert, M., Desrues, J., Bésuelle, P., and Viggiani, G. (2007), "Volumetric digital image correlation applied to X-ray microtomography images from triaxial compression tests on argillaceous rock", in: *Strain*, Vol. 43, No. 3, pp. 193–205 (cit. on pp. 21, 22, 32).

Leroueil, S. and Vaughan, P. (1990), "The general and congruent effects of structure in natural soils and weak rocks", in: *Géotechnique*, Vol. 40, No. 3, pp. 467–488 (cit. on p. 102).

Liu, Y., Sun, W., Yuan, Z., and Fish, J. (2016), "A nonlocal multiscale discrete-continuum model for predicting mechanical behavior of granular materials", in: *International Journal for Numerical Methods in Engineering*, Vol. 106, No. 2, pp. 129–160 (cit. on p. 106).

Lo, T.-w., Coyner, K. B., and Toksöz, M. N. (1986), "Experimental determination of elastic anisotropy of Berea sandstone, Chicopee shale, and Chelmsford granite", in: *Geophysics*, Vol. 51, No. 1, pp. 164–171 (cit. on pp. 17, 19).

Louis, L., Baud, P., and Wong, T.-f. (2009), "Microstructural inhomogeneity and mechanical anisotropy associated with bedding in Rothbach sandstone", in: *Pure and applied geophysics*, Vol. 166, No. 5-7, pp. 1063–1087 (cit. on pp. 17, 18, 92).

Louis, L., David, C., Metz, V., Robion, P., Menendez, B., and Kissel, C. (2005), "Microstructural control on the anisotropy of elastic and transport properties in undeformed sandstones", in: *International Journal of Rock Mechanics and Mining Sciences*, Vol. 42, No. 7-8, pp. 911–923 (cit. on pp. 18, 19).

Louis, L., David, C., and Robion, P. (2003), "Comparison of the anisotropic behaviour of undeformed sandstones under dry and saturated conditions", in: *Tectonophysics*, Vol. 370, No. 1-4, pp. 193–212 (cit. on pp. 17–19, 89).

Louis, L., Wong, T.-F., and Baud, P. (2007), "Imaging strain localization by X-ray radiography and digital image correlation: Deformation bands in Rothbach sandstone", in: *Journal of Structural Geology*, Vol. 29, No. 1, pp. 129–140 (cit. on pp. 17, 18, 21, 22).

Louis, L., Wong, T.-f., Baud, P., and Tembe, S. (2006), "Imaging strain localization by X-ray computed tomography: discrete compaction bands in Diemelstadt sandstone", in: *Journal of Structural Geology*, Vol. 28, No. 5, pp. 762–775 (cit. on p. 21).

Mair, K., Elphick, S., and Main, I. (2002), "Influence of confining pressure on the mechanical and structural evolution of laboratory deformation bands", in: *Geophysical Research Letters*, Vol. 29, No. 10, pp. 49–1 (cit. on pp. 7, 13).

Marinelli, F. and Buscarnera, G. (2015), "Parameter calibration for high-porosity sandstones deformed in the compaction banding regime", in: *International Journal of Rock Mechanics and Mining Sciences*, Vol. 78, pp. 240–252 (cit. on pp. 100, 102, 104).

Martinez-Martinez, J., Fusi, N., Galiana-Merino, J. J., Benavente, D., and Crosta, G. B. (2016), "Ultrasonic and X-ray computed tomography characterization of progressive fracture damage in low-porous carbonate rocks", in: *Engineering Geology*, Vol. 200, pp. 47–57 (cit. on p. 19).

Matheron, G. (1989), *Estimating and choosing. An essay on probability in practice. Translated from the French and with a preface by AM Hasofer* (cit. on p. 56).

Matheron, G. (1963), "Principles of geostatistics", in: *Economic geology*, Vol. 58, No. 8, pp. 1246–1266 (cit. on pp. 55, 56).

Mees, F., Swennen, R., Van Geet, M., and Jacobs, P. (2003), "Applications of X-ray computed tomography in the geosciences", in: *Geological Society, London, Special Publications*, Vol. 215, No. 1, pp. 1–6 (cit. on pp. 21, 41).

Menéndez, B., Zhu, W., and Wong, T.-F. (1996), "Micromechanics of brittle faulting and cataclastic flow in Berea sandstone", in: *Journal of structural geology*, Vol. 18, No. 1, pp. 1–16 (cit. on pp. 2, 7, 8, 12, 13, 67, 100).

Millien, A. (1993), "Comportement anisotrope du grès des Vosges: élasto-plasticité, localisation, rupture", PhD thesis, Grenoble 1 (cit. on pp. 18, 91).

Mollema, P. and Antonellini, M. (1996), "Compaction bands: a structural analog for anti-mode I cracks in aeolian sandstone", in: *Tectonophysics*, Vol. 267, No. 1, pp. 209–228 (cit. on pp. 2, 9, 11, 84).

Mowar, S., Zaman, M., Stearns, D., and Roegiers, J.-C. (1996), "Micro-mechanisms of pore collapse in limestone", in: *Journal of Petroleum Science and Engineering*, Vol. 15, No. 2-4, pp. 221–235 (cit. on pp. 1, 14–16, 67).

Mukunoki, T., Otani, J., Obara, Y., and Kaneko, K. (2004), "Artifacts of X-Ray CT data in the analysis of geomaterial properties", in: *X-ray CT for Geomaterials*, pp. 95–101 (cit. on p. 43).

Needleman, A. (1988), "Material rate dependence and mesh sensitivity in localization problems", in: *Computer methods in applied mechanics and engineering*, Vol. 67, No. 1, pp. 69–85 (cit. on p. 106).

Ngan-Tillard, D., Verwaal, W., Mulder, A., Engin, H., and Ulusay, R. (2011), "Application of the needle penetration test to a calcarenite, Maastricht, the Netherlands", in: *Engineering Geology*, Vol. 123, No. 3, pp. 214–224 (cit. on p. 25).

Nguyen, G. D., Nguyen, C. T., Bui, H. H., and Nguyen, V. P. (2016), "Constitutive modelling of compaction localisation in porous sandstones", in: *International Journal of Rock Mechanics and Mining Sciences*, Vol. 83, pp. 57–72 (cit. on p. 100).

Niandou, H., Shao, J., Henry, J., and Fourmaintraux, D. (1997), "Laboratory investigation of the mechanical behaviour of Tournemire shale", in: *International Journal of Rock Mechanics and Mining Sciences*, Vol. 34, No. 1, pp. 3–16 (cit. on pp. 17, 18).

Nova, R. (1980), "The failure of transversely isotropic rocks in triaxial compression", in: *International Journal of Rock Mechanics and Mining Sciences & Geomechanics Abstracts*, vol. 17, 6, Elsevier, pp. 325–332 (cit. on p. 17).

Nova, R., Castellanza, R., and Tamagnini, C. (2003), "A constitutive model for bonded geomaterials subject to mechanical and/or chemical degradation", in: *International Journal for Numerical and Analytical Methods in Geomechanics*, Vol. 27, No. 9, pp. 705–732 (cit. on p. 100).

Nur, A. and Simmons, G. (1969), "Stress-induced velocity anisotropy in rock: An experimental study", in: *Journal of Geophysical Research*, Vol. 74, No. 27, pp. 6667–6674 (cit. on p. 19).

Olsson, W. and Holcomb, D. (2000), "Compaction localization in porous rock", in: *Geophysical Research Letters*, Vol. 27, No. 21, pp. 3537–3540 (cit. on pp. 20, 99).

Olsson, W. A. (1999), "Theoretical and experimental investigation of compaction bands in porous rock", in: *Journal of Geophysical Research: Solid Earth*, Vol. 104, No. B4, pp. 7219–7228 (cit. on pp. 8, 99).

Olsson, W. A. (2001), "Quasistatic propagation of compaction fronts in porous rock", in: *Mechanics of Materials*, Vol. 33, No. 11, pp. 659–668 (cit. on p. 99).

Pan, B., Qian, K., Xie, H., and Asundi, A. (2009), "Two-dimensional digital image correlation for in-plane displacement and strain measurement: a review", in: *Measurement science and technology*, Vol. 20, No. 6, p. 062001 (cit. on pp. 22, 62).

Papazoglou, A., Shahin, G., Marinelli, F., Dano, C., Buscarnera, G., and Viggiani, G. (2017), "Localized Compaction in Tuffeau de Maastricht: Experiments and Modeling", in: *International Workshop on Bifurcation and Degradation in Geomaterials*, Springer, pp. 481–488 (cit. on p. 105).

Park, C. and Nutt, S. (2001), "Anisotropy and strain localization in steel foam", in: *Materials Science and Engineering: A*, Vol. 299, No. 1-2, pp. 68–74 (cit. on pp. 18, 82).

Perzyna, P. (1966), "Fundamental problems in viscoplasticity", in: *Advances in applied mechanics*, Vol. 9, pp. 243–377 (cit. on pp. 106, 107).

Peters, W. and Ranson, W. (1982), "Digital imaging techniques in experimental stress analysis", in: *Optical engineering*, Vol. 21, No. 3, p. 213427 (cit. on p. 22).

Ramamurthy, T., Rao, G. V., and Singh, J. (1993), "Engineering behaviour of phyllites", in: *Engineering Geology*, Vol. 33, No. 3, pp. 209–225 (cit. on p. 17).

Remeysen, R. and Swennen, K. (2010), "Combination of dual energy microfocus computed tomography and petrography for objective 3D reservoir characterization", in: *Advances in X-ray Tomography for Geomaterials*, Vol. 118, p. 155 (cit. on p. 21).

Roscoe, K. (1963), "The determination of strains in soils by an X-ray method", in: *Civ. Engng Publ. Wks Rev.* Vol. 58, pp. 873–876 (cit. on p. 21).

Rozenbaum, O. and Roscoat, S. R. du (2014), "Representative elementary volume assessment of three-dimensional x-ray microtomography images of heterogeneous materials: Application to limestones", in: *Physical Review E*, Vol. 89, No. 5, p. 053304 (cit. on pp. 21, 54).

Rudnicki, J. W. (2004), "Shear and compaction band formation on an elliptic yield cap", in: *Journal of Geophysical Research: Solid Earth*, Vol. 109, No. B3 (cit. on p. 100).

Rudnicki, J. W. and Rice, J. (1975), "Conditions for the localization of deformation in pressure-sensitive dilatant materials", in: *Journal of the Mechanics and Physics of Solids*, Vol. 23, No. 6, pp. 371–394 (cit. on pp. 5, 102, 104).

Rudnicki, J. (2013), "2011 Drucker Medal Paper: Localized Compaction in Porous Sandstones", in: *Journal of Applied Mechanics*, Vol. 80, No. 6, p. 061025 (cit. on p. 8).

Ruiz De Argandona, V., Rodriguez-Rey, A., Celorio, C., Calleja, L., and Del Rio, L. S. (2003), "Characterization by X-ray computed tomography of water absorption in a limestone used as building stone in the Oviedo Cathedral (Spain)", in: *Geological Society, London, Special Publications*, Vol. 215, No. 1, pp. 127–134 (cit. on p. 21).

Santamarina, J. C., Klein, A., and Fam, M. A. (2001), "Soils and waves: Particulate materials behavior, characterization and process monitoring", in: *Journal of Soils and Sediments*, Vol. 1, No. 2, pp. 130–130 (cit. on p. 19).

Sayers, C. and Kachanov, M. (1995), "Microcrack-induced elastic wave anisotropy of brittle rocks", in: *Journal of Geophysical Research: Solid Earth*, Vol. 100, No. B3, pp. 4149–4156 (cit. on p. 19).

Schreyer, H. and Neilsen, M. (1996), "Analytical and numerical tests for loss of material stability", in: *International Journal for Numerical Methods in Engineering*, Vol. 39, No. 10, pp. 1721–1736 (cit. on p. 106).

Scott Jr, T. E. and Abousleiman, Y. (2004), *Acoustical imaging and mechanical properties of soft rock and marine sediments*, tech. rep., University of Oklahoma (US) (cit. on p. 20).

Selvadurai, A. and Głowacki, A. (2008), "Permeability hysterisis of limestone during isotropic compression", in: *Groundwater*, Vol. 46, No. 1, pp. 113–119 (cit. on p. 14).

Shahin, G., Cil, M., and Buscarnera, G. (2018), "Assessment of statistical homogeneity in chemically treated granular materials", in: *Géotechnique Letters*, Vol. 8, No. 1, pp. 32–39 (cit. on p. 56).

Shahin, G., Desrues, J., Pont, S. D., Combe, G., and Argilaga, A. (2016), "A study of the influence of REV variability in double-scale FEM× DEM analysis", in: *International Journal for Numerical Methods in Engineering*, Vol. 107, No. 10, pp. 882–900 (cit. on p. 112).

Shibuya, S., Koseki, J., and Kawagushi, T. (2005), "Recent developments in deformation and strength testing og geomaterials", in: *Deformation characteristics of geomaterials. Taylor & Francis Group, London*, pp. 3–26 (cit. on p. 19).

Singh, M., Samadhiya, N., Kumar, A., Kumar, V., and Singh, B. (2015), "A nonlinear criterion for triaxial strength of inherently anisotropic rocks", in: *Rock Mechanics and Rock Engineering*, Vol. 48, No. 4, pp. 1387–1405 (cit. on p. 17).

Smits, R., De Waal, J., Van Kooten, J., *et al.* (1988), "Prediction of abrupt reservoir compaction and surface subsidence caused by pore collapse in carbonates", in: *SPE formation evaluation*, Vol. 3, No. 02, pp. 340–346 (cit. on pp. 14, 15).

Soriano, I., Ibraim, E., Andò, E., Diambra, A., Laurencin, T., Moro, P., and Viggiani, G. (2017), "3D fibre architecture of fibre-reinforced sand", in: *Granular Matter*, Vol. 19, No. 4, p. 75 (cit. on p. 54).

Stanchits, S. A., Lockner, D. A., and Ponomarev, A. V. (2003), "Anisotropic changes in P-wave velocity and attenuation during deformation and fluid infiltration of granite", in: *Bulletin of the Seismological Society of America*, Vol. 93, No. 4, pp. 1803–1822 (cit. on p. 19).

Stanchits, S., Fortin, J., Gueguen, Y., and Dresen, G. (2009), "Initiation and propagation of compaction bands in dry and wet Bentheim sandstone", in: *Pure and Applied Geophysics*, Vol. 166, No. 5-7, pp. 843–868 (cit. on p. 20).

Stefanou, I. and Sulem, J. (2014), "Chemically induced compaction bands: Triggering conditions and band thickness", in: *Journal of Geophysical Research: Solid Earth*, Vol. 119, No. 2, pp. 880–899 (cit. on p. 120).

Sternlof, K. R., Karimi-Fard, M., Pollard, D., and Durlofsky, L. (2006), "Flow and transport effects of compaction bands in sandstone at scales relevant to aquifer and reservoir management", in: *Water Resources Research*, Vol. 42, No. 7 (cit. on p. 9).

Sternlof, K. R., Rudnicki, J. W., and Pollard, D. D. (2005), "Anticrack inclusion model for compaction bands in sandstone", in: *Journal of Geophysical Research: Solid Earth*, Vol. 110, No. B11 (cit. on pp. 9, 11).

Sternlof, K. R. (2005), "Structural geology, propagation mechanics and hydraulic effects of compaction bands in sandstone.", in: (cit. on p. 9).

Sulem, J. and Ouffroukh, H. (2006), "Shear banding in drained and undrained triaxial tests on a saturated sandstone: Porosity and permeability evolution", in: *International journal of rock mechanics and mining sciences*, Vol. 43, No. 2, pp. 292–310 (cit. on p. 1).

Sun, W., Andrade, J. E., Rudnicki, J. W., and Eichhubl, P. (2011), "Connecting microstructural attributes and permeability from 3D tomographic images of in situ shear-enhanced compaction bands using multiscale computations", in: *Geophysical Research Letters*, Vol. 38, No. 10 (cit. on p. 8).

Sutton, M., Wolters, W., Peters, W., Ranson, W., and McNeill, S. (1983), "Determination of displacements using an improved digital correlation method", in: *Image and vision computing*, Vol. 1, No. 3, pp. 133–139 (cit. on p. 22).

Tagliaferri, F., Waller, J., Andò, E., Hall, S. A., Viggiani, G., Bésuelle, P., and DeJong, J. T. (2011), "Observing strain localisation processes in bio-cemented sand using x-ray imaging", in: *Granular Matter*, Vol. 13, No. 3, pp. 247–250 (cit. on p. 54).

Tembe, S., Vajdova, V., Wong, T.-f., and Zhu, W. (2006), "Initiation and propagation of strain localization in circumferentially notched samples of two porous sandstones", in: *Journal of Geophysical Research: Solid Earth*, Vol. 111, No. B2 (cit. on pp. 7, 13, 73).

Tengattini, A. (2015), "A micro-mechanical study of cemented granular materials", in: (cit. on p. 59).

Tondi, E., Antonellini, M., Aydin, A., Marchegiani, L., and Cello, G. (2006), "The role of deformation bands, stylolites and sheared stylolites in fault development in carbonate grainstones of Majella Mountain, Italy", in: *Journal of structural geology*, Vol. 28, No. 3, pp. 376–391 (cit. on pp. 2, 9, 11, 84).

Tudisco, E., Andò, E., Cailletaud, R., and Hall, S. A. (2017), "TomoWarp2: a local digital volume correlation code", in: *SoftwareX*, Vol. 6, pp. 267–270 (cit. on pp. 41, 61).

Tudisco, E., Hall, S., Charalampidou, E. M., Kardjilov, N., Hilger, A., and Sone, H. (2015a), "Full-field measurements of strain localisation in sandstone by neutron tomography and 3D-volumetric digital image correlation", in: *Physics Procedia*, Vol. 69, pp. 509–515 (cit. on pp. 61, 62).

Tudisco, E., Roux, P., Hall, S. A., Viggiani, G. M., and Viggiani, G. (2015b), "Timelapse ultrasonic tomography for measuring damage localization in geomechanics laboratory tests", in: *The Journal of the Acoustical Society of America*, Vol. 137, No. 3, pp. 1389–1400 (cit. on p. 20).

Vajdova, V., Baud, P., and Wong, T.-f. (2004a), "Compaction, dilatancy, and failure in porous carbonate rocks", in: *Journal of Geophysical Research: Solid Earth*, Vol. 109, No. B5 (cit. on pp. 2, 7, 15, 67, 72).

Vajdova, V., Baud, P., and Wong, T.-f. (2004b), "Permeability evolution during localized deformation in Bentheim sandstone", in: *Journal of Geophysical Research: Solid Earth*, Vol. 109, No. B10 (cit. on pp. 2, 12).

Vajdova, V., Baud, P., Wu, L., and Wong, T.-f. (2012), "Micromechanics of inelastic compaction in two allochemical limestones", in: *Journal of Structural Geology*, Vol. 43, pp. 100–117 (cit. on pp. 2, 7, 8, 12, 13, 15, 16, 72, 84).

Vajdova, V. and Wong, T.-F. (2003), "Incremental propagation of discrete compaction bands: Acoustic emission and microstructural observations on circumferentially notched samples of Bentheim", in: *Geophysical Research Letters*, Vol. 30, No. 14 (cit. on pp. 13, 20).

Vajdova, V., Zhu, W., Chen, T.-M. N., and Wong, T.-f. (2010), "Micromechanics of brittle faulting and cataclastic flow in Tavel limestone", in: *Journal of Structural Geology*, Vol. 32, No. 8, pp. 1158–1169 (cit. on pp. 8, 13, 16).

Van Geet, M., Lagrou, D., and Swennen, R. (2003), "Porosity measurements of sedimentary rocks by means of microfocus X-ray computed tomography (μCT)", in: *Geological Society, London, Special Publications*, Vol. 215, No. 1, pp. 51–60 (cit. on p. 21).

Viggiani, G., Andò, E., Takano, D., and Santamarina, J. (2014), "Laboratory X-ray tomography: A valuable experimental tool for revealing processes in soils", in: *Geotechnical Testing Journal*, Vol. 38, No. 1, pp. 61–71 (cit. on p. 45).

Viggiani, G., Bésuelle, P., Hall, S., and Desrues, J. (2010), "Sand deformation at the grain scale quantified through X-ray imaging", in: *Advances in Computed Tomography for Geomaterials: GeoX 2010*, pp. 1–16 (cit. on p. 54).

Viggiani, G. (2009), "Mechanisms of localized deformation in geomaterials: an experimental insight using full-field measurement techniques", in: *Mechanics of Natural Solids*, Springer, pp. 105–125 (cit. on pp. 22, 62).

Viggiani, G. and Hall, S. A. (2012), "Full-field measurements in experimental geomechanics: historical perspective, current trends and recent results", in: *ALERT Doctoral School*, pp. 3–67 (cit. on pp. 19, 120).

Vinegar, H. J. and Wellington, S. L. (1987), "Tomographic imaging of three-phase flow experiments", in: *Review of Scientific Instruments*, Vol. 58, No. 1, pp. 96–107 (cit. on p. 21).

Wang, W., Sluys, L., and De Borst, R. (1997), "Viscoplasticity for instabilities due to strain softening and strain-rate softening", in: *International Journal for Numerical Methods in Engineering 40 (20), 3839-3864.(1997)* (cit. on p. 107).

Weinberg, R. F., Veveakis, E., and Regenauer-Lieb, K. (2015), "Compaction-driven melt segregation in migmatites", in: *Geology*, Vol. 43, No. 6, pp. 471–474 (cit. on pp. 7, 9).

Wellington, S. L., Vinegar, H. J., *et al.* (1987), "X-ray computerized tomography", in: *Journal of Petroleum Technology*, Vol. 39, No. 08, pp. 885–898 (cit. on p. 21).

Withjack, E. *et al.* (1988), "Computed tomography for rock-property determination and fluid-flow visualization", in: *SPE formation evaluation*, Vol. 3, No. 04, pp. 696–704 (cit. on p. 21).

Wong, R. and Arthur, J. (1985), "Induced and inherent anisotropy in sand", in: *Geotechnique*, Vol. 35, No. 4, pp. 471–481 (cit. on p. 17).

Wong, T.-f. and Baud, P. (2012), "The brittle-ductile transition in porous rock: A review", in: *Journal of Structural Geology*, Vol. 44, pp. 25–53 (cit. on pp. 2, 7, 73, 99, 100).

Wong, T.-f., Baud, P., and Klein, E. (2001), "Localized failure modes in a compactant porous rock", in: *Geophysical Research Letters*, Vol. 28, No. 13, pp. 2521–2524 (cit. on pp. 2, 7, 8).

Wong, T.-f., David, C., and Menendez, B. (2004), "Mechanical compaction", in: *Mechanics of Fluid-Saturated Rocks*, Elsevier, pp. 55–114 (cit. on pp. 1, 14).

Wong, T.-f., David, C., and Zhu, W. (1997), "The transition from brittle faulting to cataclastic flow in porous sandstones: Mechanical deformation", in: *Journal of Geophysical Research: Solid Earth*, Vol. 102, No. B2, pp. 3009–3025 (cit. on pp. 1, 2, 7, 8, 12, 73, 99, 100).

Wong, T.-f., Szeto, H., and Zhang, J. (1992), "Effect of loading path and porosity on the failure mode of porous rocks", in: *Applied Mechanics Reviews*, Vol. 45, No. 8, pp. 281–293 (cit. on pp. 12, 20).

Wood, D. M. (1990), *Soil behaviour and critical state soil mechanics*, Cambridge university press (cit. on p. 100).

Wu, H., Papazoglou, A., Viggiani, G., Dano, C., and Zhao, J. (2018a), "3D multiscale modeling of compaction bands in Tuffeau de Maastriht", in: *In preparation* (cit. on p. 121).

Wu, H., Guo, N., and Zhao, J. (2018b), "Multiscale modeling and analysis of compaction bands in high-porosity sandstones", in: *Acta Geotechnica*, Vol. 13, No. 3, pp. 575–599 (cit. on p. 121).

Wu, X. Y., Baud, P., and Wong, T.-f. (2000), "Micromechanics of compressive failure and spatial evolution of anisotropic damage in Darley Dale sandstone", in: *International Journal of Rock Mechanics and Mining Sciences*, Vol. 37, No. 1-2, pp. 143–160 (cit. on pp. 2, 7, 8, 12).

Xie, S., Shao, J., and Xu, W. (2011), "Influences of chemical degradation on mechanical behaviour of a limestone", in: *International Journal of Rock Mechanics and Mining Sciences*, Vol. 48, No. 5, pp. 741–747 (cit. on p. 120).

Yuan, C., Chareyre, B., and Darve, F. (2016), "Pore-scale simulations of drainage in granular materials: finite size effects and the representative elementary volume", in: *Advances in water resources*, Vol. 95, pp. 109–124 (cit. on p. 55).

Zhang, J., Wong, T.-F., and Davis, D. M. (1990a), "Micromechanics of pressure-induced grain crushing in porous rocks", in: *Journal of Geophysical Research: Solid Earth*, Vol. 95, No. B1, pp. 341–352 (cit. on pp. 2, 12, 67, 84).

Zhang, J., Wong, T., Davis, D., *et al.* (1990b), "High pressure embrittlement and shear-enhanced compaction Berea sandstone: Acoustic emission measurement and microstructural observation", in: *The 31th US Symposium on Rock Mechanics (USRMS)*, American Rock Mechanics Association (cit. on p. 20).

Zhao, J., Wu, H., and Guo, N. (2016), "The evolving nature of compaction bands in highly porous sandstone: a multiscale view", in: (cit. on p. 121).

Zhu, W., Baud, P., Vinciguerra, S., and Wong, T.-f. (2011), "Micromechanics of brittle faulting and cataclastic flow in Alban Hills tuff", in: *Journal of Geophysical Research: Solid Earth*, Vol. 116, No. B6 (cit. on p. 13).

Zhu, W., Baud, P., and Wong, T.-f. (2010), "Micromechanics of cataclastic pore collapse in limestone", in: *Journal of Geophysical Research: Solid Earth*, Vol. 115, No. B4 (cit. on pp. 2, 8, 12–14, 16, 72, 119).

Zhu, W. and Wong, T.-f. (1997), "The transition from brittle faulting to cataclastic flow: Permeability evolution", in: *Journal of Geophysical Research: Solid Earth*, Vol. 102, No. B2, pp. 3027–3041 (cit. on pp. 2, 12).

Zijlstra, J. J. P. (1994), *Sedimentology of the Late Cretaceous and Early Tertiary (tuffaceous) chalk of northwest Europe*, Faculteit Aardwetenschappen (cit. on p. 25).